Perturbative QCD in Event Generation

Thesis submitted for the degree of

Doctor of Philosophy

by

Stefan Höche

Institute for Particle Physics Phenomenology

University of Durham

Durham 2008

Abstract

This thesis is concerned with the simulation of particle physics processes involving strong interactions in modern event generators. New algorithms to reinstate colour in colour-ordered amplitudes through colour dressing are presented and their analytical and numerical properties are discussed in detail. The colour-dressed Berends-Giele recursive relations are extended to the full Standard Model Lagrangian and implemented into the numerical program COMIX for large multiplicity matrix element computation. New algorithms for phase space integration are proposed, whereof one is capable to effectively couple colour and momentum sampling. Comparisons to other high-multiplicity generators are shown. QCD parton evolution and the CKKW algorithm to correctly include real next-to-leading order corrections are revisited. New types of jet measures are proposed for the merging of matrix elements and parton showers and their analytical and numerical properties are discussed. The implementation into the event generator SHERPA is presented using two different types of matrix element generators. Corresponding results and comparisons are shown. A further comparison between different types of merging algorithms is presented, including various numerical codes, which implement different merging approaches. Finally, the implementation of BFKL evolution in a Markovian approach is introduced and corresponding results from a numerical simulation are presented. Implications on event generation for current and future colliders are discussed throughout.

Acknowledgements

Firstly I would like to thank my supervisor, Frank Krauss, for his continuous support and the efforts he made to establish contact with people who have later become collaborators and friends. I acknowledge many interesting discussions with him and I am grateful for inspiration and encouragement during difficult periods.

I am indebted to my colleagues, who contributed to making my efforts a success, especially Frank Siegert, Steffen Schumann, Tanju Gleisberg, Jan Winter and Andreas Schälicke. I enjoyed working with them and our discussions have greatly improved my understanding of physics.

Thanks go to my collaborators, especially Claude Duhr, Fabio Maltoni and Thomas Teubner, who broadened my horizon and opened my view for various topics beyond the scope of this thesis. I am grateful for numerous discussions and explanations which lead to many interesting results.

Thanks also go to the staff at the IPPP in Durham, the CP^3 in Louvain-la-Neuve and the ITP in Dresden, especially to the secretaries Linda Wilkinson, Clare Thompson, Ginette Tabordon and Gundula Schädlich, who always helped to organise my life at work. I am grateful to Phil Roffe, Graeme Stewart and David Ambrose-Griffith for sorting out numerous computing problems and their help with the Grid.

I want to thank my friends for the enjoyable time we spent together. Your presence made every day appear a little brighter than it was. I thank my family for their love and support during my studies and for always providing a place for retreat and recreation. Finally, I want to thank my girlfriend for opening my mind and for the way she changed my life. Thank you, 胡欣 for making me smile every day.

Declaration

The work in this thesis is based on research carried out at the Institute for Particle Physics Phenomenology, Department of Physics, University of Durham, England, the Centre for Particle Physics and Phenomenology, Université Catholique de Louvain, Louvain-la-Neuve, Belgium and the Institut für theoretische Physik, Technische Universität Dresden, Dresden, Germany. No part of this thesis has been submitted elsewhere for any other degree or qualification.

The research described in this thesis was carried out in collaboration with C. Duhr, Dr. T. Gleisberg, Dr. F. Krauss, Prof. Dr. F. Maltoni, Dr. S. Schumann, F. Siegert and Dr. J.-C. Winter. It is based on the following works (in order of appearance in the text)

- C. Duhr, S. Höche and F. Maltoni,
  Color-dressed recursive relations for multi-parton amplitudes,
  JHEP **08** (2006), 062, [hep-ph/0607057].

- T. Gleisberg and S. Höche,
  Comix, a new matrix element generator,
  arXiv:0808.3674 [hep-ph].

- T. Gleisberg, S. Höche, F. Krauss and R. Matyskiewicz,
  How to calculate colourful cross-sections efficiently,
  arXiv:0808.3672 [hep-ph].

- S. Höche, F. Krauss, S. Schumann and F. Siegert,
  A comprehensive approach to CKKW merging,
  in preparation.

- J. Alwall et al.,
  Comparative study of various algorithms for the merging of parton showers and matrix elements in hadronic collisions,
  Eur. Phys. J. **C53** (2008), 473–500, [arXiv:0706.2569 [hep-ph]].

- S. Höche, F. Krauss and T. Teubner,
  Multijet events in the k_T-factorisation scheme,
  to be published in Eur. Phys. J. **C**, [arXiv:0705.4577 [hep-ph]].

Contents

Introduction

Particle physics at the high-energy frontier is nowadays largely centred around ground-based collider experiments. Examples for such experiments are the CDF and DØ collaborations at the Tevatron (Fermilab), the Zeus and H1 collaborations at Hera (DESY) and the Atlas and CMS collaborations at the upcoming LHC (CERN). The ultimate goal in current collider physics is to reveal the mechanism of electroweak symmetry breaking, the last ingredient missing to finally validate the Standard Model (SM) of particle physics. The Standard Model predicts the existence of a fundamental massive scalar particle, responsible for this symmetry breaking, the Higgs-particle. Bounds have been set on its potential mass by former experiments like LEP, but it has not directly been observed so far. Despite the tremendous success of the Standard Model, it is thus suggestive to speculate about potential theories going beyond it. Such theories would have to incorporate the Standard Model as an effective theory at scales where it has already been validated. From the theoretical point of view, the most natural extension of a theory like the Standard Model would be Supersymmetry (SUSY), introducing a new set of particles which carry exactly the same quantum numbers as their Standard Model counterparts, but differ in spin by one half. Supersymmetric models are particularly appealing, because they extend the Standard Model by the only nontrivial symmetry, which is not yet implemented. The fact that SUSY particles have not been observed so far, however, implies that, if Supersymmetry exists, it must be broken and the scale of SUSY breaking must lie beyond the energy region accessible in current experiments. Other prominent models are extra dimensional models, which assume the existence of additional space time dimensions and can eventually incorporate the fourth fundamental force, gravity.

However likely or unlikely a given model might be, all potential signatures at future colliders like the LHC have in common, that they will potentially be hidden by overwhelming Standard Model backgrounds. The large open phase space leads to emission of, in principle, arbitrarily many particles. In particular, the nature of quantum chromodynamics (QCD), turns out to be especially intriguing in this context. QCD is one of the most challenging theories today because the nonabelian structure of its Lagrangian and the vanishing gluon mass induce a running of the respective coupling, α_s, that leads to an increasing coupling with decreasing scale. At scales which are to be probed in collider experiments, QCD partons are free, however in the low-scale regime, where detectors operate, they form bound states, which carry no QCD charge. This poses two problems for LHC phenomenology.

Firstly, the evolution properties of QCD in the transition from high to low scales must be determined as accurately as possible and the corresponding evolution must be modelled to account for potential radiation effects that would affect the measurement. Secondly, assumptions have to be made about the transformation of partons into hadrons and the hadrons' decays.

Event generation

To compare theoretical predictions and experimental events in a detector, there are essentially two different strategies. Either the experimental signature is corrected back to the parton level through "running hadronisation and QCD evolution backwards", or the full final state is simulated by a computer program including all aspects described above. The former can be viewed as the "experimentalists approach" to validate a given prediction, while the latter is the "phenomenologists approach". It leads to the construction of computer programs known as event generators.

Event generators rely on the factorisation of an event into different stages, corresponding to different energy scales. This is pictorially represented by Fig. 1. In general the simulation starts with the hard process (dark red blob), where perturbation theory is applicable due to correspondingly high scales. This part of the simulation is handled by matrix element (ME) generators. QCD evolution is then run from the hard scale down to the hadronisation scale, which is of the order of $\Lambda_{QCD} \approx 1$ GeV. This leads to emission of further QCD partons and

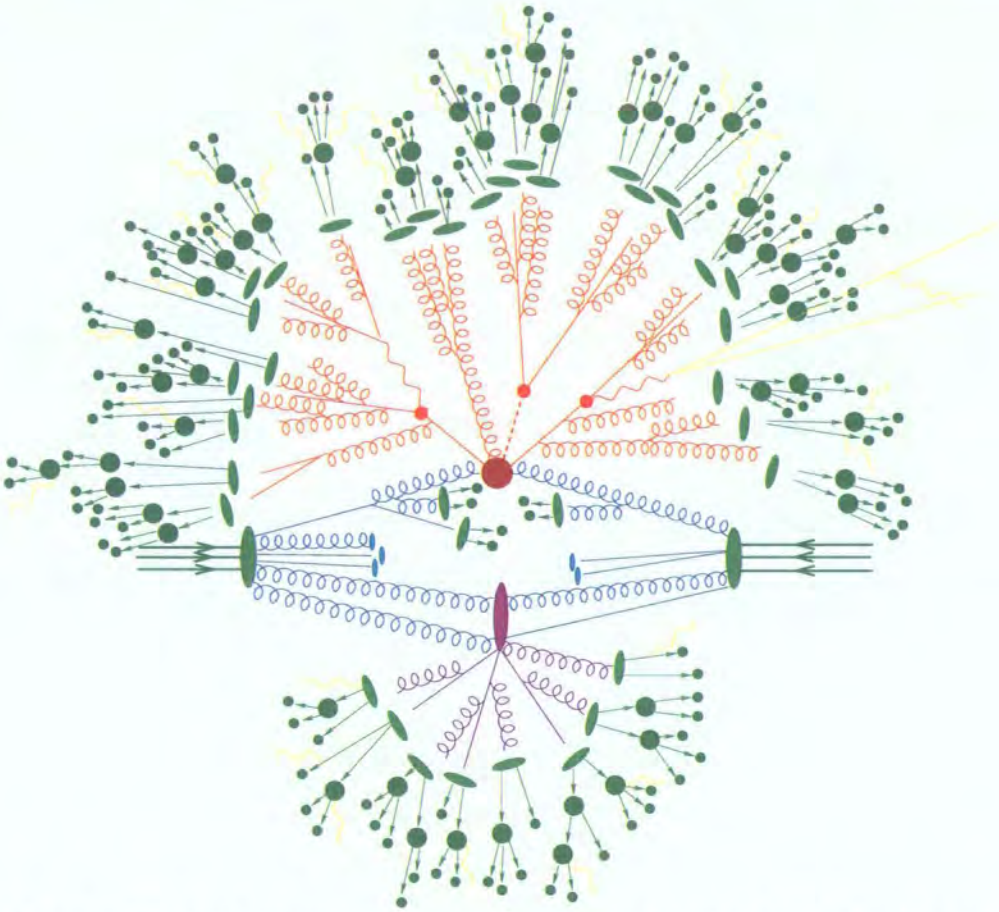

Fig. 1 Pictorial representation of a $t\bar{t}h$ event as produced by an event generator. The hard interaction (big red blob) is followed by the decay of both top quarks and the Higgs boson (small red blobs). Additional hard QCD radiation is produced (red) and a secondary interaction takes place (purple blob) before the final state partons hadronise (light green blobs) and hadrons decay (dark green blobs). Photon radiation occurs at any stage (yellow).

is handled by shower generators. Partons are now transformed into primary hadrons (light green blobs) through application of a fragmentation model and afterwards decayed into observed particles. A particularly difficult scenario might arise in hadronic collisions, which is depicted by the purple blob in Fig. 1. Remnants of incoming hadrons can themselves undergo a hard or semihard interaction, which then spoils the nice factorisation picture. This effect has been observed experimentally [1] and is addressed in a number of theoretical models [2, 3, 4, 5]. It is commonly referred to as the hard underlying event. Unfortunately, however, a correct quantum mechanical treatment is, at present, out of reach.

The most prominent examples of event generators are the well-established PYTHIA [6] and HERWIG [7] programs. They have been constructed over the past decades alongside with

experimental discoveries and most of the features visible in past and present experiments can be described through them. However, both the need for higher precision to meet the challenges of new energy scales at the LHC, and the complexity of final states at those scales have demanded those codes to be rewritten in a modern programming language. Object oriented frameworks will then allow to easily implement and test new physics models and potential variants of the old ones. Corresponding efforts led to the construction of the programs PYTHIA 8 [8] and HERWIG ++ [9].

Besides those rewrites, new programs have become available, which aim at a more accurate description of the hard perturbative regime through full next-to-leading order calculations, like MCFM [10]. Also, methods have been proposed for the consistent combination of fixed order corrections with shower programs, describing QCD evolution [11, 12]. Corresponding algorithms are implemented for example in MC@NLO [13] and HERWIG ++ [14].

In some cases, full next-to leading order calculations turn out to be quite cumbersome. Generally difficulties increase even more when going to next-to-next-to-leading order. On the other hand, the major part of real corrections stems from higher order tree-level matrix elements. If the aim is to correctly describe multi-jet topologies, rather than total rates, the preferred choice might be a tool, which takes these effects into account. As the need for better predictions in QCD processes with many particles in the final state has become clear, a substantial activity on developing corresponding techniques and tools has spurred. Several codes are now available that can compute corresponding cross sections and generate events in a fully automatic way. The most prominent examples are certainly ALPGEN [15], HELAC [16], MADGRAPH [17] and AMEGIC++ [18]. However, only AMEGIC++ is part of a fully equipped event generation framework, the SHERPA event generator.

The event generator SHERPA

SHERPA [19] is an acronym for Simulation of High Energy Reactions of PArticles. It stands for a fully equipped event generation framework, that has been constructed from scratch and is entirely written in the modern, object oriented programming language C++. It includes the automatic matrix element generator AMEGIC++, the parton cascade APACIC++ [20], a multiple parton interaction module, a fragmentation module [21], a hadron and tau decay

library [22] and a program for the simulation of QED radiation [23]. Over the past years, many improvements have been made and many additional features have been included, for example a shower based on Catani-Seymour dipole factorisation [24] and a dipole shower [25]. However, not all of the new features are publicly available yet and in the following, the default configuration of SHERPA is described.

AMEGIC++ is a tree level matrix element generator, based on Feynman diagrams, that is employed for hard matrix element generation throughout SHERPA. It implements a number of interaction models. Besides those for the Standard Model, Feynman rules are included for the MSSM [26], the ADD model [27], effective Higgs couplings to gluons, and others. The generator has been validated in a large number of processes [27, 26]. To evaluate single amplitudes, the helicity methods introduced in Refs. [28] are employed. Feynman diagrams are constructed and sorted according to their respective colour structure. A colour matrix for the full squared matrix element is computed using standard rules. Each single Feynman diagram is then decomposed into basic building blocks in the helicity formalism. The standard phase space integration as realised in AMEGIC++ relies on the factorisation techniques presented in Ref. [29], together with the multi-channel methods introduced in Ref. [30]. Single channels are constructed according to the pole structure of the diagrams leading to the full amplitude and are further refined using adaptive techniques [31]. Other phase space generators, according to Refs. [32, 33] are available. Recently Catani-Seymour dipole subtraction has been automated within AMEGIC++ [34].

QCD parton evolution is accounted for in SHERPA by the program APACIC++. APACIC++ is a standard parton cascade, ordered in virtuality, which implements initial and final state evolution and includes QED radiation effects. QCD coherence is included approximately by imposing an explicit angular veto in subsequent branchings. A particular feature of APACIC++ is that it has been set up for the merging with real next-to-leading order matrix elements, as delivered by AMEGIC++, through the Catani-Krauss-Kuhn-Webber (CKKW) algorithm [35,36]. This approach allows to consistently combine matrix elements of different final state multiplicities with parton showers, while the apparent problem of double counting large logarithmic enhancements is avoided. This has been realised within SHERPA in a fully general way, i.e. no intervention by the user is needed and it can be applied to any QCD associated process.

Underlying events are, in the framework of SHERPA, simulated by the AMISIC++ program [37], which implements a model for multiple parton scatterings [2]. This model essentially assumes that the underlying event in hard processes is generated by a sequence of independent hard scatterings, ordered in transverse momentum, which are connected only by the incoming hadrons and common hadronisation of final states. Care must be taken that, when employed in conjunction with the CKKW algorithm, the scale set by the hard process is respected and that it is chosen independent of the final state multiplicity. A corresponding algorithm is implemented into AMISIC++ in full generality. The original model withing PYTHIA has been extended in a similar way at the same time [3] and a model for PDF effects beyond naive rescaling has been incorporated [38].

For the last step of simulation, namely the fragmentation of partons into hadrons and the subsequent hadron decays, SHERPA has long been relying on the Lund string model [39] in the implementation of PYTHIA [40] and the respective decay routines. However, a new type of cluster fragmentation [41] has recently been developed and is now available in the code. It is essentially based on the continuation of a dipole shower model into the nonperturbative region, where the strong coupling is parametrised and can be tuned to better fit the data. The kinematics of cluster splittings into other clusters or hadrons are chosen according to Lorentz invariant evolution parameters. A hadron decay module has recently been completed, which includes a tau decay library and the simulation of all types of mixing effects for neutral mesons.

SHERPA itself is the framework, which puts together all the above and arranges the various phases of event generation. It contains common tool sets and implements the initialisation of the generator as well as the interaction with external software packages through standard interfaces. SHERPA has successfully been employed in experimental analyses [42] and is one of the most advanced new generation simulation programs today.

Motivation for this work

Compared to previous experiments, the LHC as next generation collider will pose completely new challenges to both the experimental and the theoretical community. It operates at the highest centre-of-mass energies and provides enormous luminosity. On the experimental

side, data acquisition, storage and processing therefore require the creation of a world-wide network for computing needs, the so-called Grid [43]. On the theoretical side, demands for higher precision to correctly model signals and backgrounds of new physics necessitate the construction of modern event generators.

As mentioned above, a great challenge in this respect is to correctly simulate production and evolution of QCD partons once they are generated in conjunction with a hard interaction. The correct quantum mechanical treatment of colour has significant impact on the respective results. A proper algorithm for merging matrix elements and parton showers including colour correlations must be incorporated in the simulation. Better shower models are nowadays available, yet it remains to establish the numerical programs for combining them with hard matrix elements. Perturbative QCD computations for large multiplicities need to be carried out in an automated way at tree- and loop-level, which necessitates the refinement of old and construction of new methods for numerics. Corresponding codes must be easy to deploy on the Grid.

Modern event generators are not only required to simulate hard QCD processes, however. For example the underlying event might contain semihard or even soft interactions, which are poorly described by perturbative QCD. A related issue is the reggeisation of the gluon and the respective link to the Pomeron, which governs the rise of the total cross section with increasing centre-of-mass energy. Corresponding questions can eventually be addressed at the LHC, leading to new insight about the behaviour of QCD at low scales. Hadronisation and hadron decay models will potentially be refined in the future due to better measurement of related parameters. Better simulation in this area can have significant impact on the understanding of physics at much higher energy scales.

In general, modern and flexible event generators are indispensable tools for data analysis. In the near future new and improved simulation programs will therefore replace the well-established traditional ones, allowing a wider range of applicability and more modular frameworks. The key idea is to offer phenomenologists an interface to hadron level events, where new ideas and better theoretical models can easily be implemented such that they can quickly be probed in experiments. At the same time the description of Standard Model backgrounds shall be improved. The construction, validation and extension of event generators is therefore one of the principal tasks of particle physics phenomenology today. This

thesis aims at contributing to this field through improving methods for perturbative QCD simulation within the framework of the event generator SHERPA.

Outline of this thesis

This thesis is divided into two parts. The first part is concerned with the computation of hard perturbative matrix elements and the efficient sampling of the corresponding phase space. As outlined above, this is one of the key ingredients for any physics simulation through an event generator. The basic formalism for matrix element computation is introduced and recent progress in the field is briefly outlined. A new approach for the recursive computation of QCD and QCD-associated amplitudes is then presented. New methods for phase space sampling are introduced, which allow the simulation of previously inaccessible signatures. A fully general numerical implementation of the corresponding algorithms into the program COMIX [44], within the framework of the SHERPA event generator is presented and results are compared to other high-multiplicity matrix element generators, such as AMEGIC++ and ALPGEN.

The second part of the thesis deals with the simulation of DGLAP and BFKL evolution as well as multi-jet-merging procedures. The basic concepts of parton shower generation are presented and the parton cascade APACIC++ is introduced. The CKKW algorithm as a method to systematically include real next-to-leading order corrections through appropriate matrix elements and merging with the parton shower is presented as an example for multi-jet merging. Improvements and extensions of the original algorithm are discussed, such as a method to incorporate colour information from colour sampled matrix elements. Using different matrix element generators, a comparison is performed for e^+e^--annihilation into hadrons and Drell-Yan lepton pair production. Other merging prescriptions are briefly introduced and a comparison between the results from SHERPA and other generators is presented. Finally a new strategy for the generation of BFKL evolution in a Markovian approach is introduced.

The two parts of the thesis are separately summarised. Implications of new or improved techniques of event generation for phenomenology and experiment are outlined and the impact on future event generators is discussed.

Part I

Computation of matrix elements

1 Fixed order perturbative QCD

The aim of this section is to introduce techniques for the computation of perturbative QCD tree-level matrix elements at fixed order. The motivation to develop methods beyond the traditional Feynman diagram approach are twofold. Firstly, it turns out that often the final formulae for QCD amplitudes have a much simpler structure than anticipated during intermediate steps of the computation. It might happen that there is even a convenient interpretation of the result, for example in terms of QCD antenna functions [45]. The traditional diagrammatic approach might hide such simplifications or analogies through an unnecessary complicated structure of intermediate terms. It is worthwhile to circumvent these complications, if possible. For example it turns out that many analytical perturbative QCD computations are greatly alleviated using novel techniques like the Britto-Cachazo-Feng (BCF) on-shell recursion discussed below. Secondly, one might gain additional insight into the underlying structure of perturbative QCD through techniques which yield results that are simple and easy to interpret. For example soft and collinear factorisation properties of QCD tree amplitudes can be understood in a very convenient way through the CSW technique [46, 47].

On the other hand it turns out that many of the newly emerging methods are very suited to solve a particular physical problem only, like for example the computation of a scattering amplitude in a certain helicity assignment of external particles. They can of course be invoked to yield results for the full theory, but in practice "old fashioned" methods are often much more suited for the task and more generally applicable.

Which technique to compute QCD scattering amplitudes is employed, thus depends very much on the purpose of the computation itself. Whenever an analytical result is desired,

one would rather focus on methods that yield the most compact analytical expressions and not care about their numerical evaluation. A popular example for this is the colour-dressed BCF recursion relation, presented in Ref. [48], which has a stunningly simple form. On the other hand, it leads to a factorial proliferation of terms, once a result must be computed numerically. Therefore, whenever the aim is the numerical evaluation of amplitudes and thus the computation of physical cross sections, the focus will be on the simplest implementation in terms of computer algebra and the best algorithmic choice to save computation time. At this point it is mostly found that traditional recursive methods to compute scattering amplitudes are the better alternatives [49, 48, 50].

The outline of this chapter is as follows. Firstly various methods to separate the amplitude computation into colour factors and the computation of planar diagrams are introduced. This point is crucial for both the basic CSW and the basic BCF relations. In Chapter 2, it will be shown how to reinstate colour information in the computation. Secondly, the Weyl-van der Waerden formalism to compute helicity amplitudes is reviewed, since it is one of the basic ingredients for the discussions in the following chapters. It is outlined how the analytical computation of tree-level amplitudes is performed in this method. Maximally helicity violating (MHV) amplitudes, which will be essential for the discussion of the CSW and the BCF relations, are derived. The Berends-Giele (BG), CSW and BCF relations are presented.

1.1 Colour Decompositions

In this section the method of colour decomposition is briefly outlined and the available results for tree-level QCD amplitudes with n gluons are presented as an example. Emphasis is given to those aspects which will play an important role in the following chapters.

The basic idea of a colour decomposition is to factorise the information on the gauge structure from the kinematics. Results are mostly formulated for an arbitrary number of colours N_C. This allows, for example in the context of a parton shower picture, cf. Part II, Chapter 1, to interpret results in the large N_C limit. In this context, quarks may thus carry a fundamental colour index $i = 1, \ldots, N_C$, antiquarks carry a fundamental "anticolour" index $\bar{\jmath} = 1, \ldots, N_C$ and gluons usually carry an adjoint colour index $a = 1, \ldots, N_C^2 - 1$. The

fundamental interaction between quarks and gluons is mediated by a term proportional $T^a_{i\bar{j}}$, T being the generators of $SU(N)$ in the fundamental representation. Gluons couple through f^{abc}, with f the being the structure constants of $SU(N)$. In the notation employed here, T's are normalised according to

$$T^a_{i\bar{j}} T^b_{\bar{j}i} = \delta^{ab} , \tag{1.1}$$

which allows some simplification in further computations. Structure constants are defined through

$$\left[T^a, T^b\right]_{i\bar{j}} = i f^{abc} T^c_{i\bar{j}} . \tag{1.2}$$

This definition immediately yields the relation

$$\begin{aligned} f^{abc} \operatorname{Tr}\left(T^c, \left[T^{d_1}, \left[T^{d_2}, \ldots \left[T^{d_{n-1}}, T^{d_n}\right] \ldots\right]\right]\right) = \\ - i \operatorname{Tr}\left(T^a, \left[T^b, \left[T^{d_1}, \ldots \left[T^{d_{n-1}}, T^{d_n}\right] \ldots\right]\right]\right) , \end{aligned} \tag{1.3}$$

which can be employed to rewrite a string of structure constants in terms of fundamental representation matrices. As an example, consider the amplitude $\mathcal{A}$ for n gluons of colours $a_1, a_2, \ldots, a_n$. Using Eq. (1.3) one can prove that, at tree level, such an amplitude can be decomposed as [51]

$$\mathcal{A}(1, \ldots, n) = \sum_{\sigma \in S_{n-1}} \operatorname{Tr}\left[T^{a_1} T^{a_{\sigma_2}} \ldots T^{a_{\sigma_n}}\right] A(1, \sigma_2, \ldots, \sigma_n) , \tag{1.4}$$

where the sum is over all $(n-1)!$ permutations of $(2, \ldots, n)$. Each trace corresponds to a particular colour structure. The factor associated with each colour structure, A, is called a colour-ordered amplitude. It is also referred to as a dual amplitude or partial amplitude. It depends on the four-momenta p_i and polarisation vectors ε_i of the n gluons, represented simply by the particle index in its argument. The colour-ordered amplitudes are far simpler to calculate than the full amplitude $\mathcal{A}$, since they contain only planar graphs and thus a much smaller number of Feynman diagrams contribute to them. They also have remarkable theoretical properties. Among those, a special role is played by the Kleiss-Kuijf relations [52]. These are linear relations amongst the amplitudes directly inherited from

the gauge structure, i.e., from colour, which in the case of n-gluon amplitudes reduce the number of linearly-independent amplitudes to $(n-2)!$. It is then clear that the number of terms in Eq. (1.4) cannot be minimal. This decomposition is, however neither unique nor special and other colour decompositions might be more suited for a particular problem. Eq. (1.4) is universally used to illustrate the idea of colour decompositions and to define the full amplitude $\mathcal{A}$ in terms of colour-ordered amplitudes A. It can be shown, however, that the above definition of colour-ordered amplitudes does not depend on the actual colour basis.

Recently, another decomposition has been introduced, which is based on colour flows [16,53]. This decomposition arises when treating the $SU(N)$ gluon field as an $N_C \times N_C$ matrix $(A_\mu)_{i\bar{\jmath}}$ $(i, \bar{\jmath} = 1, \ldots, N_C)$, rather than as a one-index field A^a_μ. To understand why this might be helpful, consider the term $T^a_{i\bar{\jmath}} T^a_{k\bar{l}}$, corresponding to the sum of all gluons propagating between two quark lines, i.e. the gluon propagator. This term can be decomposed as

$$T^a_{i\bar{\jmath}} T^a_{k\bar{l}} = \delta_{i\bar{l}}\delta_{k\bar{\jmath}} - \frac{1}{N_C}\delta_{i\bar{\jmath}}\delta_{k\bar{l}} \quad \leftrightarrow$$

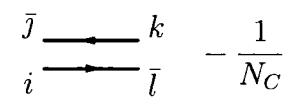

$$- \frac{1}{N_C}$$

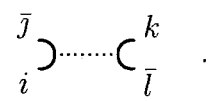

. (1.5)

Regarding these two terms, it becomes apparent why the basis for this decomposition is called the colour-flow basis. Both terms correspond to connecting indices of fundamental $SU(N)$ objects. Their sum gives a projection which exactly yields the $N_C^2 - 1$ degrees of freedom of the gluon field. Correspondingly, the elementary quark-gluon vertex is proportional to delta functions connecting the gluon and quark lines and quark lines are simple delta functions. Gauge couplings have a more complicated structure, which will be explained in detail in Chapter 2. The major advantage of this decomposition is that any colour factor can be decomposed into a product of delta functions. This allows a straightforward implementation into computer programs, since no matrix multiplications of complex valued matrices have to be performed, but only integer comparisons. Corresponding codes are therefore often much faster, even if the natural colour basis is not the colour-flow basis and therefore the number of terms in the sum over permutations is not minimal. This will be discussed in more detail in Chapter 2.

Within the colour-flow basis, the n-gluon amplitude may be decomposed as

$$\mathcal{A}(1,\ldots,n) = \sum_{\sigma\in S_{n-1}} \delta_{i_1}^{\bar{\jmath}_{\sigma_2}} \delta_{i_{\sigma_2}}^{\bar{\jmath}_{\sigma_3}} \cdots \delta_{i_{\sigma_n}}^{\bar{\jmath}_1} A(1,\sigma_2,\ldots,\sigma_n) \,, \tag{1.6}$$

where the sum is over all $(n-1)!$ permutations of $(2,\ldots,n)$. The partial amplitudes that appear in this decomposition are the same as in the decomposition in the fundamental representation. As can be seen here, another nice feature of the colour-flow decomposition is that the colour factors in front of each amplitude are either zero or one. A similar decomposition exists for all tree-level parton amplitudes including any number of quark pairs, gluons and colour singlet objects.

A third decomposition of the multi-gluon amplitude exists, which is based on the adjoint representation of $SU(N)$ rather than the fundamental representation [54]. It can be inferred from Eq. (1.3) using

$$(F^{a_2}F^{a_3}\cdots F^{a_{n-1}})_{a_1 a_n} = \mathrm{Tr}\left(T^{a_1},[T^{a_2},\ldots[T^{a_{n-1}},T^{a_n}]\ldots]\right) \,, \tag{1.7}$$

where $(F^a)_c^b = -if^{abc}$ are the adjoint-representation matrices of $SU(N)$. The n-gluon amplitude in this decomposition may be written as

$$\mathcal{A}(1,\ldots,n) = \sum_{\sigma\in S_{n-2}} (F^{a_{\sigma_2}}F^{a_{\sigma_3}}\cdots F^{a_{\sigma_{n-1}}})_{a_1 a_n} A(1,\sigma_2,\ldots,\sigma_{n-1},n) \,, \tag{1.8}$$

where the sum is over all $(n-2)!$ permutations of $(2,\ldots,n-1)$. The indices corresponding to the first and the last gluon are taken as "references" and are not included in the permutations. The partial amplitudes that appear in this decomposition are the same as in the other decomposition, but only $(n-2)!$ linearly-independent amplitudes are needed. In this respect this formulation is "minimal" as there is no redundancy and the Kleiss-Kuijf relations are embodied in the colour factors. As will be elaborated upon in Chapter 2, there exists a remarkable formal similarity with the BCF recursive relations, where two gluons are also taken as a reference to build up the full amplitude.

1.2 The Weyl-van der Waerden spinor formalism

In this section a brief introduction to the spinor formalism employed in the computation of helicity amplitudes is presented. The discussion closely follows Refs. [55, 56], where the algorithm was introduced in great detail. The focus will be on massless fermions and gauge particles, however masses can be introduced, for example in the formalism presented in Ref. [57]. This will be discussed in Chapter 3.

Although solutions to the Dirac and Maxwell equations are in principle known, the actual implementation in a given computation can be quite cumbersome. If an inconvenient spinor basis or unsuitable polarisation vectors are chosen, the computation can be unnecessarily complicated. A convenient way to define spinors is to employ the Weyl-van der Waerden formalism [58].

The basic formalism

Spinors in the $D(\frac{1}{2},0)$ and $D(0,\frac{1}{2})$ representation of the Lorentz group are called right- and left-handed Weyl spinors, respectively. They are defined through dotted and undotted spinor indices, such that ψ_a is a covariant (right-handed) and $\psi^{\dot{a}}$ is a contravariant (left-handed) spinor. Complex conjugation amounts to dotting and undotting indices, according to

$$\psi_{\dot{a}} = (\psi_a)^* , \qquad \psi^a = \left(\psi^{\dot{a}}\right)^* . \tag{1.9}$$

Spinor indices are lowered and raised using the spinor metric, given in terms of the ε tensor

$$\epsilon^{ab} = \epsilon^{\dot{a}\dot{b}} = \epsilon_{ab} = \epsilon_{\dot{a}\dot{b}} = \begin{pmatrix} 0 & 1 \\ -1 & 0 \end{pmatrix} . \tag{1.10}$$

To compute polarisation vectors and to describe the fundamental interactions between vectors and fermions, the matrices σ^μ are defined. They allow to decompose a four-vector, which

is an object of the $D(\frac{1}{2},\frac{1}{2})$ representation of the Lorentz group in terms of two spinors.

$$\sigma^{\mu\,\dot{a}b} = \left(\sigma^0, \vec{\sigma}\right) , \qquad \sigma^{\mu}_{a\dot{b}} = \left(\sigma^0, -\vec{\sigma}\right) , \tag{1.11}$$

where $\sigma^0 = \mathrm{I}$ is the 2×2 unit matrix and $\vec{\sigma}$ are the Pauli matrices. Using these definitions, an arbitrary real four vector k^μ can be rewritten as a 2×2 matrix

$$k_{\dot{a}b} = \sigma^{\mu}_{\dot{a}b} k_\mu = \begin{pmatrix} k^+ & k_\perp \\ k_\perp^* & k^- \end{pmatrix} , \quad \text{where} \quad \begin{aligned} k^\pm &= k^0 \pm k^3 \\ k_\perp &= k^1 + ik^2 \end{aligned} . \tag{1.12}$$

For massless vectors, one has $\vec{k}_\perp^2 = k^+ k^-$ and therefore a spinor $\xi(k)$ can be determined such that $k_{\dot{a}b} = \xi_{\dot{a}} \xi_b$.

$$k_{\dot{a}b} = \xi_{\dot{a}}(k)\, \xi_b(k) , \quad \text{where} \quad \xi_a(k) = \begin{pmatrix} \sqrt{k^+} \\ \sqrt{k^-}\, e^{i\phi_k} \end{pmatrix} , \quad \phi_k = \arg k_\perp . \tag{1.13}$$

Employing the definition of σ^μ, Eq. (1.11) again, conversely one obtains $2k^\mu = \sigma^{\mu}_{\dot{a}b} \xi^{\dot{a}} \xi^b$. Note that the above definition of ξ is not unique. Firstly, an arbitrary phase can be multiplied without changing the result. Secondly, Eq. (1.12) is ambiguous itself, because the x-, y- and z-direction along which $k_\perp$ and $k^\pm$ are defined can be changed through a rotation of the Pauli matrices. This can be referred to as the spinor gauge and the actual definition of the Pauli matrices as the preferred basis amounts to a gauge fixing.

In order to obtain the decomposition of a massive vector in terms of the above defined Weyl spinors, it is customary to employ the following decomposition of a massive four vector into massless ones

$$k^\mu = b^\mu - \kappa a^\mu , \quad \text{where} \quad \kappa = \frac{k^2}{2\,ak} . \tag{1.14}$$

In this respect, a^μ is an arbitrary light-like four-vector. Selecting a certain a^μ amounts to a gauge choice for the decomposition. According to the above formulae, one obtains

$$k^\mu = \frac{1}{2}\, \sigma^{\mu}_{\dot{a}b}\, b^{\dot{a}} b^b - \frac{\kappa}{2}\, \sigma^{\mu}_{\dot{a}b}\, a^{\dot{a}} a^b . \tag{1.15}$$

It is convenient to define the inner products in spinor space through

$$\langle \xi\eta \rangle = \xi_a \eta^a , \qquad [\xi\eta] = \xi_{\dot{a}} \eta^{\dot{a}} , \tag{1.16}$$

which immediately yields the relation $[\xi\eta] = \langle \xi\eta \rangle^*$. Due to the spinor metric ϵ, the inner product is antisymmetric in its arguments and the Schouten identity holds

$$\langle \phi\psi \rangle \langle \xi\eta \rangle + \langle \phi\xi \rangle \langle \eta\psi \rangle + \langle \phi\eta \rangle \langle \psi\xi \rangle = 0 . \tag{1.17}$$

For further computations, a shorthand notation is introduced which denotes the spinor $\xi_a(k_i)$ determined from a massless four vector k_i through Eq. (1.13) as $|k_i\rangle$ or $|i\rangle$ and the corresponding $\xi^{\dot{a}}(k_i)$ as $|k_i]$ or $|i]$. In full analogy $[i|\sigma^\mu|j\rangle = \sigma^{\mu\,\dot{a}b} \xi_{\dot{a}}(k_i) \xi_b(k_j)$. The invariant mass of a pair of massless particles described by the four vectors k_i and k_j is then given by

$$2\, k_i k_j = \frac{1}{2} [i|\sigma^\mu|i\rangle [j|\sigma_\mu|j\rangle = \langle ij \rangle \, [ji] . \tag{1.18}$$

Thus it can be seen that the spinor products are, up to a phase, square roots of Lorentz invariants. It is known that the final result for the squared amplitude will be directly expressible in terms of Lorentz invariants. Therefore all unphysical phases occurring due to gauge choices in the spinor products must cancel, which can be employed as a consistency check of the calculation.

Wave functions for helicity eigenstates

In this subsection, explicit Dirac spinors and polarisation vectors will be constructed employing the Weyl-van der Waerden formalism. A Dirac spinor belongs to the $D(\frac{1}{2}, 0) \oplus D(0, \frac{1}{2})$ representation of the Lorentz group and can be represented in terms of Weyl spinors as

$$\Psi = \begin{pmatrix} \phi^{\dot{a}} \\ \psi_a \end{pmatrix} . \tag{1.19}$$

The corresponding Dirac matrices read

$$\gamma^\mu = \begin{pmatrix} 0 & \sigma^{\mu\,\dot{a}b} \\ \sigma^\mu_{a\dot{b}} & 0 \end{pmatrix}, \qquad \gamma^5 = i\gamma^0\gamma^1\gamma^2\gamma^3 = \begin{pmatrix} -\sigma^0 & 0 \\ 0 & \sigma^0 \end{pmatrix}. \tag{1.20}$$

Covariant and contravariant spinors ψ_a and $\phi^{\dot{a}}$ can be singled out using the projectors

$$P_{R,L} = P_\pm = \frac{1 \pm \gamma^5}{2}. \tag{1.21}$$

The Dirac equation for a particle of mass m and four-momentum p^μ can be solved by employing the plane wave solutions $\Psi = \exp\{\pm ikx\}\,\Psi^\pm(k)$, which leads to the following Eigenspinor problem

$$0 = (p^\mu\gamma_\mu - m)\,u = \begin{pmatrix} -m & 0 & p^- & -p^*_\perp \\ 0 & -m & -p_\perp & p^+ \\ p^+ & p^*_\perp & -m & 0 \\ p_\perp & p^- & 0 & -m \end{pmatrix} u\,. \tag{1.22}$$

Eigenvalues are $\lambda = m \pm \sqrt{p^2}$. Defining the variables $\bar{p} = \mathrm{sgn}\,(p_0)\,|\vec{p}|$ and $\hat{p} = (\bar{p}, \vec{p}\,)$, a possible set of Eigenspinors is given by [57]

$$\begin{aligned} u_+(p,m) &= \frac{1}{\sqrt{2\bar{p}}}\begin{pmatrix} \sqrt{p_0 - \bar{p}}\,\chi_+(\hat{p}) \\ \sqrt{p_0 + \bar{p}}\,\chi_+(\hat{p}) \end{pmatrix}, \quad v_-(p,m) = \frac{1}{\sqrt{2\bar{p}}}\begin{pmatrix} -\sqrt{p_0 - \bar{p}}\,\chi_+(\hat{p}) \\ \sqrt{p_0 + \bar{p}}\,\chi_+(\hat{p}) \end{pmatrix}, \\ u_-(p,m) &= \frac{1}{\sqrt{2\bar{p}}}\begin{pmatrix} \sqrt{p_0 + \bar{p}}\,\chi_-(\hat{p}) \\ \sqrt{p_0 - \bar{p}}\,\chi_-(\hat{p}) \end{pmatrix}, \quad v_+(p,m) = \frac{1}{\sqrt{2\bar{p}}}\begin{pmatrix} \sqrt{p_0 + \bar{p}}\,\chi_-(\hat{p}) \\ -\sqrt{p_0 - \bar{p}}\,\chi_-(\hat{p}) \end{pmatrix}. \end{aligned} \tag{1.23}$$

The above definition has the apparent advantage, that massless spinors have two nonzero components only. This, together with Eqs. (1.20) greatly simplifies the computation for

massless theories. The Weyl spinors $\chi_\pm(p)$ read

$$\begin{aligned}\chi_+(\hat{p}) &= \frac{1}{\sqrt{\hat{p}^+}}\begin{pmatrix}\hat{p}^+\\ \hat{p}_\perp\end{pmatrix} = \begin{pmatrix}\sqrt{\hat{p}^+}\\ \sqrt{\hat{p}^-}e^{i\phi_{\hat{p}}}\end{pmatrix}\\ \chi_-(\hat{p}) &= \frac{e^{i\pi}}{\sqrt{\hat{p}^+}}\begin{pmatrix}-\hat{p}_\perp^*\\ \hat{p}^+\end{pmatrix} = \begin{pmatrix}\sqrt{\hat{p}^-}e^{-i\phi_{\hat{p}}}\\ -\sqrt{\hat{p}^+}\end{pmatrix}.\end{aligned} \tag{1.24}$$

They are orthogonal and normalised to $2\,|\hat{p}_0|$. The Eigenspinors $u_\pm$ and $v_\pm$ are thus orthogonal and normalised to $2m$ and $-2m$, respectively. In the following, the notation of Ref. [55] is adopted and massless Dirac spinors are also denoted using

$$u_\pm(k) = v_\mp(k) = |k^\pm\rangle\,, \qquad \bar{u}_\pm(k) = \bar{v}_\mp(k) = \langle k^\pm|\,. \tag{1.25}$$

Polarisation vectors for external vector bosons are constructed according to Ref. [56]. For massless gauge bosons the wave function V^μ satisfies Maxwell's equations and the Ansatz $V^\mu = \exp\{-ikx\}\,\varepsilon_\pm^\mu(k)$ can be made. One possible set of polarisation vectors is then given by

$$\varepsilon_\pm^\mu(p,k) = \pm\frac{\langle k^\mp|\gamma^\mu|p^\mp\rangle}{\sqrt{2}\,\langle k^\mp|p^\pm\rangle}\,. \tag{1.26}$$

In this context, k is an arbitrary light-like gauge vector, which must not be parallel to the momentum p. The above definition yields the polarisation sum of a light-like axial gauge

$$\sum_{\lambda=\pm}\varepsilon_\lambda^\mu(k,p)\varepsilon_\lambda^{\nu\,*}(k,p) = -g^{\mu\nu} + \frac{k^\mu p^\nu + k^\nu p^\mu}{kp}\,. \tag{1.27}$$

For massive vector bosons the wave function must satisfy Proca's equation and one obtains one additional polarisation

$$\varepsilon_\pm^\mu(p,k) = \pm\frac{\langle k^\mp|\gamma^\mu|b^\mp\rangle}{\sqrt{2}\,\langle k^\mp|b^\pm\rangle}\,, \qquad \varepsilon_0^\mu(p,k) = \frac{1}{m}\left(\langle b^-|\gamma^\mu|b^-\rangle - \kappa\langle k^-|\gamma^\mu|k^-\rangle\right), \tag{1.28}$$

where, as introduced above, $b = p - \kappa k$ and $\kappa = p^2/2pk$. Again k is an arbitrary light-like

gauge vector. The polarisation sum is however independent of k and reads

$$\sum_{\lambda=\pm,0} \varepsilon_\lambda^\mu(k,p)\varepsilon_\lambda^{\nu *}(k,p) = -g^{\mu\nu} + \frac{p^\mu p^\nu}{p^2} . \tag{1.29}$$

Note that the computation of terms like in Eq. (1.28) can be simplified by using the identities

$$\begin{aligned} \langle k^+|\gamma^\mu|p^+\rangle &= [k|\sigma^\mu|p\rangle , & \langle k^-|p^+\rangle &= \langle kp\rangle , \\ \langle k^-|\gamma^\mu|p^-\rangle &= \langle k|\sigma^\mu|p] , & \langle k^+|p^-\rangle &= [kp] . \end{aligned} \tag{1.30}$$

Equation (1.30) implies that for massless QCD, the two component Weyl-van der Waerden spinors are sufficient to compute any given scattering amplitude.

Connection to the helicity formalism

Another formalism to compute helicity amplitudes, based only on Lorentz invariants has been presented in Refs. [28]. It is the basis for many modern matrix element generators, like for example AMEGIC++ and MADGRAPH. The Weyl-van der Waerden formalism can easily be translated into this helicity formalism, since only the redundant phase information encoded in the spinor products must be eliminated.

Within the Weyl-van der Waerden formalism, the following relations hold

$$|i^\pm\rangle\langle i^\pm| = \frac{1 \pm \gamma^5}{2} \not{k}_i . \tag{1.31}$$

This is, however exactly the relation which defines the basic spinors within the helicity formalism, cf. Refs. [28] and therefore the connection is immediately established. Another, more convenient way to understand the relation between the two methods was presented in Ref. [55]. A brief summary of the arguments discussed ibidem is given in the following.

Within the full scattering amplitude, any spinor string must terminate, since otherwise the dependence on unphysical phases introduced by the gauge choices described above cannot be eliminated. Such a string has the form

$$\langle i_1 i_2\rangle\,[i_2 i_3]\,\langle i_3 i_4\rangle \ldots \langle i_{2n} i_1\rangle . \tag{1.32}$$

The question is, whether there is a general method to reduce the string to minimal pieces and what these pieces look like. A solution to the problem is obtained if one realises that $1 = \langle ij\rangle [ji] / 2\, k_i k_j$. Multiple insertions of this relation will yield strings of maximum length four, which can easily be evaluated. If its length is two, the string will simply be a scalar product. If its length is four, with the help of Eq. (1.31) and the Fierz rearrangement

$$\langle i^-|\gamma^\mu|j^-\rangle\langle k^-|\gamma_\mu|l^-\rangle \;=\; -2\,\langle ik\rangle\,[jl]\;, \tag{1.33}$$

one obtains

$$\begin{aligned}\langle ij\rangle\,[jl]\,\langle ln\rangle\,[ni] &= \frac{1}{4}\,\langle i^-|\gamma^\mu|j^-\rangle\langle j^-|\gamma_\mu|l^-\rangle\langle l^-|\gamma^\nu|n^-\rangle\langle n^-|\gamma_\nu|i^-\rangle \\ &= \mathrm{Tr}\left(\frac{1-\gamma^5}{2}\not{k}_i\not{k}_j\not{k}_l\not{k}_n\right) \\ &= 2\left(k_ik_j\;k_lk_n - k_ik_l\;k_jk_n + k_ik_n\;k_jk_l - i\epsilon_{\mu\nu\rho\sigma}k_i^\mu k_j^\nu k_l^\rho k_n^\sigma\right)\;.\end{aligned} \tag{1.34}$$

Up to a normalisation factor and with a proper choice of vectors, this is exactly the S-function of the helicity formalism, as defined in Ref. [28]. If k_0 and k_1 are the gauge vectors with $k_0k_1 = 0$, and p_1 and p_2 the vectors of Dirac particles, the corresponding S-functions in terms of Weyl-van der Waerden spinors read

$$\begin{aligned}S(+;p_1,p_2;k_0,k_1) &= \frac{\langle p_1p_2\rangle\,[p_2k_0]\,\langle k_0k_1\rangle\,[k_1p_1]}{\sqrt{4\,p_1k_0\;p_2k_0}} \\ S(-;p_1,p_2;k_0,k_1) &= \frac{[p_1p_2]\,\langle p_2k_0\rangle\,[k_0k_1]\,\langle k_1p_1\rangle}{\sqrt{4\,p_1k_0\;p_2k_0}}\end{aligned} \tag{1.35}$$

Equation (1.34) can be employed to transform results obtained with the the two different methods into each other.

1.3 The Berends-Giele recursive relations

In Ref. [59], Berends and Giele introduced the colour-ordered n-point gluon off-shell current J^μ, which can be defined as the sum of all colour-ordered Feynman diagrams with n external on-shell legs and a single off-shell leg with polarisation μ. The colour-ordered off-shell currents can then be constructed using the Berends-Giele recursive relations

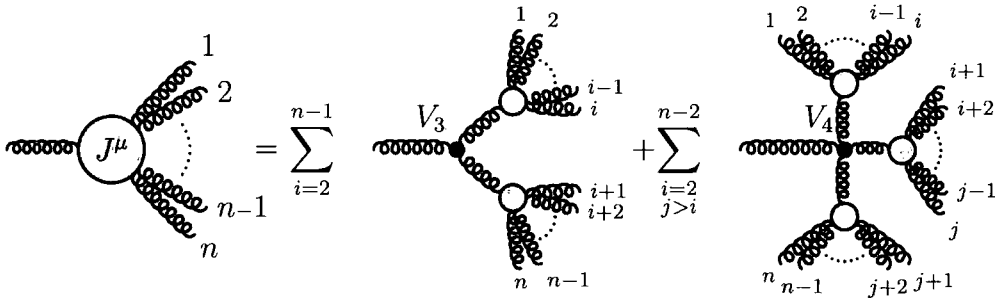

Fig. 1.1 Pictorial representation of the Berends-Giele recursive relations, Eq. (1.36)

$$J^\mu(1,2,\ldots,n) = \frac{-i}{P_{1,n}^2}\left\{\sum_{k=1}^{n-1} V_3^{\mu\nu\rho}(P_{1,k},P_{k+1,n})\,J_\nu(1,\ldots,k)J_\rho(k+1,\ldots,n) + \sum_{j=1}^{n-2}\sum_{k=j+1}^{n-1} V_4^{\mu\nu\rho\sigma} J_\nu(1,\ldots,j)J_\rho(j+1,\ldots,k)J_\sigma(k+1,\ldots,n)\right\}, \tag{1.36}$$

where the momentum sum $P_{i,j}$ is defined through

$$P_{i,j} = \sum_{k=i}^{j-1} p_k\,, \tag{1.37}$$

and where $V_3^{\mu\nu\rho}(P_{1,k},P_{k+1,n})$ and $V_4^{\mu\nu\rho\sigma}$ are the colour-ordered three and four-gluon vertices defined in Ref. [55].

$$\begin{aligned} V_3^{\mu\nu\rho}(P,Q) &= i\frac{g_s}{\sqrt{2}}\left(g^{\nu\rho}(P-Q)^\mu + 2g^{\rho\mu}Q^\nu - 2g^{\mu\nu}P^\rho\right), \\ V_4^{\mu\nu\rho\sigma} &= i\frac{g_s^2}{2}\left(2g^{\mu\rho}g^{\nu\sigma} - g^{\mu\nu}g^{\rho\sigma} - g^{\mu\sigma}g^{\nu\rho}\right). \end{aligned} \tag{1.38}$$

The algorithm is schematically depicted in Fig. 1.1. A full $n+1$-gluon amplitude is obtained by amputating the off-shell propagator and contracting the remaining quantity with the external polarisation of gluon $n+1$.

$$A(1,\ldots,n+1) = \varepsilon_{n+1}^\mu \frac{P_{1,n}^2}{i} J_\mu(1,\ldots,n)\,. \tag{1.39}$$

Similar recursions exists for the off-shell quark currents [59]. For some exceptional cases Eq. (1.36) can be solved in closed form [59, 60]. In particular one obtains the n-gluon

off-shell current with like-sign helicity gluons

$$J^{\mu}(1^+,\ldots,n^+) \;=\; g_s^{n-2}\,\frac{\langle k^-|\gamma^{\mu}\not{P}_{1,n}|k^+\rangle}{\sqrt{2}\langle k1\rangle\langle 12\rangle\ldots\langle n{-}1\,n\rangle\langle nk\rangle}. \tag{1.40}$$

It can be used to prove the form of maximally helicity violating (MHV) or Parke-Taylor tree amplitudes, which was first conjectured by Parke and Taylor in Ref. [61] and proved by Berends and Giele in Ref. [59]. Such amplitudes correspond to the "mostly plus" ("mostly minus") helicity assignment, where only two of n gluons have negative (positive) helicity. They are given by the simple formulae

$$\begin{aligned} A(1^+,\ldots,i^-,\ldots,j^-,\ldots,n^+) &= i\,g_s^{n-2}\,\frac{\langle ij\rangle^4}{\langle 12\rangle\ldots\langle n{-}1\,n\rangle\langle n1\rangle}\,, \\ A(1^-,\ldots,i^+,\ldots,j^+,\ldots,n^-) &= i\,g_s^{n-2}\,\frac{[ij]^4}{[12]\ldots[n{-}1\,n]\,[n1]}\,. \end{aligned} \tag{1.41}$$

The applicability of Berends-Giele type recursive relations in analytical calculations is somewhat limited due to the explicit occurrence of four-vectors and polarisations. For this reason, however they allow a straightforward implementation into computer programs and are hence particularly suited for numerical analysis. In Chapter 3, the concept of Berends-Giele type recursive relations will therefore be extended to the full Standard Model.

1.4 The CSW vertex rules

The aim of this section is to introduce the CSW vertex rules, which are one of the major theoretical improvements in the understanding of perturbative QCD in recent years. In this respect, unexpected progress has come from twistor-inspired methods [62], which have provided new techniques to compute analytic results for gauge amplitudes both at tree and one-loop level [63]. These new methods go back to a correspondence between a weakly coupled $\mathcal{N} = 4$ Super Yang-Mills theory and a certain type of string theory. The key point in this correspondence is that all tree-level colour-ordered amplitudes are related to algebraic curves in twistor space. In Ref. [64] it was shown that this leads to the CSW vertex rules. These rules state that it is possible to build arbitrary colour-ordered amplitudes from MHV amplitudes, which, in this context will also be referred to as MHV vertices [62,63,64]. These "elementary" vertices are connected by scalar propagators, thus eventually building up a full

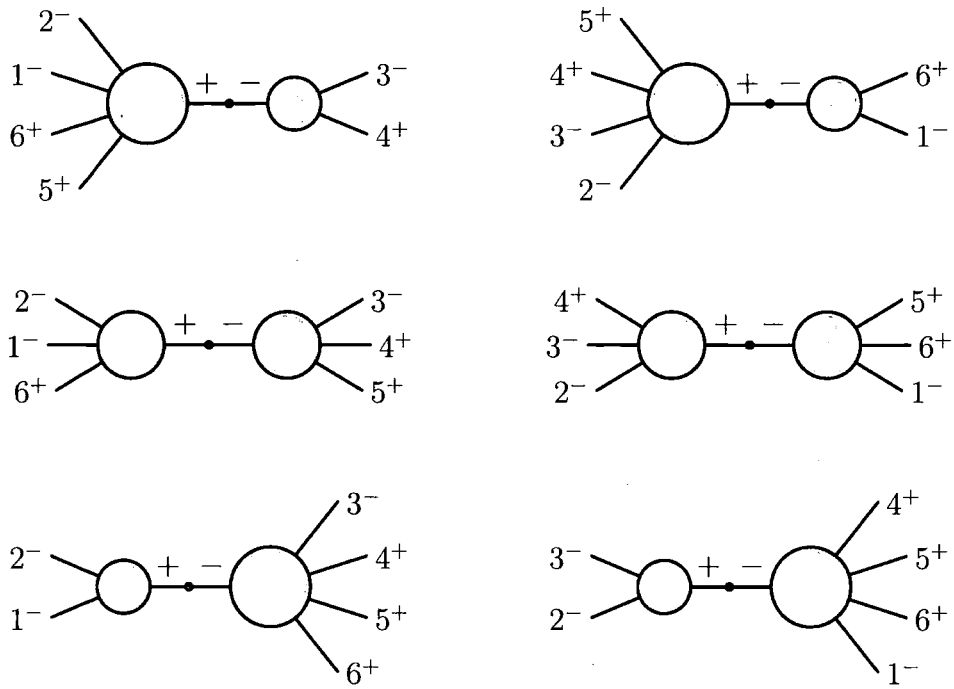

Fig. 1.2 The six MHV graphs for the computation of the 6-gluon non-MHV amplitude $A(-,-,-,+,+,+)$ in the CSW formalism. Gluons are represented by straight lines, while grey blobs denote MHV amplitudes.

n-gluon amplitude with $n-l$ like-sign helicity gluons through $l-1$ MHV amplitudes. Each off-shell leg with momentum P then corresponds to a spinor $P_{a\dot{a}}\eta^{\dot{a}}$, using some arbitrary contravariant reference spinor $\eta^{\dot{a}}$.

The CSW rules for constructing an arbitrary n-gluon colour-ordered amplitude are

1. For $n-l$ like-sign helicity gluons, draw all possible graphs connecting $l-1$ MHV vertices. In this context the 3-gluon MHV vertex must be included, since intermediate particles are off-shell and therefore the 3-gluon MHV amplitude does not vanish.

2. While maintaining their cyclic ordering, match the n external indices onto the above defined graphs, respecting the helicity assignment of the gluons. Typically this will eliminate a number of possible graphs.

This procedure is exemplified in Fig. 1.2, where all MHV graphs contributing to the 6-gluon amplitude $A(-,-,-,+,+,+)$ are shown. The algorithm can be reformulated such that only skeleton graphs containing the external legs with opposite sign helicity have to be drawn, while the like-sign helicity legs are distributed along the vertices as needed. In this context, only a single skeleton graph contributes to any non-MHV six-gluon amplitude.

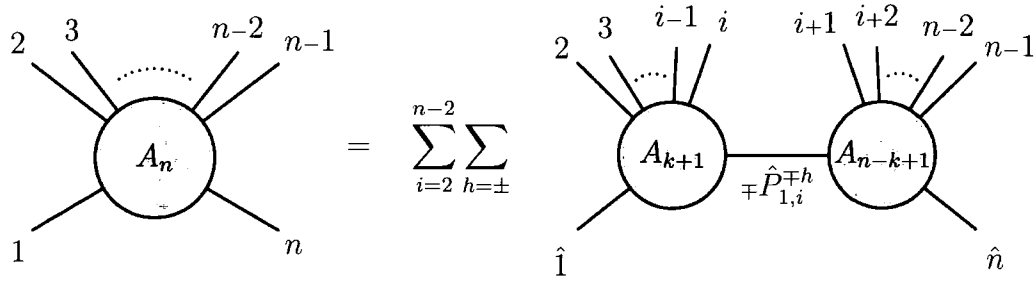

Fig. 1.3 Pictorial representation of the BCF recursive relations, Eq. (1.42).

The CSW rules imply that an n-point colour-ordered amplitude may have contributions from MHV vertices involving up to n particles. The number of different vertices is thus growing steadily with the number of particles, which makes it impossible to put for example Berends-Giele recursive relations and the CSW rules on the same footing. This problem has also been addressed in Ref. [65] and will be dealt with in Chapter 2, where it is shown how the CSW vertex rules can be rewritten in a truly recursive fashion.

1.5 The BCF recursive relations

In this section, the BCF recursive relations, presented in Refs. [66] shall be introduced. Like the CSW vertex rules presented above, they are an outcome of major theoretical improvements in the calculation of higher order QCD corrections. They state that any tree-level colour-ordered amplitude can be constructed from products of two on-shell amplitudes of fewer particles, multiplied by a simple scalar propagator. These new calculational tools have allowed to derive expressions for multi-parton amplitudes [67], which have simple and compact analytic forms.

Assuming an n-gluon amplitude with 1 and n being opposite sign helicity gluons, the BCF recursive relations read

$$A_n(1,2,\ldots,n) = \sum_{k=2}^{n-2} A_{k+1}\left(\hat{1},2,\ldots,k,-\hat{P}^{-h}_{1,k}\right)\frac{1}{P^2_{1,k}}A_{n-k+1}\left(\hat{P}^{h}_{1,k},k+1,\ldots,\hat{n}\right), \qquad (1.42)$$

where a sum over the helicities h of the intermediate gluon is implicit, and

$$\begin{aligned}\hat{P}_{1,k} &= P_{1,k} + z\lambda_n\tilde{\lambda}_1 \,, \\ \hat{p}_1 &= p_1 + z\lambda_n\tilde{\lambda}_1 \,, \\ \hat{p}_n &= p_n - z\lambda_n\tilde{\lambda}_1 \,.\end{aligned} \tag{1.43}$$

In this context λ_i and $\tilde{\lambda}_i$ are the co- and contravariant spinor components of the light-like momenta $p_i^{a\dot{b}} = \lambda_i^a \tilde{\lambda}_i^{\dot{b}}$. The shift parameter z is defined through

$$z = \frac{P_{1,k}^2}{\langle n|P_{1,k}|1]} \,. \tag{1.44}$$

The last two lines of Eq. (1.43) correspond to shifting the co- and contravariant components of p_1 and p_n, respectively. It is easily seen that $\hat{p}_1$ and $\hat{p}_n$ still have a factorised form and are therefore complex valued light-like vectors. This is in contrast to the CSW vertex rules, where intermediate gluon lines are off-shell. The subamplitudes in the BCF recursion are, however still not gauge invariant objects. Namely, the choice of reference opposite sign helicity gluons corresponds to a gauge choice, which enters the subamplitudes through dependence on the shift parameter z. Similar recursive relations exist for amplitudes with quarks and for QED processes. Equation (1.42) is schematically depicted in Fig. 1.3.

2 Colour dressed recursive relations for QCD

So far, many extensions of the twistor-inspired methods introduced in Chapter 1 have been constructed, in particular generalisations to include scalars [68], fermions [69] and photons [70]. In this chapter another new extension of the CSW and BCF techniques is presented. It is shown that it is possible to reformulate the twistor-inspired recursive relations for the colour-ordered amplitudes in terms of full amplitudes. The motivations are twofold. The first is mostly theoretical and stems from the observation of an interesting similarity between the colour decomposition Eq. (1.8), based on the adjoint representation, and the BCF recursive relations which suggested the existence of a formulation that embodies both. The second is more pragmatic and aims at establishing whether the new twistor-inspired recursive relations are an improvement also at the numerical level. In order to make a consistent comparison with the most efficient algorithms available [15,71], a recursive formulation which includes colour is necessary. In the standard approach where the colour-ordered amplitudes are calculated analytically (or numerically), one has to sum over the permutations of the colour orderings to obtain the full amplitude. This algorithm has an intrinsic factorial growth and cannot compete with the available numerical methods which only grow exponentially. In this chapter a general method to reinstate colour into the recursive relations for colour-ordered amplitudes is derived and applied to the BCF and to a modified version of the CSW relations.

This chapter is organised as follows. In Sec. 2.1 a simple derivation of the colour-dressed counterpart of the Berends-Giele recursive relations is presented, which serves as an illus-

tration of the method that will be applied later. In Section (2.2) the CSW vertex rules are reformulated in terms of simple new three-point effective vertices and the corresponding colour-dressed version is derived. In Sec. 2.3 one of the main results is proved, which is the colour-dressed version of the BCF relations, Eq. (2.43). Its most important features are discussed. Section 2.4 contains numerical results on the evaluation of multi-gluon amplitudes obtained using the different colour-dressed recursive relations, focusing on the comparison with known techniques.

2.1 Colour dressed Berends-Giele relations

Upon inspecting Eq. (1.36) it is easy to see that the four-gluon vertex appearing in the Berends-Giele recursive relations introduces a larger number of possible combinations of subcurrents than the three-gluon vertex. It is however possible to simplify the recursion by decomposing all four-gluon vertices into three-vertices including a tensor particle. This is schematically depicted in Fig. 2.1. Using this decomposition, the Berends-Giele recursive relations can be rewritten such that only three-point vertices are present

$$\begin{aligned} J^{\mu}(1,2,\ldots,n) \;=\; & \frac{-i}{P^2_{1,n}} \sum_{k=1}^{n-1} \Big\{ V_3^{\mu\nu\rho}\left(P_{1,k}, P_{k+1,n}\right) J_\nu(1,\ldots,k) J_\rho(k+1,\ldots,n) \\ & + V_T^{\nu\mu\alpha\beta} J_\nu(1,\ldots,k) J_{\alpha\beta}(k+1,\ldots,n) + V_T^{\mu\sigma\alpha\beta} J_{\alpha\beta}(1,\ldots,k) J_\sigma(k+1,\ldots,n) \Big\}\,, \end{aligned} \tag{2.1}$$

where $J_{\alpha\beta}$ is a tensor off-shell current, and $V_T^{\mu\nu\alpha\beta}$ is the tensor-gluon vertex, defined as

$$V_T^{\mu\nu\rho\sigma} = \frac{ig}{2}\left(g^{\mu\rho}g^{\nu\sigma} - g^{\mu\sigma}g^{\nu\rho}\right). \tag{2.2}$$

As there exists no one-point tensor off-shell current, all such currents appearing in Eq. (2.1) are defined as zero. The tensor off-shell currents can be easily constructed recursively from gluon off-shell currents

$$J_{\mu\nu}(1,2,\ldots,n) = iD_{\mu\nu\alpha\beta}\, V_T^{\sigma\rho\alpha\beta} \sum_{k=1}^{n-1} J_\rho(1,\ldots,k) J_\sigma(k+1,\ldots,n), \tag{2.3}$$

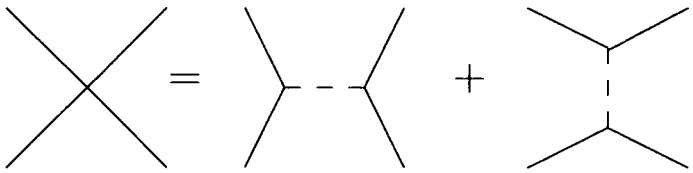

Fig. 2.1 Diagrammatic representation of the decomposition of the colour-ordered four-gluon vertex.

where $iD_{\mu\nu\alpha\beta}$ is the colour-ordered tensor "propagator", defined as

$$iD_{\mu\nu\rho\sigma} = -\frac{i}{2}\left(g^{\mu\rho}g^{\nu\sigma} - g^{\mu\sigma}g^{\nu\rho}\right). \tag{2.4}$$

A systematic method to dress colour-ordered recursive relations with colour is now presented in order to obtain recursive relations for the colour-dressed off-shell currents. In the colour-flow decomposition, a colour-dressed gluon off-shell current can be written as

$$\mathcal{J}^{\mu}_{I\bar{J}}(1,2,\ldots,n) = \sum_{\sigma\in S_n} \delta^{\bar{J}}_{i_{\sigma_1}} \delta^{\bar{J}_{\sigma_1}}_{i_{\sigma_2}} \ldots \delta^{\bar{J}_{\sigma_n}}_{I} J^{\mu}(\sigma_1,\sigma_2,\ldots,\sigma_n), \tag{2.5}$$

where $(I,\bar{J})$ is the colour of the off-shell leg. A colour-dressed tensor off-shell current can be obtained similarly. During the colour dressing of the Berends-Giele recursive relations, Eq. (2.1), the pure gluon vertices and the tensor-gluon vertices can be dealt with separately. After inserting Eq. (2.1), into the colour-flow decomposition, Eq. (2.5), the three-gluon vertex part reads

$$\frac{-i}{P^2_{1,n}} \sum_{\sigma\in S_n} \sum_{k=1}^{n-1} \delta^{\bar{J}}_{i_{\sigma_1}} \delta^{\bar{J}_{\sigma_1}}_{i_{\sigma_2}} \ldots \delta^{\bar{J}_{\sigma_n}}_{I} V_3^{\mu\nu\rho}\left(P_{\sigma_1,\sigma_k}, P_{\sigma_{k+1},\sigma_n}\right) J_{\nu}(\sigma_1,\ldots,\sigma_k) J_{\rho}(\sigma_{k+1},\ldots,\sigma_n), \tag{2.6}$$

where

$$\begin{aligned} P_{\sigma_1,\sigma_k} &= p_{\sigma_1} + p_{\sigma_2} + \ldots + p_{\sigma_k}, \\ P_{\sigma_{k+1},\sigma_n} &= p_{\sigma_{k+1}} + p_{\sigma_{k+2}} + \ldots + p_{\sigma_n}. \end{aligned} \tag{2.7}$$

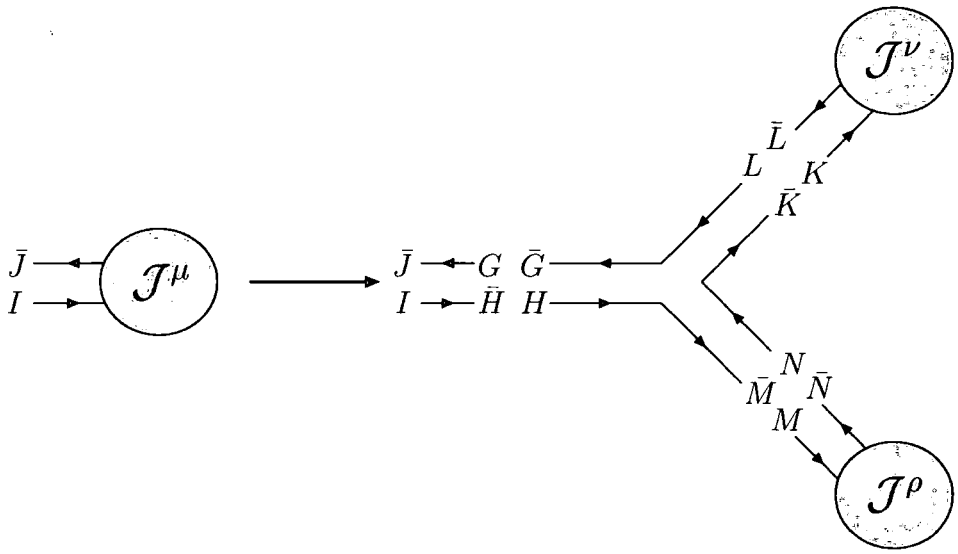

Fig. 2.2 Diagrammatic representation of the decomposition Eq. (2.8) of the colour factor of the three-gluon vertex part.

The colour factor appearing in Eq. (2.6) can be written as (cf. Fig. 2.2)

$$\delta^{\bar{J}}_{i_{\sigma_1}}\delta^{\bar{J}_{\sigma_1}}_{i_{\sigma_2}}\ldots\delta^{\bar{J}_{\sigma_n}}_{I} = \delta^{\bar{J}}_{G}\delta^{\bar{H}}_{I}\quad \delta^{\bar{G}}_{L}\delta^{\bar{K}}_{N}\delta^{\bar{M}}_{H}\quad \delta^{\bar{L}}_{i_{\sigma_1}}\ldots\delta^{\bar{J}_{\sigma_k}}_{K}\quad \delta^{\bar{N}}_{i_{\sigma_{k+1}}}\ldots\delta^{\bar{J}_{\sigma_n}}_{M}, \tag{2.8}$$

where

- $\delta^{\bar{J}}_{G}\delta^{\bar{H}}_{I}$ is the colour structure of the propagator appearing in the Berends-Giele recursive relations.

- $\delta^{\bar{L}}_{i_{\sigma_1}}\ldots\delta^{\bar{J}_{\sigma_k}}_{K}$ is the colour structure of the subcurrent $J_\nu(\sigma_1,\ldots,\sigma_k)$, where the off-shell leg ν has colour $(K,\bar{L})$.

- $\delta^{\bar{N}}_{i_{\sigma_{k+1}}}\ldots\delta^{\bar{J}_{\sigma_n}}_{M}$ is the colour structure of the subcurrent $J_\rho(\sigma_{k+1},\ldots,\sigma_n)$, where the off-shell leg ρ has colour $(M,\bar{N})$.

- $\delta^{\bar{G}}_{L}\delta^{\bar{K}}_{N}\delta^{\bar{M}}_{H}$ is part of the colour structure of a three-gluon vertex to which the off-shell legs μ, ν, ρ with colours $(G,\bar{H})$, $(K,\bar{L})$, $(M,\bar{N})$ are attached.

An ordered partition of a set E into two independent parts is now defined as a pair (π_1,π_2) of subsets of E such that $\pi_1\oplus\pi_2 = E$, which means $(\pi_1,\pi_2)\neq(\pi_2,\pi_1)$. Furthermore, an (unordered) partition of a set E into two independent parts is a set $\{\pi_1,\pi_2\}$ of subsets of E such that $\pi_1\oplus\pi_2 = E$ and $\{\pi_1,\pi_2\} = \{\pi_2,\pi_1\}$. These definitions can easily be extended to

partitions of a set E into $n > 2$ independent parts, for both the ordered and the unordered case.

In the case encountered here $E = \{1, 2, \ldots, n\}$. The set of all ordered partitions of E into two independent parts will be denoted by $OP(n, 2)$, while the set of all (unordered) partitions of E into two independent parts is denoted by $P(n, 2)$. Using these definitions, the sum over permutations appearing in Eq. (2.6) can be decomposed as follows: For a given value of k,

- Choose an ordered partition $\pi = (\pi_1, \pi_2)$ in $OP(n, 2)$ such that $\#\pi_1 = k$, where $\#\pi_1$ is the number of elements in the set π_1.
- Fix the first k elements of the permutation to be in the subset π_1.
- Sum over all permutations of the first k elements and over all permutations of the last $n - k$ elements.
- Sum over all possible choices for the ordered partition $\pi = (\pi_1, \pi_2)$.

This is equivalent to the replacement

$$\sum_{k=1}^{n-1} \sum_{\sigma \in S_n} \rightarrow \sum_{\pi \in OP(n,2)} \sum_{\sigma \in S_k} \sum_{\sigma' \in S_{n-k}} . \tag{2.9}$$

The three-gluon vertex part now reads

$$\begin{aligned} &\delta_G^{\bar{J}} \delta_I^{\bar{H}} \frac{-i}{P_{1,n}^2} \sum_{\pi \in OP(n,2)} \sum_{\sigma \in S_k} \sum_{\sigma' \in S_{n-k}} \delta_L^{\bar{G}} \delta_N^{\bar{K}} \delta_H^{\bar{M}} \; V_3^{\mu\nu\rho} \left(P_{\sigma_{\pi^1}, \sigma_{\pi^k}}, P_{\sigma'_{\pi^{k+1}}, \sigma'_{\pi^n}} \right) \\ &\quad \delta^{\bar{L}}_{i_{\sigma_{\pi^1}}} \ldots \delta_K^{\bar{J}_{\sigma_{\pi^k}}} J_\nu(\sigma_{\pi^1}, \ldots, \sigma_{\pi^k}) \; \delta^{\bar{N}}_{i_{\sigma'_{\pi^{k+1}}}} \ldots \delta_M^{\bar{J}_{\sigma'_{\pi^n}}} J_\rho(\sigma'_{\pi^{k+1}}, \ldots, \sigma'_{\pi^n}), \end{aligned} \tag{2.10}$$

where $\pi_1 = \{\pi^1, \pi^2 \ldots, \pi^k\}$ and $\pi_2 = \{\pi^{k+1}, \pi^{k+2}, \ldots, \pi^n\}$.

Clearly, $P_{\sigma_{\pi^1}, \sigma_{\pi^k}}$ and $P_{\sigma'_{\pi^{k+1}}, \sigma'_{\pi^n}}$ only depend on the choice of the ordered partition $\pi = (\pi_1, \pi_2)$, but not on the order of the elements in π_1 and π_2. Therefore one can define

$$\begin{aligned} P_{\pi_1} &= p_{\pi^1} + p_{\pi^2} + \ldots + p_{\pi^k}, \\ P_{\pi_2} &= p_{\pi^{k+1}} + p_{\pi^{k+2}} + \ldots + p_{\pi^n}. \end{aligned} \tag{2.11}$$

It is now possible to identify several subcurrents in this expression, namely

$$\begin{aligned}\mathcal{J}_\nu^{K\bar{L}}(\pi_1) &= \sum_{\sigma\in S_k} \delta^{\bar{L}}_{i_{\sigma_{\pi^1}}} \ldots \delta_K^{\bar{j}_{\sigma_{\pi^k}}} J_\nu(\sigma_{\pi^1},\ldots,\sigma_{\pi^k}),\\ \mathcal{J}_\rho^{M\bar{N}}(\pi_2) &= \sum_{\sigma'\in S_{n-k}} \delta^{\bar{N}}_{i_{\sigma'_{\pi^{k+1}}}} \ldots \delta_M^{\bar{j}_{\sigma'_{\pi^n}}} J_\rho(\sigma'_{\pi^{k+1}},\ldots,\sigma'_{\pi^n}),\end{aligned} \tag{2.12}$$

such that the three-gluon vertex part reads

$$\delta_G^{\bar{J}}\delta_I^{\bar{H}}\,\frac{-i}{P^2_{1,n}} \sum_{\pi\in OP(n,2)} \delta_L^{\bar{G}}\delta_N^{\bar{K}}\delta_H^{\bar{M}}\; V_3^{\mu\nu\rho}(P_{\pi_1},P_{\pi_2})\;\mathcal{J}_\nu^{K\bar{L}}(\pi_1)\;\mathcal{J}_\rho^{M\bar{N}}(\pi_2). \tag{2.13}$$

In Ref. [53] it was shown that the (colour-dressed) three-gluon vertex can be expressed in the colour-flow decomposition as

$$\mathcal{V}_3^{\mu\nu\rho}(P_{\pi_1},P_{\pi_2}) = \delta_L^{\bar{G}}\delta_N^{\bar{K}}\delta_H^{\bar{M}}\; V_3^{\mu\nu\rho}(P_{\pi_1},P_{\pi_2}) + \delta_N^{\bar{G}}\delta_L^{\bar{M}}\delta_H^{\bar{K}}\; V_3^{\mu\rho\nu}(P_{\pi_2},P_{\pi_1}), \tag{2.14}$$

where for brevity, the colour indices of the vertex are not written explicitly. So, finally the three-gluon vertex part can be written as

$$\delta_G^{\bar{J}}\delta_I^{\bar{H}}\,\frac{-i}{P^2_{1,n}} \sum_{\pi\in P(n,2)} \mathcal{V}_3^{\mu\nu\rho}(P_{\pi_1},P_{\pi_2})\,\mathcal{J}_\nu^{K\bar{L}}(\pi_1)\;\mathcal{J}_\rho^{M\bar{N}}(\pi_2). \tag{2.15}$$

Now the tensor-gluon part in the Berends-Giele recursive relations, Eq. (2.1) is addressed. From Fig. 2.3 it can be seen that for the s-channel appearing in the decomposition of the four-gluon vertex, each tensor-gluon vertex has the same colour-flow structure as a three-gluon vertex. The t-channel contribution is similar. Therefore the tensor-gluon vertex can be written in the colour-flow decomposition as

$$\mathcal{V}_T^{\mu\nu\alpha\beta} = \delta_{i_1}^{\bar{J}}\delta_{i_2}^{\bar{j}_1}\delta_I^{\bar{j}_2}\; V_T^{\mu\nu\alpha\beta} + \delta_{i_2}^{\bar{J}}\delta_{i_1}^{\bar{j}_2}\delta_I^{\bar{j}_1}\; V_T^{\nu\mu\alpha\beta}, \tag{2.16}$$

where $(I,\bar{J})$ is the colour of the tensor particle. The colour dressing of the tensor-gluon part in Eq. (2.1) is hence exactly the same as for the pure gluon part, leading to

$$\sum_{\pi\in OP(n,2)} \delta_L^{\bar{G}}\delta_N^{\bar{K}}\delta_H^{\bar{M}}\;\Big\{\, V_T^{\nu\mu\alpha\beta}\mathcal{J}_\nu^{K\bar{L}}(\pi_1)\mathcal{J}_{\alpha\beta}^{M\bar{N}}(\pi_2) + V_T^{\mu\nu\alpha\beta}\mathcal{J}_{\alpha\beta}^{K\bar{L}}(\pi_1)\mathcal{J}_\nu^{M\bar{N}}(\pi_2)\,\Big\}. \tag{2.17}$$

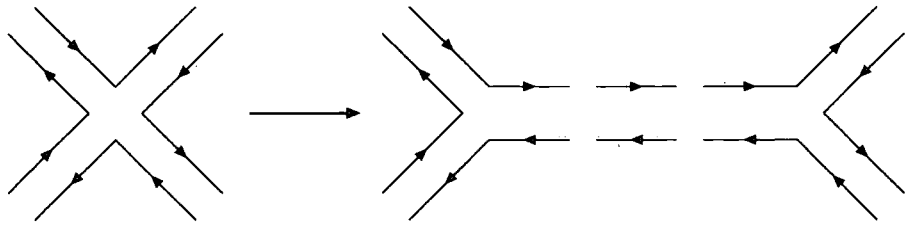

Fig. 2.3 Colour-flow structure of the s-channel contribution to the four gluon vertex.

As the sum runs over all elements in $OP(n,2)$, one can exchange π_1 and π_2 as well as the colour indices $(K,\bar{L})$ and $(M,\bar{N})$ in the last term. Using Eq. (2.16) the tensor part now becomes

$$\sum_{\pi\in OP(n,2)} \mathcal{V}_T^{\mu\nu\alpha\beta}\mathcal{J}_\nu^{K\bar{L}}(\pi_1)\mathcal{J}_{\alpha\beta}^{M\bar{N}}(\pi_2). \tag{2.18}$$

Hence the colour-dressed recursive relations with all four-gluon vertices replaced by tensor particles read

$$\begin{aligned}\mathcal{J}_\mu^{I\bar{J}}(1,\ldots,n) = D_{\mu\nu}(P_{1,n})\Bigg[&\sum_{\pi\in P(n,2)} \mathcal{V}_3^{\nu\rho\sigma}(P_{\pi_1},P_{\pi_2})\ \mathcal{J}_\rho^{K\bar{L}}(\pi_1)\mathcal{J}_\sigma^{M\bar{N}}(\pi_2)\\ &+\sum_{\pi\in OP(n,2)} \mathcal{V}_T^{\mu\rho\alpha\beta}\,\mathcal{J}_\rho^{K\bar{L}}(\pi_1)\,\mathcal{J}_{\alpha\beta}^{M\bar{N}}(\pi_2)\Bigg].\end{aligned} \tag{2.19}$$

To complete the colour dressing of the Berends-Giele recursive relations, one has to apply the colour-dressing method introduced above to the recursive relations for the off-shell tensor-currents, Eq. (2.3). Both the colour-dressed vertex and the colour-dressed off-shell tensor-current have the same form as in the pure gluon case and the recursive relations for the tensor particle, Eq. (2.3), have the same structure as for the three-gluon vertex part in the previous section. Therefore, one can immediately write down the colour-dressed recursive relations for the off-shell tensor-current

$$\mathcal{J}_{\mu\nu}^{I\bar{J}}(1,2,\ldots,n) = iD_{\mu\nu\alpha\beta}\mathcal{V}_T^{\sigma\rho\alpha\beta}\sum_{\pi\in P(n,2)} \mathcal{J}_\rho^{K\bar{L}}(\pi_1)\mathcal{J}_\sigma^{M\bar{N}}(\pi_2). \tag{2.20}$$

The two recursive relations, Eq. (2.19) and Eq. (2.20), can be solved simultaneously to

construct colour-dressed gluon off-shell currents for arbitrary n. The full colour-dressed scattering amplitude is then recovered be putting the off-shell leg on-shell. This result is equivalent to the Dyson-Schwinger algorithm presented in Ref. [72]. It should be noticed that the colour-dressed recursive relations have the same form as the colour-ordered Berends-Giele recursive relations, Eq. (2.1) and Eq. (2.3). The only difference between the colour-ordered and the colour-dressed case is that in the latter one sums over unordered objects and no permutations need to be taken into account. This is a general feature which will turn out to be common to all colour-dressed recursive relations.

2.2 Colour dressed CSW vertex rules

In this section the colour-dressing of the CSW vertex rules introduced in Chapter 1 is presented. As noted in Sec. 1.4, the original version of the CSW rules is not a truly recursive relation in the sense of the Berends-Giele or BCF recursion. Hence firstly a new method to decompose an MHV vertex into three-point vertices involving an auxiliary particle is introduced and recursive relations for both the auxiliary particle and the scalar propagators are presented. Once these relations have been obtained, the corresponding colour dressing is performed.

In analogy to the Berends-Giele recursive relations one defines an n-point scalar off-shell current $J_h(1,\ldots,n)$ as the sum of all MHV diagrams with n external on-shell legs, and one off-shell leg with helicity h. Note that in the context of the CSW rules, it makes sense to talk about the helicity of an off-shell particle. As the off-shell continuation of the spinors involves an arbitrary reference spinor $\eta^{\dot{a}}$, the scalar off-shell currents are not gauge invariant objects. However, the $\eta^{\dot{a}}$ dependence drops out in the end [64]. This scalar off-shell current can be easily constructed employing the CSW rules:

$$J_h(1,\ldots,n) = \frac{1}{P_{1,n}^2}\Bigg[\sum_{i=1}^{n-1} A_3\left(-P_{1,n}^{-h},\, P_{1,i}^{h_1},\, P_{i+1,n}^{h_2}\right) J_{h_1}(1,\ldots,i)\, J_{h_2}(i+1,\ldots,n) + \sum_{i=1}^{n-2}\sum_{j=i+1}^{n-1} A_4\left(-P_{1,n}^{-h},\, P_{1,i}^{h_1},\, P_{i+1,j}^{h_2},\, P_{j+1,n}^{h_3}\right) J_{h_1}(1,\ldots,i) \tag{2.21}$$
$$J_{h_2}(i+1,\ldots,j) J_{h_3}(j+1,\ldots,n) + \ldots\Bigg],$$

where the dots indicate terms with higher order MHV vertices. A sum over helicities $(h, h_1, h_2, \ldots)$ with $-h + h_1 + h_2 + \ldots = n - 4$ is implicit. According to the CSW rules, the vertices A_n correspond to off-shell continued n-point MHV amplitudes.
However, as mentioned in Sec. 1.4 in this form the CSW relations imply a factorial growth in the colour-dressed case, because of possibly large numbers of legs at single MHV vertices and the associated permutations of these legs. In order to tame this growth, the CSW relations are rewritten in a form similar to the Berends-Giele recursion with a tensor particle, where the terms in Tab. 2.1 serve as basic building blocks. First auxiliary double-lines are introduced, carrying threefold information:

- The total momentum P flowing in the double-line.
- A pair (k_l, k_r), describing the momenta flowing in each of the two lines separately. Notice that in general $k_l + k_r \neq P$.
- A pair (a, b), describing the momenta of the negative helicity legs in the corresponding MHV amplitude contained in the off-shell current. If no negative helicity gluon is attached to the double-line, then $a = b = 0$, and if only one negative helicity gluon is attached, then $b = 0$.

In order to build recursive relations where all n-point MHV vertices for $n \geq 4$ are decomposed into three-point vertices, one defines n-point (off-shell) double-line currents $J^{ab}_{uv}(1, \ldots, n)$, where $1 \leq u \leq v < n$, as the sum of all diagrams with n external on-shell legs and an (off-shell) auxiliary double-line. This line carries the information $(k_l, k_r) = (P_{1,u}, P_{v+1,n})$ and (a, b), a and b being the momenta of the negative helicity gluons attached to it. It is easy to see that all other assignments for (k_l, k_r) do not contribute in the colour-ordered case. Furthermore, in the colour-ordered case, a must be of the form $a = P_{i,j}$ with (i, j) constrained to one of the following possibilities

$$\begin{aligned} 1 \leq i \leq j \leq u, \\ u+1 \leq i \leq j \leq v, \\ v+1 \leq i \leq j \leq n \end{aligned} \tag{2.22}$$

and equivalently for b. Notice that according to the definition there are no one-point double-line currents. For later convenience one defines one-point double-line currents as zero. All

Right-handed Vertices	
	$V_{GG}^{h_i,h_j,h_k}(i,j,k) = \dfrac{\langle\alpha\beta\rangle^4}{\langle ij\rangle\langle jk\rangle\langle ki\rangle}$
	$V_{AG}^{h_i,h_j,a_kb_k}(i,j) = \dfrac{1}{\langle ij\rangle}\,\delta_{k_li}\delta_{k_rj}\,\epsilon(h_i,h_j,a_kb_k)$
	$V_{AAR}^{a_ib_i,h_j,a_kb_k}(i_l,i_r,j) = \dfrac{1}{\langle i_rj\rangle}\,\delta_{k_li_l}\delta_{k_rj}\,\epsilon(a_ib_i,h_j,a_kb_k)$
	$V_{GAR}^{a_ib_i,h_j,h_k}(i_l,i_r,j) = \dfrac{\langle\alpha\beta\rangle^4}{\langle i_rj\rangle\langle jk\rangle\langle ki_l\rangle}\,\epsilon(a_ib_i,h_j,h_k)$

Tab. 2.1 Right-handed basic building blocks in the MHV decomposition of colour-ordered amplitudes in the CSW approach. Details are given in the text.

other double-line currents can be built recursively employing the vertices given in Tab. 2.1, yielding

$$\begin{aligned} J_{uv}^{ab}(1,\ldots,n) &= \delta_{uv}\, V_{AG}^{h_1,h_2,ab}(P_{1,u},P_{u+1,n})\, J_{h_1}(1,\ldots,u)\, J_{h_2}(u+1,\ldots,n) \\ &+ (1-\delta_{uv}) \sum_{w=u}^{v-1} V_{AAR}^{a'b',h,ab}(P_{1,u},P_{w+1,v}P_{v+1,n})\, J_{uw}^{a'b'}(1,\ldots,v)\, J_h(v+1,\ldots,n)\,, \end{aligned} \tag{2.23}$$

where sums over repeated indices are always understood.

The indices α and β in Tab. 2.1 refer to the two particles with negative helicity within one MHV amplitude. The ϵ functions appearing in the vertices involving an auxiliary double-line keep track of the negative helicity gluons attached to them,

$$\epsilon \equiv \begin{cases} 1, & \text{if \#negative helicity gluons } \leq 2 \\ 0, & \text{if \#negative helicity gluons } > 2 \end{cases}\,. \tag{2.24}$$

A vertex vanishes if the number of negative helicity gluons attached to a double-line is greater than two, since this situation corresponds to a non-MHV amplitude, that has to be decomposed further by means of the CSW relations. No permutation of the incoming legs is allowed, since it would lead to double-counting. The respective rules in the $\overline{\text{MHV}}$ decomposition are obtained from the above by swapping helicities and replacing angular by

square brackets. In analogy to the double-line current, one can write the recursive relation for the scalar off-shell current in terms of double-line and scalar off-shell currents

$$J_h(1,\ldots,n) = \frac{1}{P_{1,n}^2}\sum_{k=1}^{n-1}\Bigg[V_{GG}^{h_1,h_2,h}(P_{1,k},P_{k+1,n})\,J_{h_1}(1,\ldots,k)\,J_{h_2}(k+1,\ldots,n) + \sum_{u=1}^{k-1}\sum_{v=u}^{k-1} V_{GAR}^{ab,h_1,h}(P_{1,u},P_{v+1,k},P_{k+1,n})\,J_{uv}^{ab}(1,\ldots,k)\,J_{h_1}(k+1,\ldots,n)\Bigg] . \tag{2.25}$$

Notice that the second term vanishes for $k = 1$ due to the vanishing of all one-point double-line currents.

The vertices given in Tab. 2.1 correspond to the situation where all gluons are attached on one side of the double-line. These vertices will be referred to as the *right-handed vertices*. Right-handed vertices are sufficient to construct all MHV amplitudes. However, it is convenient for the subsequent colour dressing of the CSW rules to recast Eq. (2.25) into a symmetric form. To do so, first one defines left-handed vertices where all the gluons are attached to the opposite side of the double-line. These vertices are shown in Tab. 2.2.[1] In the left-handed decomposition, the recursive relations Eq. (2.23) and Eq. (2.25) read

$$J_{uv}^{ab}(1,\ldots,n) = \delta_{uv}\,V_{AG}^{h_1,h_2,ab}(P_{1,u},P_{u+1,n})\,J_{h_1}(1,\ldots,u)\,J_{h_2}(u+1,\ldots,n) + (1-\delta_{uv})\sum_{w=u+1}^{v} V_{AAL}^{h,a'b',ab}(P_{1,u},P_{u+1,w},P_{v+1,n})\,J_h(1,\ldots,u)\,J_{wv}^{a'b'}(u+1,\ldots,n) , \tag{2.26}$$

$$J_h(1,\ldots,n) = \frac{1}{P_{1,n}^2}\sum_{k=1}^{n-1}\Bigg[V_{GG}^{h_1,h_2,h}(P_{1,k},P_{k+1,n})\,J_{h_1}(1,\ldots,k)\,J_{h_2}(k+1,\ldots,n) + \sum_{u=1}^{n-k-1}\sum_{v=u}^{n-k-1} V_{GAL}^{h_1,ab,h}(P_{1,k},P_{k+1,u},P_{v+1,n})\,J_{h_1}(1,\ldots,k)\,J_{uv}^{ab}(k+1,\ldots,n)\Bigg] . \tag{2.27}$$

Combining the right- and left-handed decompositions, it is possible to write the recursive

[1] As V_{GG} and V_{AG} are the same in both the right and left-handed decompositions, they are not listed again in Tab. 2.2.

Left-handed Vertices	
	$V_{AAL}^{h_i,a_jb_j,a_kb_k}(i,j_l,j_r) = \frac{1}{\langle ij_l\rangle}\,\delta_{k_li}\delta_{k_rj_r}\,\epsilon(h_i,a_jb_j,a_kb_k)$
	$V_{GAL}^{h_i,a_jb_j,h_k}(i,j_l,j_r) = \frac{\langle\alpha\beta\rangle^4}{\langle j_rk\rangle\langle ki\rangle\langle ij_l\rangle}\,\epsilon(h_i,a_jb_j,h_k)$

Tab. 2.2 Left-handed basic building blocks in the MHV decomposition of colour-ordered amplitudes in the CSW approach.

relations in a symmetric form involving both right-handed and left-handed vertices

$$\begin{aligned} J_{uv}^{ab}(1,\ldots,n) &= \delta_{uv}\, V_{AG}^{h_1,h_2,ab}(P_{1,u},P_{u+1,n})\, J_{h_1}(1,\ldots,u)\, J_{h_2}(u+1,\ldots,n) \\ &+ (1-\delta_{uv})\frac{1}{2}\sum_{w=u}^{v-1} V_{AAR}^{a'b',h,ab}(P_{1,u},P_{w+1,v},P_{v+1,n})\, J_{uw}^{a'b'}(1,\ldots,v)\, J_h(v+1,\ldots,n) \\ &+ (1-\delta_{uv})\frac{1}{2}\sum_{w=u+1}^{v} V_{AAL}^{h,a'b',ab}(P_{1,u},P_{u+1,w},P_{v+1,n})\, J_h(1,\ldots,u)\, J_{wv}^{a'b'}(u+1,\ldots,n) \end{aligned} \tag{2.28}$$

$$\begin{aligned} J_h(1,\ldots,n) = \frac{1}{P_{1,n}^2}\sum_{k=1}^{n-1}\Bigg[& V_{GG}^{h_1,h_2,h}(P_{1,k},P_{k+1,n})\, J_{h_1}(1,\ldots,k)\, J_{h_2}(k+1,\ldots,n) \\ &+ \frac{1}{2}\sum_{u=1}^{k-1}\sum_{v=u}^{k-1} V_{GAR}^{ab,h_1,h}(P_{1,u},P_{v+1,k},P_{k+1,n})\, J_{uv}^{ab}(1,\ldots,k)\, J_{h_1}(k+1,\ldots,n) \\ &+ \frac{1}{2}\sum_{u=1}^{n-k-1}\sum_{v=u}^{n-k-1} V_{GAL}^{h_1,ab,h}(P_{1,k},P_{k+1,u},P_{v+1,n})\, J_{h_1}(1,\ldots,k)\, J_{uv}^{ab}(k+1,\ldots,n)\Bigg]. \end{aligned} \tag{2.29}$$

These recursive relations, equivalent to the CSW vertex rules, can be solved simultaneously to construct the scalar off-shell current. The difference to the pure CSW approach without decomposition of the MHV vertices lies in the fact that the number of different vertices in Eqs. (2.28) and (2.29) is fixed and does not grow with the number of particles. The approach thereby differs from the one presented in Ref. [65]. Furthermore, as the number of different vertices is fixed and as only three-point vertices are present, these new recursive relations are well suited to be compared to the Berends-Giele recursive relations.

One can now turn to the colour dressing of the new CSW-like recursive relations. As they only contain three-point vertices, one expects the colour-dressed vertices to be of the same

form as in Eq. (2.14),

$$\mathcal{V}(P,Q) = \delta_L^{\bar{G}}\delta_N^{\bar{K}}\delta_H^{\bar{M}}\ V_R(P,Q) + \delta_N^{\bar{G}}\delta_L^{\bar{M}}\delta_H^{\bar{K}}\ V_L(Q,P). \tag{2.30}$$

In the colour-flow basis, the scalar off-shell currents are defined in the usual way

$$\mathcal{J}_h^{I\bar{J}}(1,\ldots,n) = \sum_{\sigma\in S_n} \delta_{i_{\sigma_1}}^{\bar{J}}\delta_{i_{\sigma_2}}^{\bar{J}_{\sigma_1}}\ldots\delta_I^{\bar{J}_{\sigma_n}} J_h(\sigma_1,\sigma_2\ldots,\sigma_n). \tag{2.31}$$

The colour-dressed n-point double-line currents are defined by

$$\begin{aligned}\mathcal{J}^{ab,I\bar{J}}_{\pi_l\pi_r}(\pi_l,\pi_m,\pi_r) = \sum_{\sigma\in S_u}\sum_{\sigma'\in S_{v-u}}\sum_{\sigma''\in S_{n-v}} \Bigg[&\delta_{i_{\sigma_{l,1}}}^{\bar{J}}\ldots\delta_{i_{\sigma'_{m,u+1}}}^{\bar{J}_{\sigma_{l,u}}}\ldots\delta_{i_{\sigma''_{r,v+1}}}^{\bar{J}_{\sigma'_{m,v}}}\ldots\delta_I^{\bar{J}_{\sigma''_{r,n}}}\\ &J^{ab}_{uv}(\sigma_{\pi_l},\sigma'_{\pi_m},\sigma''_{\pi_r}) + \delta_{i_{\sigma''_{r,v+1}}}^{\bar{J}}\ldots\delta_{i_{\sigma'_{m,u+1}}}^{\bar{J}_{\sigma''_{r,n}}}\ldots\delta_{i_{\sigma_{l,1}}}^{\bar{J}_{\sigma'_{m,v}}}\ldots\delta_I^{\bar{J}_{\sigma_{l,u}}}\\ &J^{ab}_{(n-v)(n-u)}(\sigma''_{\pi_r},\sigma'_{\pi_m},\sigma_{\pi_l})\Bigg],\end{aligned} \tag{2.32}$$

where π_l and π_r are two proper subsets of $\{1,2,\ldots,n\}$ referring to the momenta flowing in each line separately, $(k_l,k_r) = (P_{\pi_l},P_{\pi_r})$, and π_m is defined by $\pi_l\oplus\pi_m\oplus\pi_r = \{1,2,\ldots,n\}$ (Notice that π_m may be empty). On the right-hand side of Eq. (2.32), the indices (u,v) of the colour-ordered currents are defined by $(u,v) = (\#\pi_l, n-\#\pi_r)$ and

$$\begin{aligned}\pi_l &= \{\pi_l^1,\pi_l^2,\ldots,\pi_l^u\},\\ \pi_m &= \{\pi_m^{u+1},\pi_m^{u+2},\ldots,\pi_m^v\},\\ \pi_r &= \{\pi_r^{v+1},\pi_r^{v+2},\ldots,\pi_r^n\}.\end{aligned} \tag{2.33}$$

Finally, the symbols $\sigma_{i,j}$ are defined by $\sigma_{i,j} = \sigma(\pi_i^j)$. Notice that due to the second term appearing in Eq. (2.32), a colour-dressed n-point double-line current is symmetric in (π_l,π_r). The colour dressing is similar to the Berends-Giele case, but it contains some technical subtleties, which are explained in detail in Appendix A of Ref. [48]. They arise because the contributions from $u = v$ and $u \neq v$ in Eq. (2.32) have to be treated separately and because

the colour dressed double line current is defined in a symmetric way. The result is

$$\begin{aligned}\mathcal{J}_h^{I\bar{J}}(1,\ldots,n) =& \frac{1}{P_{1,n}^2}\Bigg[\sum_{\pi\in P(n,2)} \mathcal{V}_{GG}^{h_1,h_2,h}(P_{\pi_1},P_{\pi_2})\mathcal{J}_{h_1}^{K\bar{L}}(\pi_1)\mathcal{J}_{h_2}^{M\bar{N}}(\pi_2) \\ &+\frac{1}{2}\sum_{\pi\in OP(n,3)} \mathcal{V}_{GA}^{ab,h_1,h}(P_{\pi_1},P_{\pi_2},P_{\pi_3})\mathcal{J}_{\pi_1\pi_2}^{ab,K\bar{L}}(\pi_1,\pi_2)\mathcal{J}_{h_1}^{M\bar{N}}(\pi_3) \\ &+\frac{1}{2}\sum_{\pi\in OP(n,4)} \mathcal{V}_{GA}^{ab,h_1,h}(P_{\pi_1},P_{\pi_3},P_{\pi_4})\mathcal{J}_{\pi_1\pi_3}^{ab,K\bar{L}}(\pi_1,\pi_2,\pi_3)\mathcal{J}_{h_1}^{M\bar{N}}(\pi_4)\Bigg],\end{aligned} \tag{2.34}$$

$$\begin{aligned}\mathcal{J}_{\pi_l,\pi_r}^{ab,I\bar{J}}(\pi_l,\pi_m,\pi_r) =& \delta_{uv}\,\mathcal{V}_{AG}^{h_1,h_2,ab}(P_{\pi_l},P_{\pi_r})\mathcal{J}_{h_1}^{K\bar{L}}(\pi_l)\,\mathcal{J}_{h_2}^{M\bar{N}}(\pi_r) \\ &+(1-\delta_{uv})\frac{1}{2}\Bigg[\mathcal{V}_{AA}^{a'b',h,ab}(P_{\pi_l},P_{\pi_m},P_{\pi_r})\,\mathcal{J}_{\pi_l\pi_2}^{a'b',K\bar{L}}(\pi_l,\pi_m)\,\mathcal{J}_h^{M\bar{N}}(\pi_r) \\ &+\sum_{\pi\in OP(\pi_m,2)} \mathcal{V}_{AA}^{a'b',h,ab}(P_{\pi_l},P_{\pi_2},P_{\pi_r})\,\mathcal{J}_{\pi_l\pi_2}^{a'b',K\bar{L}}(\pi_l,\pi_1,\pi_2)\,\mathcal{J}_h^{M\bar{N}}(\pi_r) \\ &+(\pi_l\leftrightarrow\pi_r)\Bigg],\end{aligned} \tag{2.35}$$

where in Eq. (2.35) $OP(\pi_m,2)$ is the set of all ordered partitions of π_m into two independent parts.

Apart from a few subtleties, the procedure of the colour dressing is now similar to the Berends-Giele case. Again, a detailed discussion is given in Appendix A of Ref. [48]. The main differences are the following:

- As the colour-dressed vertices, Eq. (2.30), have both right and left-handed contributions, the symmetric form of the colour-ordered recursive relations, Eq. (2.28) and (2.29) is employed.

- The contributions coming from the $u=v$ and $u\neq v$ terms in Eq. (2.28) and Eq. (2.29) are treated separately. For example, the $u=v$ and $u\neq v$ contributions in Eq. (2.29) give rise to the $OP(n,3)$ and $OP(n,4)$ terms in Eq. (2.34), respectively.

Apart from these, the new CSW-like recursive relations retain the same form as the corresponding colour-ordered relations with the difference that in the colour-dressed case the sum goes over unordered objects. Furthermore, as in the colour-ordered case, the number

of different vertices is fixed and only three-point vertices appear in the recursive relations. Therefore one may compare them to the colour-dressed Berends-Giele recursive relation presented in Sec. 2.1.

2.3 Colour dressed BCF relations

In this section, the method employed to construct the colour-dressed Berends-Giele recursive relations is applied to the BCF recursive relations, presented in Ref. [66], cf. Chapter 1. Assuming that gluons 1 and n have opposite-sign helicities, the BCF recursive relations are given by Eq. (1.42).

As in Eq. (1.42) we have to choose two reference gluons, 1 and n, the colour-flow decomposition and the colour decomposition in the fundamental representation are not well suited to dress the BCF recursive relations with colour, because they allow to fix only one of the two reference gluons. The most natural colour decomposition which fixes both reference gluons is the colour decomposition in the adjoint representation, Eq. (1.8). Inserting the colour-ordered BCF relations, Eq. (1.42), into Eq. (1.8), one finds

$$\begin{aligned}\mathcal{A}_n(1,\ldots,n) = \sum_{k=2}^{n-2} \sum_{\sigma\in S_{n-2}} & \left(F^{a_{\sigma_2}}\ldots F^{a_{\sigma_{n-1}}}\right)_{a_1 a_n} A_{k+1}\left(\hat{1},\sigma_2,\ldots,\sigma_k,-\hat{P}^{-h}_{1,\sigma_k}\right) \\ & \frac{1}{P^2_{1,\sigma_k}} A_{n-k+1}\left(\hat{P}^{h}_{1,\sigma_k},\sigma_{k+1},\ldots,\sigma_{n-1},\hat{n}\right),\end{aligned} \tag{2.36}$$

where

$$P_{1,\sigma_k} = p_1 + p_{\sigma_2} + \ldots + p_{\sigma_k}. \tag{2.37}$$

For a given value of k, the sum over permutations appearing in Eq. (2.36) can be decomposed in a similar way as for the three-gluon vertex part in the Berends-Giele recursive relations. The procedure is as follows

- Choose an ordered partition $\pi = (\pi_1, \pi_2)$ of $\{2,3,\ldots,n-2,n-1\}$ such that $\#\pi_1 = k-1$.
- Fix the first $k-1$ elements of the permutation to be in the subset π_1.
- Sum over all permutations of the first $k-1$ elements and over all permutations of the

last $n-k-1$ elements.

- Sum over all possible choices for the ordered partition $\pi = (\pi_1, \pi_2)$.

This is equivalent to the replacement

$$\sum_{k=2}^{n-2} \sum_{\sigma \in S_{n-2}} \rightarrow \sum_{\pi \in OP(n-2,2)} \sum_{\sigma \in S_{k-1}} \sum_{\sigma' \in S_{n-k-1}}, \tag{2.38}$$

where by $OP(n-2,2)$ we denote the set of all ordered partitions of $\{2,3,\ldots,n-1\}$. Furthermore, for a fixed value of k, the colour factor can be written as

$$(F^{a_{\sigma_2}} \ldots F^{a_{\sigma_{n-1}}})_{a_1 a_n} = (F^{a_{\sigma_2}} \ldots F^{a_{\sigma_k}})_{a_1 x} (F^{a_{\sigma_{k+1}}} \ldots F^{a_{\sigma_{n-1}}})_{x a_n}, \tag{2.39}$$

where a sum over $x = 1,\ldots,8$ is understood.
Finally, the propagator clearly only depends on the choice of the ordered partition $\pi = (\pi_1, \pi_2)$ and not on the order of the elements in π_1 and π_2. If $\pi_1 = \{\pi^2, \pi^3, \ldots, \pi^k\}$, one defines

$$\begin{aligned} P_{1,\pi_1} &= p_1 + p_{\pi^2} + p_{\pi^3} + \ldots + p_{\pi^k}, \\ P_{\pi_2,n} &= -P_{1,\pi_1}. \end{aligned} \tag{2.40}$$

At this point it is possible to identify subamplitudes in the expression for $\mathcal{A}_n$, namely

$$\begin{aligned} \sum_{\sigma \in S_{k-1}} (F^{a_{\sigma_{\pi^2}}} \ldots F^{a_{\sigma_{\pi^k}}})_{a_1 x} A_{k+1}\left(\hat{1}, \sigma_{\pi^2}, \ldots, \sigma_{\pi^k}, -\hat{P}^{-h}_{1,\pi_1}\right) \\ = \mathcal{A}_{k+1}\left(\hat{1}, \pi_1, -\hat{P}^{-h,x}_{1,\pi_1}\right), \end{aligned} \tag{2.41}$$

$$\begin{aligned} \sum_{\sigma' \in S_{n-k-1}} \left(F^{a_{\sigma'_{\pi^{k+1}}}} \ldots F^{a_{\sigma'_{\pi^{n-1}}}}\right)_{x a_n} A_{n-k+1}\left(-\hat{P}^{-h}_{\pi_2,n}, \sigma'_{\pi^{k+1}}, \ldots, \sigma'_{\pi^{n-1}}, \hat{n}\right) \\ = \mathcal{A}_{n-k+1}\left(-\hat{P}^{-h,x}_{\pi_2,n}, \pi_2, \hat{n}\right), \end{aligned} \tag{2.42}$$

where x is the colour of the intermediate gluon.

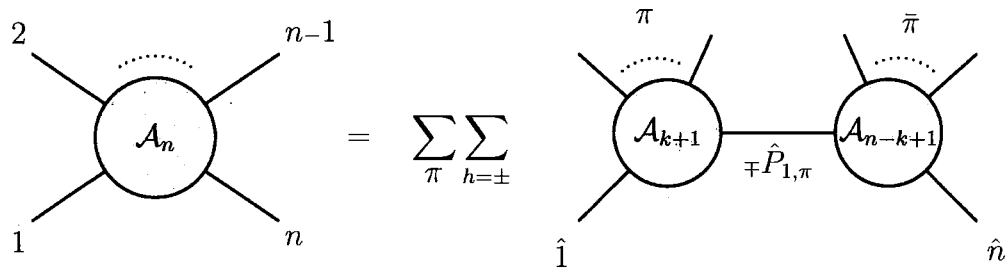

Fig. 2.4 Diagrammatic representation of the colour-dressed BCF recursive relations.

Collecting all the pieces, the colour-dressed BCF recursive relations read

$$\mathcal{A}_n(1,2,\ldots,n) = \sum_{\pi\in OP(n-2,2)} \mathcal{A}_{k+1}\left(\hat{1},\pi_1,-\hat{P}^{-h,x}_{1,\pi_1}\right)\frac{1}{P^2_{1,\pi_1}}\,\mathcal{A}_{n-k+1}\left(\hat{P}^{h,x}_{1,\pi_1},\pi_2,\hat{n}\right). \tag{2.43}$$

We emphasise that although the proof of these new recursive relations relies on the adjoint colour basis, the final result, Eq. (2.43), is independent of the choice of the basis. Furthermore, as in the case of the Berends-Giele recursive relations, we see that the form of the colour-dressed BCF recursive relations stays the same as in the colour-ordered case, with the only difference that in Eq. (2.43) the sum goes over all partitions of $\{2,3,\ldots,n-1\}$, i.e. over unordered objects. This implies that the new colour-dressed BCF recursive relations have the same properties as in the colour-ordered case, namely

1. The definition of the off-shell shifts, Eqs. (1.43), is independent of the colour.

2. As in the colour-ordered BCF recursive relations, the pole structure of the scattering amplitude is manifest in Eq. (2.43).

3. Similar to the colour-ordered case, the subamplitudes in Eq. (2.43) are not independent, but they are linked via the off-shell shifts.

The result, Eq. (2.43) obtained for amplitudes containing only gluons can be easily extended to include a single pair of massless quarks. For amplitudes containing a single $q\bar{q}$ pair, the colour decomposition reads [55]

$$\mathcal{A}_n(1_q,2,\ldots,n-1,n_{\bar{q}}) = \sum_{\sigma\in S_{n-2}} (T^{a_{\sigma_2}}\ldots T^{a_{\sigma_{n-1}}})_i^{\ \bar{j}}\ A_n\left(1_q,\sigma_2,\ldots,\sigma_{n-1},n_{\bar{q}}\right). \tag{2.44}$$

The BCF recursive relations for colour-ordered amplitudes still hold when a quark pair is included, where either a quark or a gluon can be chosen as the intermediate particle [69]. If a quark is chosen for the internal line, no sum over helicities has to be carried out, because helicity is conserved all along the fermion line. The BCF recursive relations then read

$$A_n(1_q^h, 2, \ldots, n_{\bar{q}}^{-h}) = \sum_{k=2}^{n-2} A_{k+1}\left(\hat{1}_q^h, 2, \ldots, k, -\hat{P}_{\bar{q},1k}^{-h}\right) \frac{1}{P_{q,1k}^2} A_{n-k+1}\left(\hat{P}_{q,1k}^h, k+1, \ldots, n-1, \hat{n}_{\bar{q}}^{-h}\right) , \tag{2.45}$$

where h is the helicity of the quark. Both the recursive relations and the colour decomposition have the same form as in the case of a pure gluon amplitude, with the only difference that instead of working in the adjoint representation one now has to work in the fundamental representation of $SU(3)$. So the recursive relations derived in the case of pure gluon amplitudes can be easily extended to include a single $q\bar{q}$ pair

$$\mathcal{A}_n(1_q^h, 2, \ldots, n_{\bar{q}}^{-h}) = \sum_{\pi \in OP(n-2,2)} \mathcal{A}_{k+1}\left(\hat{1}_q^h, \pi_1, -\hat{P}_{\bar{q},1\pi_1}^{-h,x}\right) \frac{1}{P_{q,1\pi_1}^2} \mathcal{A}_{n-k+1}\left(\hat{P}_{q,1\pi_1}^{h,x}, \pi_2, \hat{n}_{\bar{q}}^{-h}\right) . \tag{2.46}$$

The formula is exactly the same as in the pure gluon case, up to two small differences:

- no helicity sum has to be carried out for the internal line
- x is a colour index in the fundamental representation.

It is possible to extend this relation to include photons, by simply performing the substitution

$$(T^a)_i^{\bar{j}} \rightarrow \delta_i^{\bar{j}}. \tag{2.47}$$

From this it follows that a QED amplitude containing a single $q\bar{q}$ pair and $n-2$ photons can be written in terms of colour-ordered amplitudes as

$$\mathcal{A}_n^{QED}(1_q, 2, \ldots, n-1, n_{\bar{q}}) = \sum_{\sigma \in S_{n-2}} A_n(1_q, \sigma_2, \ldots, \sigma_{n-1}, n_{\bar{q}}). \tag{2.48}$$

Thus the above recursive relations, Eq. (2.45) still hold for QED amplitudes. This particular result has already been pointed out by Stirling and Ozeren in Ref. [70]. However, as shown there, for QED processes it is more efficient to take one of the fermions and one photon as reference particles. In fact, as there is no photon-photon vertex, all the terms in the recursive relations where both fermions are in the same subamplitude vanish, simplifying the calculation.

2.4 Numerical results

All relations for calculating multi-gluon amplitudes presented in the previous sections have been implemented into C++ Monte Carlo programs using the tools set ATOOLS and the integration package PHASIC [19]. A comparison of calculation times for helicity summed colour-ordered amplitudes versus the results obtained in Ref. [49] has been performed. The implementations yield exactly the same growth in computation time, except for the CSW rules, where one gains considerably due to rewriting the CSW vertex rules in terms of recursive relations for internal lines. Furthermore it was checked, employing the colour-flow basis, that the colour-dressed relations yield the same results as calculations employing colour-ordered amplitudes along with the colour-flow decomposition presented in Ref. [53]. Using the adjoint representation, it was checked that the colour-dressed BCF relations yield the same result as the colour-ordered ones along with a decomposition of the total amplitude in the adjoint basis.

A comparison of the computation times for the various approaches using the colour-flow basis can be found in Tab. 2.3. The colour-dressed Berends-Giele relations are the fastest method for more than five final state gluons. For less than six outgoing gluons the colour-flow decomposition using colour-ordered amplitudes calculated according to the BCF recursion performs better. In this case only few valid colour flows exist [53] and primarily (or only) MHV vertices contribute. For those the computation time increases only linearly with the number of outgoing particles in the colour-ordered BCF relations.

It is apparent that the computation times in the colour-dressed BCF and in the colour-dressed CSW case grow very fast. In the case of the CSW relations the reason is the number of types of internal lines, which is larger than in the Berends-Giele and in the BCF

Final	BG		BCF		CSW	
State	CO	CD	CO	CD	CO	CD
$2g$	0.24	0.28	0.28	0.33	0.31	0.26
$3g$	0.45	0.48	0.42	0.51	0.57	0.55
$4g$	1.20	1.04	0.84	1.32	1.63	1.75
$5g$	3.78	2.69	2.59	7.26	5.95	5.96
$6g$	14.2	7.19	11.9	59.1	27.8	30.6
$7g$	58.5	23.7	73.6	646	146	195
$8g$	276	82.1	597	8690	919	1890
$9g$	1450	270	5900	127000	6310	29700
$10g$	7960	864	64000	-	48900	-

Tab. 2.3 Computation time (s) of the $2 \to n$ gluon amplitudes for 10^4 phase space points, sampled over helicity and colour. Results are given for the colour-ordered (CO) and the colour-dressed (CD) Berends-Giele (BG), Britto-Cachazo-Feng (BCF) and Cachazo-Svrček-Witten (CSW) relations. Numbers were generated on a 2.66 GHz Xeon^{TM} CPU.

approach. In this respect it is important to note that each double line may eventually carry zero, one or two indices of attached negative helicity gluons. Additionally, in most cases two vertices exist for either of these lines (cf. Tab. 2.1), yielding a large amount of lines that finally have to be computed. However, the growth one encounters by employing this method is still not factorial but exponential. Nevertheless the factor in the exponent is still too large for the method to be competitive with the Berends-Giele approach. This fact is illustrated in Tab. 2.4, where the average number of nonzero internal lines counted either by value or by origination vertex is listed. The former corresponds to the average number of nonzero currents in the Berends-Giele approach.

Employing the colour-dressed BCF relations, a factorial growth of computation time is encountered. Three main reasons are identified:

- The subamplitudes are linked by the spinor shifts.

- The natural colour basis is the adjoint basis.

- The amplitudes are decomposed down to three-point vertices.

These points are addressed in order.

In the colour-dressed as well as in the colour-ordered BCF relations, Eqs. (2.43) and (1.42), the subamplitudes of a given decomposition are linked via the shifts Eqs. (1.43). Thus

Final State	Currents (BG)	Internal lines (CSW) by		MHV vertices (BCF) by	
		vertex	value	vertex	value
$2g$	7.04	3.48	7.56	1.98	1.98
$3g$	19.50	8.56	27.45	4.43	4.57
$4g$	44.67	18.58	109.0	14.13	18.17
$5g$	95.74	38.63	407.4	63.88	126.3
$6g$	198.8	78.25	1648	297.2	1026
$7g$	405.8	157.8	6773	1395	10330
$8g$	850.3	325.8	31340	6073	124600

Tab. 2.4 Average number of nonzero currents in the colour-dressed Berends-Giele relations, average number of internal lines in the CSW approach and average number of nonzero MHV vertices in the colour-dressed BCF relations using the colour-flow decomposition. MHV vertices in BCF are counted either by distinct value or by distinct assignment of unshifted external momenta. Internal lines in CSW are counted either by vertex or by distinct value.

the BCF relations need a recursive calculation of subamplitudes in the sense that the total amplitude is to be decomposed successively into smaller building blocks, finally yielding only three-point MHV vertices. In other words, one has to take Eq. (2.43) literally and apply a top-down approach of the computation, since for the evaluation of each subamplitude all previous spinor shifts have to be computed. Figuratively speaking, this is due to the fact that in the BCF recursion all subamplitudes "remember" which decomposition they originated from, thus inhibiting the calculation of general colour-dressed subamplitudes. This fact is also illustrated in Tab. 2.4, where the average number of distinct nonzero MHV vertices is listed along with the average number of distinct assignments of unshifted momenta at these vertices. The latter corresponds to the average number of internal lines in the CSW approach, counted by origination vertex. It grows much slower than the former, although faster than for example the average number of nonzero currents in the Berends-Giele relations.

When applying the top-down procedure of the computation described above, it is necessary to avoid the calculation of terms yielding zero due to the colour assignment of external and internal lines. This can be done in two steps. First, all valid colour flows are identified employing an algorithm similar to the one used for the Berends-Giele recursion. Second, the subamplitudes are calculated only for the valid colour structures. The calculation can be alleviated if the reference particles in the recursion are chosen such that together they

Process	Colour flow	Adjoint
$gg \to 2g$	0.78	0.86
$gg \to 3g$	0.83	0.74
$gg \to 4g$	0.94	0.60
$gg \to 5g$	1.14	0.51
$gg \to 6g$	1.44	0.44

Tab. 2.5 Ratio of the average number of nonzero MHV vertices in the colour dressed and the colour-ordered case in the colour-flow and the adjoint representation decomposition.

form a colour current having a non-vanishing contribution to the respective amplitude. Since there exists no decomposition assigning both particles to a common subamplitude, the corresponding colour current does not contribute anymore. This procedure eliminates many terms in the recursion, but it is still insufficient in the case of the colour-flow basis. In fact one expects some redundancy in the calculation of colour-ordered subamplitudes due to the dual Ward identities, which is introduced by fixing the reference particles for all possible colour flows of an amplitude simultaneously, cf. Eq. (2.43). To see this, consider a dual Ward identity of the form

$$A(2,1,3,\ldots,n) = -\sum_{l\neq 2;\ 1\leq l<n} A(1,\ldots,l,2,l+1,\ldots,n)\ . \tag{2.49}$$

Assume that particles 1 and n have been fixed to be the reference particles in the recursion and the ordering $\{2,1,3,\ldots,n\}$ yields a valid colour flow. In this case the above choice of reference particles is actually inconvenient to calculate the respective contribution to the total amplitude, since the sum on the right hand side of Eq. (2.49) could be replaced by the one term on the left hand side. This problem does not occur in the colour-ordered case, since the reference particles are chosen separately for each colour flow. To illustrate this, in Tab. 2.5 the ratio of the average number of distinct nonzero MHV vertices in the colour-dressed and the colour-ordered BCF relations is compared for the colour-flow basis and the adjoint representation incorporating all simplifications described above. In the adjoint representation the colour-dressed relations yield less terms than the colour-ordered ones, since the adjoint representation naturally avoids the problem of encountering singlet gluons, that decouple. However, much more effort is spent on the computation of colour

Process	CO		CD
	general MHV	3-point MHV	
$gg \to 2g$	1.28	2.55	1.98
$gg \to 3g$	1.84	5.51	4.57
$gg \to 4g$	7.41	19.33	18.17
$gg \to 5g$	48.78	110.7	126.3
$gg \to 6g$	318.3	714.7	1026
$gg \to 7g$	2329	5269	10330
$gg \to 8g$	20650	46890	124600

Tab. 2.6 Average number of nonzero MHV vertices in the colour-flow decomposition for the colour-ordered (CO) and the colour-dressed (CD) BCF relations.

factors in the adjoint representation [53], such that it is not the method of choice.

In the colour-dressed BCF relations each amplitude is decomposed completely into three-point vertices. In contrast, in the colour-ordered case, any MHV amplitude occurring in any step of the recursion can be evaluated immediately. To highlight the differences due to this treatment, Table 2.6 shows a comparison of the average number of distinct nonzero MHV vertices that have to be evaluated in the colour-dressed and in the colour-ordered case. The same number is given also for the colour-ordered case, when each amplitude is decomposed into three-point vertices as well.

3 Comix - A new matrix element generator

Apart from a better theoretical understanding of QCD, many attempts have been made in the past to tackle the task of numerically evaluating amplitudes with very large number of external legs [15,18,72,73]. In this context it turned out, that often the most efficient method to compute colour-ordered multi-leg amplitudes is the Berends-Giele recursion [59, 74, 49]. Correspondingly one of the fastest methods available for the computation of full scattering amplitudes are the colour-dressed Berends-Giele relations introduced in Chapter 2, which are equivalent to the Dyson-Schwinger methods employed in Refs. [16, 72]. As noted in Chapter 2 and pointed out in Refs. [48, 71], a vertex decomposition of four-gluon vertices in QCD is clearly advantageous over the standard Feynman rules, if the speed of numerical implementations is concerned. These findings raise the question, whether it is possible to construct a full set of SM Feynman rules with no four vertices present in the theory, such that recursive relations analogous to the colour-dressed Berends-Giele equations can be employed in numerical programs. That this is feasible is demonstrated in Sec. 3.1. Details on the numerical implementation in form of the new ME generator COMIX are presented in Sec. 3.2 and a multi-threading concept is discussed.

A very important part of computing cross sections for tree-level processes is, to find an efficient algorithm for phase space generation. If colours are sampled over, similar problems arise for colour space. An effective technique for phase space generation has been presented in Ref. [29]. In Sec. 3.3.1 it is observed, that it is possible to formulate the rules presented ibidem in a truly recursive fashion, i.e. on the same footing as the matrix element computa-

tion. This implies in particular, that point by point the same calculational effort is spent for computing matrix element and phase space weight. Effective colour sampling techniques are introduced in Sec. 3.3.2. Having these techniques at hand, a strategy to eventually couple colour and phase space integration is outlined and a new type of integrator based on the HAAG generator [33] is presented in Sec. 3.3.3.
A comprehensive comparison of results generated with COMIX to those generated with the two other multi-leg tree-level matrix element generators AMEGIC++ [18] and ALPGEN [15] is performed in Sec. 3.4.

3.1 Recursive relations for tree-level amplitudes in the Standard Model

As explained in Chapter 2, the calculation of multi-parton amplitudes is substantially simplified when employing Berends-Giele type recursive relations. One main reason for the simplification is that these relations allow to reuse basic building blocks of an amplitude, which are the m-particle internal off-shell currents. Another reason is that they can be easily rewritten to include three-particle vertices only. The results of Chapter 2 suggest that any numerical implementation of recursive relations should employ vertices with more than three external legs in decomposed form. In the following it will briefly be illuminated, why this is the case. In the spirit of this observation a decomposition of the remaining four vertices in the Standard Model is constructed.

3.1.1 The cost of computing a tree amplitude

For the following arguments, one considers a theory with only one particle type and a recursive relation for internal n-particle currents, which is of the functional form

$$J_n(\pi) = P_n(\pi) \sum_{N=1}^{n} \sum_{\mathcal{P}_N(\pi)} V_N(\pi_1, \ldots, \pi_N)\, J_{i_1}(\pi_1) \ldots J_{i_N}(\pi_N) \ . \tag{3.1}$$

Here J_m denote unordered m-particle currents, while V_N are $N+1$-point vertices and P_n is a propagator term. The two sums run over all possible vertex types V_N and all (unordered) partitions $P_N(\pi)$ of the set of particles π into N (unordered) subsets, respectively, cf.

Chapter 2. The full $n+1$-particle scattering amplitude can be constructed by putting an arbitrary n-particle internal off-shell current on-shell and contracting the remaining quantity with the corresponding external one-particle current.

$$A_{n+1}(\pi) = J_1(i) \frac{1}{P_n(\pi \setminus i)} J_n(\pi \setminus i) \ . \tag{3.2}$$

One now deals only with vertices of $N+1$ external legs and considers their contribution to the computation of an n-particle off-shell current. The number of vertices to evaluate per m-particle subcurrent is the Stirling number of the second kind $S(m,N)$, corresponding to the number of partitions of a set π of m integers into N subsets. The total number $V(n,N)$ of $N+1$-particle vertices to be calculated thus becomes

$$V(n,N) = \sum_{m=N}^{n} \binom{n}{m} S(m,N) \ . \tag{3.3}$$

Since the Stirling numbers $S(m,N)$ are zero for $m < N$, we can extend the sum down to zero, leading to

$$\begin{aligned} V(n,N) &= \sum_{m=0}^{n} \binom{n}{m} \frac{1}{N!} \sum_{i=0}^{N} (-1)^i \binom{N}{i} (N-i)^m \\ &= \frac{1}{(N+1)!} \sum_{i=0}^{N} (-1)^i \binom{N+1}{i} (N+1-i)^{n+1} \quad = S(n+1,N+1) \ . \end{aligned} \tag{3.4}$$

The question is now, whether a milder growth in computational complexity can be obtained, if all $N+1$-particle vertices occurring in Eq. (3.1) are decomposed in terms of two or more vertices with fewer number of external legs. When doing so, one must introduce additional pseudoparticles reflecting the structure of the decomposed vertex. Hence one has to consider the contribution arising from the presence of these pseudoparticles, too. The problem can be simplified by assuming that there is only one additional pseudoparticle, which obeys a completely independent recursion. Then the full contribution of an $N+1$-particle vertex, now being decomposed into an $M+1$- and an $N-M+1$-particle vertex becomes

$$S(n+1,N+1) \to S(n+1,M+1) + S(n+1,N-M+1) \ , \tag{3.5}$$

which can be either bigger or smaller than $S(n+1, N+1)$, depending on n, N and M. With increasing n, however the right hand side is always smaller such that the vertex decomposition becomes clearly advantageous. Similar arguments hold when introducing more than one pseudoparticle.

From this simple but general consideration it can be seen that the aim of any recursive formulation of interaction models should be, to reduce the number of external lines at interaction vertices to the lowest possible. In this section it will be shown that within the Standard Model it is possible to reduce $N_{\max}$ to two, which is the lowest possible number. For QCD interactions the results of Sec. 2.1 can be employed, where this task has already been performed and the original Berends-Giele recursive relations have been reformulated to incorporate colour.

Note that in the above arguments it is assumed that $N_{\max}$ is finite, which does not hold in general. For example the naive CSW vertex rules induce vertices with an arbitrary number of external particles, cf. Sec. 2.2. Although these rules have been reformulated in order to obtain three-point vertices only, they provide an excellent example of a recursion inducing a growth in computational complexity which, for large n, is roughly proportional to Bell numbers. To see this, consider the contributions of all N-particle vertices with $N \leq n$. Assuming all of them are evaluated, which is approximately the case when computing helicity summed amplitudes, and employing Dobinski's formula one obtains

$$\sum_{N=0}^{n} S(n+1, N+1) = \frac{1}{e} \sum_{k=0}^{\infty} \frac{k^{n+1}}{k!} = B_{n+1} \,. \tag{3.6}$$

This result has the nice interpretation of being the number of all partitions of a set of $n+1$ integer numbers into all possible subsets.

3.1.2 General form of the recursive relations

In the following $\mathcal{J}_\alpha(\pi)$ denotes an unordered SM current of type α, which receives contributions from all Feynman graphs having as external particles the on-shell SM particles in the set π and one internal particle, described by this current. The index α is a multi-index, carrying information on all quantum numbers and eventually on the pseudoparticle character of the particle. Special currents are given by the external particle currents. They

correspond to external scalars, spinors and polarisation vectors, see Sec. 1. For them there is only one multi-index $\alpha = \alpha_i$ associated with the external particle i, whereas in the general case multiple multi-indices may lead to non-vanishing internal currents. This corresponds to multiple particle types being possible as intermediate states. Assuming that only three-point vertices exist, any internal SM particle and pseudoparticle off-shell current can be written as

$$\mathcal{J}_\alpha(\pi) = P_\alpha(\pi) \sum_{\mathcal{V}_\alpha^{\alpha_1,\alpha_2}} \sum_{\mathcal{P}_2(\pi)} \mathcal{S}(\pi_1,\pi_2)\ \mathcal{V}_\alpha^{\alpha_1,\alpha_2}(\pi_1,\pi_2)\ \mathcal{J}_{\alpha_1}(\pi_1)\,\mathcal{J}_{\alpha_2}(\pi_2)\ . \tag{3.7}$$

Here $P_\alpha(\pi)$ denotes a propagator term depending on the particle type α and the set π. The term $\mathcal{V}_\alpha^{\alpha_1,\alpha_2}(\pi_1,\pi_2)$ is a vertex depending on the particle types α, α_1 and α_2 and the decomposition of the set π into disjoint subsets π_1 and π_2. The quantity $\mathcal{S}(\pi_1,\pi_2)$ is the symmetry factor associated with the decomposition of π into π_1 and π_2 and will be discussed in Sec. 3.1.4. Superscripts in this context refer to incoming particles, subscripts to outgoing particles. The sums run over all vertices in the reformulated Standard Model and all unordered partitions $\mathcal{P}_2$ of the set π into two disjoint subsets, respectively. A full unordered n-particle scattering amplitude is then given by

$$\mathcal{A}(\pi) = \mathcal{J}_{\alpha_n}(n)\ \frac{1}{P_{\bar{\alpha}_n}(\pi \setminus n)}\ \mathcal{J}_{\bar{\alpha}_n}(\pi \setminus n)\ , \tag{3.8}$$

where $\bar{\alpha}$ denotes a set of reversed particle properties. It has been proved in Sec. 2.1 that the above form is correct for pure gluonic scattering amplitudes once the four gluon vertex is suitably decomposed into two vertices involving an internal antisymmetric tensor pseudoparticle. One can thus continue to decompose the four particle vertices in electroweak interactions. Once their decomposition is complete, no further complications arise and Eq. (3.7) can be employed to compute arbitrary scattering amplitudes in the Standard Model.

3.1.3 Decomposition of electroweak four-particle vertices

A decomposition of four particle vertices with W-bosons only is suggested as

$$\begin{aligned} \mathcal{V}_{W^-\nu}^{W^-\rho,\,W^+\sigma,\,W^-\lambda} \rightarrow \quad & \mathcal{V}_{W^-\nu}^{W^-\rho,\,Z_4\gamma\delta} \cdot P_{Z_4\,\gamma\delta}^{\;\;\alpha\beta} \cdot \mathcal{V}_{Z_4\alpha\beta}^{W^+\sigma,\,W^-\lambda} \\ & + \mathcal{V}_{W^-\nu}^{W^-\lambda,\,Z_4\gamma\delta} \cdot P_{Z_4\,\gamma\delta}^{\;\;\alpha\beta} \cdot \mathcal{V}_{Z_4\alpha\beta}^{W^+\sigma,\,W^-\rho} \,. \end{aligned} \tag{3.9}$$

Here Z_4 denotes a new antisymmetric tensor pseudoparticle introduced for the vertex decomposition. Its interaction vertex reads

$$\begin{aligned} \mathcal{V}_{W^-\nu}^{W^-\rho,\,Z_4\gamma\delta} &= \frac{i}{2}\, g_w \left(g_\nu^\gamma g^{\rho\delta} - g_\nu^\delta g^{\rho\gamma}\right) \,, \\ \mathcal{V}_{Z_4\alpha\beta}^{W^+\sigma,\,W^-\rho} &= \frac{i}{2}\, g_w \left(g_\alpha^\sigma g_\beta^\rho - g_\alpha^\rho g_\beta^\sigma\right) \,. \end{aligned} \tag{3.10}$$

To obtain correct signs of four-particle vertices, the tensor pseudoparticle "propagators" is defined as

$$P_{\alpha\,\mu\nu}^{\;\;\rho\sigma} = \kappa_\alpha D_{\mu\nu}^{\rho\sigma} \qquad \text{where} \qquad \kappa_\alpha = \begin{cases} -i & \text{if} \quad \alpha = Z_4 \\ i & \text{else} \end{cases} \,, \tag{3.11}$$

and where $D_{\mu\nu}^{\rho\sigma}$ is given by Eq. (2.4). Note that the above decomposition of vertices is not unique. Also, the Z_4 pseudoparticle is not self-conjugate. This definition prevents double counting four-particle vertices involving the W boson and constructing fake $WWWW$ vertices with all W's having the same charge. The four-particle vertices involving W bosons, photons and Z-bosons are decomposed as follows

$$\begin{aligned} \mathcal{V}_{W^-\nu}^{A\rho,\,W^-\sigma,\,A\lambda} &\rightarrow \mathcal{V}_{W^-\nu}^{A\rho,\,W_4^-\gamma\delta} \cdot P_{W_4^-\,\gamma\delta}^{\;\;\alpha\beta} \cdot \mathcal{V}_{W_4^-\alpha\beta}^{W^-\sigma,\,A\lambda} + \mathcal{V}_{W^-\nu}^{A\lambda,\,W_4^-\gamma\delta} \cdot P_{W_4^-\,\gamma\delta}^{\;\;\alpha\beta} \cdot \mathcal{V}_{W_4^-\alpha\beta}^{W^-\sigma,\,A\rho} \,, \\ \mathcal{V}_{W^-\nu}^{A\rho,\,W^-\sigma,\,Z\lambda} &\rightarrow \mathcal{V}_{W^-\nu}^{A\rho,\,W_4^-\gamma\delta} \cdot P_{W_4^-\,\gamma\delta}^{\;\;\alpha\beta} \cdot \mathcal{V}_{W_4^-\alpha\beta}^{W^-\sigma,\,Z\lambda} + \mathcal{V}_{W^-\nu}^{Z\lambda,\,W_4^-\gamma\delta} \cdot P_{W_4^-\,\gamma\delta}^{\;\;\alpha\beta} \cdot \mathcal{V}_{W_4^-\alpha\beta}^{W^-\sigma,\,A\rho} \,, \\ \mathcal{V}_{W^-\nu}^{Z\rho,\,W^-\sigma,\,Z\lambda} &\rightarrow \mathcal{V}_{W^-\nu}^{Z\rho,\,W_4^-\gamma\delta} \cdot P_{W_4^-\,\gamma\delta}^{\;\;\alpha\beta} \cdot \mathcal{V}_{W_4^-\alpha\beta}^{W^-\sigma,\,Z\lambda} + \mathcal{V}_{W^-\nu}^{Z\lambda,\,W_4^-\gamma\delta} \cdot P_{W_4^-\,\gamma\delta}^{\;\;\alpha\beta} \cdot \mathcal{V}_{W_4^-\alpha\beta}^{W^-\sigma,\,Z\rho} \,. \end{aligned} \tag{3.12}$$

A new tensor pseudoparticle, W_4^-, was introduced here. Its interaction vertices are defined as

$$\begin{aligned}
\mathcal{V}_{W^-\nu}^{A\rho,W_4^-\gamma\delta} &= \frac{i}{2}\, g_w \sin\theta_W \left(g_\nu^\gamma g^{\rho\delta} - g_\nu^\delta g^{\rho\gamma}\right) , \\
\mathcal{V}_{W^-\nu}^{Z\rho,W_4^-\gamma\delta} &= \frac{i}{2}\, g_w \cos\theta_W \left(g_\nu^\gamma g^{\rho\delta} - g_\nu^\delta g^{\rho\gamma}\right) , \\
\mathcal{V}_{W_4^-\alpha\beta}^{W^-\sigma,A\rho} &= \frac{i}{2}\, g_w \sin\theta_W \left(g_\alpha^\sigma g_\beta^\rho - g_\alpha^\rho g_\beta^\sigma\right) , \\
\mathcal{V}_{W_4^-\alpha\beta}^{W^-\sigma,Z\rho} &= \frac{i}{2}\, g_w \cos\theta_W \left(g_\alpha^\sigma g_\beta^\rho - g_\alpha^\rho g_\beta^\sigma\right) .
\end{aligned} \tag{3.13}$$

Corresponding vertices exist for W^+ / W^- bosons. The decomposition of four particle vertices involving the Higgs boson introduces a new scalar pseudoparticle, which is denoted by h_4. In order not to generate fake four particle vertices is is defined not to be self-conjugate. The corresponding vertices read

$$\begin{aligned}
\mathcal{V}_h^{h,h,h} &\to \mathcal{V}_h^{h,h_4} \cdot P_{h_4} \cdot \mathcal{V}_{h_4}^{h,h} , \\
\mathcal{V}_h^{h,Z\mu,Z\nu} &\to \mathcal{V}_h^{h,h_4} \cdot P_{h_4} \cdot \mathcal{V}_{h_4}^{Z\mu,Z\nu} , \\
\mathcal{V}_h^{h,W^+\mu,W^-\nu} &\to \mathcal{V}_h^{h,h_4} \cdot P_{h_4} \cdot \mathcal{V}_{h_4}^{W^+\mu,W^-\nu} .
\end{aligned} \tag{3.14}$$

where the interactions of the h_4 pseudoparticle are defined by

$$\begin{aligned}
\mathcal{V}_{h_4}^{h,h} &= i\,\frac{m_h^2}{v^2} , \qquad & \mathcal{V}_{h_4}^{Z\mu,Z\nu} &= -i\,\frac{g_w^2}{2\,\cos^2\theta_W}\, g^{\mu\nu} , \\
\mathcal{V}_h^{h,h_4} &= i , \qquad & \mathcal{V}_{h_4}^{W^+\mu,W^-\nu} &= -i\,\frac{g_w^2}{2}\, g^{\mu\nu} ,
\end{aligned} \tag{3.15}$$

and where the scalar "propagator" of the h_4 pseudoparticle is introduced as

$$P_{h_4} = i . \tag{3.16}$$

Since all remaining vertices in the Standard Model are three point vertices, the vertex decomposition is hereby complete. The complete set of vertices employed in the recursive relations is listed in Appendix B, with the corresponding Lorentz structures given in Appendix A.

3.1.4 Prefactors of diagrams with external fermions

When calculating currents with an arbitrary number of possibly indistinguishable external fermions, one has to take into account, that each Feynman diagram contains a prefactor

$$\mathcal{S} = (-1)^{P_f(\sigma_1,\ldots,\sigma_n)} , \tag{3.17}$$

according to the number of fermion permutations P_f in the external particle assignment $\vec{\sigma} = (\sigma_1, \ldots, \sigma_n)$. To be used in the context of a recursive computation, this prefactor must be defined on a local basis in order to avoid the proliferation of information on different $\vec{\sigma}$. It is then sufficient to note that Eq. (3.17) holds on the level of interaction vertices. More precisely one can define the local prefactor $\mathcal{S}(\pi_1, \pi_2)$ of Eq. (3.7) as

$$\mathcal{S}(\pi_1, \pi_2) = (-1)^{P_f(\pi_1,\pi_2)} . \tag{3.18}$$

Here $P_f(\pi_1, \pi_2)$ counts the number of fermion permutations that is needed to restore a predefined, for example ascending index ordering when combining the sets π_1 and π_2 into the set $\pi = \pi_1 \oplus \pi_2$. Upon iterating this procedure, the correct relative prefactors $\mathcal{S}$ are obtained for each diagram.

3.2 Matrix element generation in Comix

The general formulae to recursively compute a tree-level amplitude have been stated in Sec. 3.1. External particle currents and internal Lorentz structures are computed using the Weyl-van der Waerden formalism presented in Sec. 1.2, see also Appendices A and B. As pointed out in the previous section, within the Standard Model tensor particles never occur as external states, such that there is no need to explicitly construct polarisation tensors. The aim of this section is to explain some more details on the organisation of the computation. The algorithms presented in this part of the thesis are intended to be used for large multiplicity matrix element calculations. In this context, it is often useful to sample over helicities of external particles in a Monte Carlo fashion. However, this introduces additional degrees of freedom and leads to a slower convergence of the integral. Furthermore when taking Eq. (3.7) serious, one notes that for helicity-summed ME's, it is possible to reuse currents

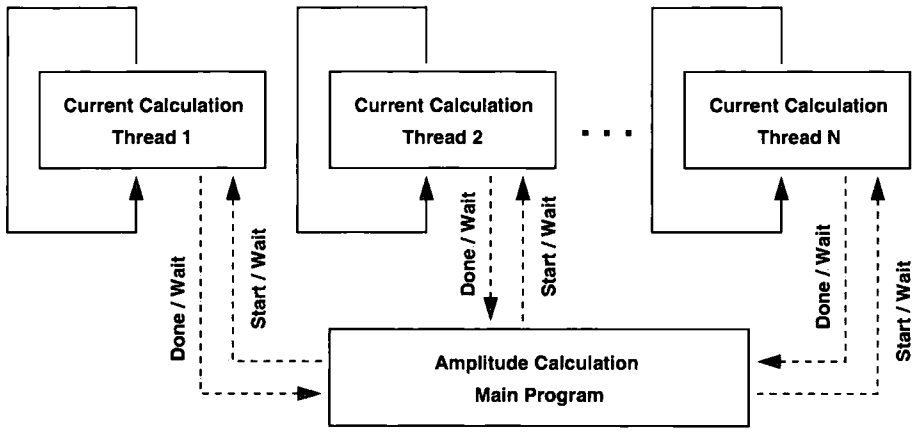

Fig. 3.1 Structure of the multi-threaded implementation for matrix element computation in COMIX. The number of threads N is variable and depends on the number of available processors. The main program communicates start and wait signals to the calculator threads, while those communicate done and wait signals to the main program. Details are explained in the text.

to compute amplitudes with different configurations. Namely if the helicities of external particles assigned to a particular current do not change, it does not need to be recomputed. This leads to a significant decrease in evaluation time for the helicity summed matrix elements compared to the naive method of computing the full amplitude afresh for different configurations. A corresponding comparison can be found in Sec. 3.4. The default choice in COMIX is helicity summation. To allow computations for very large multiplicities, however, helicity sampling can be enabled as an option.

The effective computation time per phase space point can be further reduced by a multi-threaded implementation of Eq. (3.7). Figure 3.1 shows the basic structure of this algorithm. The main advantage of Eq. (3.7) is, that in order to compute a current that depends on n external particles, it is sufficient to know all subcurrents that depend on $m < n$ external particles. This leads to a straightforward multi-threading algorithm.

- Create N threads at program startup with the following properties

  1. The thread waits for the main program to signal the start of a computation. It then signals the main program to wait.
  2. It takes a number n and computes a block of currents depending on n external particles using subcurrents depending on $m < n$ external particles. If $n = 1$, it

computes external polarisation vectors and spinors.

3. It signals the main program that the calculation is done and returns to step 1.

- For each phase space point, employ the following algorithm in the main program

1. Start with $n = 1$.
2. Split the number of currents that depend on n external particles into N blocks. Communicate n and one block to each calculator thread.
3. Signal the threads to start their computation.
   Wait for all threads to signal completion.
4. Let $n \rightarrow n + 1$ and return to step 2 if further currents need to be computed.

The efficiency of this algorithm solely depends on an efficient thread library. The overhead with a modern POSIX threading is about 10% of the total computational cost. However, if on the other hand it is possible to make use of multiple processors or multiple processor cores due to threading, the respective overhead is not of any concern, since the computation time decreases roughly proportional to the increase in processor usage.

3.3 Integration techniques in Comix

In this section two new methods for integrating over the multi-particle phase space are presented. Both of them are designed to cope especially with large numbers of outgoing particles. The first method is a fully general approach and makes use of the standard multi-channel technique [30] in a recursive fashion, i.e. the phase space sampling fits the method of generating the corresponding matrix element. The second method is designed for QCD and QCD-associated processes and employs the phase space generator HAAG [33] in conjunction with a new prescription for coupling colour and momentum sampling and the multi-channel technique.

3.3.1 Recursive algorithm for phase space integration

One of the most effective general approaches to sample the phase space of multi-particle processes is, to employ a multi-channel method according to Ref. [30] with each of the single

channels corresponding to the pole structure of a certain Feynman diagram. However, for large numbers of diagrams this is clearly not the method of choice. In the following the focus will therefore be on the recursive relations for phase space generation proposed in Ref. [29]. A separate multi-channel for each possible subamplitude is constructed on the flight according to the propagator structure. Additionally, the VEGAS [31] algorithm is employed to optimise the integration over propagator masses and polar angles in decays. The obvious drawback of this procedure is evident: It relies heavily on the assumption that the matrix element factorises according to its propagator structure. However, it is a generalisable way to tame the rather factorial growth in the number of phase space channels encountered in conventional approaches [16, 18, 17]. If the prescription is taken serious, one can factorise the full phase space weight such that it can be computed in a recursive fashion corresponding to how the matrix elements are evaluated.

Brief review of phase space factorisation

In the following a $2 \to n$ scattering process is considered. Incoming particles are denoted by a and b, outgoing particles by $1 \ldots n$. The corresponding n-particle differential phase space element reads

$$\begin{aligned} \mathrm{d}\Phi_n\left(a,b;1,\ldots,n\right) = & \left[\prod_{i=1}^{n} \frac{\mathrm{d}^4 p_i}{(2\pi)^3}\, \delta\left(p_i^2 - m_i^2\right) \Theta\left(p_{i0}\right)\right] \\ & \times (2\pi)^4\, \delta^{(4)}\left(p_a + p_b - \sum_{i=1}^{n} p_i\right) , \end{aligned} \tag{3.19}$$

where m_i are the on-shell masses of outgoing particles. Following Ref. [75], the full phase space may be factorised according to

$$\mathrm{d}\Phi_n\left(a,b;1,\ldots,n\right) = \mathrm{d}\Phi_{n-m}\left(a,b;\pi,m+1,\ldots,n\right) \frac{\mathrm{d}s_\pi}{2\pi}\, \mathrm{d}\Phi_m\left(\pi;1,\ldots,m\right) , \tag{3.20}$$

where $\pi = \{a, b, 1, \ldots, m\}$ indicates a newly introduced timelike intermediate momentum and $\bar{\pi} = \{a, b, 1, \ldots, n\} \setminus \pi$. Generally Greek indices denote a subset of all possible indices. If they appear as an incoming particles' index, they correspond to a t-channel particle with spacelike momentum, while otherwise they denote s-channels. Equation (3.20) allows to decompose the complete phase space into building blocks corresponding to the t- and s-

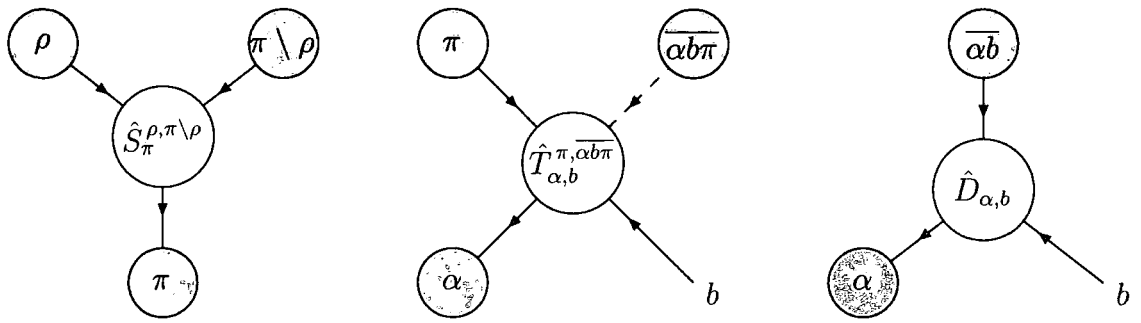

Fig. 3.2 Basic decay vertices for weight calculation. Dark blobs denote potentially nontrivial known weights, light blobs weights to be determined. Arrows indicate the weight flow, i.e. the order in which unknown weights are determined from known ones. The $\hat{D}$-vertex corresponds to overall momentum conservation.

channel decay processes $T_{\alpha,b}^{\pi,\overline{\alpha b\pi}} = \mathrm{d}\Phi_2\left(\alpha, b; \pi, \overline{\alpha b\pi}\right)$ and $S_\pi^{\rho,\pi\setminus\rho} = \mathrm{d}\Phi_2\left(\pi; \rho, \pi\setminus\rho\right)$. The above decays can be referred to as phase space vertices, while the integral $P_\pi = \mathrm{d}s_\pi/2\pi$, introduced in Eq. (3.20), will be called a phase space propagator. Within the algorithm presented here, only timelike propagators are employed.

The two vertex types are used differently in the case of weight calculation and phase space generation. Consider the t-channel decay. If a phase space point is to be diced, the new final state momenta p_π and $p_{\overline{\alpha b\pi}}$ are determined from the known initial state momenta p_α and p_b. If a weight needs to be computed, the new weight $w_\alpha^{(b)}$ is determined from the vertex weight and the input weights w_π and $w_{\overline{\alpha b\pi}}$. The corresponding situations are depicted in Figs. 3.2 and 3.3, respectively. The basic building blocks of phase space integration are summarised as follows

$$
\begin{aligned}
P_\pi &= \begin{cases} 1 & \text{if } \pi \text{ or } \bar{\pi} \text{ external} \\ \dfrac{\mathrm{d}s_\pi}{2\pi} & \text{else} \end{cases}, \\
S_\pi^{\rho,\pi\setminus\rho} &= \frac{\lambda\left(s_\pi, s_\rho, s_{\pi\setminus\rho}\right)}{16\pi^2\, 2\, s_\pi}\, \mathrm{d}\cos\theta_\rho\, \mathrm{d}\phi_\rho\,, \\
T_{\alpha,b}^{\pi,\overline{\alpha b\pi}} &= \frac{\lambda\left(s_{\alpha b}, s_\pi, s_{\overline{\alpha b\pi}}\right)}{16\pi^2\, 2 s_{\alpha b}}\, \mathrm{d}\cos\theta_\pi\, \mathrm{d}\phi_\pi
\end{aligned}
\tag{3.21}
$$

The triangular function λ is given by

$$
\lambda\left(s_a, s_b, s_c\right) = \sqrt{\left(s_a - s_b - s_c\right)^2 - 4 s_b s_c} \tag{3.22}
$$

Note that even since α might correspond to an off-shell internal particle, b always indi-

cates a fixed external incoming particle. This is essential in all further considerations and allows reusing weight factors in the Monte Carlo integration, just as currents are reused in the matrix element computation. The functions corresponding to $S_{\pi}^{\rho,\pi\setminus\rho}$ and $T_{\alpha}^{\pi,\overline{\alpha b\pi}}$ are in fact identical, since they represent a solid angle integration. In practice however the different sampling strategies proposed in Ref. [29] are employed. Additionally, overall four-momentum conservation is maintained through the vertex

$$D_{\alpha,b} = (2\pi)^4 \, \delta^{(4)} \left(p_\alpha + p_b - p_{\overline{\alpha b}} \right) . \tag{3.23}$$

Formulation of the recursive algorithm

Recursive relations for phase space integration in terms of the above quantities can then be defined through

$$\begin{aligned} \mathrm{d}\Phi_S(\pi) &= S_{\pi}^{\pi_1,\pi_2} \, P_{\pi_1} \, \mathrm{d}\Phi_S(\pi_1) \, P_{\pi_2} \, \mathrm{d}\Phi_S(\pi_2) \Big|_{(\pi_1,\pi_2)\in\mathcal{OP}(\pi)} , \\ \mathrm{d}\Phi_T^{(b)}(\alpha) &= T_{\alpha,b}^{\pi_1,\pi_2} \, P_{\pi_1} \, \mathrm{d}\Phi_S(\pi_1) \, P_{\pi_2} \, \mathrm{d}\Phi_T^{(b)}(\alpha\pi_1) \Big|_{(\pi_1,\pi_2)\in\mathcal{OP}(\overline{\alpha b})} + D_{\alpha,b} \, \mathrm{d}\Phi_S\left(\overline{\alpha b}\right) . \end{aligned} \tag{3.24}$$

The above equations correspond to selecting one possible splitting of the multi-index π or $\overline{\alpha b}$ per phase space point. One can improve the integration procedure by forming an average over all possible splittings in the spirit of a multi-channel. Let F be a generalised mean function. Then the F-mean can be used to define

$$\begin{aligned} \mathrm{d}\Phi_S(\pi) = F^{-1} \Bigg[& \left(\sum_{(\pi_1,\pi_2)\in\mathcal{OP}(\pi)} \omega_{\pi}^{\pi_1,\pi_2} \right)^{-1} \\ & \times \sum_{(\pi_1,\pi_2)\in\mathcal{OP}(\pi)} \omega_{\pi}^{\pi_1,\pi_2} \, F\left[S_{\pi}^{\pi_1,\pi_2} \, P_{\pi_1} \, \mathrm{d}\Phi_S(\pi_1) \, P_{\pi_2} \, \mathrm{d}\Phi_S(\pi_2) \right] \Bigg] , \end{aligned} \tag{3.25}$$

$$\begin{aligned} \mathrm{d}\Phi_T^{(b)}(\alpha) = F^{-1} \Bigg[& \left(\omega_{\alpha,b} + \sum_{(\pi_1,\pi_2)\in\mathcal{OP}(\overline{\alpha b})} \omega_{\alpha}^{\pi_1,\alpha\pi_1} \right)^{-1} \left(\omega_{\alpha,b} \, F\left[D_{\alpha,b} \, \mathrm{d}\Phi_S(\overline{\alpha b}) \right] \right. \\ & \left. + \sum_{(\pi_1,\pi_2)\in\mathcal{OP}(\overline{\alpha b})} \omega_{\alpha}^{\pi_1,\alpha\pi_1} \, F\left[T_{\alpha,b}^{\pi_1,\pi_2} \, P_{\pi_1} \, \mathrm{d}\Phi_S(\pi_1) \, P_{\pi_2} \, \mathrm{d}\Phi_T^{(b)}(\alpha\pi_1) \right] \right) \Bigg] . \end{aligned} \tag{3.26}$$

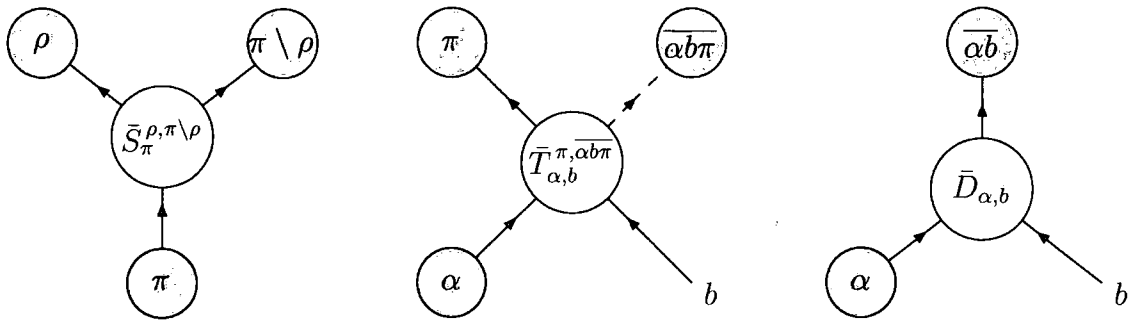

Fig. 3.3 Basic vertices for phase space generation. Grey blobs correspond to eventually off mass-shell particles. Dark blobs denote known momenta, light blobs unknown momenta. Arrows indicate the momentum flow, i.e. the order in which unknown momenta are determined from known ones. The $\bar{D}$-vertex corresponds to overall momentum conservation.

In this context the one- and no-particle phase space are defined through

$$\begin{aligned} \mathrm{d}\Phi\left(i\right) &= 1\ , \\ \mathrm{d}\Phi\left(\emptyset\right) &= 0\ . \end{aligned} \tag{3.27}$$

The function ω corresponds to a vertex-specific weight which may be adapted to optimise the integration procedure, see Ref. [30]. The second sums run over all possible S- and T-type vertices which have a correspondence in the matrix element. The full differential phase space element is given by

$$\mathrm{d}\Phi_n\left(a,b;1,\ldots,n\right) = \mathrm{d}\Phi_T\left(a\right)\ . \tag{3.28}$$

Note that Eqs. (3.25) and (3.26) in the form stated above are *not* suited to generate the sequence of final state momenta. To do so one rather has to employ the following algorithm, which corresponds to a reversion of the recursion and respects the weight factors w introduced above.

- From the set of possible vertices connecting currents in the matrix element, choose a sequence connecting all external particles in the following way:

  1. Start with the set of indices $\pi = \{b;1,\ldots,n\}$, corresponding to the unique external current of index a.
  2. From the set of possible phase space vertices connecting to π select one according

to an on the flight constructed multi-channel employing the weights w.[1] If π is a single index, stop the recursion.

3. According to the selected vertex, split π into the subsets π_1 and π_2. Repeat step 2 for these subsets.

- Fore each vertex, make use of the fact that π is equivalent to $\overline{\pi}$ and adjust the indices in an appropriate way for momentum generation. That is if any π contains b and other indices, replace π by $\overline{\pi}$.

- Order $\bar{T}$-type vertices ascending and $\bar{S}$-type vertices descending in the number of external indices connected to initial states.

- Generate the corresponding momenta starting with $\bar{T}$-type vertices.

Even though T-type vertices depend on b, since b is fixed throughout the computation of one phase space point one obtains no expressions depending on more than two particle indices. This induces the same growth of computational complexity in both the hard matrix elements and the phase space and makes the above algorithm well suited for integration of processes with large final state multiplicity. In the following this algorithm will be referred to as the Recursive Phase space Generator (RPG).

Implementation details

Since the phase space weight computation, Eq. (3.25) obeys a recursion similar to those of the matrix element calculation, Eq. (3.7), it is straightforward to implement into a numerical program along the lines of Sec. 3.2. The same techniques described for the multi-threading of matrix element calculations can be implemented for the phase space weight. In the multi-threaded version of COMIX, this weight is computed in parallel to the matrix element, which further reduces the net computation time if enough resources are available.

3.3.2 Colour sampling

For QCD and QCD associated processes with a large number of external legs, it becomes unfeasible to compute colour-summed scattering amplitudes. Instead the better strategy is

[1] Note that in this context weights have to be normalised to unity on the flight.

to sample over external colour assignments in a given representation of SU(3). According to Eqs. (1.4), (1.8) and (1.6), this selects a set of colour-ordered amplitudes which contribute to the corresponding point in colour space. This set is typically strongly reduced compared to the full set of partial amplitudes. The issue has been studied in Ref. [53] for the fundamental representation decomposition, the adjoint representation decomposition and the colour-flow decomposition. According to the findings therein and the results of Chapter 2 the colour-flow decomposition is the method best suited for sampling over colour assignments if the number of external partons is large, i.e. it provides the slowest growth in the average number of partial amplitudes per non-vanishing colour assignment. The colour-flow basis is therefore employed throughout COMIX.

In the following the focus will be on n-gluon scattering. However, the presented ideas and algorithms are straightforward to generalise for arbitrary sets of colour octet objects, such as e.g. quark-antiquark pairs.

In the colour flow decomposition each external gluon is labelled by a colour index i and an anti-colour index $\bar{\jmath}$. The colour state for an n-gluon scattering is thus given by selecting each index $i_1, \dots i_n$ and $\bar{\jmath}_1, \dots \bar{\jmath}_n$ out of three values (R, G, B) and $\left(\bar{R}, \bar{G}, \bar{B}\right)$. A specific colour flow, and thus an ordering in the sense of a colour-ordered amplitude, is specified by a permutation

$$\vec{\sigma} = (1, \sigma_2, \sigma_3, \dots, \sigma_n) \in S_{n-1} \tag{3.29}$$

of external gluon indices. This colour flow contributes to a colour assignment, if

$$\delta_{i_1}^{\bar{\jmath}_{\sigma_2}} \delta_{i_{\sigma_2}}^{\bar{\jmath}_{\sigma_3}} \cdots \delta_{i_{\sigma_n}}^{\bar{\jmath}_1} = 1 \,. \tag{3.30}$$

It is thus easy to construct an algorithm which determines all valid colour flows from a given colour assignment.

1. Set the first gluon index to $\sigma_1 = 1$. Let $k = 2$.
2. Select one of the remaining gluon indices to be σ_k.
   If $i_{\sigma_{k-1}} = \bar{\jmath}_{\sigma_k}$, let $k \to k + 1$. Otherwise this flow is invalid.
3. If $k = n + 1$ and $i_{\sigma_n} = \bar{\jmath}_{\sigma_1}$, a valid flow has been found.

Otherwise continue with step 2.

The simplest way of choosing a colour assignment is accomplished by randomly selecting the $2n$ colours for the i- and $\bar{\jmath}$-indices. Each colour is chosen with an equal probability, leading to a weight of 3^{2n}. However, only a small fraction of those assignments will have at least one colour flow. A trivial (but not sufficient) condition for non-vanishing assignments is, that the number of i-indices carrying the colour R (G,B) must be equal to the number of $\bar{\jmath}$-indices carrying the corresponding anticolour.
A more efficient way to determine colour configurations is thus proposed.

1. The n i-indices are selected randomly in (R, G, B).

2. A permutation $\vec{\sigma} = (\sigma_1, \ldots, \sigma_n)$ of n particles is selected randomly with a uniform weight.
   The anticolours of the $\bar{\jmath}$-indices are then given by

$$\bar{\jmath}_k = \overline{i_{\sigma_k}} \,, \quad \text{for} \quad k = 1, \ldots, n \tag{3.31}$$

3. Each colour assignment is weighted by

$$w \;=\; 3^n \, \frac{n!}{n_R!\, n_G!\, n_B!} \,, \tag{3.32}$$

   where n_R, n_G and n_B are the multiplicities of i-indices
   carrying the colours R, G and B, respectively.

Clearly, assignments generated by this algorithm will always fulfil the trivial condition mentioned above. Moreover, the weight is roughly proportional to the number of possible colour flows and thus already corresponds to some extent to the expected cross section for this colour configuration.

3.3.3 Combined colour-momentum integration techniques

Generally the peaking behaviour of the colour-sampled differential cross section is rather complex within the phase space and strongly different for different colour assignments. The idea must thus be to construct integrators specific for a given colour assignment, based on

the knowledge of contributing partial amplitudes. One can for example think of a variant of the algorithm described in Sec. 3.3.1, where the basic building blocks of the phase space are either available or not, depending whether there is a corresponding non-vanishing colour current present in the matrix element. However, in practice this choice does not lead to any significant improvement of the integration behaviour. A different type of integrator is thus presented, dedicated to be used with QCD and QCD associated processes, which is based on the HAAG algorithm [33]. As before purely gluonic processes will be considered as an example.

Integration of partial amplitudes and colour configurations

As a basic building block the HAAG-integrator is used, which generates momenta distributed according to a QCD antenna function [33]. Details on the implementation of the algorithm and improvements to the original version are given in Appendix C. A single HAAG-channel provides an efficient integrator for a specific squared partial amplitude, i.e. for a given colour flow. In the case of purely gluonic amplitudes averaged over helicities both obey the same symmetries w.r.t. to permutation of external particles. A specific integrator for a given colour assignment to external particles can thus be constructed as follows.

- Determine all possible colour flows for the colour configuration.
- For each colour flow add the corresponding HAAG channel to a multi-channel integrator.

However, with growing number of external particles one faces the following problem: Although the average number of contributing colour flows per colour assignment is relatively low in this decomposition, the maximal number grows factorially. Thus it quickly becomes impossible to store all data associated with the multi-channel, i.e. the contributing HAAG-channels and the internal weights. The situation gets even worse if it is intended to sample over all colour configurations, whose number is growing exponentially with the number of external particles. The solution is thus not to store anything, but generate the whole integrator on the flight.

A fast algorithm to provide all colour flows from a colour assignment is essential for this step: for a single phase space point one has to loop three times over the list of all colour

flows (which due to the possibly factorial growth cannot be stored as well).

1. To determine the normalisation of the weights α_k for each phase space channel within the multi-channel integrator, cf. Eqs. (C.11) and (C.12).

2. To select a channel for generating a phase space point with a probability given by the relative weight α_k, and

3. To compute the multi-channel weight corresponding to this phase space point.

Strategies how to define suitable α_k (beyond equal weights for all channels) are discussed below. For the HAAG channels themselves, only one per type (as defined in Appendix C) needs to be stored. Together with a corresponding permutation of final state particles they can be reused throughout the algorithm.

Optimisation techniques

The proposed integrator contains a number of parameters which can be adjusted or adapted to reduce the variance during integration.

- VEGAS maps within the HAAG channels,
- Relative weights α_k in the multi-channel generator,
- Probabilities to select colour assignments beyond the algorithms given above.

The usage of adaptive techniques such as VEGAS is somewhat limited due to the fact that the number of those parameters increases quickly with the number of particles involved in the process. Not only that it becomes impossible to calculate the matrix element for enough phase space points to adapt each parameter individually, at some point all those parameters cannot even be stored.
Thus the following strategy is applied:

1. Optimisation of the VEGAS maps refining the HAAG channels

   The number of structurally different HAAG channels is limited to one channel per type. Their optimisation is performed before the actual integration starts. To optimise a certain HAAG channel, only single squared partial amplitudes, corresponding to this

channel are computed[2]. This not only speeds up the calculation, it also provides a much cleaner environment for the adaptation of the VEGAS maps. In this step a summation over helicities is performed. Cross sections σ_t, given by the integration of a squared partial amplitude of type t over the allowed phase space, are stored.

2. The actual integration run

No further optimisation is performed. The channels are used as they emerged from the optimisation step, including the VEGAS-map and a multi-channel weight proportional to the cross section, σ_t, of the corresponding squared partial amplitude.

Best performance is achieved, if the colour assignment is selected with a probability proportional to the sum of cross sections of contributing squared partial amplitudes (as determined in step 1), instead of the weight given by Eq. (3.32). To do so, the total normalisation for the new weight must be determined summing over all colour assignments. For n-gluon processes this number is given by the following simple formula:

$$N = (n-2)!\, 3^n \sum_{i=0}^{n-2} \sigma_{\min(i,n-i-2)} \,, \tag{3.33}$$

where the $\sigma_{\min(i,n-i-2)}$ is the cross section of a squared partial amplitude of the type "$\min(i, n-i-2)$". The reweighting can be achieved by a simple hit-or-miss method.

For the integration run it is a matter of choice whether to sum or sample over helicities. All practical tests for up to the 11-gluon process favoured summation. Beyond that, however, it seems to become too costly to compute summed matrix elements, thus a sampling should be considered.

In the context of this work, the above algorithm will be referred to as the Colour Sampling Integrator (CSI).

[2]During this step the full result can not be determined since potential interferences between partial amplitudes are ignored. However, it is sufficient for computing the leading $1/N_C$ limit for n gluon processes, using the fact that in the colour flow decomposition (as well as in the fundamental representation decomposition) interferences are always subleading.

3.4 Results

In this section selected results generated with COMIX are presented. The focus will be on the special feature of this new generator, to be suitable in particular for computation of large multiplicity matrix elements.

3.4.1 Helicity summation vs. helicity sampling

Firstly the effect of suitable matrix element generation in the helicity summed mode of COMIX is illustrated, cf. Sec. 3.2. To this end, computation times for helicity summed and helicity sampled matrix elements in purely gluonic processes are compared in Tab. 3.1. The naive ratio between the two is the number of possible helicity assignments of the respective amplitude, $2^n - 2(n+1)$, with n the number of external gluons. This ratio corresponds to computing the amplitude afresh for each of the different helicity assignments. Employing the ideas presented in Sec. 3.2, however it is found that this value overestimates the real computational cost by up to a factor of ≈ 7. Obviously this statement is process dependent. The general feature, however is that there is a gain when computing helicity summed matrix elements. For the computation of cross sections this type of calculation might be preferred over the helicity sampled mode, especially when using customary phase space integration methods such as presented in the previous chapter.

3.4.2 Performance of the Colour Sampling Integrator

In this subsection a comparison of gluon production cross sections is presented to illustrate both the performance of the CSI and the efficiency of the matrix element generation. The first setup employs a fixed centre-of-mass energy. The parameters are those of Refs. [76,53], i.e. $\alpha_S = 0.12$ and

$$p_{Ti} > 60\ \text{GeV}\,, \qquad |\eta_i| < 2\,, \qquad \Delta R_{ij} > 0.7\,, \tag{3.34}$$

for all final state gluons i and pairs of gluons i, j. Integration results are summarised in Tab. 3.2. Perfect agreement with the results in the literature is observed and new predictions for the processes $gg \to 11g$ and $gg \to 12g$ are given. Results have been generated with the

CSI, except for the $2 \to 11$ and $2 \to 12$ process, where RAMBO [32] has been employed. In order to examine the performance of the new phase space generator in a more realistic scenario, the same partonic processes are investigated at the LHC. The Tevatron Run II k_T algorithm [77][3] to define a cut on the multi particle phase space. The respective results are summarised in Tab. 3.3. It can be seen that the CSI performs very well in both cases, even for large multiplicities, such that the respective cross sections can be computed with good precision.

Figures 3.4 and 3.5 show the convergence behaviour of the CSI for various gluon multiplicities. Since the computation of $2 \to 8$ and $2 \to 9$ gluon processes is quite cumbersome, it is worthwhile to switch to the helicity sampled mode in that case. Correspondingly the performance of the CSI in helicity summed and helicity sampled mode is compared in Fig. 3.5.

3.4.3 Comparison with other matrix element generators

The performance of COMIX can be compared directly to those of other matrix element generators. In a first step computation times for colour-ordered amplitudes in COMIX and a dedicated code implementing the CSW vertex rules in non-recursive form are considered. Corresponding results are displayed in Tab. 3.5. Similar to what was observed in Sec. 2.4, it is found that the CSW vertex rules lead to a significant speed-up for low multiplicities, while for high multiplicities the implementation of the Berends-Giele recursion in COMIX is superior. Given that this is found on the level of colour-ordered amplitudes, further improvement for full matrix elements can be expected.

Next, QCD jet production and Drell-Yan lepton pair production are investigated. A number of integration times for different jet multiplicities are compared between AMEGIC++, COMIX and the dedicated code employing CSW rules. The stopping criterion corresponds to reaching a certain precision level in the integration. The setup listed in Tab. 3.4, originally established for the MC4LHC workshop [78], is employed but cuts are replaced by the following

- $p_{\perp,i} > 30$ GeV, $|\eta_i| < 5$

[3]Note that the replacement $\Delta R_{ij}^2 \to \cosh \Delta\eta_{ij} - \cos \Delta\phi_{ij}$ is made in order to match the Durham measure for final state clusterings.

- 66 GeV $< m_{ll} <$ 116 GeV
- CDF Run II k_T algorithm [77] with $k_T > 30$ GeV, D=0.7 and $\Delta R_{ij}^2 \to \cosh \Delta\eta_{ij} - \cos \Delta\phi_{ij}$.

Corresponding cross sections and integration times are listed in Tab. 3.6 – Tab. 3.8. It should be noted that this comparison does not only test the efficiency of the matrix element computation, but rather the overall performance of the generator. It is therefore a vital benchmark to asses the usefulness of COMIX.

Finally, cross sections obtained with COMIX are compared to results from other matrix element generators. As references AMEGIC++ [18] and ALPGEN [15] are employed. The original setup for the comparison has been established during the MC4LHC workshop [78]. For a comprehensive comparison of results from all participating projects, see ibidem. Input parameters are listed in Tab. 3.4. All results from COMIX are generated with the RPG presented in Sec. 3.3.1. Cross sections are summarised in Tab. 3.9 – Tab. 3.13. We find good agreement for all processes attempted so far.

A measure for the efficiency of a phase space generator is given by the ratio of the average over the maximal weight $\langle w \rangle / w_{\max}$, i.e. the efficiency for generating events of unit weight using a hit-or-miss method. However, as discussed in Ref. [79], the maximum weight and thus this ratio is a numerically rather unstable quantity, determined by very rare events in the high tail of the weight distribution. In Tab. 3.11 the more stable quantity $\langle w \rangle / w_{\max}^{\varepsilon}$ is therefore listed, where the reduced maximum weight $w_{\max}^{\varepsilon}$ is defined such that $1 - \langle \min(w, w_{\max}^{\varepsilon}) \rangle / \langle w \rangle = \varepsilon \ll 1$. It turns out that a reasonably good performance can be achieved, even for very large multiplicities.

Process	Time [ms / pt]		Ratio	Gain
	sum	sample		
$gg \to 2g$	0.073	0.025	2.9	2.1
$gg \to 3g$	0.339	0.060	5.7	3.5
$gg \to 4g$	1.67	0.149	11	4.5
$gg \to 5g$	8.98	0.427	21	5.3
$gg \to 6g$	49.6	1.39	36	6.6
$gg \to 7g$	298	4.32	69	7.1
$gg \to 8g$	1990	13.6	146	6.9
$gg \to 9g$	13100	43.7	300	6.7
$gg \to 10g$	96000	138	695	5.9

Tab. 3.1 Computation time for multi-gluon scattering matrix elements sampled over colour configurations. Displayed times are averages for a single evaluation of the colour-dressed BG recursion relation, when summing and sampling over helicity configurations, respectively. Additionally in the last column, labelled 'Gain' the inverse ratio of evaluation times multiplied by the naive ratio $2^n - 2(n+1)$ is given, where n is the number of external gluons. Numbers were generated on a 2.80 GHz Pentium® 4 CPU.

gg → ng	Cross section [pb]				
n	8	9	10	11	12
$\sqrt{s}$ [GeV]	1500	2000	2500	3500	5000
Comix	0.755(3)	0.305(2)	0.101(7)	0.057(5)	0.026(1)
Phys. Rev. D67(2003)014026	0.70(4)	0.30(2)	0.097(6)		
Nucl. Phys. B539(1999)215	0.719(19)				

Tab. 3.2 Cross sections for multi-gluon scattering at the centre of mass energy $\sqrt{s}$, using the phase space cuts specified in Eq. (3.34), compared to literature results. In parentheses the statistical error is stated in units of the last digit of the cross section.

gg → ng	Cross section [pb]			
n	7	8	9	10
Comix	2703(14)	407.0(36)	66.5(13)	15.2(26)

Tab. 3.3 Multi-gluon cross sections at the LHC with $\sqrt{d} \geq 20$ GeV and d defined as in Ref. [77], except that $\Delta R_{ij}^2 \to \cosh \Delta\eta_{ij} - \cos \Delta\phi_{ij}$. In parentheses the statistical error is stated in units of the last digit of the cross section.

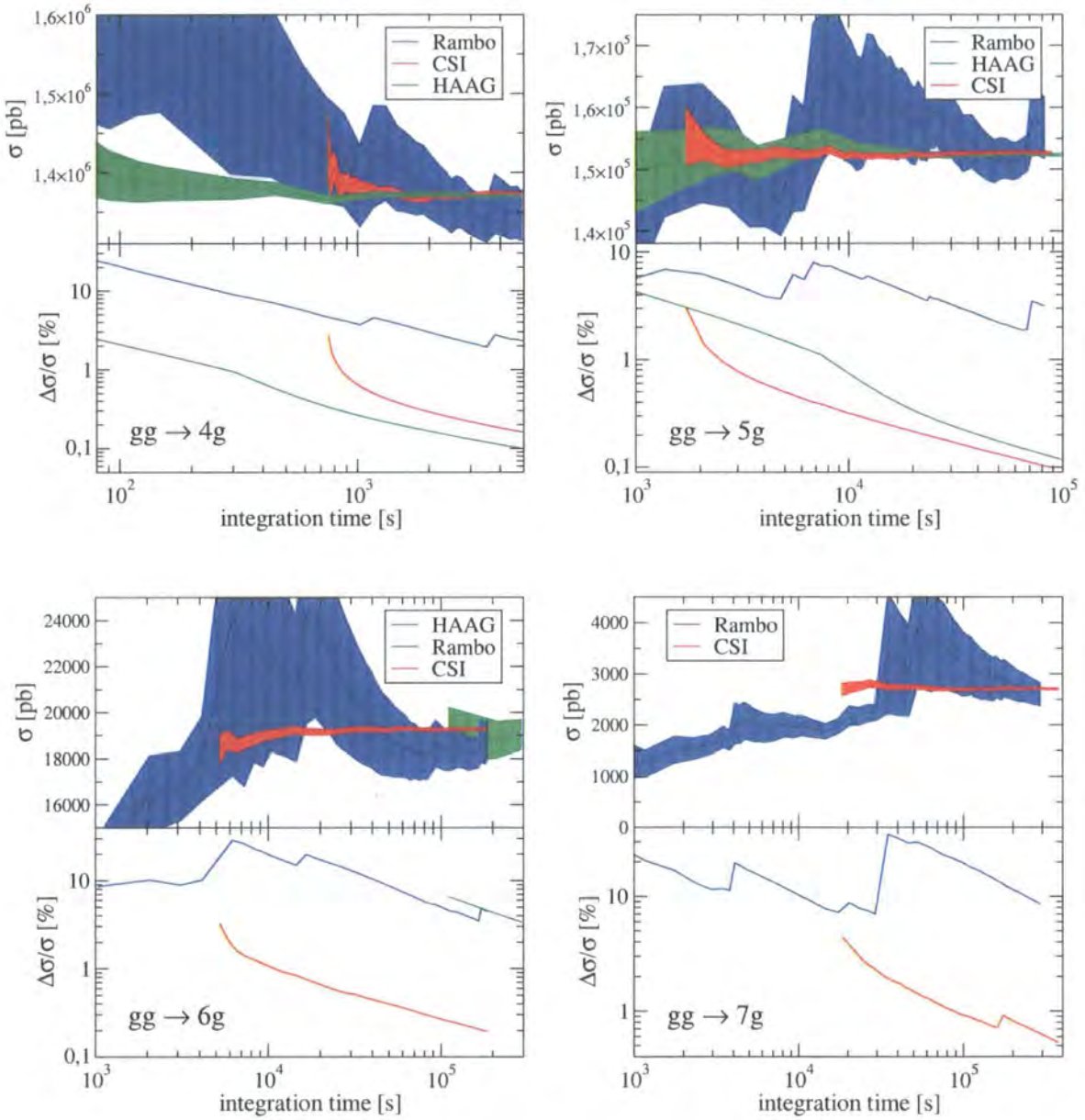

Fig. 3.4 Overall integration performance for multi-gluon scattering. Upper panels display the Monte Carlo estimate of the cross section with the corresponding 1σ statistical error band as a function of the total integration time. Lower panels show the relative statistical error. HAAG denotes the phase space integrator described in Appendix C, applied on colour- and helicity-summed ME, generated using the CSW recursion. CSI denotes the integrator discussed in Sec. 3.3.3, applied on colour-sampled and helicity-summed MEs, generated using the CDBG recursion. Results for RAMBO were generated using colour- and helicity-sampled ME's form the CDBG recursion. Calculations have been performed on a 2.66 GHz Xeon^{TM} CPU

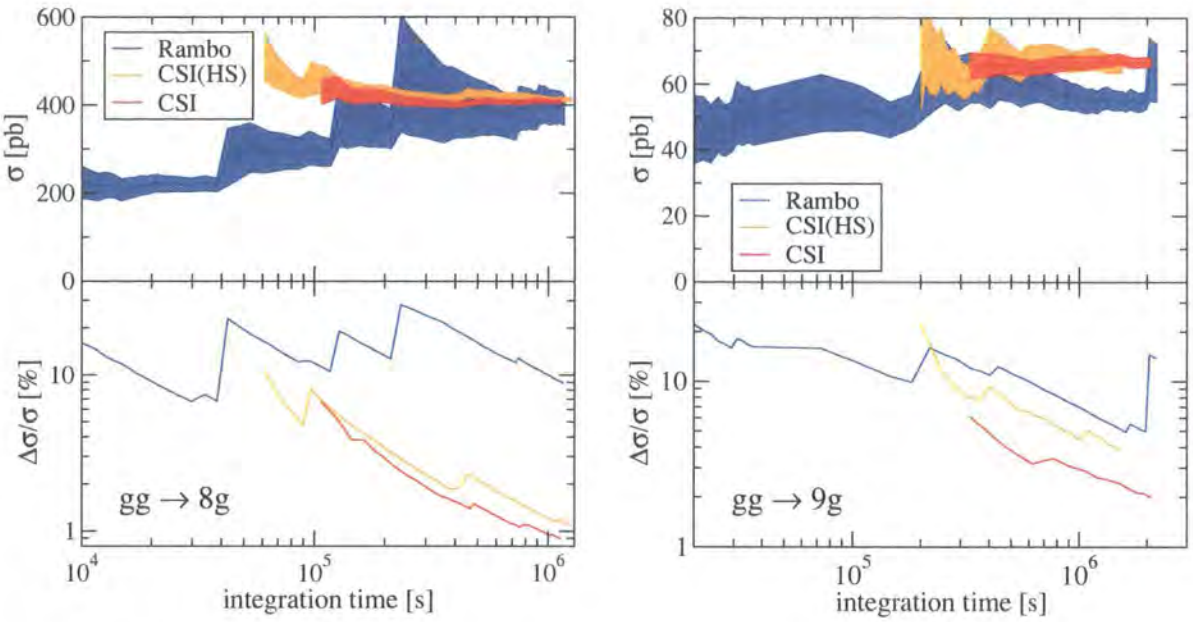

Fig. 3.5 Overall integration performance for multi-gluon scattering, continued from Fig. 3.4. Additionally, for the CSI a sampling over helicity is considered, denoted by CSI(HS).

Parameter	Value
EW parameters in the G_μ scheme	
G_F	1.16639×10^{-5}
α_{QED}	$1/132.51$
$\sin^2\theta_W$	0.2222
M_W	80.419 GeV
M_Z	91.188 GeV
m_H	120 GeV
CKM matrix	
V_{ud}, V_{cs}	0.975
QCD parameters	
PDF set	CTEQ6L1
α_s	0.130
μ_F, μ_R	M_Z
jet, initial parton	g, u, d, s, c

Parameter	Value
Non-zero fermion masses (no evolution)	
m_b	4.7 GeV
m_t	174.3 GeV
m_τ	1.777 GeV
Widths (fixed width scheme)	
Γ_W	2.048 GeV
Γ_Z	2.446 GeV
Γ_H	3.7×10^{-3} GeV
Γ_t	1.508 GeV
Γ_τ	2.36×10^{-12} GeV
Cuts	
$p_{\perp,i}$	> 20 GeV
$\lvert\eta_i\rvert$	< 2.5
ΔR_{ij}	> 0.4
no cuts on particles of $m > 3$ GeV and ν_l	

Tab. 3.4 Parameters for the MC4LHC comparison setup.

Process	Time per ME BG [s]	Time per ME CSW [s]	BG/CSW
$gg \to 2g$	8.42×10^{-6}	1.18×10^{-6}	7.1
$gg \to 3g$	3.19×10^{-5}	3.31×10^{-6}	9.6
$gg \to 4g$	1.13×10^{-4}	6.09×10^{-5}	2.0
$gg \to 5g$	3.58×10^{-4}	2.91×10^{-4}	1.3
$gg \to 6g$	1.17×10^{-3}	6.38×10^{-3}	0.20
$gg \to 7g$	3.99×10^{-3}	5.66×10^{-2}	0.079
$q\bar{q} \to 2g$	6.20×10^{-6}	1.02×10^{-6}	6.1
$q\bar{q} \to 3g$	2.18×10^{-5}	2.46×10^{-6}	8.9
$q\bar{q} \to 4g$	6.91×10^{-5}	4.59×10^{-5}	1.5
$q\bar{q} \to 5g$	2.15×10^{-4}	2.34×10^{-4}	0.92
$q\bar{q} \to 6g$	6.53×10^{-4}	4.00×10^{-3}	0.16
$q\bar{q} \to 7g$	2.03×10^{-3}	3.11×10^{-2}	0.065
$q\bar{q} \to q\bar{q}$	2.86×10^{-6}	1.56×10^{-6}	1.8
$q\bar{q} \to q\bar{q}\ g$	1.17×10^{-5}	3.26×10^{-6}	3.6
$q\bar{q} \to q\bar{q}\ 2g$	4.99×10^{-5}	5.92×10^{-5}	0.84
$q\bar{q} \to q\bar{q}\ 3g$	1.94×10^{-4}	2.90×10^{-4}	0.67
$q\bar{q} \to q\bar{q}\ 4g$	7.16×10^{-4}	4.93×10^{-3}	0.15
$q\bar{q} \to q\bar{q}\ 5g$	2.86×10^{-3}	3.69×10^{-2}	0.076
$q\bar{q} \to q'\bar{q}'$	2.24×10^{-6}	1.06×10^{-6}	2.1
$q\bar{q} \to q'\bar{q}'\ g$	8.97×10^{-6}	1.96×10^{-6}	4.6
$q\bar{q} \to q'\bar{q}'\ 2g$	2.87×10^{-5}	3.39×10^{-5}	0.85
$q\bar{q} \to q'\bar{q}'\ 3g$	8.18×10^{-5}	1.55×10^{-4}	0.59
$q\bar{q} \to q'\bar{q}'\ 4g$	2.70×10^{-4}	2.48×10^{-3}	0.11
$q\bar{q} \to q'\bar{q}'\ 5g$	8.13×10^{-4}	1.84×10^{-2}	0.044
$q\bar{q} \to Z(\to e^-e^+)$	3.84×10^{-6}	3.88×10^{-6}	0.99
$q\bar{q} \to Z(\to e^-e^+)\ g$	1.02×10^{-5}	6.85×10^{-6}	1.5
$q\bar{q} \to Z(\to e^-e^+)\ 2g$	2.57×10^{-5}	6.90×10^{-5}	0.37
$q\bar{q} \to Z(\to e^-e^+)\ 3g$	7.06×10^{-5}	2.95×10^{-4}	0.24
$q\bar{q} \to Z(\to e^-e^+)\ 4g$	1.95×10^{-4}	3.72×10^{-3}	0.052

Tab. 3.5 Average computation time for partial amplitudes in multi-jet processes, summed over helicity configurations. Displayed are averages for single evaluation, employing colour-dressed Berends-Giele recursion and CSW vertex rules. Numbers were generated on a 2.53 GHz Intel® Core™2 Duo T9400 CPU.

$pp \to n$ jets gluons only	$n = 2$	$n = 3$	$n = 4$	$n = 5$	$n = 6$
σ [pb]	$8.915 \cdot 10^7$	$5.454 \cdot 10^6$	$1.150 \cdot 10^6$	$2.757 \cdot 10^5$	$7.95 \cdot 10^4$
stat. error	0.1%	0.1%	0.2%	0.5%	1%
	integration time for given stat. error [s]				
CDBG ⊗ RPG	159	5050	33000	38000	74000
CDBG ⊗ CSI	-	780	6930	6800	12400
CSW ⊗ HAAG	4	165	1681	12800	$2 \cdot 10^6$
CSW ⊗ CSI	-	480	6500	11900	197000
AMEGIC ⊗ HAAG	6	492	41400	-	-

Tab. 3.6 Cross section and evaluation times for different matrix element (phase space) generation methods for multi-gluon scattering at the LHC. Numbers were generated on a 2.53 GHz Intel® Core™2 Duo T9400 CPU. For cuts and parameter settings, cf. the text and Tab. 3.4.

$pp \to n$ jets ≤ 2 quark lines	$n = 2$	$n = 3$	$n = 4$	$n = 5$	$n = 6$
σ [pb]	$1.5129 \cdot 10^8$	$1.1198 \cdot 10^7$	$2.831 \cdot 10^6$	$8.13 \cdot 10^5$	$2.71 \cdot 10^5$
stat. error	0.1%	0.1%	0.2%	0.5%	1%
	integration time for given stat. error [s]				
CDBG ⊗ RPG	525	10800	25600	59000	113000
CSW ⊗ HAAG	16	730	12300	120000	$2 \cdot 10^7$
AMEGIC ⊗ HAAG	19	1530	78000	-	-

Tab. 3.7 Cross section and evaluation times for different matrix element (phase space) generation methods for multi-jet production at the LHC. Numbers were generated on a 2.53 GHz Intel® Core™2 Duo T9400 CPU. For cuts and parameter settings, cf. the text and Tab. 3.4.

$pp \to Z+$ jets	$n = 0$	$n = 1$	$n = 2$	$n = 3$	$n = 4$
σ [pb]	1080.8	121.67	54.67	23.59	11.22
stat. error	0.1%	0.1%	0.1%	0.2%	0.5%
	integration time for given stat. error [s]				
CDBG ⊗ RPG	15	364	6400	16400	54000
AMEGIC ⊗ MC	7	98	1060	10400	310000
CSW ⊗ MC	12	210	4100	57000	1500000

Tab. 3.8 Cross section and evaluation times for different matrix element (phase space) generation methods for $Z+$jet production at the LHC. Numbers were generated on a 2.53 GHz Intel® Core™2 Duo T9400 CPU. For cuts and parameter settings, cf. the text and Tab. 3.4.

σ [μb]	Number of jets						
jets	2	3	4	5	6	7	8
Comix	331.0(4)	22.72(6)	4.95(2)	1.232(4)	0.352(1)	0.1133(5)	0.0369(3)
ALPGEN	331.7(3)	22.49(7)	4.81(1)	1.176(9)	0.330(1)		
AMEGIC++	331.0(4)	22.78(6)	4.98(1)	1.238(4)			

σ [μb]	Number of jets						
$b\bar{b}$ + QCD jets	0	1	2	3	4	5	6
Comix	471.2(5)	8.83(2)	1.813(8)	0.459(2)	0.150(1)	0.0531(5)	0.0205(4)
ALPGEN	470.6(6)	8.83(1)	1.822(9)	0.459(2)	0.150(2)	0.053(1)	0.0215(8)
AMEGIC++	470.3(4)	8.84(2)	1.817(6)				

σ [pb]	Number of jets						
$t\bar{t}$ + QCD jets	0	1	2	3	4	5	6
Comix	754.8(8)	745(1)	518(1)	309.8(8)	170.4(7)	89.2(4)	44.4(4)
ALPGEN	755.4(8)	748(2)	518(2)	310.9(8)	170.9(5)	87.6(3)	45.1(8)
AMEGIC++	754.4(3)	747(1)	520(1)				

σ [pb]	Number of jets						
$e^+\nu_e$ + QCD jets	0	1	2	3	4	5	6
Comix	5434(5)	1274(2)	465(1)	183.0(6)	77.5(3)	33.8(1)	14.7(1)
ALPGEN	5423(9)	1291(13)	465(2)	182.8(8)	75.7(8)	32.5(2)	13.9(2)
AMEGIC++	5432(5)	1279(2)	466(2)	185.2(5)	77.3(4)		

σ [pb]	Number of jets						
$e^-\bar{\nu}_e$ + QCD jets	0	1	2	3	4	5	6
Comix	3911(4)	1011(2)	362(1)	137.1(3)	54.9(2)	22.4(1)	9.26(4)
ALPGEN	3904(6)	1013(2)	364(2)	136(1)	53.6(6)	21.6(2)	8.7(1)
AMEGIC++	3903(4)	1012(2)	363(1)	137.6(3)	54.8(6)		

σ [pb]	Number of jets						
e^-e^++ QCD jets	0	1	2	3	4	5	6
Comix	723.5(4)	187.9(3)	69.7(2)	27.14(7)	11.09(4)	4.68(2)	2.02(2)
ALPGEN	723.4(9)	188.3(3)	69.9(3)	27.2(1)	10.95(5)	4.6(1)	1.85(1)
AMEGIC++	723.0(8)	188.2(3)	69.6(2)	27.21(6)	11.1(1)		

σ [pb]	Number of jets						
$\nu_e\bar{\nu}_e$ + QCD jets	0	1	2	3	4	5	6
Comix	3266(3)	715.9(8)	266.6(7)	105.0(3)	44.4(2)	19.11(7)	8.30(7)
ALPGEN	3271(1)	717.4(5)	267.4(4)	105.4(2)	43.7(2)	18.68(8)	7.88(5)
AMEGIC++	3270(1)	717.3(7)	266.3(6)	105.4(3)	44.3(5)		

Tab. 3.9 Cross sections in the MC4LHC comparison [78] setup. In parentheses the statistical error is stated in units of the last digit of the cross section. Note that for AMEGIC++ and COMIX all subprocesses are considered, while ALPGEN is restricted to up to four quarks. Taking this into account, all values agree within $2\,\sigma$

σ [nb]	Number of jets					
γ + QCD jets	1	2	3	4	5	6
Comix	89.5(2)	19.65(6)	7.52(3)	2.664(8)	1.000(5)	0.387(2)
AMEGIC++	89.6(1)	19.60(5)	7.59(2)	2.64(2)		

σ [pb]	Number of jets					
$e^-\bar{\nu}_e + b\bar{b}$ + QCD jets	0	1	2	3	4	5
Comix	9.40(2)	9.81(3)	6.82(5)	4.32(4)	2.47(2)	1.28(2)
ALPGEN	9.34(4)	9.85(6)	6.82(6)	4.18(7)	2.39(5)	
AMEGIC++	9.37(1)	9.86(2)	6.98(3)	4.31(6)		

σ [pb]	Number of jets					
$e^-e^+ + b\bar{b}$ + QCD jets	0	1	2	3	4	5
Comix	18.90(3)	6.81(2)	3.07(3)	1.536(9)	0.763(6)	0.37(1)
ALPGEN	18.95(8)	6.80(3)	2.97(2)	1.501(9)	0.78(1)	
AMEGIC++	18.90(2)	6.82(2)	3.06(4)			

Tab. 3.10 Cross sections in the MC4LHC comparison [78] setup. In parentheses the statistical error is stated in units of the last digit of the cross section. Note that for AMEGIC++ and COMIX all subprocesses are considered, while ALPGEN is restricted to up to four quarks. Taking this into account, all values agree within 2σ.

efficiency	Number of jets						
jets	2	3	4	5	6	7	8
$\varepsilon = 10^{-3}$	$9.3{\cdot}10^{-2}$	$7.8{\cdot}10^{-3}$	$2.1{\cdot}10^{-3}$	$7.0{\cdot}10^{-4}$	$3.6{\cdot}10^{-4}$	$1.3{\cdot}10^{-4}$	$6.1{\cdot}10^{-5}$
$\varepsilon = 10^{-6}$	$3.1{\cdot}10^{-2}$	$3.8{\cdot}10^{-3}$	$1.5{\cdot}10^{-3}$	$4.3{\cdot}10^{-4}$	$2.4{\cdot}10^{-4}$	$9.9{\cdot}10^{-5}$	$5.8{\cdot}10^{-5}$

efficiency	Number of jets						
$e^+\nu_e$ + QCD jets	0	1	2	3	4	5	6
$\varepsilon = 10^{-3}$	$1.5{\cdot}10^{-1}$	$2.4{\cdot}10^{-2}$	$9.1{\cdot}10^{-3}$	$2.0{\cdot}10^{-3}$	$6.7{\cdot}10^{-4}$	$1.9{\cdot}10^{-4}$	$3.1{\cdot}10^{-5}$
$\varepsilon = 10^{-6}$	$1.6{\cdot}10^{-2}$	$4.5{\cdot}10^{-3}$	$3.3{\cdot}10^{-3}$	$1.2{\cdot}10^{-3}$	$4.3{\cdot}10^{-4}$	$1.3{\cdot}10^{-4}$	$2.8{\cdot}10^{-5}$

Tab. 3.11 Efficiencies for processes in the MC4LHC comparison [78] setup.

σ [nb]	Number of jets n	
QCD jets	7	8
$gg \to ng$	49.1(4)	14.2(3)
$gg \to (n-2)g\,2q$	17.0(1)	6.0(1)
$gg \to (n-4)g\,4q$	1.69(1)	0.74(5)
$gg \to (n-6)g\,6q$	0.0401(5)	0.0297(8)
$gg \to 8q$	-	0.000158(5)
$gq \to (n-1)g\,1q$	30.5(2)	9.9(2)
$gq \to (n-3)g\,3q$	8.46(6)	3.38(6)
$gq \to (n-5)g\,5q$	0.565(7)	0.332(8)
$gq \to (n-7)g\,7q$	0.00501(6)	0.0067(2)
$qq \to ng$	0.0209(1)	0.0067(1)
$qq \to (n-2)g\,2q$	4.97(4)	1.84(3)
$qq \to (n-4)g\,4q$	1.044(9)	0.477(9)
$qq \to (n-6)g\,6q$	0.0374(3)	0.0291(5)
$qq \to 8q$	-	0.000223(4)

Tab. 3.12 Subprocess cross sections in the MC4LHC comparison [78] setup. In parentheses the statistical error is stated in units of the last digit of the cross section.

σ [pb]	Number of jets n	
$e^+\nu_e$ + QCD jets	5	6
$qq \to e^+\nu_e\, ng$	0.256(2)	0.0768(6)
$qq \to e^+\nu_e\,(n-2)g\,2q$	6.49(3)	2.92(3)
$qq \to e^+\nu_e\,(n-4)g\,4q$	0.591(3)	0.449(8)
$qq \to e^+\nu_e\,6q$	-	0.00640(7)
$gq \to e^+\nu_e\,(n-1)g\,1q$	20.0(1)	8.21(8)
$gq \to e^+\nu_e\,(n-3)g\,3q$	4.03(2)	2.14(2)
$gq \to e^+\nu_e\,(n-5)g\,5q$	0.0741(4)	0.094(1)
$gg \to e^+\nu_e\,(n-2)g\,2q$	2.13(1)	0.775(5)
$gg \to e^+\nu_e\,(n-4)g\,4q$	0.1817(9)	0.1058(7)
$gg \to e^+\nu_e\,6q$	-	0.001403(7)

Tab. 3.13 Subprocess cross sections in the MC4LHC comparison [78] setup. In parentheses the statistical error is stated in units of the last digit of the cross section.

4 Conclusions

In this part of the thesis, a new approach to calculate multi-parton amplitudes has been presented, which extends the recursive relations for colour-ordered amplitudes to relations for full coloured amplitudes. It was shown how colour can be included in the colour-stripped recursive relations coming from twistor-inspired methods that do not have a straightforward relation with a standard perturbative Lagrangian approach. Numerical properties of the corresponding algorithms have been studied in detail.

In general the new colour-dressed recursive relations are much more suitable for a numerical implementation since they naturally avoid the factorial growth implicit in taking the sum over permutations of possible colour flows in an amplitude. The taming of the factorial growth to an exponential one is easily proved in the colour-dressed formulation of the Berends-Giele recursive relations which are found to be the same as the Schwinger-Dyson approach introduced in Ref. [71] and equivalent to the ALPHA algorithm of Ref. [76]. Using a similar approach but exploiting the adjoint colour basis decomposition, Eq. (1.8), a new formulation of the BCF relations, Eq. (2.43), has been proved which involves the full amplitudes, including colour, and retains the same formal simplicity as the original formulation. Finally, the CSW relations have been considered. They were recast into a form similar to the Berends-Giele relation through the introduction of a new type of three-point vertices and effective particles, Eqs. (2.28) and (2.29). It is interesting to note, that while for the Berends-Giele relations the colour dressing is straightforward due to the close correspondence to the standard quantum field theory perturbative approach, this is far less trivial for the BCF and CSW relations, for which there is no direct relation to these techniques.

To test the numerical efficiency of the different formulations, all corresponding algorithms

were implemented into numerical programs and squared amplitudes for $2 \to n$ gluon scattering were computed, performing the sum over helicities and colours with a Monte Carlo method. The corresponding results clearly show the numerical superiority of the recursive formulation by Berends and Giele over all twistor-inspired methods, both from the point of view of the growth of complexity with n and the simplicity of the implementation. For the colour-ordered amplitude formulation, the results of Ref. [49] are confirmed, except for the CSW relations, on which considerable improvement is achieved by bringing them to the same level of complexity as the BCF relations. The colour-dressed formulations of the BCF and CSW relations perform worse than the corresponding colour-dressed Berends-Giele relations for different reasons. The BCF relations are penalised by their top-down structure, i.e. the fact that for each helicity and colour configuration the decomposition in terms of amplitudes with smaller multiplicity has to be found, and by the fact that their natural (and minimal) colour basis is the adjoint basis which is computationally quite heavy. The "improved" colour-dressed CSW relations instead suffer from the presence of a large number of elementary line types and effective three-point vertices which eventually affect the overall growth of the algorithm.

The colour-dressed Berends-Giele recursive relations lead to the construction of the new tree-level matrix element generator COMIX, which is especially suited for large multiplicity processes. In this context, a new technique to recursively compute phase space integrals has been presented, which is based on the assumed pole structure of the integrand, i.e. the Feynman diagrams leading to the full amplitude. This method induces at most the same growth in computational complexity as the matrix element computation in the colour-dressed Berends-Giele approach and is therefore a major improvement over current algorithms.

The performance of the new generator has been analysed and results have been compared to those of other matrix element generators. It is observed that the new algorithms perform very well and promising results for large multiplicity processes are obtained. COMIX can therefore be considered an excellent supplementary generator for large multiplicities, which is especially helpful in the context of a matrix element parton shower merging. This will be considered in the second part of the thesis. The treatment of colour in COMIX makes the algorithm well suited for such an interface, since the colour structure of the matrix element

does not need to be guessed from kinematics, it is rather fixed on a point by point basis. Finally, a new type of integrator for QCD processes has been suggested, which is based on the HAAG generator and couples the sampling in colour and momentum space. Especially for large multiplicity processes it leads to a faster convergence of the integral than all other algorithms, essentially because information on possible partial amplitudes is included in the sampling.

To conclude, present methods for matrix element computation have been improved and extended in this part of the thesis. The new colour-dressed recursive relations are a major theoretical improvement. The colour-dressed Berends-Giele recursive relations lend themselves nicely into a numerical implementation which even suggested that a corresponding algorithm for phase space integration should exist. This algorithm has been presented.

Part II

Generation of parton showers

1 QCD parton evolution

With the startup of the LHC, high-energy particle physics will enter a new era, where the tremendous centre-of-mass energy of 14 TeV opens a window to the search for new physics and more detailed study of known phenomena. The large energy involved in the production of interesting signals then typically gives rise to large radiative QCD corrections, which need to be described by event generators. Hard matrix elements have to be evaluated at scales, which are far from the hadronisation scale and the large open phase space can lead to the production of many additional particles. When calculated at fixed order inclusively, such radiative corrections appear as the finite remainder after the cancellation of divergences from real and virtual contributions. Under the assumption of good convergence of the perturbative series, they are small or at least decrease with increasing number of strong couplings involved.

There is however no possibility to observe the fully inclusive cross section for the $\mathcal{O}(\alpha_S)$ correction to any given QCD process. Every experiment will have a resolution criterion (most commonly defined in $\Delta R = \sqrt{\Delta\eta^2 + \Delta\phi^2}$), which determines the minimum separation of two separately resolved QCD partons. This implies a different approach to QCD associated processes, which proceeds in terms of measurable "jets". Experimentally a jet is seen as nothing but a bunch of collimated particles entering the detector. In the framework of perturbative QCD, these particles are thought to emerge from the resolved part of radiation stemming from a common initiating parton. The ultimate goal on the experimental side is to construct an algorithm, which translates one interpretation into the other, such that experimental signatures can be compared to perturbative QCD calculations. On theoretical grounds, the aim is to describe the evolution of QCD partons such, that at any resolution

scale the correct radiation pattern is produced.

The standard theoretical framework to achieve both of these aims are the Dokshitzer-Gribov-Lipatov-Altarelli-Parisi (DGLAP) equations [80, 81], which govern the evolution of fragmentation functions and parton distribution functions. The key observation is that next-to leading order corrections, if unintegrated below a certain resolution scale do not manifest themselves as poles but turn into large logarithms of the form $\log(Q^2/Q_0^2)$, where Q is the initial scale of parton production and Q_0 is the resolution scale. These logarithms, together with the logarithmic terms contained in the strong coupling α_s, have to be resummed to all orders to obtain a finite cross section. They exponentiate and give rise to Sudakov form factors $\Delta_a(q^2, Q^2)$ [82, 83], which are interpreted as the no-emission probability for a given parton a that evolves from scale Q to scale q without any resolvable radiation at q. Such expressions play an essential role in the construction of shower algorithms.

The outline of this part of the thesis is as follows. Firstly the basics of QCD parton evolution are discussed at hand of the leading order DGLAP equations. Fragmentation functions and parton distribution functions are introduced. Their respective Q^2–evolution under the DGLAP equations is discussed and the correspondence with shower algorithms is pointed out. A shower algorithm for Q^2–evolution is briefly introduced. The merging with explicit real next–to–leading order corrections under an extension of the CKKW prescription is discussed in detail. A new k_T–type measure, based on the respective shower evolution is presented and the implications of this definition are outlined. This part concludes with the presentation of BFKL evolution and a novel algorithm for generating $\ln(1/x)$ parton evolution in a Markovian approach. The striking similarity with parton shower generation is pointed out.

1.1 Final state parton evolution

QCD parton evolution and the occurrence of jets can be understood theoretically when the structure of perturbative amplitudes is examined in the kinematical regime where intrajet evolution takes place, i.e. where two or more partons become close in phase space. Whenever this happens, any QCD matrix element squared factorises into a matrix element squared containing the combined "mother" parton and a universal function describing the splitting

into external particles, cf. Refs. [84]. In other words, the theory becomes semiclassical and can be understood in a Markovian approach, where a single initiating parton develops a cascade of independent branchings, see also Refs. [85]. This is the basic concept of any shower Monte Carlo. Potential differences then arise in the factorisation scheme only.

The most commonly used scheme is collinear factorisation. In this context two massless final state partons i and j become collinear, if $\mathrm{k}_\perp^2 \to 0$ in the following decomposition of their momenta.

$$p_i^\mu = z\,p^\mu + \frac{\mathrm{k}_\perp^2}{z}\frac{n^\mu}{2\,pn} + k_\perp^\mu\,, \qquad p_i = (1-z)\,p^\mu + \frac{\mathrm{k}_\perp^2}{1-z}\frac{n^\mu}{2\,pn} - k_\perp^\mu\,. \tag{1.1}$$

Here p denotes the collinear direction, while n determines how the collinear direction is approached. The two light-like vectors p and n can be interpreted as reference vectors in "+"– and "–"– direction of a Sudakov parametrisation [82]. It is easy to see that

$$\mathrm{k}_\perp^2 = z(1-z)\,2p_ip_j\,, \tag{1.2}$$

such that the collinear limit is approached if $z(1-z)\,2p_ip_j \to 0$. It is observed that in this limit to $\mathcal{O}(\alpha_s)$ any azimuthally summed QCD associated differential cross section factorises as

$$\mathrm{d}\sigma_{n+1}\left(\ldots,i,\ldots,j,\ldots\right) = \mathrm{d}\sigma_n\left(\ldots,\{ij\},\ldots\right)\frac{\mathrm{d}s_{ij}}{s_{ij}}\,\mathrm{d}z\,\frac{\alpha_s}{2\pi}\,\hat{P}_{a_{ij}a_i}(z)\,, \tag{1.3}$$

where $s_{ij} = (p_i+p_j)^2$ and a_i and a_{ij} are the flavours of parton i and the combined mother parton $\{ij\}$, respectively. The functions $\hat{P}_{ab}(z)$ are regularised Altarelli–Parisi splitting kernels [81]. They describe the collinear splitting of parton a into parton b and are given by

$$\begin{aligned}
\hat{P}_{qq} &= C_F\left[\frac{1+z^2}{(1-z)_+} + \frac{3}{2}\delta(1-z)\right]\,, \qquad \hat{P}_{qg} = C_F\,\frac{1+(1-z)^2}{z}\,,\\
\hat{P}_{gg} &= 2C_A\left[\frac{z}{(1-z)_+} + \frac{1-z}{z} + z(1-z)\right] + \delta(1-z)\,\frac{11C_A - 4n_fT_R}{6}\,,\\
\hat{P}_{gq} &= T_R\left[\,z^2 + (1-z)^2\,\right]\,,
\end{aligned} \tag{1.4}$$

where $C_A = N_C$, $C_F = (N_C^2-1)/2N_C$ and $T_R = 1/2$. The "+"–prescription employed above

is defined as follows: If $F(z)$ is a function of z, which exhibits a single singularity at $z = 1$, the corresponding + -function $(F(z))_+$ reads

$$(F(z))_+ = \lim_{\beta\to 0}\left\{ F(z)\theta(1-z-\beta) - \delta(1-z-\beta)\int_0^{1-\beta} \mathrm{d}z\, F(z)\right\} . \tag{1.5}$$

Based on the factorisation formula, Eq. (1.3), electron–positron annihilation into hadrons at leading and next–to–leading order can now be investigated as an example to introduce master equations for standard final state parton showers. The derivation presented here closely follows Refs. [86] and [87].

Hadronic final states and fragmentation functions

In terms of the Born cross section σ_B, the total next–to–leading order cross section for electron–positron annihilation into a specific hadron h with energy fraction $x = E_h/Q$ at scale Q^2 reads [86]

$$\begin{aligned}\frac{\mathrm{d}\sigma^h(x,Q^2)}{\mathrm{d}x} = \sigma_B \int_x^1 \frac{\mathrm{d}z}{z}\Bigg\{ &\sum_{i=1}^{n_f} e_{q_i}^2 \left[D^h_{0,q_i}(x/z) + D^h_{0,\bar{q}_i}(x/z)\right] \\ &\left[(1+\frac{\alpha_s}{\pi})\,\delta(1-z) + \frac{\alpha_s}{2\pi}\hat{P}_{qq}(z)\log(Q^2/m^2) + \ldots\right] \\ &+ 2\sum_{i=1}^{n_f} e_{q_i}^2\, D^h_{0,g}(x/z)\left[\frac{\alpha_s}{2\pi}\hat{P}_{qg}(z)\log(Q^2/m^2) + \ldots\right]\Bigg\} ,\end{aligned} \tag{1.6}$$

It is universally employed to introduce the concept of fragmentation functions, which are nothing but a parametrisation of the unknown nonperturbative dynamics in the formation of hadrons. Terms containing the Altarelli–Parisi splitting functions correspond to the emission of a real, resolvable parton, while the δ–function implements the Born and virtual contributions. The dots stand for higher order contributions, which are regularisation-scheme dependent and do not play a role at leading logarithmic order. The functions $D^h_{0,a}$ are bare fragmentation functions, which describe the transition of parton a into hadron h. They are not observable since they probe the z–dependent transition of a specific parton into a hadron and are therefore unphysical. Moreover, Eq. (1.6) depends on an unphysical regularisation parameter m, which is a fictious gluon mass or a dimensional parameter, depending on the regularisation scheme. Observable fragmentation functions to $\mathcal{O}(\alpha_s)$ are

therefore introduced through

$$D_a^h(x,Q^2) = \bar{D}_{0,a}^h(x,Q^2) + \int_x^1 \frac{\mathrm{d}z}{z}\frac{\alpha_s}{2\pi}\sum_{b=q,g}\hat{P}_{ab}(z)\log(Q^2/\mu^2)\,\bar{D}_{0,b}^h(x/z,Q^2) + \dots . \quad (1.7)$$

such that to $\mathcal{O}(\alpha_s)$

$$\frac{\mathrm{d}\sigma^h(x,Q^2)}{\mathrm{d}x} = \sigma_B\left(1+\frac{\alpha_s}{\pi}\right)\int_x^1\frac{\mathrm{d}z}{z}\sum_{i=1}^{n_f}e_{q_i}^2\left[D_{q_i}^h(x/z,Q^2)+D_{\bar{q}_i}^h(x/z,Q^2)\right], \quad (1.8)$$

The scale μ introduced above is an arbitrary scale, used to factor off mass singularities. As a consequence, the dependence of σ on the unphysical parameter m, which was present in Eq. (1.6), is absorbed completely into the bare fragmentation functions $\bar{D}_{0,a}^h$. This factorisation property has been proved to hold to arbitrary order in perturbation theory [87]. To $\mathcal{O}(\alpha_s)$ it can be understood as the definition

$$\bar{D}_{0,a}^h(x,Q^2) = \int_x^1\frac{\mathrm{d}z}{z}D_{0,a}^h(x/z,Q^2)\left[\delta(1-z)+\frac{\alpha_s}{2\pi}\hat{P}_{aa}(z)\log(\mu^2/m^2)+\dots\right], \quad (1.9)$$

Finally, to $\mathcal{O}(\alpha_s)$ one obtains

$$\frac{\mathrm{d}D_a^h(x,Q^2)}{\mathrm{d}\log(Q^2/\mu^2)} = \int_x^1\frac{\mathrm{d}z}{z}\frac{\alpha_s(Q^2)}{2\pi}\sum_{b=q,g}\hat{P}_{ab}(z)\,D_b^h(x/z,Q^2), \quad (1.10)$$

This is the usual Altarelli-Parisi form of the leading order equations that govern the Q^2 evolution of fragmentation functions [81]. Note that due to the z–integration region, it is mandatory to implement the Altarelli-Parisi kernels in their regularised form, since $P_{qq}(z)$ and $P_{gg}(z)$ are naively divergent for $z \to 1$. It will turn out, however that for a Monte Carlo simulation unregularised splitting functions can be employed. A pictorial interpretation of Eq. (1.10) is shown in Fig. 1.1.

Final state parton showers

Equation (1.10) is not suited to compute the Q^2-evolution of full QCD final states in a Monte Carlo program, because it describes the behaviour of an inclusive quantity, which is related to employing the regularised Altarelli-Parisi kernels in "+"–prescription. This implies, however

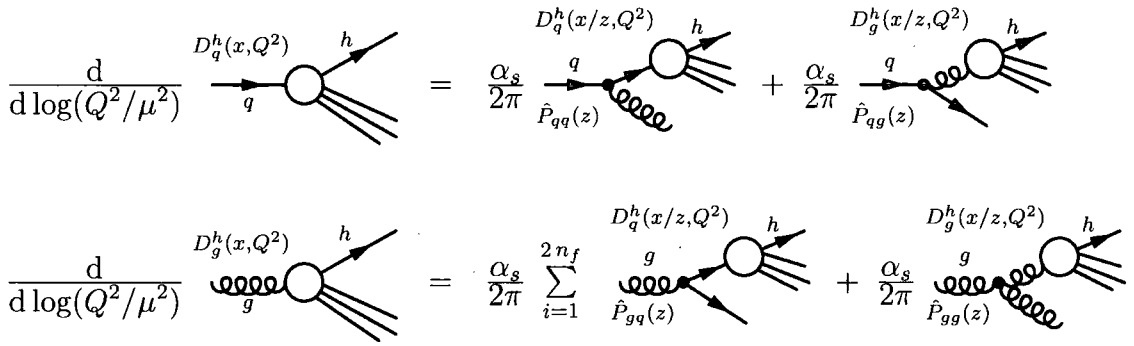

Fig. 1.1 Pictorial representation of the Q^2–evolution of fragmentation functions, Eq. (1.10). Shown are both, the quark– and gluon fragmentation functions.

that two partons can come infinitely close in phase space before they hadronise. Given enough time, any parton thus has the chance to radiate infinitely many collinear partons or soft gluons before it hadronises. Such a scenario would obviously be unphysical, since the scale where radiation takes place somewhen falls below the hadronisation scale Λ, and hadrons are formed.

Equation (1.10) must take this effect into account, which can be achieved through an additional term, describing virtual and unresolvable parton emission. The leading order equation for Q^2-evolution of the fragmentation functions then reads

$$\begin{aligned}\frac{\mathrm{d}D_a^h(x,Q^2)}{\mathrm{d}\log(Q^2/\mu^2)} &= \int_x^{z_{\max}} \frac{\mathrm{d}z}{z}\,\frac{\alpha_s(Q^2)}{2\pi} \sum_{b=q,g} P_{ab}(z)\, D_b^h(x/z,Q^2) \\ &\quad - D_a^h(x,Q^2) \int_{\xi_{\min}}^{\xi_{\max}} \mathrm{d}\xi\,\frac{\alpha_s(Q^2)}{2\pi} \sum_{b=q,g} \frac{1}{2}\, P_{ba}(\xi)\,.\end{aligned} \tag{1.11}$$

The factor 1/2 in the loss term avoids double counting final states when summing over all parton species. The bounds on ξ and the upper bound on z remain to be fixed. They depend on the resolution criterion for parton emission and are therefore related to the hadronisation scale Λ. Note that in Eq. (1.11) the Altarelli-Parisi splitting functions appear in unregularised form, which amounts to dropping the "+"–prescription and terms containing δ functions in Eq. (1.4). To solve Eq. (1.11), it is convenient to introduce the Sudakov form

factor

$$\Delta_a(\mu^2,Q^2) \;=\; \exp\left\{ -\int_{\mu^2}^{Q^2} \frac{\mathrm{d}t}{t} \int_{\xi_{\min}}^{\xi_{\max}} \mathrm{d}\xi \sum_{b=q,g} \frac{\alpha_s}{2\pi}\frac{1}{2} P_{ba}(\xi) \right\} , \tag{1.12}$$

which is interpreted as the resummation of the loss term in Eq. (1.11) to all orders. It corresponds to the no-emission probability for parton a during the transition from Q to μ in unconstrained parton evolution. Equation (1.11) can then be rewritten as

$$\begin{aligned} &\frac{\mathrm{d}}{\mathrm{d}\log(Q^2/\mu^2)} \frac{D_a^h(x,Q^2)}{\Delta_a(\mu^2,Q^2)} = \\ &\qquad \frac{1}{\Delta_a(\mu^2,Q^2)} \int_x^{z_{\max}} \frac{\mathrm{d}z}{z} \frac{\alpha_s(Q^2)}{2\pi} \sum_{b=q,g} P_{ab}(z)\, D_b^h(x/z,Q^2) , \end{aligned} \tag{1.13}$$

The fraction of partons a, produced at Q^2, which does not branch between Q^2 and q^2 is given by

$$\begin{aligned} \Pi_a(x,q^2,Q^2) &= 1 - \frac{\Delta_a(\mu^2,Q^2)}{D_a^h(x,Q^2)} \int_{q^2}^{Q^2} \frac{\mathrm{d}q^2}{q^2} \frac{\mathrm{d}}{\mathrm{d}\log(q^2/\mu^2)} \frac{D_a^h(x,q^2)}{\Delta_a(\mu^2,q^2)} \\ &= \frac{\Delta_a(\mu^2,Q^2)\, D_a^h(x,q^2)}{\Delta_a(\mu^2,q^2)\, D_a^h(x,Q^2)} . \end{aligned} \tag{1.14}$$

In a Monte Carlo simulation, Eq. (1.14) can be employed to decide whether or not a parton branches at scale q^2 by selecting a random number $\mathcal{R} \in [0,1]$ and solving $\Pi_a(x,q^2,Q^2) = \mathcal{R}$ for q^2. Then a corresponding z has to be found according to Eq. (1.13) and an azimuthal angle for the branching must be selected. This procedure is, however not the method of choice. Most commonly, the presence of a particular final state hadron of type h, assumed in the above derivation, is not of interest. One rather tries to simulate the full Q^2 evolution of the complete final state produced through a hard scattering matrix element at the same time. In other words, rather than a constrained evolution, where in the last step a specific hadron h with momentum fraction x needs to be produced, an unconstrained evolution is considered. In this case the Sudakov form factor, Eq. (1.12) becomes

$$\Delta_a(\mu^2,Q^2) = \exp\left\{ -\int_{\mu^2}^{Q^2} \frac{\mathrm{d}t}{t} \int_{\xi_{\min}}^{\xi_{\max}} \mathrm{d}\xi \sum_{b=q,g} \frac{\alpha_s}{2\pi}\frac{1}{2} P_{ab}(\xi) \right\} . \tag{1.15}$$

Note that due to the forward evolution picture, splitting functions have their parton labels

reversed. The ξ integration is restricted by the resolution criterion. Most commonly the corresponding boundaries are fixed through a transverse momentum cutoff. If for example t is interpreted as $2p_b p_c$ and one requires $4k_\perp^2 > t_0$, Eq. (1.2) implies

$$\min\{z, 1-z\} \geq \frac{1}{2}\left[1 - \sqrt{1 - \frac{t_0}{t}}\right] . \tag{1.16}$$

The probability for a resolved branching of parton a at scale q^2 now reads

$$\Pi\left(q^2, Q^2\right) = \frac{\Delta_a(\mu^2, Q^2)}{\Delta_a(\mu^2, q^2)} . \tag{1.17}$$

A branching scale q^2 can therefore be found in a Monte Carlo fashion by solving $\Pi_a(q^2, Q^2) = \mathcal{R}$ for q^2. The corresponding value of z and the branching type should be selected according to $\mathrm{d}\log\Delta_a(q^2, Q^2)/\mathrm{d}\log(Q^2/\mu^2)$.

1.2 Initial state parton evolution

Similar to the final state parton evolution introduced above, initial state partons can undergo branching during the evolution from the hadronisation scale Λ to the hard scale Q^2 of the process under consideration. A relatively clean environment for the analysis of initial state parton evolution is obtained in deep inelastic scattering (DIS). In this case, the most general form of the hard matrix element squared reads

$$\overline{|\mathcal{M}|}^2 = \frac{(4\pi\alpha_{\mathrm{QED}})^2}{Q^4} L_{\mu\nu} W^{\mu\nu} , \tag{1.18}$$

where $Q^2 = -q^2$ and q is the virtual photon four momentum. The tensors $L_{\mu\nu}$ and $W^{\mu\nu}$ describe the interaction of the electron and the proton, respectively and contain the spin averaging factors. It is easily seen that, if p and p' are the electron's four momenta before and after the scattering, at leading order in α_{QED}

$$L_{\mu\nu} = 2\left[p_\mu p'_\nu + p'_\mu p_\nu - g_{\mu\nu}\, pp'\right] . \tag{1.19}$$

For the hadronic tensor no closed form can be given because the dynamics of the interaction between virtual photon and proton are partly nonperturbative. The possible structures of $W^{\mu\nu}$ are however limited by current conservation, which requires $q_\mu W^{\mu\nu}$ and $q_\nu W^{\mu\nu}$ to vanish. The most general Ansatz therefore reads [88]

$$W_{\mu\nu} = -W_1 \left(g_{\mu\nu} - \frac{q_\mu q_\nu}{q^2} \right) + \frac{W_2}{M^2} \left(p_\mu - \frac{Pq\, q_\mu}{q^2} \right) \left(p_\nu - \frac{Pq\, q_\nu}{q^2} \right) , \tag{1.20}$$

where P_μ is the nucleon momentum and M is its mass. The terms W_1 and W_2 are structure functions, which parametrise the unknown dynamics of the process. It is customary to characterise the interaction through Q^2 and the parameter

$$x = \frac{Q^2}{2Pq} , \tag{1.21}$$

called Bjørken–x. Then one defines new structure functions F_1 and F_2, based on W_1 and W_2 through

$$F_1(x, Q^2) = M\, W_1(x, Q^2) , \qquad F_2(x, Q^2) = \frac{Q^2}{2Mx} W_2(x, Q^2) . \tag{1.22}$$

Similar to the above procedure for fragmentation functions, parton distribution functions (PDFs) can now be introduced through investigation of the full next–to–leading order corrections to electron–parton scattering and the comparison with the structure functions F_1 and F_2. The derivation closely follows Refs. [86] and [87].

Hadronic initial states and parton distribution functions

The QCD next–to–leading order expression for $\mathcal{F}_2(x, Q^2) = F_2(x, Q^2)/x$ reads [86]

$$\begin{aligned} \mathcal{F}_2(x, Q^2) = \int_x^1 \frac{\mathrm{d}z}{z} \Bigg\{ & \sum_{i=1}^{n_f} e_{q_i}^2 \left[f_{0,q}^p(x/z, Q^2) + f_{0,\bar{q}}^p(x/z, Q^2) \right] \\ & \left[\delta(1-z) + \frac{\alpha_s}{2\pi} \hat{P}_{qq}(z) \log(Q^2/m^2) + \ldots \right] \\ & + 2 \sum_{i=1}^{n_f} e_{q_i}^2 f_{0,g}^p(x/z, Q^2) \left[\frac{\alpha_s}{2\pi} \hat{P}_{gq}(z) \log(Q^2/m^2) + \ldots \right] \Bigg\} . \end{aligned} \tag{1.23}$$

As in Eq. (1.6), the dots stand for higher order contributions, which are regularisation scheme dependent and m denotes a regularisation scheme dependent mass scale. The functions $f^p_{0,a}$ are bare parton distributions. Note that in contrast to the final state case, the term proportional to $\delta(1-z)$ is unaltered by the $\mathcal{O}(\alpha_s)$ corrections. This is because the function $\mathcal{F}_2$ is factorisation scheme dependent and the $\mathcal{O}(\alpha_s)$ corrections to the total cross sections appear in the respective function $\mathcal{F}_1(x,Q^2) = 2F_1(x,Q^2)$ only. Similar to the final state case, mass singularities can be factored out using

$$\bar{f}^p_{0,a}(x,Q^2) = \int_x^1 \frac{\mathrm{d}z}{z}\, f^p_{0,a}(x/z)\left[\delta(1-z) + \frac{\alpha_s}{2\pi}\hat{P}_{aa}(z)\log(\mu^2/m^2) + \dots\right] . \tag{1.24}$$

Physical parton distributions in terms of $\bar{f}^p_{0,a}$ are then defined through

$$f^p_a(x,Q^2) = \bar{f}^p_{0,a}(x/z,Q^2) + \int_x^1 \frac{\mathrm{d}z}{z}\,\frac{\alpha_s}{2\pi}\sum_{b=q,g}\hat{P}_{ba}(z)\,\log(Q^2/\mu^2)\,\bar{f}^p_{0,b}(x/z,Q^2) + \dots , \tag{1.25}$$

such that to $\mathcal{O}(\alpha_s)$

$$\mathcal{F}_2(x,Q^2) = \sum_{i=1}^{n_f} e^2_{q_i}\left[f^p_{q_i}(x,Q^2) + f^p_{\bar{q}_i}(x,Q^2)\right] . \tag{1.26}$$

Like for the fragmentation functions D^h_a, any dependence on the unphysical regularisation parameter m has dropped from Eq. (1.25). To $\mathcal{O}(\alpha_s)$ one thus obtains

$$\frac{\mathrm{d}f^p_a(x,Q^2)}{\mathrm{d}\log(Q^2/\mu^2)} = \int_x^1 \frac{\mathrm{d}z}{z}\,\frac{\alpha_s(Q^2)}{2\pi}\sum_{b=q,g}\hat{P}_{ba}(z)\,f^p_b(x/z,Q^2) . \tag{1.27}$$

This is the familiar form of the DGLAP equations for parton distribution functions [80,81]. Their Q^2-evolution is schematically depicted in Figure 1.2.

Note that Eqs. (1.27) and (1.10) differ only by the interchange of the splitting functions $\hat{P}_{qg}$ and $\hat{P}_{gq}$. This is due to the fact that Q^2 evolution of the parton densities proceeds towards the hard scattering, while evolution of the fragmentation functions proceeds away from it.

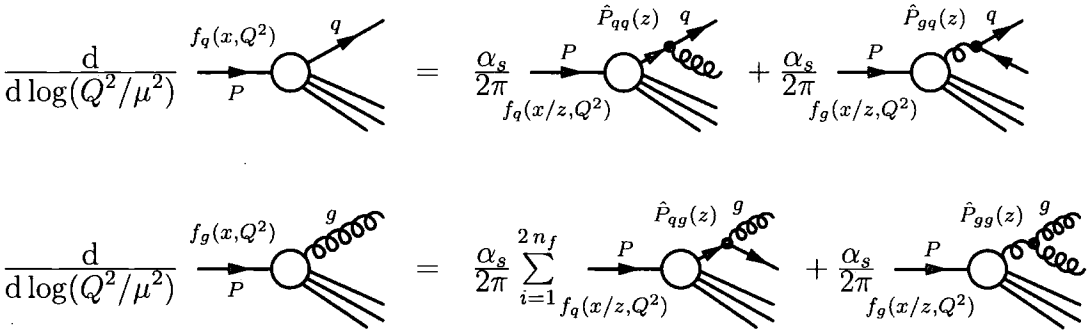

Fig. 1.2 Pictorial representation of the DGLAP evolution of parton densities, Eq. (1.27). Shown are both, the quark– and the gluon distribution.

Initial state parton showers

Equation (1.27) describes an inclusive quantity, and in order to obtain an equation which is suited for Monte Carlo simulations, one should introduce a resolution criterion. This directly translates into an additional loss term, leading to the modified equation

$$\begin{aligned}\frac{\mathrm{d}f_a^p(x,Q^2)}{\mathrm{d}\log(Q^2/\mu^2)} = &\int_x^{z_{\max}} \frac{\mathrm{d}z}{z}\,\frac{\alpha_s(Q^2)}{2\pi}\sum_{b=q,g} P_{ba}(z)\, f_b^p(x/z,Q^2) \\ &- f_a^p(x,Q^2)\int_{\xi_{\min}}^{\xi_{\max}} \mathrm{d}\xi\,\frac{\alpha_s(Q^2)}{2\pi}\sum_{b=q,g}\frac{1}{2}\,P_{ab}(\xi)\,.\end{aligned} \tag{1.28}$$

The factor 1/2 in the loss term avoids double counting s and t channel partons when summing over all possible parton splittings. To solve Eq. (1.28), one introduces the Sudakov form factor

$$\bar{\Delta}_a(\mu^2,Q^2) = \exp\left\{-\int_{\mu^2}^{Q^2}\frac{\mathrm{d}t}{t}\int_{\xi_{\min}}^{\xi_{\max}}\mathrm{d}\xi\sum_{b=q,g}\frac{\alpha_s}{2\pi}\frac{1}{2}\,P_{ab}(\xi)\right\}, \tag{1.29}$$

which is interpreted as the resummation of the loss term in Eq. (1.28), cf. Eq. (1.12). Note however, that Eqs. (1.12) and (1.29) differ by the interchange of P_{qg} and P_{gq}, corresponding to the direction of parton evolution. Employing this Sudakov form factor, Eq. (1.28) can be

rewritten as

$$\frac{\mathrm{d}}{\mathrm{d}\log(Q^2/\mu^2)}\frac{f_a^p(x,Q^2)}{\bar{\Delta}_a(\mu^2,Q^2)} = \frac{1}{\bar{\Delta}_a(\mu^2,Q^2)}\int_x^{z_{\max}}\frac{\mathrm{d}z}{z}\frac{\alpha_s(Q^2)}{2\pi}\sum_{b=q,g}P_{ba}(z)\,f_b^p(x/z,Q^2)\,, \tag{1.30}$$

Hence the fraction of partons a, produced at Q^2, which does not branch between Q^2 and q^2 is given by

$$\begin{aligned}\bar{\Pi}_a(x,q^2,Q^2) &= 1-\frac{\bar{\Delta}_a(\mu^2,Q^2)}{f_a^p(x,Q^2)}\int_{q^2}^{Q^2}\frac{\mathrm{d}\bar{q}^2}{\bar{q}^2}\frac{\mathrm{d}}{\mathrm{d}\log(\bar{q}^2/\mu^2)}\frac{f_a^p(x,\bar{q}^2)}{\bar{\Delta}_a(\mu^2,\bar{q}^2)}\\ &= \frac{\bar{\Delta}_a(\mu^2,Q^2)\,f_a^p(x,q^2)}{\bar{\Delta}_a(\mu^2,q^2)\,f_a^p(x,Q^2)}\,.\end{aligned} \tag{1.31}$$

In a Monte Carlo simulation, Eq. (1.31) is employed to decide whether or not a parton branches at scale q^2 by selecting a random number $\mathcal{R}\in[0,1]$ and solving $\bar{\Pi}_a(x,q^2,Q^2)=\mathcal{R}$ for q^2. Then a corresponding z is chosen according to Eq. (1.30) and an azimuthal angle for the branching is selected. In contrast to final state parton evolution, it is convenient to employ this prescription because type and momentum of the incoming hadron are fixed. The above procedure then assures that no branching is generated which violates either momentum conservation or the Q^2 evolution of the PDFs. Care must be taken, however that the analytic parton distributions employed in $\bar{\Pi}(x,q^2,Q^2)$ are determined with the same input as the shower evolution, i.e. running coupling and splitting kernels must be determined at the same order and in the same regularisation scheme and the same factorisation scheme must be employed.

As explained in Ref. [87], Eq. (1.31) can be rewritten such that the backward evolution formalism introduced in Ref. [89] is recovered. This means that the following equality holds

$$\bar{\Pi}_a(x,q^2,Q^2) = \exp\left\{-\int_{q^2}^{Q^2}\frac{\mathrm{d}\bar{q}^2}{\bar{q}^2}\int_x^{z_{\max}}\frac{\mathrm{d}z}{z}\frac{\alpha_s(\bar{q}^2)}{2\pi}\sum_{b=q,g}P_{ba}(z)\frac{f_b^p(x/z,\bar{q}^2)}{f_a^p(x,\bar{q}^2)}\right\}. \tag{1.32}$$

For the initial state shower algorithm presented in Chapter 3, Eq. (1.32) is employed to generate the branching scale q^2.

1.3 Coherent branching

In the following, the most important correction to leading logarithmic parton evolution as discussed in the previous sections will be introduced. Although being a quantum interference effect, it essentially amounts to an ordering criterion for partons in the Q^2 evolution and can thus be implemented in a probabilistic fashion. Namely, additional radiation initiated by a QCD parton is found to be confined to a cone with opening angle determined by the direction of the parton and its colour partner [90]. A similar effect is observed in QED and can be interpreted in a convenient way. If a parton radiates QCD quanta with inverse wavelength larger than the transverse momentum between the parton and its colour partner, the radiated particle cannot resolve the individual colour charge of the radiating parton. In this case, radiation can only stem from a particle which emits with the combined colour charge, as illustrated below. The following presentation closely follows Ref. [87].

Consider the colour-ordered mostly plus n-gluon MHV amplitude

$$A_n(\ldots,i^-,\ldots,j^-,\ldots) = ig_s^{n-2}\frac{\langle ij\rangle^4}{\langle 12\rangle\langle 23\rangle\ldots\langle n{-}1n\rangle\langle n1\rangle}\,. \tag{1.33}$$

Defining the dipole contribution

$$D_{ij}^k = \frac{\langle ij\rangle}{\langle ik\rangle\langle kj\rangle}\,, \tag{1.34}$$

this amplitude can be written as

$$\begin{aligned} A_n(\ldots,i^-,\ldots,j^-,\ldots) &= ig_s^{n-2}\frac{\langle ij\rangle^4}{\langle 1n\rangle\langle n1\rangle}\prod_{k=2}^{n} D_{1k}^{k-1} \\ &= ig_s^{n-2}\frac{\langle ij\rangle^4}{\langle mP(m)\rangle\langle P(m)m\rangle}\prod_{k\neq m} D_{mk}^{P(k)}\,, \quad 1\leq m\leq n\,, \end{aligned} \tag{1.35}$$

where $P(k)$ is defined such that it yields the next index to the left of k, which is not equal to m, eventually employing cyclicity. The last equality trivially holds because of cyclic invariance of the amplitude.

Now let either of the positive helicity gluons become soft, say gluon l. The reference indices m and $P(m)$ can always be chosen different from l, since otherwise the amplitude would vanish. Hence the associated divergence is isolated in a single dipole contribution $D^l_{mP^{-1}(l)}$

and the colour-ordered amplitude factorises like

$$A_n(\ldots,i^-,\ldots,j^-,\ldots) \;=\; A_{n-1}(\ldots,i^-,\ldots,j^-,\ldots)\, D^l_{mP^{-1}(l)}\,, \tag{1.36}$$

Similar considerations hold for non-MHV amplitudes [47], since these are easily composed from MHV amplitudes in the CSW formalism, cf. Part I, Sec 2.2. The squared amplitude in the large N_C limit thus factorises as

$$\left|A_n(\ldots,i^-,\ldots,j^-,\ldots)\right|^2 \;=\; \left|A_{n-1}(\ldots,i^-,\ldots,j^-,\ldots)\right|^2 \tilde{W}^l_{mP^{-1}(l)}\,, \tag{1.37}$$

where

$$\tilde{W}^k_{ij} \;=\; \left|D^k_{ij}\right|^2 \;=\; \frac{p_i p_j}{p_i p_k\, p_k p_j}\,. \tag{1.38}$$

This factor is part of the typical "antenna" structure of QCD amplitudes. Effectively it describes not only soft, but also collinear divergences of the amplitude, where the collinear direction is given by the reference momenta i and j. To analyse its analytic properties, it is customary to define a dimensionless variable W^k_{ij} and decompose Eq. (1.38) in the following way

$$W^k_{ij} \;=\; E_k^2\, \tilde{W}^k_{ij} \;=\; W_{ik,j} + W_{jk,i}\,, \tag{1.39}$$

where

$$W_{ik,j} \;=\; \frac{1}{2}\left(\frac{E_k^2\, p_i p_j - E_k E_j\, p_i p_k}{p_i p_k\, p_j p_k} + \frac{E_i E_k}{p_i p_k}\right)\,. \tag{1.40}$$

The phase space integral corresponding to the emission of gluon k contains the solid angle integration $\mathrm{d}\theta_k\,\mathrm{d}\phi_k$. To carry out this integration, it is convenient to define the z–axis along the direction of parton i and let $\phi_k = \phi_{j,k}$. The azimuthal average of $W_{ik,j}$ then reads

$$\begin{aligned}\overline{W}^{\phi}_{ik,j} &= \frac{1}{2\pi}\int_0^{2\pi} \mathrm{d}\phi_{j,k}\, W_{ik,j} \\ &= \frac{1}{2}\,\frac{1}{1-\cos\theta_{i,k}}\left[\,1 + (\cos\theta_{ik} - \cos\theta_{ij})\,\frac{1}{2\pi}\int_0^{2\pi}\frac{\mathrm{d}\phi_{j,k}}{1-\cos\theta_{ij,k}}\,\right]\,.\end{aligned} \tag{1.41}$$

Changing variables $\phi_{j,k} \to z = \exp\{i\phi_{j,k}\}$, the integral can be solved using Cauchy's theorem, where the only pole which lies inside the integration region is given by

$$z_- = \frac{a}{b} - \sqrt{\frac{a^2}{b^2} - 1}\,, \quad \text{where} \quad \begin{aligned} a &= 1 - \cos\theta_{i,j}\cos\theta_{i,k} \\ b &= \sin\theta_{i,j}\sin\theta_{i,k} \end{aligned} \,. \tag{1.42}$$

Hence the azimuthally averaged dipole contribution $W_{ik,j}$ is given by

$$\overline{W}^{\phi}_{ik,j} = \frac{\Theta\left(\theta_{i,j} - \theta_{i,k}\right)}{1 - \cos\theta_{i,k}} \,. \tag{1.43}$$

It vanishes if the emission angle of gluon k lies outside a cone whose opening angle is determined by the parent partons. To first approximation QCD colour coherence can thus be implemented through angular ordered parton evolution. Similar considerations hold in QED, where the angular ordering constraint is known as the Chudakov effect [91]. The only difference arises from the fact that photons carry no QED charge and therefore at least one fermion line must be present in the process.

For finite N_C, the situation becomes slightly more complicated. A convenient method to analyse the implications is to introduce colour charge operators $\mathbf{T}$ for QCD partons, such that $\mathbf{T}_i \cdot \mathbf{T}_j$, when inserted into the appropriate matrix element squared, determines the colour correlation between parton i and j. This amounts to the combined colour charge, which leads to the emission of QCD radiation off the parton pair ij. The concept is explained in some more detail in Ref. [92]. The colour charge operators squared give the Casimir operators $\mathbf{T}_i^2 = 4/3$, if i is a quark and $\mathbf{T}_i^2 = 3$, if i is a gluon. For colour singlets, $\mathbf{T}_i^2$ vanishes. Each eikonal, Eq. (1.38), is now preceded by a corresponding colour charge operator, such that the full dipole contribution reads

$$\mathbf{W}^k_{ij} = -\mathbf{T}_i \cdot \mathbf{T}_j \, W^k_{ij} \,. \tag{1.44}$$

In electron–positron annihilation into quarks, for example the situation corresponds exactly to what has been previously found, because $\mathbf{T}_i + \mathbf{T}_j = 0$. If the radiation from a three parton final state as depicted in figure 1.3 is considered, one obtains a case which is more typical for QCD. If m denotes an emitted gluon, the radiation pattern is given by

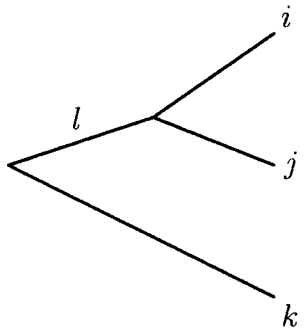

Fig. 1.3 Three parton final state as described by equation (1.45).

$$\begin{aligned}\mathbf{W}^m_{ijk} &= -\,\mathbf{T}_i\cdot\mathbf{T}_j\,W^m_{ij} - \mathbf{T}_j\cdot\mathbf{T}_k\,W^m_{jk} - \mathbf{T}_k\cdot\mathbf{T}_i\,W^m_{ik} \\ &= \frac{1}{2}\,\big[\,\mathbf{T}_i^2\,(\,W^m_{ij}+W^m_{ik}-W^m_{jk}\,)+\mathbf{T}_j^2\,(\,W^m_{jk}+W^m_{ij}-W^m_{ik}\,) \\ &\qquad +\mathbf{T}_k^2\,(\,W^m_{ik}+W^m_{jk}-W^m_{ij}\,)\,\big]\ .\end{aligned} \tag{1.45}$$

Now it is assumed that i and j are close to each other thus forming a system l, which carries the net colour charge $\mathbf{T}_i+\mathbf{T}_j = \mathbf{T}_l = -\mathbf{T}_k$. Using the decomposition (1.39) and noticing that for small angles between i and j

$$\begin{aligned}&W_{im,k} \approx W_{jm,k} \approx W_{lm,k}\ , \\ &\tilde{W}^{(j)}_{im,k} \approx \tilde{W}^{(i)}_{jm,k} \approx \tilde{W}^{(ij)}_{lm,k}\end{aligned} \tag{1.46}$$

where

$$\begin{aligned}\tilde{W}^{(i)}_{jm,k} &= \frac{1}{2}\,(\,W_{im,k}-W_{im,j}\,)\ , \\ \tilde{W}^{(ij)}_{lm,k} &= \begin{cases} W_{lm,k} & \text{for}\quad \theta_{lm} > \theta_{ij} \\ 0 & \text{for}\quad \theta_{lm} < \theta_{ij} \end{cases} \qquad \text{after averaging over } \varphi\ .\end{aligned} \tag{1.47}$$

Equation (1.45) can then be written as

$$\mathbf{W}_{ijk} \approx \mathbf{T}_i^2\,W^{(i)}_{im,j} + \mathbf{T}_j^2\,W^{(j)}_{im,j} + \mathbf{T}_k^2\,W^{(k)}_{km,l} + \mathbf{T}_l^2\,\tilde{W}^{(ij)}_{lm,k}\ . \tag{1.48}$$

This equation has a rather simple interpretation. Each parton itself radiates proportional to its colour charge squared, while additional radiation comes from coherent emission off the pair ij if the emission angle θ_{lm} exceeds the opening angle θ_{ij} of the pair. The partons then

radiate proportional to their combined colour charge squared, $\mathbf{T}_l^2$. This formalism may be extended to higher orders thus leading to a coherent branching formalism. In its simplest interpretation this translates into an angular ordering constraint for the partons emitted in each step of the parton shower evolution described above, i. e. to the explicit condition

$$\theta_i \leq \theta_{i-1} \tag{1.49}$$

for each parton i in the timelike shower evolution and also for each parton i in the backwards evolution for spacelike parton showers.

2 Matrix element improved evolution

The leading logarithmic QCD evolution presented in Chapter 1 and its next–to–leading corrections through angular ordering are often insufficient for QCD phenomenology. Key problems are the following

- The total cross section in any given process is not altered by the shower evolution. Full next–to–leading order corrections should thus be implemented to stabilise the prediction of event rates.

- Kinematic distributions might differ from the prediction of the parton shower due to spin correlations between final state partons. Next–to–leading order real emission matrix elements should thus be employed to correct evolution kernels for the most important emissions.

The above issues have been addressed in a number of ways. The most traditional method consists in reweighting the emission off QCD particles in a hard process described by the parton shower with the respective exact matrix element, expressed in terms of shower variables [93,94]. Unfortunately, the applicability of this method, however elegant, is constrained to those cases, where the parton shower expression exceeds the matrix element, such that a traditional hit-or-miss reweighting can be employed. In practice, it is therefore limited to a few cases such as the production of a gluon in electron–positron annihilation to quarks, top-quark decay plus emission of an additional gluon, or the production of vector bosons in hadron collisions.

In the past years, new and powerful methods for the systematic inclusion of higher order effects into event generation have been developed. They can be seen as a major theoretical

improvement in the detailed understanding of complicated event topologies. The first of these new methods provides means to consistently match NLO calculations for specific processes with the parton shower and has been incorporated into the MC@NLO program [13]. The basic idea here is to organise the counter-terms necessary to cancel real and virtual infrared divergences in such a way that the first emission of the parton shower is recovered. This allows the generation of kinematic configurations through matrix elements, which can eventually be fed into a parton shower Monte Carlo. Several applications of the original approach to different processes have been presented [11]. A further improvement, aiming at an enhanced independence of both the specific process and the parton shower is provided by the POWHEG-method [12], which uses the ratio of the actual real radiation matrix element and the original leading order one to generate the hardest emission. This approach has been implemented for various processes [14].

An alternative approach, aiming at an improved description of multi-jet topologies, has been described in Refs. [35,36] and applied in Refs. [95] to the case of W and Z production and the production of pairs of these bosons at the Tevatron and the LHC. The idea there is to separate the phase space for parton emission into two domains, a region of jet production and a regime of intra-jet evolution. The separation is achieved through a $k_\perp$-type jet measure [96]. Then matrix elements for different parton multiplicities are used to describe the production of a corresponding number of jets, whereas the parton shower is constrained such that it does not produce any additional jets. Leading higher-order effects are added to the various matrix elements by reweighting them with appropriate Sudakov form factors and with ratios of the strong coupling α_s taken at the $k_\perp$-scales of the individual jet emissions. Independence of the overall result on the cut in jet measure is achieved by the interplay of Sudakov form factors and the vetoed parton shower with suitable starting conditions. The method is one of the cornerstones of the event generator SHERPA. A similar approach has been formulated in Ref. [97] for the case of a dipole cascade. Another, similar but simplified method has been presented in Ref. [98]. The respective differences have been investigated in the example of W-production at the Tevatron and the LHC [99,100].

The outline of this chapter is as follows. In Sec. 2.1 the strategies for phase space separation are refined and the theoretical background of the merging approach is presented. Section 2.2 deals with the actual event generation algorithm. Section 2.3 is devoted to the treatment

of colour and a detailed description of the merging for colour-sampled matrix elements as produced for example by the COMIX generator, cf. Part I, Chapter 3.

2.1 Merging of matrix elements and showers

Merging matrix elements with showers combines two essentially different approaches to perturbative QCD. Hard matrix elements are exact at some fixed order in the strong coupling α_s and are therefore efficient in describing exclusive events with fixed jet multiplicity. Showers are needed to generate the QCD radiation pattern especially at lower scales, close to the hadronisation scale Λ_{QCD}. Their application is mandatory to resum large logarithmic corrections due to Bremsstrahlung effects. Best results can be expected, if the two approaches are combined consistently, such that each of them operates in those regions of phase space that it describes best.

The central idea for such a merging algorithm is, to replace certain evolution kernels in the shower by appropriate matrix elements, thus reinstalling information about the full hard process under consideration. Directly implementing a ratio of hard matrix elements in form of a splitting kernel has the apparent disadvantage, that the respective phase space integration proceeds in terms of shower kinematics and is thus hard to optimise in a generic way. A better technique is to first compute the matrix element and then reweight it such that, to the accuracy of the shower, the corresponding shower expression is obtained. If this strategy is pursued, the corresponding no-emission probabilities of the shower must be known. This is, however easily achieved because they emerge directly from the evolution equations on which the shower is based.

Only one additional ingredient is eventually needed, namely a measure, which defines how to separate matrix element and shower domain. It will be shown in the following, that a general form of this measure can be found, which is based on the soft and collinear behaviour of QCD at next-to-leading order.

Master evolution equations

To exemplify the general idea of the merging approach, prototypical evolution equations for parton showers are introduced, similar to what was presented in Chapter 1.

$$\frac{\partial g_a(z,t)}{\partial \log(t/\mu^2)} = \int_z^{\zeta_{\max}} \frac{\mathrm{d}\zeta}{\zeta} \sum_{b=q,g} \mathcal{K}_{ba}(\zeta,t)\, g_b(z/\zeta,t) - g_a(z,t) \int_{\xi_{\min}}^{\xi_{\max}} \mathrm{d}\xi \sum_{b=q,g} \xi\, \mathcal{K}_{ab}(\xi,t)\ . \quad (2.1)$$

In this context, g may denote either a fragmentation function or a parton distribution function, cf. for example Refs. [101]. This function can also explicitly depend on the splitting variable ζ, like in the case of angular ordered DGLAP evolution [90]. This does, however not complicate the formalism because corresponding terms do not modify the Sudakov form factor. As far as such evolution is concerned, the corresponding notation in Eq. (2.1) is implicit. The first term on the right hand side corresponds to resolvable emission, while the second (related through unitarity) describes unresolved branchings and virtual contributions. The variable t is the evolution parameter, while z is the splitting variable of the scheme. The evolution kernels $\mathcal{K}_{ab}$ are obtained from appropriate $N+1$- and N-particle matrix elements. Schematically

$$\mathcal{K}_{ab}(z,t) = \lim_{t\to 0} \frac{1}{\sigma_a^{(N)}(\Phi_N)} \frac{\mathrm{d}^2\sigma_b^{(N+1)}(z,t;\Phi_N)}{\mathrm{d}\log(t/\mu^2)\,\mathrm{d}z}\ . \quad (2.2)$$

Here Φ_N denotes the respective N-particle phase space configuration, which does not play a role for the limiting behaviour of $\sigma_b^{(N+1)}(z,t;\Phi_N)$. Equation (2.2) conversely implies that one can substitute any splitting kernel $\mathcal{K}_{ab}$ with an appropriate ratio of matrix elements, because respective differences are always subleading. For the most common case of standard DGLAP evolution, cf. Chapter 1, the kernels are easily identified through

$$\mathcal{K}_{ab}(z,t) \to \frac{\alpha_s(z,t)}{2\pi} P_{ab}(z)\ , \quad (2.3)$$

with $P_{ab}(z)$ being the standard DGLAP splitting functions. If Eq. (2.1) is written in inclusive form, i.e. $\xi_{\min} \to 0$, $\xi_{\max}, \zeta_{\max} \to 1$, the last term vanishes because of momentum sum rules for the kernels. In exclusive form, where the ζ- and ξ-boundaries are determined by a resolution criterion for parton emission, it can be expressed as the logarithmic derivative of

the Sudakov form factor [82, 83]

$$\Delta_a(\mu^2, t) = \exp\left\{ -\int_{\mu^2}^{t} \frac{\mathrm{d}\bar{t}}{\bar{t}} \int_{\xi_{\min}}^{\xi_{\max}} \mathrm{d}\xi \sum_{b=q,g} \frac{1}{2} \mathcal{K}_{ab}(\xi, \bar{t}) \right\} . \tag{2.4}$$

The factor $1/2$ is equivalent to ξ under the integral and the sum over parton species and avoids double-counting identical decay channels, cf. Chapter 1. Equation (2.4) has the generic form of a no-emission probability given in terms of the scales μ^2 and t. Potential differences between shower algorithms implementing QCD evolution arise due to different evolution kernels $\mathcal{K}$ or different interpretation of the evolution and splitting variables. This in turn corresponds to the choice of a factorisation scheme. If Eq. (2.1) is modified accordingly, the kernels can also incorporate more than two partons, for example in the case of dipole [102, 103, 25] or dipole-like [104, 105, 24] cascades.

Branching probabilities for showers

As explained in the previous chapter, no-branching probabilities for unconstrained (forward) and constrained (backward) shower evolution can be derived from Eq. (2.1) [87]. They read (cf. Eqs. (1.17), (1.14) and (1.31))

$$\mathcal{P}^{(F)}_{\mathrm{no},a}(t, t') = \frac{\Delta_a(\mu^2, t')}{\Delta_a(\mu^2, t)} = \exp\left\{ -\int_{t}^{t'} \frac{\mathrm{d}\bar{t}}{\bar{t}} \int_{\zeta_{\min}}^{\zeta_{\max}} \mathrm{d}\zeta \sum_{b=q,g} \frac{1}{2} \mathcal{K}_{ab}(\zeta, \bar{t}) \right\} , \tag{2.5}$$

and

$$\begin{aligned} \mathcal{P}^{(B)}_{\mathrm{no},a}(z, t, t') &= \frac{\Delta_a(\mu^2, t')\, g_a(z, t)}{\Delta_a(\mu^2, t)\, g_a(z, t')} \\ &= \exp\left\{ -\int_{t}^{t'} \frac{\mathrm{d}\bar{t}}{\bar{t}} \int_{z}^{\zeta_{\max}} \frac{\mathrm{d}\zeta}{\zeta} \sum_{b=q,g} \mathcal{K}_{ba}(\zeta, \bar{t}) \frac{g_b(z/\zeta, \bar{t})}{g_a(z, \bar{t})} \right\} . \end{aligned} \tag{2.6}$$

The standard procedure for constructing a parton shower algorithm is, to write the branching probability $\mathcal{P}_{\mathrm{branch,\,a}}$ as $\mathcal{P}_{\mathrm{branch,\,a}}(t, t') = \partial \mathcal{P}_{\mathrm{no,\,a}}(t, t')/\partial \log(t/\mu^2)$. Given a current evolution scale t', a new scale t is then chosen according to this probability.

Definition of a jet measure

An important aspect, however obvious, becomes manifest in Eqs. (2.5) and (2.6). QCD branchings are logarithmically enhanced at large values of the evolution kernels $\mathcal{K}$. In corresponding regions of phase space, the hard matrix element must be regularised due to infra-red divergences. The occurrence of these divergences is not specific for a certain factorisation scheme, but is rather a property of QCD. A good definition of a jet measure for the purpose of phase space separation will arise, if these arguments are taken into account. Consider two partons i and j, which can (in terms of flavour) originate from a common mother parton $\widetilde{ij}$. The following jet measure is then proposed[1]

$$Q_{ij}^2 = 2p_ip_j \min\left\{\frac{1}{C_{i,j}}, \frac{1}{C_{j,i}}\right\}, \tag{2.7}$$

where

$$C_{i,j} = \max_k \begin{cases} \dfrac{p_ip_k}{(p_i+p_k)p_j} - \dfrac{m_i^2}{2p_ip_j} & \text{if } j = g \\ 1 & \text{else} \end{cases}, \tag{2.8}$$

The maximum in Eq. (2.8) takes into account all possible colour partners k of the combined parton $\widetilde{ij}$.

In the following it is shown that this jet measure indeed correctly identifies soft and collinear parton splittings in QCD matrix elements and is thus suited to separate matrix element and shower domain in the envisaged merging approach.

Soft limit

If the energy of a single gluon j tends to zero in any fixed direction q, described through $p_j = \lambda q$, $\lambda \to 0$, the above jet measure behaves as

$$\frac{1}{Q_{ij}^2} \to \frac{1}{\lambda^2}\frac{1}{2p_iq}\left[\frac{p_ip_k}{(p_i+p_k)q} - \frac{m_i^2}{2p_iq}\right]. \tag{2.9}$$

The corresponding singularity of the matrix element is thus correctly identified, cf. Ref. [107].

[1] A similar approach, but tailored to experimentally observable quantities and based on existing algorithms has been chosen in Ref. [106].

Quasi-collinear limit

Consider partons i, j and k with $p_{ij} = p_i + p_j$ and let the light-like helper vectors l and n be given by

$$\begin{aligned} p_{ij} &= l + \alpha_{ij}\, n \\ p_k &= n + \alpha_k\, l\,. \end{aligned} \tag{2.10}$$

This system has the solution

$$l = \frac{1}{1-\alpha_{ij}\alpha_k}\,(p_{ij} - \alpha_{ij}\, p_k)\,, \qquad n = \frac{1}{1-\alpha_{ij}\alpha_k}\,(p_k - \alpha_k\, p_{ij})\,, \tag{2.11}$$

where $\alpha_{ij} = p_{ij}^2/\gamma$, $\alpha_k = p_k^2/\gamma$ and $\gamma = 2\,ln = p_{ij}p_k + \sqrt{(p_{ij}p_k)^2 - p_{ij}^2 p_k^2}$, cf. Ref. [108]. The momenta p_i and p_j can now be expressed in terms of l, n and a transverse component $k_\perp$.

$$\begin{aligned} p_i^\mu &= z\, l^\mu + \frac{m_i^2 + \mathrm{k}_\perp^2}{z}\,\frac{n^\mu}{2\,ln} + k_\perp^\mu \\ p_j^\mu &= (1-z)\, l^\mu + \frac{m_j^2 + \mathrm{k}_\perp^2}{1-z}\,\frac{n^\mu}{2\,ln} - k_\perp^\mu\,. \end{aligned} \tag{2.12}$$

A relation for p_{ij}^2 is immediately obtained.

$$p_{ij}^2 - m_i^2 - m_j^2 = \frac{\mathrm{k}_\perp^2}{z(1-z)} - \frac{1-z}{z}\,m_i^2 - \frac{z}{1-z}\,m_j^2\,. \tag{2.13}$$

Taking the quasi-collinear limit amounts to the simultaneous rescaling [109]

$$\mathrm{k}_\perp \to \lambda \mathrm{k}_\perp\,, \qquad m_i \to \lambda m_i\,, \qquad m_j \to \lambda m_j\,, \qquad m_{ij} \to \lambda m_{ij}\,. \tag{2.14}$$

Then, $2\,p_i p_j \to \lambda^2 (p_{ij}^2 - m_i^2 - m_j^2)$ and one obtains, independent of k

$$\frac{1}{Q_{ij}^2} \to \frac{1}{2\,\lambda^2}\,\frac{1}{p_{ij}^2 - m_i^2 - m_j^2}\,\max\left\{\tilde{C}_{i,j}\,,\,\tilde{C}_{j,i}\right\}\,, \tag{2.15}$$

where

$$\tilde{C}_{i,j} = \begin{cases} \dfrac{2\,z}{1-z} - \dfrac{m_i^2}{p_i p_j} & \text{if } j = g \\ 2 & \text{else} \end{cases} . \tag{2.16}$$

Equation (2.16) corresponds to the leading term of the massive Altarelli-Parisi splitting function for $z \to 1$ [109]. The corresponding term for $z \to 0$ (if present) is restored by $C_{j,i}$.

Shower histories from matrix elements

In order to obtain suitable starting conditions for showers from arbitrary matrix elements, a clustering algorithm needs to be defined, which corresponds to "running the shower evolution backwards" on the respective matrix element. It identifies how, in a shower picture, the matrix element would have been composed from a lower multiplicity matrix element and a shower branching. Applied iteratively, it leads to the definition of a core process, which cannot be further decomposed and a sequence of shower branchings yielding the actual final state. The tasks for the algorithm are thus twofold: Firstly, within an arbitrary n-parton final state the most probable parton splitting in terms of shower evolution starting with $n-1$ partons needs to be found. Secondly, corresponding partons must be recombined to obtain the respective final state. In order to construct this algorithm, one simply has to "invert" the shower evolution, which gives the following recipe:

The measure of the cluster algorithm is defined by the shower evolution kernels.
The recombination scheme is given by the inverted shower kinematics.

This prescription, together with the above definition of a jet measure lends itself nicely into a straightforward merging algorithm, based on the CKKW approach, which will be discussed in the following sections.

Construction of the merging algorithm

As stated before, the basic idea of the merging algorithm is, to separate matrix element and shower domain through a cut in jet measure. This corresponds to a simple phase space slicing. Evolution kernels for matrix element and shower domain are therefore defined as

$$\begin{aligned} \mathcal{K}_{ab}^{\mathrm{ME}}(\xi,\bar{t}) &= \mathcal{K}_{ab}(\xi,\bar{t})\,\Theta\left[Q_{ab}(\xi,\bar{t})-Q_{\mathrm{cut}}\right] \\ \mathcal{K}_{ab}^{\mathrm{PS}}(\xi,\bar{t}) &= \mathcal{K}_{ab}(\xi,\bar{t})\,\Theta\left[Q_{\mathrm{cut}}-Q_{ab}(\xi,\bar{t})\right]\,, \end{aligned} \tag{2.17}$$

where Q_{ab} denotes the jet measure defined along the lines of Sec. 2.1. Correspondingly, one obtains the Sudakov form factors

$$\Delta_a^{\mathrm{ME/PS}}(\mu^2,t) \;=\; \exp\left\{-\int_{\mu^2}^{t}\frac{\mathrm{d}\bar{t}}{\bar{t}}\int_{\xi_{\mathrm{min}}}^{\xi_{\mathrm{max}}}\mathrm{d}\xi\sum_{b=q,g}\frac{1}{2}\,\mathcal{K}_{ab}^{\mathrm{ME/PS}}(\xi,\bar{t})\right\}\,, \tag{2.18}$$

which will be called matrix element and shower Sudakov, respectively. They are related to the full Sudakov form factor, Eq. (2.4), through

$$\Delta_a(\mu^2,t) \;=\; \Delta_a^{\mathrm{PS}}(\mu^2,t)\,\Delta_a^{\mathrm{ME}}(\mu^2,t)\,. \tag{2.19}$$

Equation (2.19) effectively encodes the complete merging approach. The ultimate goal is, to replace $\mathcal{K}^{\mathrm{ME}}$ with a ratio of matrix elements, according to Eq. (2.2). During the following rewrite of the evolution equations it will simply be identified, how the factorisation property of Sudakov form factors must then be interpreted and employed for event generation. The reasoning is straightforward:

Correcting evolution kernels through higher order matrix elements, one must respect the master evolution equation, Eq. (2.1)*. The accuracy generated by the factorisation scheme will then be fully restored.*

No further proof is needed to show the correctness of the algorithm at any logarithmic order, because this follows directly from the accuracy implemented in the shower evolution. In other words, the proposed merging scheme does not impair the logarithmic accuracy of the shower.

One starts by defining the conditional backward no-branching probability in the parton shower domain[2]

$$\begin{aligned}\mathcal{P}^{(B)\,\mathrm{PS}}_{\mathrm{no},a}(z,t,t') &= \frac{\Delta^{\mathrm{PS}}_a(\mu^2,t')\,\tilde{g}_a(z,t)}{\Delta^{\mathrm{PS}}_a(\mu^2,t)\,\tilde{g}_a(z,t')} \\ &= \exp\left\{-\int_t^{t'}\frac{\mathrm{d}\bar{t}}{\bar{t}}\int_z^{\zeta_{\max}}\frac{\mathrm{d}\zeta}{\zeta}\sum_{b=q,g}\mathcal{K}^{\mathrm{PS}}_{ba}(\zeta,\bar{t})\,\frac{\tilde{g}_b(z/\zeta,\bar{t})}{\tilde{g}_a(z,\bar{t})}\right\}.\end{aligned} \tag{2.20}$$

It corresponds to the modified evolution equation

$$\frac{\partial}{\partial\log(t/\mu^2)}\log\frac{\tilde{g}_a(z,t)}{\Delta^{\mathrm{PS}}_a(\mu^2,t)} = \int_z^{\zeta_{\max}}\frac{\mathrm{d}\zeta}{\zeta}\sum_{b=q,g}\mathcal{K}^{\mathrm{PS}}_{ba}(\zeta,t)\,\frac{\tilde{g}_b(z/\zeta,t)}{\tilde{g}_a(z,t)}\,. \tag{2.21}$$

Equation (2.20) differs with respect to the standard shower evolution because of the Θ-function, restricting emissions to $Q < Q_{\mathrm{cut}}$, i.e. the shower domain. Its interpretation is therefore straightforward and gives a rule for the modified shower algorithm in the merging:

Standard shower evolution is implemented, but radiation with $Q > Q_{\mathrm{cut}}$ is vetoed.

Moreover, if backward evolution is concerned, as for the case of an initial state backward shower, the initial scale of PDF's is set by the core process of the event.
If Eq. (2.20) is employed as is, the newly defined functions $\tilde{g}$ do not obey the same evolution as the original functions g. The factorisation scheme is thus violated. If the two evolutions shall agree, one has to ensure that the full no-branching probability in the merging approach is given by Eq. (2.6). This leads to the definition of the no-emission probability for the matrix element domain

$$\mathcal{P}^{(B)\,\mathrm{ME}}_{\mathrm{no},a}(t,t') = \frac{\mathcal{P}^{(B)}_{\mathrm{no},a}(z,t,t')}{\mathcal{P}^{(B)\,\mathrm{PS}}_{\mathrm{no},a}(z,t,t')} = \frac{\Delta^{\mathrm{ME}}(\mu^2,t')}{\Delta^{\mathrm{ME}}(\mu^2,t)}\,. \tag{2.22}$$

It is interesting to note, that this probability is independent of z, which effectively is an outcome of the factorisation properties of PDF's and FF's. Assuming a "most probable" shower history corresponding to the current matrix element is obtained through the clustering algorithm outlined above, the following rule is obtained:

[2]From here on the focus will be on backward evolution. The corresponding reasoning for forward evolution follows trivially.

The weight, Eq. (2.22), is assigned to any leg with production scale t' and decay scale t found during backward clustering. Strong couplings are evaluated at the nodal scales of parton recombination.

The reasoning is easily explained. Hard matrix elements in the factorisation scheme of the shower have the same limiting behaviour as the splitting kernels $\mathcal{K}$, once colour adjacent parton ensembles become close in phase space. Backward clustering will identify a hierarchical structure for the factorisation of hard matrix elements into lower multiplicity matrix elements and splitting kernels. Eventually, a core process is found, which cannot be further decomposed and which corresponds to the starting conditions for a respective shower evolution. Matrix elements, however do not implement the no-branching probabilities generated by showers. Also the strong coupling is evaluated at a common scale, rather than the nodal scales of splittings. Corresponding corrections must therefore be implemented.

Total cross sections

An immediate consequence of the general idea for merging matrix elements with showers is, that the total cross section can only be influenced by the difference between full hard matrix elements and the corresponding product of splitting kernels times the core process. In this respect, Eq. (2.21) must be interpreted in the following way:

To compute hadronic cross sections, PDF's must be evaluated at the scale of the core process defined through backward clustering.

This prescription is independent of the multiplicity of the matrix element, because backward showering starts at the scale of the core process. A mismatch in the two scales would lead to ill-defined backward no-branching probabilities and would hence violate the factorisation scheme.

Note on the hierarchy of scales

A common effect of the merging algorithm is, that during backward clustering hard matrix elements, no strict hierarchy is found in the jet measures. As can be inferred from the above arguments, this is however not necessary once proper Sudakov form factors are computed and the shower is properly vetoed. The reason is that factorisation of hard matrix elements is guaranteed in the ordering parameter of the shower evolution, rather than the jet measure. Any clustering algorithm constructed according to the above recipe respects this ordering.

2.2 The improved CKKW algorithm

The original form of the merging method was proposed in Ref. [35] for e^+e^- collisions and extended to hadronic initial states in Ref. [36]. It approximately implements the above constructed algorithm. According to Sec. 2.1, the necessary steps for an improved prescription, employing jet measures and clustering algorithms introduced above are as follows

- Relevant multi-jet cross sections for the process under consideration are calculated with the phase space restriction $Q > Q_{\text{cut}}$. Strong couplings are computed such that they give an overestimate, which can later on be reweighted. PDF's are evaluated at the scale set by the core process.

1. Events are generated according to the above defined cross sections with kinematics determined by the respective matrix elements.

2. The most probable parton history of the final state is determined through backward clustering. The clustering is guided by information from the matrix element, which means that only those parton histories may be identified, which have a corresponding Feynman diagram.

3. The event is accepted or rejected according to a kinematics dependent weight, which corresponds to evaluating strong couplings in the shower scheme and computing the no-branching probability, Eq. (2.22), for each matrix element parton.

4. The shower evolution is started with suitably defined scales for intermediate and final

state particles. During showering, any emission harder than Q_{cut} is vetoed. Intermediate partons undergo evolution.

Modified weighting procedure

The above algorithm has the apparent drawback, that the no-emission probability Eq. (2.22) must be computed at a stage, where, in terms of computer algebra, little is known about the shower and its evolution. Ideally, however it should result as a direct consequence of shower branchings which fall in the realm of matrix elements and are thus forbidden. To obtain a corresponding prescription, the above algorithm is slightly reformulated.

Firstly, the logarithmic derivative of the no-branching probabilities $\mathcal{P}_{\text{no},a}^{(B)\,\text{ME/PS}}$ is defined as

$$\mathcal{I}_a^{(B)\,\text{ME/PS}}(z,\bar{t}) = \int_z^{\zeta_{\max}} \frac{\mathrm{d}\zeta}{\zeta} \sum_{b=q,g} \mathcal{K}_{ba}^{\text{ME/PS}}(\zeta,\bar{t}) \frac{g_b(z/\zeta,\bar{t})}{g_a(z,\bar{t})} \,. \tag{2.23}$$

From Eq. (2.6) one then obtains the full branching probability in terms of $\mathcal{I}^{(B)\,\text{ME/PS}}$

$$\mathcal{P}_{\text{branch},a}^{(B)\,\text{ME}\oplus\text{PS}}(z,t,t') = \left[\, \mathcal{I}_a^{(B)\,\text{ME}}(z,t) + \mathcal{I}_a^{(B)\,\text{PS}}(z,t) \,\right] \exp\left\{ -\int_t^{t'} \frac{\mathrm{d}\bar{t}}{\bar{t}}\, \mathcal{I}_a^{(B)}(z,\bar{t}) \right\} , \tag{2.24}$$

where $\mathcal{I}_a^{(B)} = \mathcal{I}_a^{(B)\,\text{ME}} + \mathcal{I}_a^{(B)\,\text{PS}}$. Equation (2.24) corresponds to generating an ordering parameter t in unconstrained shower evolution, i.e. without the restriction $Q < Q_{\text{cut}}$. The first term in the square bracket is however given by hard matrix elements through Eq. (2.2). In order not to double count this contribution, corresponding branchings must lead to rejection of the entire event. This modifies the respective cross section by

$$\sigma \to \sigma \cdot \mathcal{P}_{\text{no},a}^{(B)\,\text{ME}}(t,t') \,. \tag{2.25}$$

Since corresponding events are rejected, the remaining branching probability for accepted shower steps is given by (cf. the description of the veto algorithm, for example in Ref. [110])

$$\mathcal{P}^{(B)\,\mathrm{PS}}_{\mathrm{branch},\,a}(z,t,t') = \mathcal{I}^{(B)\,\mathrm{PS}}_{a}(z,t)\,\exp\left\{-\int_t^{t'}\frac{\mathrm{d}\bar{t}}{\bar{t}}\,\mathcal{I}^{(B)}_{a}(z,\bar{t})\right\} \times \exp\left\{\int_t^{t'}\frac{\mathrm{d}\bar{t}}{\bar{t}}\,\left[\mathcal{I}^{(B)}_{a}(z,\bar{t}) - \mathcal{I}^{(B)\mathrm{PS}}_{a}(z,\bar{t})\right]\right\}, \tag{2.26}$$

which yields exactly the vetoed shower algorithm described by Eq. (2.20).
One therefore obtains the modified rules

3. The event is accepted or rejected according to a kinematics dependent weight, which corresponds to evaluating strong couplings in the shower scheme.

4. The shower evolution is started with suitably defined scales for intermediate and final state particles. Intermediate partons undergo evolution. During showering, any emission harder than Q_{cut} leads to rejection of the event.

Effectively, even the two above steps can be combined through evaluating strong couplings during the shower evolution.

Highest multiplicity treatment

An apparent problem of the merging algorithm is, that only a very limited number of final state multiplicities can normally be generated through full matrix elements. Hence the matrix element domain will eventually not contain enough radiation, as explained in the following.
Assume that $N = N_{\mathrm{max}}$ emissions in the matrix element domain have been generated through the above defined algorithm. This means that up to this point, the branching probability, Eq. (2.24) has been employed, as it should be. Beyond this point, no further emission can be generated through matrix elements, so the branching probability becomes

$$\mathcal{P}^{(B)\,\mathrm{ME}\oplus\mathrm{PS}}_{\mathrm{branch},\,a}(z,t,t') \;\to\; \mathcal{P}^{(B)\,\mathrm{ME}}_{\mathrm{no},\,a}(t,t')\,\frac{\partial\mathcal{P}^{(B)\,\mathrm{PS}}_{\mathrm{no},\,a}(z,t,t')}{\partial\log(t/\mu^2)}\,. \tag{2.27}$$

Relation (2.27) would obviously violate factorisation, because of the missing derivative, corresponding to the integrated kernel from Eq. (2.2).

This problem can be circumvented by implementing standard shower evolution beyond the last matrix element emission.[3] This prescription is referred to as the highest multiplicity treatment. It guarantees, that the shower respects the description of hard radiation throughout the regime where matrix elements are applicable, while still filling the remaining phase space.

In virtuality ordered DGLAP evolution, this procedure approximately corresponds to setting a local veto scale $Q_{\text{cut}} \to Q_{\text{min}}$ if $N = N_{\text{max}}$, where Q_{min} is the minimum jet measure found during backward clustering. The reason is the following: Because of dimensional arguments, Q^2 must be proportional to the ordering variable t. Following Sec. 2.1, it cannot increase over t, since only soft and soft-collinear terms have to be matched in addition to collinear ones, see also Sec. 3.1. Moreover, any matrix element branching is likely to be close to the phase space cut Q_{cut}. Now assume the jet measure veto scale for shower branchings is set to Q_{min}. On average, the parton shower domain then extends only slightly into the matrix element regime. The corresponding error, generated by shower evolution where matrix element branchings exist, is small. On the other hand, setting the veto scale Q_{min} effectively acts like setting an upper evolution scale t_{cut}, from where unconstrained evolution is possible.

2.3 The treatment of colour

The treatment of colour is a central issue when dealing with matrix element and shower generation in QCD processes. As explained in Chapter 1, QCD coherence effects are determined by colour correlations between partons. When matrix elements are combined with parton showers, this poses a certain problem, because the colour partners of each parton have to be defined in the large N_C limit. Hence the hard matrix element must be interpreted in this limit. The problem is more easily solved, if an algorithm is employed, which unambiguously assigns a certain set of colours to external particles in the hard matrix element. The basic idea is rather than to sum over colours, to sample them in a Monte Carlo fashion, cf. Part I, Chapter 3.

Consider an n-gluon amplitude $\mathcal{A}(1,\ldots,n)$. This amplitude can be decomposed in the

[3]The term "beyond" refers to the ordering parameter t. Note that the respective scale is set globally for the event, because the matrix element connects all shower evolutions.

colour flow basis as [53], cf. Part I, Eq. (1.6)

$$\mathcal{A}(1,\ldots,n) = \sum_{\sigma\in S_{n-1}} \delta_{i_1}^{\bar{\jmath}_{\sigma_2}}\delta_{i_{\sigma_2}}^{\bar{\jmath}_{\sigma_3}}\ldots\delta_{i_{\sigma_n}}^{\bar{\jmath}_1}\, A(1,\sigma_2,\ldots,\sigma_n)\ . \tag{2.28}$$

Here i_{σ_k} and $\bar{\jmath}_{\sigma_k}$ denote the 3- and $\bar{3}$-index of parton σ_k, respectively and the sum runs over all possible permutations of the set $\{2,\ldots,n\}$. The quantities $A(1,\sigma_2,\ldots,\sigma_n)$ are called colour-ordered or partial amplitudes. They depend on the kinematics of the process only. All information about colour is incorporated in their respective prefactors. Therefore any colour-ordered amplitude only contains planar diagrams, which greatly alleviates its computation. A convenient way to interpret Eq. (2.28) is to consider it the decomposition of the full QCD amplitude into subamplitudes in the large N_C limit. If the result from the matrix element calculation is to be fed into a shower program, the corresponding colour connections are thus readily determined if one picks one of the terms in the sum as the most probable colour structure and identifies the colour flow according to its colour factor. In this context one can make use of the fact that interference terms between two different colour structures are always subleading in N_C.[4]

An algorithm to identify the most probable colour structure could thus look as follows (cf. Ref. [76])

1. Compute the full matrix element with randomly assigned colours for external QCD partons.

2. Identify all possible permutations $\{1,\vec{\sigma}\}$ which give a non-zero value of

$$\delta_{i_1}^{\bar{\jmath}_{\sigma_2}}\delta_{i_{\sigma_2}}^{\bar{\jmath}_{\sigma_3}}\cdots\delta_{i_{\sigma_n}}^{\bar{\jmath}_1}\ . \tag{2.29}$$

   Label them by $\vec{\sigma}_i$ and compute the corresponding partial amplitudes $A(1,\vec{\sigma}_i)$.

3. If $N_{\vec{\sigma}}$ is the number of identified permutations, choose a partial amplitude with probability

$$P_{\vec{\sigma}_i} = \frac{|A(1,\vec{\sigma}_i)|^2}{\sum_{j=1}^{N_{\vec{\sigma}}}|A(1,\vec{\sigma}_j)|^2} \tag{2.30}$$

[4] This argument holds in the colour flow decomposition and the fundamental decomposition. For the latter, see for example Ref. [51].

Because of the way, potential partial amplitudes are identified in the colour-flow decomposition, this prescription is similar to the following simplified strategy

1. Compute the full matrix element with randomly assigned colours for external QCD partons.

2. Assign colours in the large N_C limit at random, but respecting the actual point in colour space. That is, two partons may only be colour adjacent at large N_C, if they were colour adjacent at finite N_C.

3. Identify the corresponding permutation $\vec{\sigma}$ and compute the partial amplitude $A(1,\vec{\sigma})$. Accept the configuration with probability

$$P_{\vec{\sigma}} = \frac{|A(1,\vec{\sigma})|^2}{|\mathcal{A}(1,\ldots,n)|^2} \tag{2.31}$$

The drawback of the latter algorithm seems to be, that potentially many points have to be drawn for the colour assignment at large N_C. In practice, this is however sufficiently fast compared to evaluating all possible partial amplitudes. Also, in principle the full amplitude squared, $|\mathcal{A}(1,\ldots,n)|^2$, might be much smaller than the sum of partial amplitudes squared, such that acceptance probabilities are modified. The algorithm is still sufficiently accurate, since respective differences are always subleading in N_C.
Matrix element configurations might exist, which do not allow an immediate projection onto large N_C because of the U(1) pseudo-gluon. In this case, a new point in colour space can safely be assigned, because the respective contribution to the total cross section is subleading.

3 Multi-jet merging with SHERPA

The intention of this chapter is twofold. Firstly, the basic parton shower algorithm currently employed within SHERPA shall be presented, which is the standard parton cascade APACIC++ [20]. It is essentially based on the formalism introduced in Secs. 1.1 and 1.2, while the angular ordering constraint introduced in Sec. 1.3 is implemented through an explicit veto. A jet measure along the lines of Sec. 2.1, but specifically adapted for usage in APACIC++ is proposed.

Secondly, differences in the merging algorithms for different matrix element generators within the SHERPA framework are studied. An extended comparison, also including different shower generators is in preparation [111]. With the two available matrix element generators, AMEGIC++ and COMIX a unique opportunity is given to to study and cross-check merging systematics within the same framework. In particular the effect of colour sampling on the merging can thus be investigated. An application of the procedure to the production and decay of top pairs at the LHC and a potential ILC is presented.

3.1 The parton shower APACIC++

Final state showering in APACIC++ proceeds along the lines of Ref. [112]. DGLAP evolution of QCD partons is simulated through $1 \to 2$ splittings, governed by the forward no-branching probability, Eq. (2.5). The evolution kernels defined in Sec. 2.1 are therefore given by the Altarelli-Parisi kernels

$$\mathcal{K}_{ab}(\tilde{z},t) \to \frac{\alpha_s(\tilde{z},t)}{2\pi} P_{ab}(\tilde{z}) \,, \tag{3.1}$$

Here a denotes the flavour of the splitting parton, and $P_{ab}(\tilde{z})$ are the unregularised Altarelli-Parisi kernels in four dimensions for the splitting $a \to bc$. For massive partons, splitting functions including mass effects can be employed [109]. Evolution and splitting variable are defined through

$$t = p_a^2 - m_a^2 , \qquad \text{and} \qquad \tilde{z} = \frac{E_b}{E_a} , \tag{3.2}$$

m_a being the on-shell mass of parton a. The splitting variable $\tilde{z}$ is related to the light-cone momentum fraction $z = p_b^+/p_a^+$ (with the "+"-direction defined by p_a) through

$$2\,\tilde{z}\kappa E_a^2 + z\,(p_a^2 - \kappa^2 E_a^2) = p_a^2 + m_b^2 - m_c^2 , \quad \text{where} \quad \kappa = 1 + \sqrt{1 - \frac{p_a^2}{E_a^2}} \tag{3.3}$$

Although defined in a seemingly not covariant way, the splitting variable is actually Lorentz invariant. This can be seen by investigating electron-positron annihilation in the centre-of-mass frame of the intermediate virtual photon or Z-boson, where $z = (p_b P)/(p_a P)$ and $P = p_{\gamma^*/Z} = (Q, \vec{0})$ acts as a gauge fixing vector.

Colour coherence during evolution is guaranteed by an explicit angular veto, which means that a branching is rejected if the opening angle of the emission is larger than the one in the previous branching. The strong coupling, in Eq. (3.1) is evaluated at the scale set by the transverse momentum $\mathrm{k}_\perp$ defined in light-cone kinematics

$$\mathrm{k}_\perp^2 = z(1-z)\,2p_b p_c - (1-z)^2\,m_b^2 - z^2\,m_c^2 . \tag{3.4}$$

Initial state showering proceeds in the backward evolution picture along the lines of Ref. [89]. The no-branching probability is then given by Eq. (2.6) with the above identification of the evolution kernels in terms of DGLAP splitting functions. The splitting variable $\tilde{z}$ is reinterpreted as

$$\tilde{z} \to \bar{z} = \frac{\hat{s}}{\hat{s}'} , \tag{3.5}$$

$\hat{s}$ and $\hat{s}'$ being the partonic centre-of-mass energies before and after the branching, respectively. This immediately yields the relation $x' = x/\bar{z}$, thus partially defining the kinematics

after branching.

An important issue for DGLAP shower algorithms is the convention to implement kinematic constraints once a splitting generates recoil due to the branching parton going off mass-shell. The recoil strategy seems ambiguous because the branching equations are independent of it. In fact however, for the derivation of the DGLAP equation, it is assumed that there is a spectator parton aligned along the same axis as the splitter, but with opposite direction. This leads to the following approach for APACIC++

- In final state showering, the parton which originates from the same splitting as the branching parton takes the recoil. This amounts to redefining the splitting variable of the respective branching by

$$\tilde{z} \to \tilde{z}' = \left(\tilde{z} - \frac{t_a + t_b - t_c}{2\,t_a}\right)\sqrt{\frac{(t_a - t_b' - t_c')^2 - 4\,t_b'\,t_c'}{(t_a - t_b - t_c)^2 - 4\,t_b\,t_c}} + \frac{t_a + t_b' - t_c'}{2\,t_a}\,, \tag{3.6}$$

  where t and t' denote original and reassigned virtualities, respectively. The reassignment is performed only after both partons have eventually split.

- In initial state branchings all remaining partons take the recoil. For any splitting $b \to a$ the process is redefined with parton b rather than a aligned along the beam axis and $\hat{s} \to \hat{s}' = \hat{s}/z$.

Local definition of a jet measure

As outlined in Sec. 2.1, the measure of a clustering algorithm for APACIC++ must be based on the evolution kernels, Eqs. (3.1). The separation of two partons i and j in the APACIC++ scheme is therefore defined through

$$Q_{ij}^2 = 2\,p_i\,p_j\,\min\left\{\frac{1}{C_{i,j}}\,,\,\frac{1}{C_{j,i}}\right\}\,, \tag{3.7}$$

If both partons are in the final state, according to the interpretation of $\tilde{z}$ as an energy fraction

$$C_{i,j} = \begin{cases} \dfrac{z_{i,j}}{1 - z_{i,j}} & \text{if} \quad j = g \\ 1 & \text{else} \end{cases}\,, \quad \text{where} \quad z_{i,j} = \frac{E_i}{E_i + E_j}\,, \tag{3.8}$$

For initial state partons $j \to b^{\pm}$, because of Eq. (3.5) we have

$$C_{i,b^{\pm}} = \begin{cases} \dfrac{x_i}{x_{b^{\pm}} - x_i} & \text{if} \quad ib^{\pm} = g \\ 1 & \text{else} \end{cases}, \qquad C_{b^{\pm},i} = \begin{cases} \dfrac{x_{b^{\pm}} - x_i}{x_i} & \text{if} \quad i = g \\ 1 & \text{else} \end{cases}, \tag{3.9}$$

with x_i and $x_{b^{\pm}}$ being light-cone momentum fractions with respect to the incoming hadron producing initial state parton $b^{\pm}$ and $ib^{\pm}$ denoting the t-channel parton which emerges from the splitting. The above measure represents the identification of potentially divergent structures in the hard matrix element through the shower scheme employed in APACIC++. It is now demonstrated that both, the soft and the collinear limit of QCD are matched and that the jet measure, Eq. (3.7) can therefore also be employed to regularise next-to-leading order real emission matrix elements.

Soft limit

If the energy of a single final state gluon j tends to zero in any fixed direction q, described by $p_j = \lambda q$, $\lambda \to 0$, the above jet measure behaves as

$$Q_{ij}^2 \to \lambda^2 \, 2 p_i \, q \begin{cases} z_{q,i} & \text{if } i,j \text{ final states} \\ x_q / x_b & \text{else} \end{cases}. \tag{3.10}$$

The corresponding singularity of the matrix element is thus identified. Neither the definition of energy fractions $z_{i,j}$ in Eq. (3.8) nor the definition of x_i do, however project onto the correct eikonals, which would involve the potential colour partners of the splitting parton [113], cf. Sec. 2.1. Hence the phase space for soft gluon radiation is overestimated by Eq. (3.7). This is due to the fact that only the double leading logarithmic part of branchings is considered in the soft gluon limit. Matrix element contributions are then cut off too early (in terms of jet measure) when performing matrix element parton shower merging.

Collinear limit

The collinear limit for partons i and j is defined through the uniform rescaling $\vec{k}_\perp \to \lambda \vec{k}_\perp$ [81], cf. Sec. 2.1. For the current splitting kinematics, the transverse momentum can be defined as $\vec{k}_\perp = \vec{p}_i - \vec{p}_{ij}(\vec{p}_i \, \vec{p}_{ij})/\vec{p}_{ij}^{\,2}$. In this case $z_{i,j}$ is constant (x_i and x_b are constant)

and for final state singularities the jet measure, Eq. (3.7) behaves as

$$Q_{ij}^2 \to \lambda^2\, 2 p_i p_j \min\left\{ \frac{1}{\tilde{C}_{i,j}}, \frac{1}{\tilde{C}_{j,i}} \right\}, \quad \text{where} \quad \tilde{C}_{i,j} = \begin{cases} \dfrac{z_{i,j}}{1-z_{i,j}} & \text{if } j = g \\ 1 & \text{else} \end{cases}, \tag{3.11}$$

with a corresponding relation for initial state singularities. Equation (3.11) identifies the leading part of the corresponding Altarelli-Parisi splitting function and thus corresponds to Eq. (2.15) in the massless limit.

3.2 Comparative studies with APACIC++

In the following, results from an implementation of the improved CKKW merging prescription are presented. APACIC++ is employed as the corresponding shower generator, while the two programs AMEGIC++ and COMIX are used to provide hard matrix elements. In the first part, e^+e^- annihilation into hadrons is discussed, while the second part deals with Drell-Yan lepton pair production. The two processes offer the possibility, to study both pure final state and final plus initial state parton evolution. Initial state evolution is more complex due to the constraint that outermost partons in the shower have to match up with the beam hadron content. A proper understanding of final state evolution is therefore mandatory, before one can turn to combined showering. Additionally, an application of the new merging techniques to the production and decay of $t\bar{t}$ pairs at the LHC and a linear collider is presented. It is observed that, at hadron colliders, hard matrix elements predict $p_\perp$ and η spectra for jets originating from the $t\bar{t}$ production process, which are significantly different from pure parton shower results.

Jet production in e^+e^- collisions

For this study, a configuration according to the setup of the LEP e^+e^--collider, Run I, was chosen, i.e. $\sqrt{s} = 91.25$ GeV. At the level of hard matrix elements, jets are equivalent to the QCD partons d, u, s, c, b and gluon. The maximal number of jets, N_{max} is selected such that event generation can easily be performed with AMEGIC++, which restricts N_{max} to 5. Results are given at the hadron level, i.e. after showering and hadronisation. It can be

argued that it would be more appropriate, to quote results at the parton level because this offers the possibility to study merging systematics without having to worry about potential smearing effects from hadronisation, decays and photon radiation. However, another effect is then underestimated, which is the distribution of colour in the final state and its potential effects on hadronisation. Especially for the merging with COMIX this could play a vital role, as explained in Sec. 2.3

Differential k_T-jet rates are chosen as observables. In the context of this work, the differential rate $y_{n\,n+1}$ gives the distribution of normalised jet measures $Q_{n\,n+1}$, where $n+1$ jets are clustered to n jets according to the k_T-algorithm presented in Refs. [96]. y is related to Q through simple rescaling $y = Q^2/s$. Given that similar measures are used to separate matrix element and shower domain in the CKKW algorithm, it can be expected to see the largest merging systematics in these observables. Especially when varying the separation cut Q_{cut}, the region around the respective cut values usually shows the biggest differences, which makes the k_T-jet rates preferred observables for the study.

The following separation cuts have been used in the simulation:

- $\log_{10} y_{\text{cut}} = -2.5 \leftrightarrow Q_{\text{cut}} = 5.131\,\text{GeV}$
- $\log_{10} y_{\text{cut}} = -2.0 \leftrightarrow Q_{\text{cut}} = 9.125\,\text{GeV}$
- $\log_{10} y_{\text{cut}} = -1.5 \leftrightarrow Q_{\text{cut}} = 16.227\,\text{GeV}$

Figure 3.2 shows the three differential jet rates y_{23}, y_{34}, and y_{45} for the two generator combinations. As expected, deviations are biggest around the respective cut values. None of the samples, however leads to variations exceeding 10%. Also, none of them shows a clearly lower variation than others around the separation cut. It can hence be concluded that the impact of colour correlations in the final state is properly described through both, the merging with colour summed and with colour sampled matrix elements.

Drell-Yan lepton pair production

The aim of the analysis presented in this section is, to study potential differences with respect to pure final state parton evolution. This is achieved by investigating Drell-Yan pair production at the Tevatron, Run I. The criteria for event generation are $p\bar{p}$ collisions

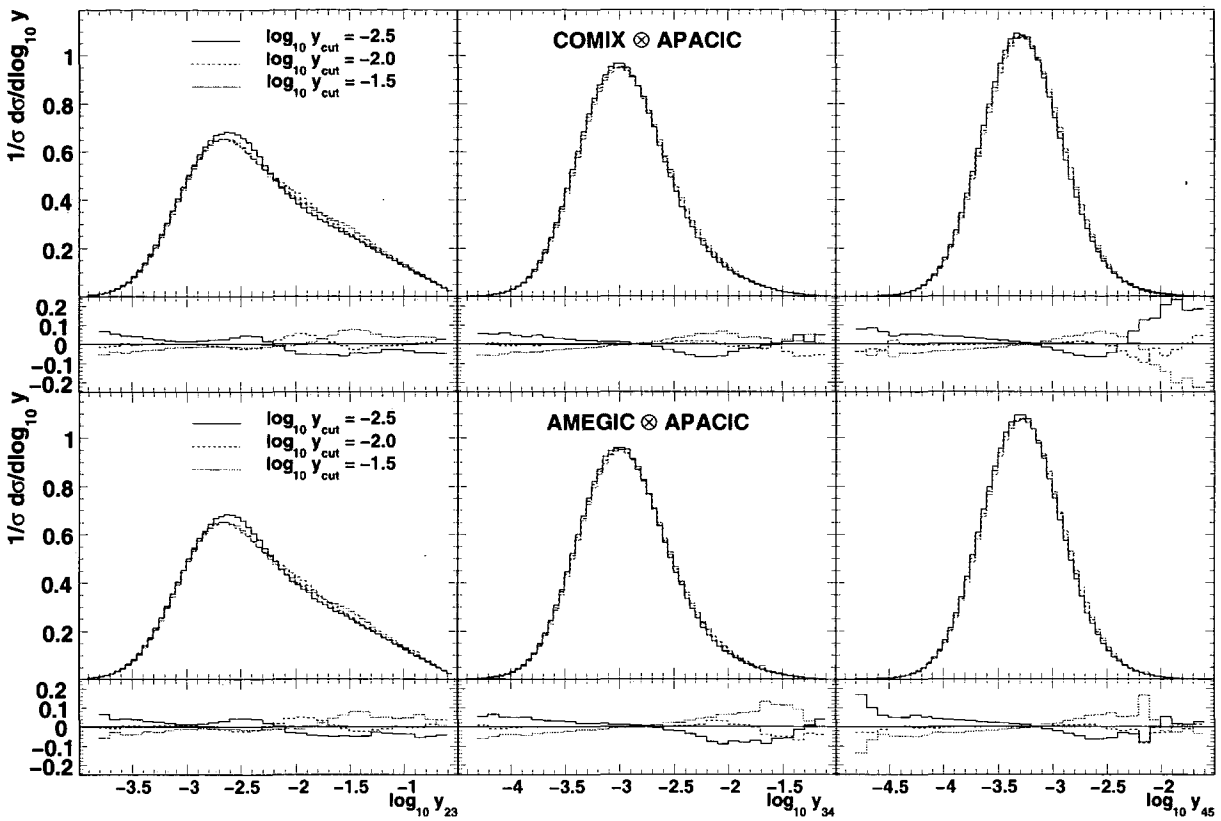

Fig. 3.1 Differential jet rates in $e^+e^- \to$ jets using the Durham jet measure [96] and the E-scheme for parton recombination. Shown are the results for the combination of AMEGIC++ (first row) and COMIX (second row) with APACIC++.

at $\sqrt{s} = 1800\,\text{GeV}$ and a mass window of the Drell-Yan pair of $66\,\text{GeV} < m_{l^+l^-} < 116\,\text{GeV}$. For the hard process, CKKW merged samples of $p\bar{p} \to e^+e^- + N$ jets were produced, with the maximum jet multiplicity restricted to $N_{\max} = 3$, which corresponds to a jet multiplicity of 5 for the e^+e^--case.

Analyses have been carried out on parton level, with the two different generator combinations also employed for the previous study. The choice not to include hadronisation and hadron decays in the simulation is motivated by the fact, that also the underlying event would have to be simulated. This could, however add extra hard radiation to the event, which is not the current object of interest and should therefore be avoided.

The tests are again concerned with differential jet rates. For this analysis, the CDF Run II k_T algorithm [77] has been employed to define jets. The phase space separation cut takes the following values

- $Q_{\text{cut}} = 15\,\text{GeV} \leftrightarrow \log_{10}(Q_{\text{cut}}/\text{GeV}) = 1.18$

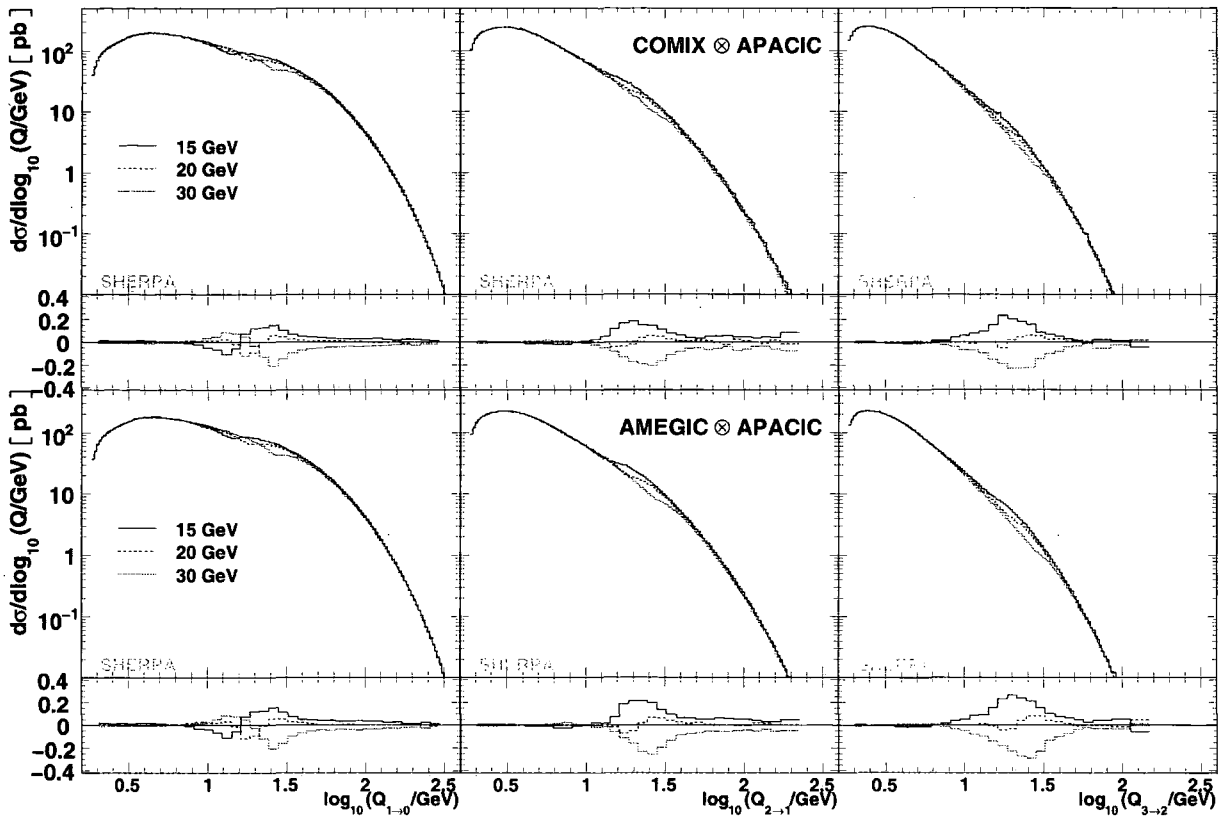

Fig. 3.2 Differential jet rates in $p\bar{p} \to e^+e^-$ employing the CDF Run II k_T algorithm [77]. Shown are the results for the combination of AMEGIC++ (first row) and COMIX (second row) with APACIC++.

- $Q_{\text{cut}} = 20\,\text{GeV} \leftrightarrow \log_{10}(Q_{\text{cut}}/\text{GeV}) = 1.30$
- $Q_{\text{cut}} = 30\,\text{GeV} \leftrightarrow \log_{10}(Q_{\text{cut}}/\text{GeV}) = 1.48,$

As expected and as explained in Sec 3.2, systematic differences occur predominantly around the merging cuts. They are of the order of 20%, as can be seen in Figure 3.2.

3.3 Application to $t\bar{t}$ production and decay

It is worthwhile to study the implications of the improved CKKW formalism for relevant processes at future colliders. An example for such a process, which plays a significant role, both as a signal for a better measurement of Standard Model parameters and as a background to new physics searches, is top quark pair production. In the context of this thesis, the process will be investigated at the LHC and a potential linear collider (ILC) operating at a centre-of-mass energy of 500 GeV. Firstly, modifications of the parton shower

are presented, which are needed for a proper simulation of radiation from the decaying heavy quarks. Then a comparison between the pure parton shower approach and the CKKW merging is drawn, highlighting that proper real next-to-leading order corrections might be crucial for this kind of process. Systematics in the merging of decay processes are briefly discussed.

Parton shower modifications

The QCD radiation pattern in heavy flavour decay has been thoroughly investigated in Refs. [94, 114]. In this thesis, a rather simple strategy is employed. QCD radiation off the decaying heavy particle is described by the standard parton shower with massive splitting functions, except for two modifications:

1. In ordinary final state parton showering, the mother particle goes off-shell, while the daughters retain their respective on-shell masses. In showering off decaying heavy particles, on the contrary, the mother particle retains its on-shell mass, while the daughter of the same flavour goes off-shell with decreased virtuality.

2. The maximally allowed phase space volume in a branching process of a decaying particle is reduced by the factor

$$w_{\mathrm{PS}} = \frac{|\mathrm{p}'^{cm}_{a/b}|}{|\mathrm{p}^{cm}_{a/b}|} = \sqrt{\frac{t}{t'}\frac{(t'-t_b-t_c)^2-4t_bt_c}{(t-t_b-t_c)^2-4t_bt_c}}\,, \tag{3.12}$$

   where t and t' are the virtualities of the decaying particle before and after the emission and t_b and t_c are the virtualities of the decay products. This correction weight corresponds to a decrease in phase space volume due to a decrease in three-momentum $|\mathrm{p}^{cm}_{a/b}|$ in the centre-of-mass frame of the decayed parton.

The corresponding radiation pattern of APACIC++ is shown in Fig. 3.3 for the decay $t \to W^+bg$. The quantities x_1 and x_3 are defined as [94]

$$x_1 = \frac{2\,p_W p_t - m_W^2}{m_t^2}\,, \quad x_3 = \frac{2\,p_g p_t}{m_t^2} \tag{3.13}$$

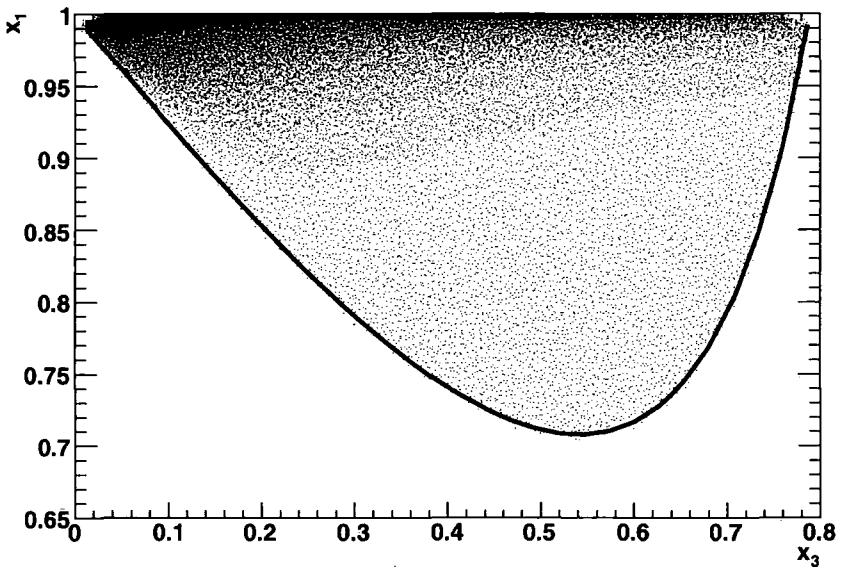

Fig. 3.3 Dalitz plot for the decay process $t \to Wbg$. The phase space boundary, computed according to Ref. [94], is depicted by the solid line. It can be seen that APACIC++ completely fills the phase space, while the largest part of emissions lies in the soft-quasi-collinear region (upper left corner).

Treatment of decay products

To correctly describe the decay process of the heavy flavour, it is vital to respect spin correlations between production and decay amplitudes. Within the algorithm presented here, this is done by firstly computing the full matrix element for production and decay of the heavy flavour and then adding in the parton evolution of the intermediate quark. In this respect, it must be defined, how the kinematics of the decay products are to be reconstructed, once a parton emission occurred in the shower. The following strategy is used:

1. If the decaying heavy particle keeps its mass, i.e. if the radiation occurs in the production part of the process, the decay products are simply boosted into the new centre-of-mass frame of the decayer.

2. If the decaying heavy particle does not keep its mass, i.e. if the radiation occurs in the decay part of the process, the decay products are reconstructed such that in the centre-of-mass frame of the daughter the momenta point into the same direction as they did in the centre-of-mass frame of the mother before.

The CKKW approach for heavy resonances

The combination of matrix elements and parton showers in production and decay of strongly interacting heavy resonances is based on using a (potentially Breit-Wigner improved) narrow width approximation to compute the corresponding hard matrix elements. This allows to cut the propagator of the decaying particle such that there are two separate processes, the production and the decay of the heavy flavour. Both are spin-and colour correlated but can be computed as on-shell matrix elements and are therefore gauge invariant. Through the identification of the decaying intermediate particle, a parton shower can independently be assigned to its production and decay. Within SHERPA, the narrow with approximation is realised by projecting the full matrix element on those amplitudes, which include the resonances as intermediate states, thus summing over its degrees of freedom, such as spin, momentum and colour. The full amplitude therefore factorises into a production and a decay part, connected with a propagator. For a number of intermediate states, labelled by i,

$$\mathcal{A}^{(n)} = \mathcal{A}_{\text{prod}}^{(n_{\text{prod}})} \otimes \prod_{i \in \text{decays}} \mathcal{P}_i \mathcal{A}_{\text{dec}_i}^{(n_i)} , \tag{3.14}$$

such that the total number of outgoing particles is given by $n_{\text{tot}} = n_{\text{prod}} + \sum_i (n_i - 1)$. Upon application of the CKKW merging algorithm and when integrating over the phase space of the outgoing particles, jet measures Q between strongly interacting particles must be larger than a critical value Q_{cut}. Due to the factorised structure of the process, this critical value can be specified per subprocess, i.e. there may be different values $Q_{\text{prod}} = Q_{\text{cut}}(\text{prod})$ and $Q_{\text{dec},i} = Q_{\text{cut}}(\text{dec}_i)$. When reweighting the hard matrix element with Sudakov form factors, these different cutoff values must be employed. Furthermore, the highest multiplicity treatment as described in Sec. 2.1 is to be applied separately in each subamplitude.

Once a particular kinematics is chosen for the hard matrix element, the parton shower history is identified as in the standard merging prescription. Since the full amplitude factorises over time-like propagators, only particles belonging to the same subamplitudes $\mathcal{A}_{\text{prod}}$ or $\mathcal{A}_{\text{dec},i}$ can be combined. Sudakov reweighting for the production of resonant intermediate particles also takes places according to the original prescription, cf. Chapter 2. Finally the jet veto is applied separately within each part of the parton showers related to a different

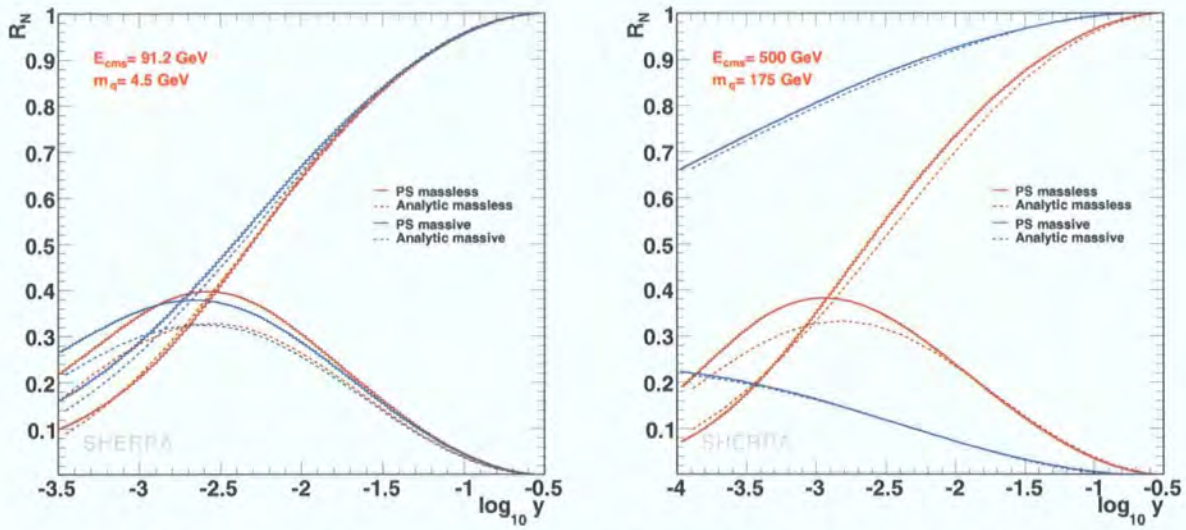

Fig. 3.4 Comparison of the Durham 2- and 3-jet rates for massive quarks, calculated according to Ref. [115], with results from APACIC++. Good agreement is found between the parton shower result (solid histogram) and the analytical calculation (dashed line). For reference, results with massless quarks are also shown.

subamplitude with the corresponding veto scale $Q_{\text{cut}}(\text{proc})$.

To summarise, the above prescription translates into the CKKW method being applied separately and completely independent for each subamplitude $\mathcal{A}_{\text{prod}}$ and $\mathcal{A}_{\text{dec},i}$ of the process under consideration.

Preliminary results

For the numerical analyses in this subsection the reweighting with analytic Sudakov form factors is employed, cf. Sec. 2.1. It must therefore be assured that those match the respective distributions generated by the parton shower. A corresponding comparison is shown in Fig. 3.4. Predictions from APACIC++ and an analytic calculation performed in Ref. [115] are displayed for the Durham k_T-jet rates at a linear collider operating at 500 GeV.

Figure 3.5 shows the impact of description of additional hard radiation through appropriate matrix elements in the case of $t\bar{t}$-production at the LHC. Subsamples from a given matrix element configuration are displayed in colour with the colour code explained above each figure. The following notation is employed

- The first number denotes the additional jet multiplicity in the $t\bar{t}$ production process.

- The second and third numbers denote the additional jet multiplicity in the t and $\bar{t}$ decay processes, respectively.

It is clearly seen that subsamples including an additional hard jet in the production process (1-0-0, 1-1/0-0/1 and 1-1-1 (not displayed)) generate a much harder transverse momentum spectrum of the $t\bar{t}$ pair and much harder k_T-jet rates as the pure parton shower. This is because of possible hard initial state radiation, which is poorly described in the shower approach. Simultaneously, this radiation deforms the pseudorapidity spectrum of the first additional hard jet (identified through k_T-clustering and Monte Carlo truth based b-tagging). It is seen that the pure parton shower approach predicts a dip at central rapidity, while the merged sample does not show this feature.

In Fig. 3.6 a consistency check of the merging in decay processes is presented. As an example, the production of a $t\bar{t}$-pair at a linear collider operating at 500 GeV is chosen. The phase space separation cut is varied from 9 GeV to 28 GeV, which gives a reasonable estimate of associated uncertainties. At first glance (inferred from the difference between predictions, shown in the lower panels of Fig. 3.6), these uncertainties seem to be quite large. However, it must be noted that this is actually "twice" the theoretical uncertainty generated by the merging because the separation cut is varied in both, the t and the $\bar{t}$ decay process. Variation in the production process induces smaller uncertainties.

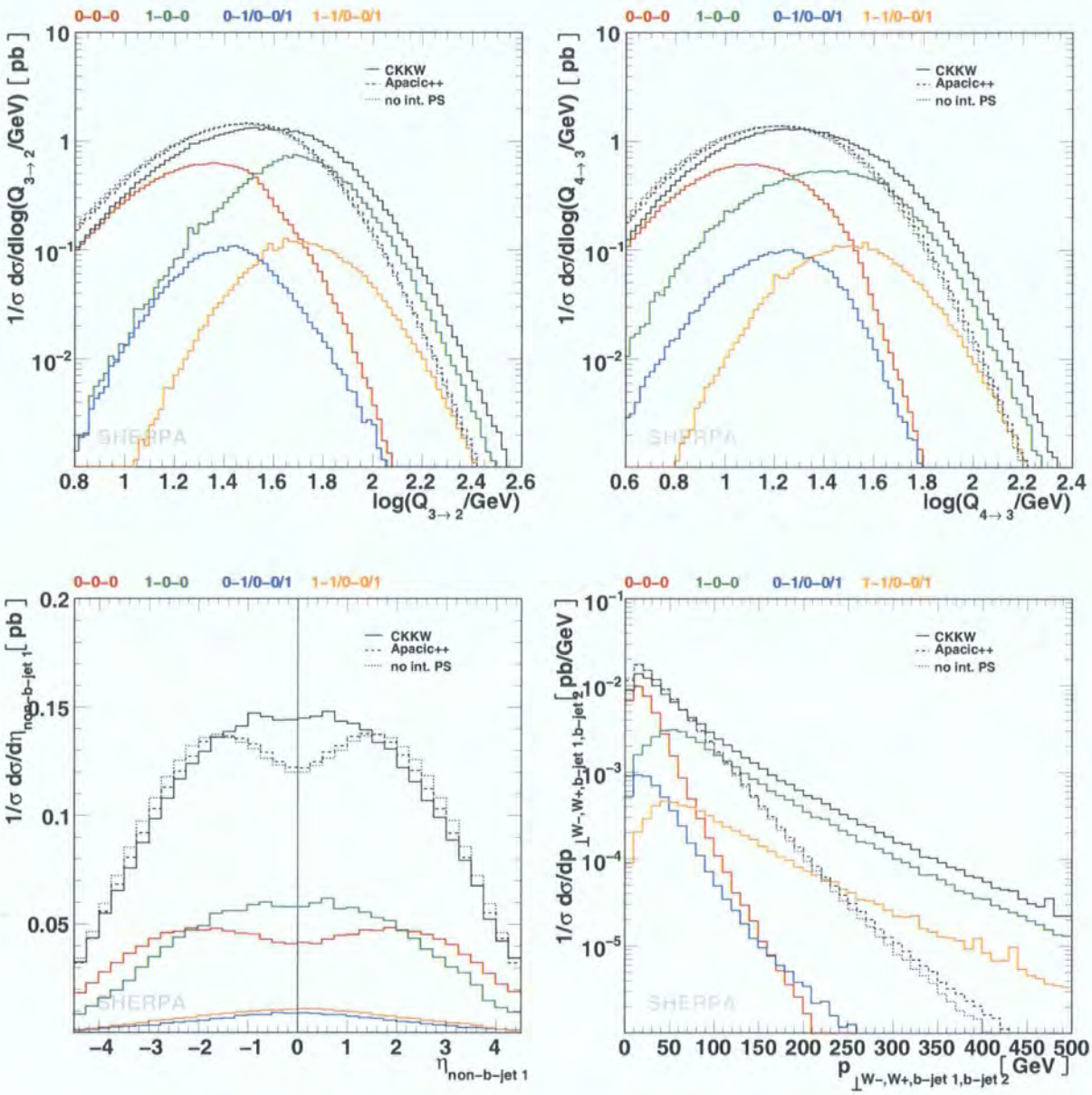

Fig. 3.5 Comparison of the k_T 2- and 3-jet rates (upper panels), the rapidity of the first extra jet and the transverse momentum of the "reconstructed" $t\bar{t}$-pair (lower panels) in $pp \to t\bar{t} \to W^+W^-b\bar{b} + jets$ events at $\sqrt{s} = 14$ TeV. Shown is a comparison between the pure parton shower result (no int. PS), parton shower with radiation off intermediate top quarks (Apacic++) and a CKKW-merged sample. Contributions from various matrix element configurations are highlighted in colour for the merged sample, with the colour code indicating the additional jet multiplicity in the production $\otimes$ t-decay $\otimes$ $\bar{t}$-decay process. Here, up to one extra jet has been simulated through the matrix element.

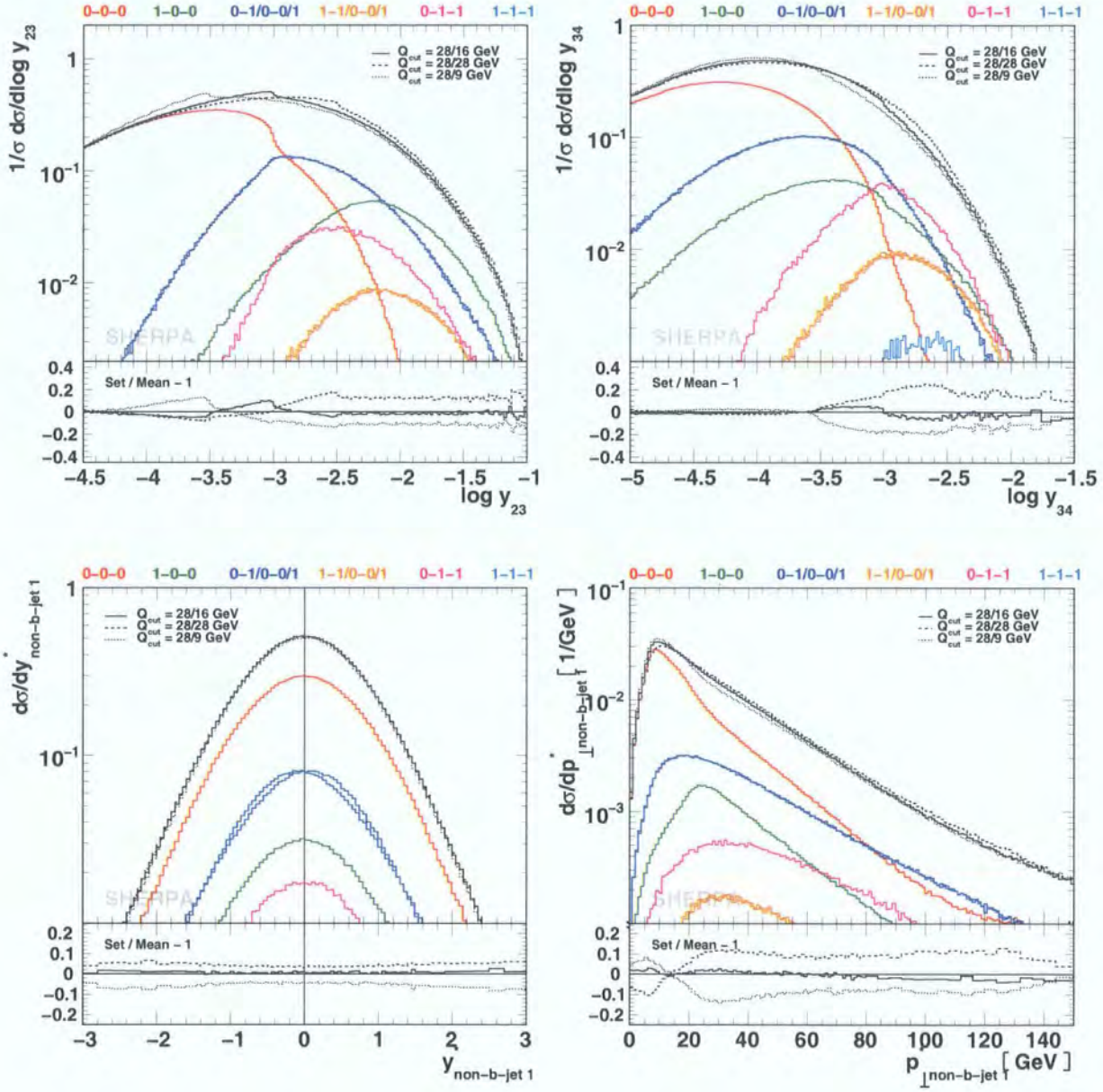

Fig. 3.6 Comparison of the Durham 2- and 3-jet rates (upper panels) and the rapidity and transverse momentum of the first extra jet with respect to the axis of the reconstructed $t\bar{t}$-pair (lower panels) in $e^+e^- \to t\bar{t} \to W^+W^-b\bar{b} + jets$ events at $\sqrt{s} = 500$ GeV for different values of Q_{cut}. Contributions from the various matrix element configurations are highlighted in colour, with the colour code indicating the additional jet multiplicity in the production $\otimes$ t-decay $\otimes$ $\bar{t}$-decay process.

4 Comparison with other generators

In this chapter, a comprehensive comparison of implementations of multi-jet merging prescriptions is presented, where W^+-production is chosen as core process. Three different merging approaches are compared, the CKKW scheme presented in the previous chapters, the Lönnblad scheme, and the MLM scheme. This comparison has be published in Ref. [100]. It is an evolution and extension of the work in Ref. [116], where implementations of CKKW were presented for HERWIG and the so-called pseudo-shower alternative to CKKW using PYTHIA, as well as the results of an approach inspired by the MLM-scheme. The work presented here considers the predictions of five different codes, ALPGEN, ARIADNE, HELAC, MADEVENT and SHERPA. ALPGEN implements the MLM scheme, where the results shown here are obtained with the HERWIG shower; ARIADNE the Lönnblad scheme; HELAC the MLM scheme, but results will be shown with the PYTHIA shower; MADEVENT uses a variant of the MLM scheme, based on the CKKW parametrisation of the multi-parton phase space. This list of codes therefore covers a broad spectrum of alternative multi-jet merging approaches and, in particular, includes all the programs used as reference event generators for multi-jet production by the Tevatron and LHC experimental collaborations. For those, results are shown relative to publicly available versions, therefore providing valuable information on the systematics involved in the generation of multi-jet configurations by the experiments. A preliminary study, limited to the ALPGEN, ARIADNE and SHERPA codes, was presented in Ref. [99].

4.1 Merging procedures

In general, the different merging procedures in the various codes follow a similar strategy:

1. A jet measure is defined and all relevant cross sections including jets are calculated for the process under consideration. I.e. for the production of a final state X in pp-collisions, the cross sections for the processes $pp \to X + n$ jets with $n = 0, 1, \ldots, n_{\max}$ are evaluated.

2. Hard parton samples are produced with a probability proportional to the respective total cross section, in a corresponding kinematic configuration following the matrix element.

3. The individual configurations are accepted or rejected with a dynamical, kinematics-dependent probability that includes both effects of running couplings and of Sudakov form factors. In case the event is rejected, step 2 is repeated, i.e. a new parton sample is selected, possibly with a new number of jets.

4. The parton shower is invoked with suitable initial conditions for each of the legs. In some cases, like, e.g. in the MLM procedure described below, this step is performed together with the step before, i.e. the acceptance/rejection of the jet configuration. In all cases the parton shower is constrained not to produce any extra jet. Stated in other words: configurations that would fall into the realm of matrix elements with a higher jet multiplicity are vetoed in the parton shower step.

The merging procedures discussed below differ from the CKKW prescription and with respect to each other mainly

- in the jet definition used in the matrix elements
- in the way the acceptance/rejection of jet configurations stemming from the matrix element is performed
- and in details concerning the starting conditions of and the jet vetoing inside the parton shower.

The CKKW approach in SHERPA

In general, the CKKW implementation in SHERPA, as presented in the previous chapters is employed. It must be noted however that in contrast to what is introduced there, the internal jet definition follows a different strategy. Namely jet measures for hadronic collisions are defined along the lines of Refs. [95, 117]

$$\begin{aligned} Q_{ij}^2 &= \frac{\min\left\{p_{i\perp}^2, p_{j\perp}^2\right\}}{D^2}\left[\cosh(\eta_i-\eta_j)-\cos(\phi_i-\phi_j)\right], \\ Q_{ib^\pm}^2 &= p_{i\perp}^2 . \end{aligned} \tag{4.1}$$

Also, the highest jet multiplicity is dealt with as presented ibidem and backward clustering proceeds by means of a k_T-algorithm with the above measure and employing the E-scheme. According to Ref. [118] the regularisation of initial state soft and collinear singularities through $Q_{ib^\pm}$ is equivalent to employing dimensional regularisation in the $\overline{\text{MS}}$ subtraction scheme. Other schemes are presented e.g. in Refs. [90, 119]. The D-parameter is introduced in Ref. [77]. It corresponds to a first approximation of $C_{i,b^\pm}$ in Eq. 3.9.

The Dipole Cascade and CKKW

The merging prescription developed for the dipole cascade in the ARIADNE program [103] is similar to CKKW, but differs in the way the shower history is constructed, and in the way the Sudakov form factors are calculated. Also, since the ARIADNE cascade is ordered in transverse momentum the treatment of starting scales is simplified. Before going into details of the merging prescription, it is useful to describe the basics of the dipole cascade, since it is different from conventional parton showers.

The dipole model [102] as implemented in the ARIADNE program is based on iterating $2 \to 3$ dipole splittings instead of the usual $1 \to 2$ partonic splittings in a conventional parton shower. Gluon emission is modeled as coherent radiation from colour-anti-colour charged parton pairs. This has the advantage of e.g. including first order corrections to the matrix elements for $e^+e^- \to q\bar{q}$ in a natural way and it also automatically includes the coherence effects modeled by angular ordering in conventional showers. The process of quark-anti-quark production does not come in as naturally, but can be added [120]. The emissions in the dipole cascade are ordered according to an invariant transverse momentum

defined as

$$k_\perp^2 = \frac{s_{13}s_{32}}{s_{123}}, \tag{4.2}$$

where s_{ij} is the squared invariant mass of parton i and j, with the emitted parton having index 3.

When applied to hadronic collisions, the dipole model does not separate between initial- and final-state gluon radiation. Instead all gluon emissions are treated as coming from final-state dipoles [121]. To be able to extend the dipole model to hadron collisions, spatially extended coloured objects are introduced to model the hadron remnants. Dipoles involving hadron remnants are treated in a manner similar to normal final-state dipoles. However, since the hadron remnant is considered to be an extended object, emissions with small wavelength are suppressed. This is modeled by only allowing a fraction of the remnant to take part in the emission. The fraction that is resolved during the emission is given by

$$a(k_\perp) = \left(\frac{\mu}{k_\perp}\right)^\alpha, \tag{4.3}$$

where μ is the inverse size of the remnant and α is the dimensionality. These are semi-classical parameters, which have no correspondence in conventional parton cascades, where instead a suppression is obtained by ratios of quark densities in the backward evolution. The main effect is that the dipole cascade allows harder gluon emissions in the beam directions, enabling it to describe properly e.g. forward jet rates measured at HERA (see e.g. [122]).

There are two additional forms of emissions, which need to be included in the case of hadronic collisions. One corresponds to an initial state $g \to q\bar{q}$. This does not come in naturally in the dipole model, but is added by hand in a way similar to that of a conventional initial-state parton shower [123]. The other corresponds to the initial-state $q \to gq$ (with the gluon entering into the hard sub-process), which could be added in a similar way, but this has not yet been implemented in ARIADNE.

A different model, based on a perturbative interpretation, where emissions in hadron collisions stem from initial-final and initial-initial dipoles was presented in Ref. [25]. This model yields very promising results in hadron-hadron collisions. It has, however not been investigated in deep inelastic scattering yet.

When implementing CKKW for the dipole cascade [97, 124], the procedure is slightly different from what has been described above. Rather than using the standard $k_\perp$-algorithm to cluster the state produced by the matrix-element generator, a complete set of intermediate partonic states, S_i, and the corresponding emission scales, $q_{\perp i}$ are constructed, which correspond to a complete dipole shower history. Hence, for each state produced by the matrix-element generator, basically the question *how would ARIADNE have generated this state* is answered. Note, however, that this means that only coloured particles are clustered, which differs from eg. SHERPA, where also the W and its decay products are involved in the clustering.

The Sudakov form factors are then introduced using the Sudakov veto algorithm. The idea is that the Sudakov form factors used in ARIADNE should be reproduced. This is done by performing a trial emission starting from each intermediate state S_i with $q_{\perp i}$ as a starting scale. If the emitted parton has a $q_\perp$ higher than $q_{\perp i+1}$ the state is rejected. This correspond to keeping the state according to the no-emission probability in ARIADNE, which is exactly the Sudakov form factor.

The MLM procedure

The so-called MLM "matching" algorithm is described as follows.

1. The first step is the generation of parton-level configurations for all final-state parton multiplicities n up to a given N ($W + N$ partons). They are defined by the following kinematical cuts:

$$p_\perp^{\text{part}} > p_\perp^{\min} , \quad |\eta_{\text{part}}| < \eta_{\max} , \quad \Delta R_{jj} > R_{\min} , \tag{4.4}$$

   where $p_\perp^{\text{part}}$ and η_{part} are the transverse momentum and pseudo-rapidity of the final-state partons, and ΔR_{jj} is their minimal separation in the (η, ϕ) plane. The parameters $p_\perp^{\min}$, $\eta_{\max}$ and $R_{\min}$ are called generation parameters, and are the same for all $n = 1, \ldots, N$.

2. The renormalisation scale is set according to the CKKW prescription. The necessary tree branching structure is defined for each event, allowing however only branchings,

which are consistent with the colour structure of the event, which in ALPGEN is extracted from the matrix-element calculation [76]. For a pair of final-state partons i and j, the $k_\perp$-measure defined by

$$d_{ij} = \Delta R_{ij}^2 \min(p_{\perp i}^2, p_{\perp j}^2) \,, \tag{4.5}$$

is used, where $\Delta R_{ij}^2 = \Delta\eta_{ij}^2 + \Delta\phi_{ij}^2$, while for a pair of initial/final-state partons one has

$$d_{ij} = p_\perp^2, \tag{4.6}$$

i.e. the $p_\perp^2$ of the final-state one.

3. The $k_\perp$-value at each vertex is used as a scale for the relative power of α_s. The factorisation scale for the parton densities is given by the hard scale of the process, $Q_0^2 = m_W^2 + p_{\perp W}^2$. It may happen that the clustering process stops before the lowest-order configuration is reached. This is the case, e.g., for an event like $u\bar{u} \to Wc\bar{s}g$. Flavour conservation allows only the gluon to be clustered, since $u\bar{u} \to Wc\bar{s}$ is a LO process, first appearing at $\mathcal{O}(\alpha_s^2)$. In such cases, the hard scale Q_0 is adopted for all powers of α_s corresponding to the non-merged clusters.

4. Events are then showered, using PYTHIA or HERWIG. The evolution for each parton starts at the scale determined by the default PYTHIA and HERWIG algorithms on the basis of the kinematics and colour connections of the event. The upper veto cutoff to the shower evolution is given by the hard scale of the process, Q_0. After evolution, a jet cone algorithm is applied to the partons produced in the perturbative phase of the shower. Jets are defined by a cone size R_{clus}, a minimum transverse energy $E_\perp^{\text{clus}}$ and a maximum pseudo-rapidity $\eta_{\text{max}}^{\text{clus}}$. The parameters are called matching parameters, and should be kept the same for all samples $n = 0, 1, \ldots, N$. Jets such defined provide the starting point for the matching procedure, described in the next point. In the default implementation, $R_{\text{clus}} = R_{\text{min}}$, $\eta_{\text{max}}^{\text{clus}} = \eta_{\text{max}}$ and $E_\perp^{\text{clus}} = p_\perp^{\text{min}} + \max(5\ \text{GeV}, 0.2 \times p_\perp^{\text{min}})$ are assumed, but these can be varied as part of the systematics assessment. To ensure a complete coverage of phase space, however, it is necessary that $R_{\text{clus}} \geq R_{\text{min}}$,

$\eta^{\text{clus}}_{\text{max}} \leq \eta_{\text{max}}$ and $E^{\text{clus}}_{\perp} \geq p^{\text{min}}_{\perp}$.

5. Starting from the hardest parton, the jet which is closest to it in (η, ϕ) is selected. If the distance between the parton and the jet centroid is smaller than $1.5 \times R_{\text{clus}}$, one says that the parton and the jet *match*. The matched jet is removed from the list of jets, and the matching test for subsequent partons is performed. The event is fully matched if each parton matches to a jet. Events, which do not match, are rejected. A typical example is when two partons are so close that they cannot generate independent jets, and therefore cannot match. Another example is when a parton is too soft to generate its own jet, again failing matching.

6. Events from the parton samples with $n < N$, which survive matching, are then required not to have extra jets. If they do, they are rejected, a suppression, which replaces the Sudakov reweighting used in the CKKW approach. This prevents the double counting of events, which will be present in, and more accurately described by, the $n+1$ sample. In the case of $n = N$, events with extra jets can be kept since they will not be generated by samples with higher n. Nevertheless, to avoid double counting, it is required that their transverse momentum be smaller than that of the softest of the matched jets.

When all the resulting samples from $n = 0, \ldots, N$ are combined, one obtains an inclusive W+jets sample. The harder the threshold for the energy of the jets used in the matching, $E^{\text{clus}}_{\perp}$, the fewer the events rejected by the extra-jet veto (i.e. smaller Sudakov suppression), with a bigger role given to the shower approximation in the production of jets. Using lower thresholds would instead enhance the role of the matrix elements even at lower $E_{\perp}$, and lead to larger Sudakov suppression, reducing the role played by the shower in generating jets. The matching/rejection algorithm ensures that these two components balance each other. This algorithm is encoded in the ALPGEN generator [98, 15], where evolution with both HERWIG and PYTHIA are enabled. However, in the framework of this study, the parton shower evolution has been performed by HERWIG.

The MADEVENT approach

The approach used in MADGRAPH/MADEVENT [125, 17] is based on the MLM prescription, but uses a different jet algorithm for defining the scales in α_s and for the jet matching. The

phase space separation between the different multi-jet processes is achieved using the $k_\perp$-measure as in SHERPA (Eq. (4.1) with $D = 1$), while the Sudakov reweighting is performed by rejecting showered events that do not match to the parton-level jets, as in ALPGEN. This approach allows more direct comparisons with SHERPA, including the effects of changing the $k_\perp$-cutoff scale. The details of the procedure are as follows.

Matrix-element multi-parton events are produced using MADGRAPH/MADEVENT version 4.1 [73], with a cutoff $Q_{\text{min}}^{\text{ME}}$ in clustered $k_\perp$. The multi-parton state from the matrix-element calculation is clustered according to the $k_\perp$-algorithm, but allowing only clusterings that are compatible with the Feynman diagrams of the process, which are provided to MADEVENT by MADGRAPH. The factorisation scale, i.e., the scale used in the parton densities, is taken to be the clustering momentum in the last $2 \to 2$ clustering (the "central process"), usually corresponding to the transverse mass, $m_\perp$, of the W boson. The $k_\perp$-scales of the QCD clustering nodes are used as scales in the calculation of the various powers of α_s.

As in the ALPGEN procedure, no Sudakov reweighting is performed. Instead, the virtuality-ordered shower of PYTHIA 6.4 [6] is used to shower the event, with the starting scale of the shower set to the factorisation scale. The showered (but not yet hadronised) event is then clustered to jets using the $k_\perp$-algorithm with a jet measure cutoff $Q_{\text{min}}^{\text{jet}} > Q_{\text{min}}^{\text{ME}}$, and the matrix-element partons are matched to the resulting jets, in a way, which differs from the standard MLM procedure. A parton is considered to be matched to the closest jet if the jet measure $Q(\text{parton}, \text{jet})$ is smaller than the cutoff $Q_{\text{min}}^{\text{jet}}$. Events where not all partons are matched to jets are rejected. For events with parton multiplicity smaller than the highest multiplicity, the number of jets must be equal to the number of partons. For events with the highest multiplicity, N jets are reconstructed, and partons are considered to be matched if $Q(\text{parton}, \text{jet}) < Q_N^{\text{parton}}$, the smallest $k_\perp$-measure in the matrix-element event. This means that extra jets below Q_N^{parton} are allowed, similar to the Sherpa treatment. The standard MLM scheme with cone jets is implemented as an alternative.

HELAC implementation of the MLM procedure

HELAC generates events for all possible processes at hadron and lepton colliders within the Standard Model and has been successfully tested with up to 10 particles in the final state [72, 126, 127]. It implements the MLM procedure as described above, where partons

from the matrix-element calculation are matched to jets constructed after parton showering. Parton-level events are generated with a $p_{\perp\min}$ threshold, a minimum parton separation, $R_{\min}$, and a maximum pseudo-rapidity, $\eta_{\max}$. In order to extract the necessary information for reweighting, initial- and final-state partons are clustered backwards as described for the MLM procedure, where again the colour information extracted from the matrix-element calculation is used as a constraint on the allowed clusterings. For every node, a factor of $\alpha_s(Q^2)/\alpha_s(Q_0^2)$ is multiplied into the weight of the event, with Q being the nodal scale of clustering. For unclustered vertices as well as for the scale used in the parton densities, the hard scale of the process $Q_0^2 = m_W^2 + p_{\perp W}^2$ is used. Events from HELAC are output in Les Houches event file format [128]. This output is read into PYTHIA version 6.4 [6], where the virtuality-ordered parton shower is constructed. For each event, a cone jet-algorithm is applied to all partons resulting from the shower evolution. Resulting jets are defined by $E_{\perp\min}^{\text{clus}}$, $\eta_{\max}^{\text{clus}}$ and by a jet cone size R_{clus}. Partons in the parton-level event are then matched to one of the constructed jets. Starting from the parton with the highest $p_\perp$, the closest jet ($1.5 \times R_{\text{clus}}$) is selected in the pseudo-rapidity/azimuthal-angle space. All subsequent partons are matched iteratively to jets. If this is impossible, the event is rejected. Additionally, for $n < N$, matched events with the number of jets greater than n are rejected, whereas for $n = N$, i.e. the highest multiplicity, events with extra jets are kept only if the extra jets are softer than the N matched jets.

4.2 General properties of the event generation for the study

In the following sections the case of W+multi-jet production is presented as an example for multi-jet merging. This is one of the most studied final states because of its important role as a background to top quark studies at the Tevatron. At the LHC, W+jets, as well as the similar Z+jets processes, will provide the main irreducible backgrounds to signals such as multi-jet plus missing transverse energy, typical for Supersymmetry and other manifestations of new physics. The understanding of W+multi-jet production at the Tevatron is therefore an essential step towards the validation and tuning of the tools presented here, prior to their utilisation at the LHC.

The CDF and DØ experiments at the Tevatron collider have reported cross-section measurements for W+multi-jet final states, both from Run I [129] and, in preliminary form, from Run II [130]. The Run I results typically refer to detector-level quantities, and a comparison with theoretical predictions requires to process the generated events through a detector simulation. These tests were performed in the context of the quoted analyses, using the LO calculations available at the time, showing a good agreement within the large statistical, systematic and theoretical uncertainties. The preliminary CDF result from Run II [130] is instead corrected for all detector effects, and expressed in terms of *true* jet energies. In this form it is therefore suitable for direct comparison with theory predictions. Measurements of Z+multi-jet rates are also crucial, but suffer from lower statistics w.r.t. the W case. A Run II measurement of jet $p_\perp$ spectra in Z+multi-jet events from DØ has been compared to the predictions of SHERPA in Ref. [131], showing again a very good agreement. Preliminary CDF results on the spectra of the first and second jet in Z+jet events have been compared against parton-level NLO results [132]. For both the W and Z cases, the forthcoming analyses of the high-statistics sample now available at the Tevatron will provide valuable inputs for more quantitative analyses of the codes presented here.

For each of the codes, a large set of observables is calculated, addressing inclusive properties of the events (transverse momentum spectrum of the W and of leading jets) as well as geometric correlations between the jets. What is presented and discussed here is a subset of the studies, which illustrates the main features of the comparison between the different codes. A preliminary account of these results, limited to the ALPGEN, ARIADNE and SHERPA codes, was presented in Ref. [99]. More complete studies of the systematics of each individual code have been [95, 124, 133] or will be presented elsewhere by the respective authors.

The existence in each of the codes of parameters specifying the details of the merging algorithms presents an opportunity to tune each code so as to best describe the data. This tuning should be seen as a prerequisite for a quantitative study of the overall theoretical systematics: after the tuning is performed on a given set of final states (e.g. the W+jets considered here), the systematics for other observables or for the extrapolation to the LHC can be obtained by comparing the difference in extrapolation between the various codes. Here it would be advantageous if future analysis of Tevatron data would provide spectra corrected for detector effects in a fashion suitable for a direct comparison against theoretical

predictions.

The following two sections present results for the Tevatron ($p\bar{p}$ collisions at 1.96 TeV) and for the LHC (pp at 14 TeV). The elements of the analysis common to all codes are the following:

- *Event samples.* Tevatron results refer to the combination of W^+ and W^- bosons, while at the LHC only W^+ are considered. All codes have generated parton-level samples according to matrix elements with up to 4 final-state partons, i.e. $N = 4$. Partons are restricted to the light-flavour sector and are taken to be massless. The Yukawa couplings of the quarks are neglected. The PDF set CTEQ6L has been used with $\alpha_s(m_Z) = 0.118$. Further standard-model parameters used were: $m_W = 80.419$ GeV, $\Gamma_W = 2.048$ GeV, $m_Z = 91.188$ GeV, $\Gamma_Z = 2.446$ GeV, the Fermi constant $G_\mu = 1.16639 \cdot 10^{-2}$ GeV^{-2}, $\sin^2\theta_W = 0.2222$ and $\alpha_{\text{EM}} = 1/132.51$.

- *Jet definitions.* Jets were defined using Paige's GETJET cone-clustering algorithm, with a calorimeter segmentation of $(\Delta\eta, \Delta\phi) = (0.1, 6°)$ extended over the range $|\eta| < 2.5$ ($|\eta| < 5$), and cone size of 0.7 (0.4) for the Tevatron (LHC). At the Tevatron (LHC) jets with $E_\perp > 10$ (20) GeV and pseudo-rapidity $|\eta| < 2$ (4.5) are required. For the analysis of the differential jet rates denoted as d_i, the Tevatron Run II $k_\perp$-algorithm [77][1] was applied to all final-state particles fulfilling $|\eta| < 2.5$ (5). The $k_\perp$-measure used in the algorithm is given by equations (4.5) and (4.6).

In all cases, except the d_i plots, the analysis is done at the hadron level, but without including the underlying event. The d_i plots were done to check the details of the merging and are therefore done at parton level to avoid any smearing effects from hadronisation. For all codes, the systematic uncertainties are investigated by varying the merging scale and by varying the scale in α_s and, for some codes, in the parton density functions. For ALPGEN and HELAC, the scale in α_s has been varied only in the α_s-reweighting of the matrix elements, while for the others the scale was also varied in the parton cascade. Note that varying the scale in the final-state parton showers will spoil the tuning done to LEP data for the cascades. A consistent way of testing the scale variations would require retuning of hadronisation parameters. However, a strong dependence on the hadronisation parameters

[1] More precisely, the implementation in the `ktclus` package [134] was employed (`IMODE=5`, or `4211`).

in the observables considered here should not be expected, and no attempt to retune has therefore been made.

The parameter choices specific to the individual codes are as follows:

- ALPGEN: The parton-level matrix elements were generated with ALPGEN [98, 15] and the subsequent evolution used the HERWIG parton shower according to the MLM procedure. Version 6.510 of HERWIG was used, with its default shower and hadronisation parameters. The *default* results for the Tevatron (LHC) were obtained using parton-level cuts (see Eq. (4.4)) of $p_\perp^{\min} = 8$ (15) GeV, $\eta_{\max} = 2.5$ (5), $R_{\min} = 0.7$ (0.4) and matching defined by $E_\perp^{\text{clus}} = 10$ (20) GeV, $\eta_{\max}^{\text{clus}} = \eta_{\max}$ and $R_{\text{clus}} = R_{\min}$. The variations used in the assessment of the systematics cover:

  - different thresholds for the definition of jets used in the matching: $E_\perp^{\text{clus}} = 20$ and 30 GeV for the Tevatron, and $E_\perp^{\text{clus}} = 30$ and 40 GeV for the LHC. These thresholds were applied to the partonic samples produced with the default generation cuts, as well as to partonic samples produced with higher $p_\perp^{\min}$ values. No difference was observed in the results, aside from an obviously better generation efficiency in the latter case. In the following studies of the systematics, the two threshold settings will be referred to as ALPGEN parameter sets ALptX, where X labels the value of the threshold. Studies with different values of R_{clus} and $R_{\min}$ were also performed, leading to marginal changes, which will not be documented here.

  - different renormalisation scales at the vertices of the clustering tree: $\mu = \mu_0/2$ and $\mu = 2\,\mu_0$, where μ_0 is the default $k_\perp$-value. In the following studies of the systematics, these two settings will be referred to as ALPGEN parameter sets ALscL (for "Low") and ALscH (for "High").

  The publicly available version V2.10 of the code was used to generate all the ALPGEN results.

- ARIADNE: The parton-level matrix elements were generated with MADEVENT and the subsequent evolution used the dipole shower in ARIADNE according to the procedure outlined in Sec. 4.1. Hadronisation was performed by PYTHIA.

For the *default* results at the Tevatron (LHC) the parton-level cuts were $p_{\perp\min} = 10$ (20), $R_{jj} < 0.5$ (0.4) and, in addition, a cut on the maximum pseudo-rapidity of jets, $\eta_{j\max} = 2.5$ (5.0). The variations used in the assessment of the systematics cover:

- different values of the merging scales $p_{\perp\min} = 20$ and 30 GeV for the Tevatron (30 and 40 GeV for the LHC). In the following studies of the systematics, these two settings will be referred to as ARIADNE parameter sets ARptX.
- a change of the soft suppression parameters in Eq. (4.3) from the default values of $\mu = 0.6$ GeV and $\alpha = 1$, to $\mu = 0.6$ GeV and $\alpha = 1.5$ (taken from a tuning to HERA data [135]). This setting will be referred to as ARs.
- different values of the scale in α_s: $\mu = \mu_0/2$ and $\mu = 2\,\mu_0$ were used (ARscL and ARscH). This scale change was used in α_s evaluations in the program.

- HELAC: The parton-level matrix elements were generated with HELAC and the phase space generation is performed by PHEGAS [16]. The subsequent evolution used the default virtuality-ordered shower in PYTHIA 6.4 [6] according to the MLM procedure. Hadronisation was performed by PYTHIA.

  The *default* results for the Tevatron (LHC) were obtained using parton-level cuts of $p_{\perp\min} = 8$ (15) GeV, $\eta_{\max} = 2.5$ (5), $R_{\min} = 0.7$ (0.4) and matching defined by $E^{\text{clus}}_{\perp\min} = 10$ (20) GeV, $\eta^{\text{clus}}_{\max} = 2$ (4.5) and $R^{\text{clus}}_{\min} = 0.7$ (0.4). The variations used in the assessment of the systematics cover:

  - different thresholds for the definition of jets used in the matching: $E^{\text{clus}}_{\perp\min} = 30$ GeV for the Tevatron, and $E^{\text{clus}}_{\perp\min} = 40$ GeV for the LHC. In the following studies of the systematics, these two settings will be referred to as HELAC parameter sets HELptX, where X labels the value of the threshold.
  - different renormalisation scales at the vertices of the clustering tree: $\mu = \mu_0/2$ and $\mu = 2\,\mu_0$, where μ_0 is the default $k_\perp$-value. In the following studies of the systematics, these two settings will be referred to as HELAC parameter sets HELscL and HELscH.

- MADEVENT: The parton-level matrix elements were generated with MADEVENT and the subsequent evolution used the PYTHIA shower according to the modified MLM

procedure in MADEVENT described above. Hadronisation was performed by PYTHIA.

For the *default* results at the Tevatron (LHC) the value of the merging scale has been chosen to $k_{\perp 0} = 10$ (20) GeV. The variations used in the assessment of the systematics cover:

- different values of the merging scale $k_{\perp 0} = 20$ and 30 GeV for the Tevatron, and $k_{\perp 0} = 30$ and 40 GeV for the LHC. In the following studies of the systematics, these two settings will be referred to as MADEVENT parameter sets MEktX.
- different values of the scales used in the evaluation of α_s, in both the matrix element generation and the parton shower: $\mu = \mu_0/2$ and $\mu = 2\,\mu_0$, where μ_0 is the default $k_\perp$-value. These two settings will be referred to as MADEVENT parameter sets MEscL and MEscH.

- SHERPA: The parton-level matrix elements used within SHERPA have been obtained from the internal matrix-element generator AMEGIC++ [18]. Parton showering has been conducted by APACIC++ [20] whereas the combination of the matrix elements with this parton shower has been accomplished according to the CKKW procedure[2]. The hadronisation of the shower configurations has been performed by PYTHIA 6.214, which has been made available through an internal interface.

  For the *default* Tevatron (LHC) predictions, the value of the merging scale has been chosen to $k_{\perp 0} = 10$ (20) GeV. All SHERPA predictions for the Tevatron (LHC) have been obtained by setting the internally used D-parameter (cf. Eq. (4.1)) through $D = 0.7$ (0.4). Note that, these two choices directly determine the generation of the matrix elements in SHERPA. The variations used in the assessment of the systematics cover:

  - first, different choices of the merging scale $k_{\perp 0}$. Values of 20 and 30 GeV, and 30 and 40 GeV have been used for the Tevatron and the LHC case, respectively. In the following studies of the systematics, these settings will be referred to as SHERPA parameter sets SHktX where X labels the value of the internal jet scale.

[2]Beyond the comparison presented here, SHERPA predictions for W plus multi-jets and W-pairs plus multi-jets have already been validated and studied for Tevatron and LHC energies in Refs. [95].

- and, second, different values of the scales used in any evaluation of the α_s *and* the parton distribution functions[3]. Two cases have been considered, $\mu = \mu_0/2$ and $\mu = 2\,\mu_0$. The choice of the merging scale is as in the default run, where μ_0 denotes the corresponding $k_\perp$-values. In the subsequent studies of the systematics these two cases are referred to as SHERPA parameter sets SHscL and SHscH. It should be stressed that these scale variations have been applied in a very comprehensive manner, i.e. in both the matrix-element and parton-showering phase of the event generation.

All SHERPA results presented in this comparison have been obtained with the publicly available version 1.0.10.

4.3 Tevatron Studies

Event rates

In this section the comparison among inclusive jet rates is presented. These are shown in Tab. 4.1. For each code, in addition to the default numbers, the results of the various individual alternative choices used to assess the systematics uncertainty are displayed. In Tab. 4.2 the "additional jet fractions", namely the rates $\sigma(W+n+1 \text{ jets})/\sigma(W+n \text{ jets})$ are listed, once again covering all systematic sets of all codes. Fig. 4.1, finally, shows graphically the cross-section systematic ranges: for each multiplicity, rates are normalised to the average of the default values of all the codes.
It should be noted that the scale changes in all codes lead to the largest rate variations. This is reflected in the growing size of the uncertainty with larger multiplicities, a consequence of the higher powers of α_s. Furthermore it is noted that the systematic ranges of all codes have regions of overlap.

Kinematical distributions

Firstly, in Fig. 4.2 the inclusive $E_\perp$ spectra of the leading 4 jets are shown. The absolute rate predicted by each code is used, in units of pb/GeV. The relative differences with respect

[3]For example, the analytical Sudakov form factors used in the matrix-element reweighting hence vary owing to their intrinsic α_s-coupling dependence.

Code	σ[tot]	$\sigma[\geq 1$ jet]	$\sigma[\geq 2$ jet]	$\sigma[\geq 3$ jet]	$\sigma[\geq 4$ jet]
ALPGEN, def	**1933**	**444**	**97.1**	**18.9**	**3.2**
ALpt20	1988	482	87.2	15.5	2.8
ALpt30	2000	491	82.9	12.8	2.1
ALscL	2035	540	135	29.7	5.5
ALscH	1860	377	72.6	12.7	2.0
ARIADNE, def	**2066**	**477**	**87.3**	**13.9**	**2.0**
ARpt20	2038	459	76.6	12.8	1.9
ARpt30	2023	446	67.9	11.3	1.7
ARscL	2087	553	116	21.2	3.6
ARscH	2051	419	67.8	9.5	1.3
ARs	2073	372	80.6	13.2	2.0
HELAC, def	**1960**	**356**	**70.8**	**13.6**	**2.4**
HELpt30	1993	373	68.0	12.5	2.4
HELscL	2028	416	95.0	20.2	3.5
HELscH	1925	324	55.1	9.4	1.4
MADEVENT, def	**2013**	**381**	**69.2**	**12.6**	**2.8**
MEkt20	2018	375	66.7	13.3	2.7
MEkt30	2017	361	64.8	11.1	2.0
MEscL	2013	444	93.6	20.0	4.8
MEscH	1944	336	53.2	8.6	1.7
SHERPA, def	**1987**	**494**	**107**	**16.6**	**2.0**
SHkt20	1968	465	85.1	12.4	1.5
SHkt30	1982	461	79.2	10.8	1.3
SHscL	1957	584	146	25.2	3.4
SHscH	2008	422	79.8	11.2	1.3

Tab. 4.1 Cross sections (in pb) for the inclusive jet rates at the Tevatron, according to the default and alternative settings of the various codes.

to the ALPGEN results, in this figure and all other figures of this section, are shown in the lower in-sets of each plot, where for the code X the quantity $(\sigma(X) - \sigma_0)/\sigma_0$ is plotted, σ_0 being the values of the ALPGEN curves.

There is generally good agreement between the codes, except for ARIADNE, which has a harder $E_\perp$ spectra for the leading two jets. There it is also found that SHERPA is slightly harder than ALPGEN and HELAC, while MADEVENT is slightly softer.

Fig. 4.3 shows the inclusive η spectra of the leading 4 jets, all normalised to unit area. There is a good agreement between the spectra of ALPGEN, HELAC and MADEVENT, while ARIADNE and SHERPA spectra appear to be broader, in particular for the sub-leading jets. This broadening is expected for ARIADNE since the gluon emissions there are essentially

Code	$\sigma^{[\geq 1]}/\sigma^{[tot]}$	$\sigma^{[\geq 2]}/\sigma^{[\geq 1]}$	$\sigma^{[\geq 3]}/\sigma^{[\geq 2]}$	$\sigma^{[\geq 4]}/\sigma^{[\geq 3]}$
ALPGEN, def	**0.23**	**0.22**	**0.19**	**0.17**
ALpt20	0.24	0.18	0.18	0.18
ALpt30	0.25	0.17	0.15	0.16
ALscL	0.27	0.25	0.22	0.19
ALscH	0.20	0.19	0.17	0.16
ARIADNE, def	**0.23**	**0.18**	**0.16**	**0.15**
ARpt20	0.23	0.17	0.17	0.15
ARpt30	0.22	0.15	0.16	0.16
ARscL	0.26	0.21	0.18	0.17
ARscH	0.20	0.16	0.14	0.14
ARs	0.18	0.22	0.16	0.15
HELAC, def	**0.18**	**0.20**	**0.19**	**0.18**
HELpt30	0.19	0.19	0.18	0.19
HELscL	0.21	0.23	0.21	0.17
HELscH	0.17	0.17	0.17	0.15
MADEVENT, def	**0.19**	**0.18**	**0.18**	**0.22**
MEkt20	0.19	0.18	0.20	0.20
MEkt30	0.18	0.18	0.17	0.18
MEscL	0.22	0.21	0.21	0.24
MEscH	0.17	0.16	0.16	0.20
SHERPA, def	**0.25**	**0.22**	**0.16**	**0.12**
SHkt20	0.24	0.18	0.15	0.12
SHkt30	0.23	0.17	0.14	0.12
SHscL	0.30	0.25	0.17	0.13
SHscH	0.21	0.19	0.14	0.12

Tab. 4.2 Cross-section ratios for $(n+1)/n$ inclusive jet rates at the Tevatron, according to the default and alternative settings of the various codes.

unordered in rapidity, which means that the Sudakov form factors applied to the matrix-element-generated states include also a $\log(1/x)$ resummation absent in the other programs.

Fig. 4.4a shows the inclusive $p_\perp$ distribution of the W boson, with absolute normalisation in pb/GeV. This distribution reflects in part the behaviour observed for the spectrum of the leading jet, with ARIADNE harder than SHERPA, which, in turn, is slightly harder than ALPGEN, HELAC and MADEVENT. The region of low momenta, $p_{\perp W} < 50$ GeV, is expanded in Fig. 4.4b. Fig. 4.4c shows the η distribution of the leading jet, η_1, when its transverse momentum is larger than 50 GeV. The curves are absolutely normalised, so that it is clear how much rate is predicted by each code to survive this harder jet cut. The $|\eta|$ separation between the W and the leading jet of the event above 30 GeV is shown in Fig. 4.4d,

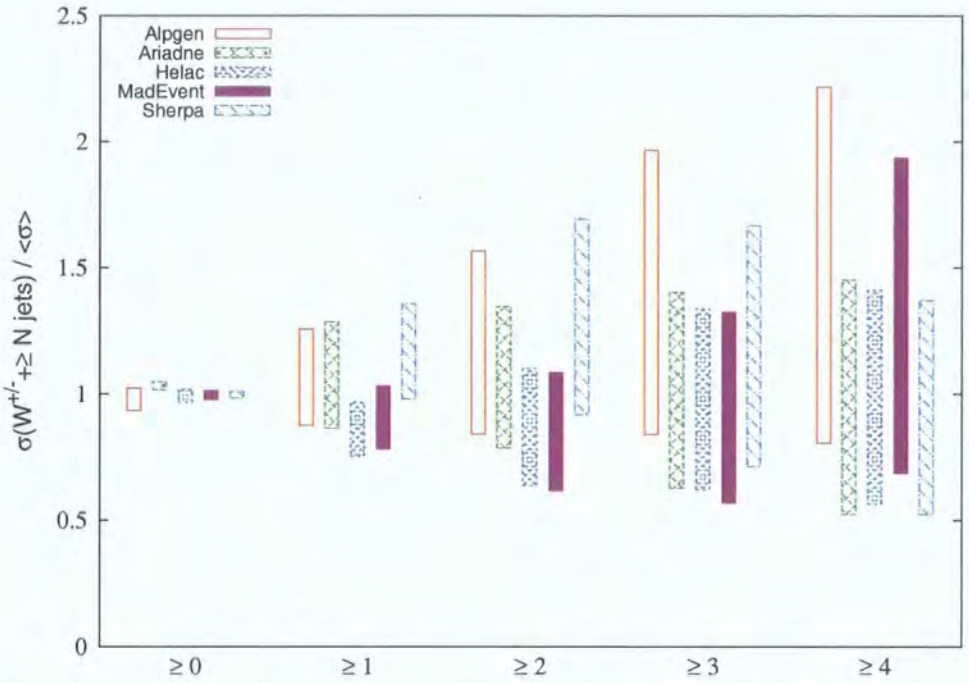

Fig. 4.1 Range of variation for the Tevatron cross-section rates of the five codes, normalised to the average value of the default settings for all codes in each multiplicity bin.

normalised to unit area. Here it is found that ARIADNE has a broader correlation, while HELAC and MADEVENT are somewhat more narrow than ALPGEN and SHERPA.

In Fig. 4.6 the merging scales d_i as obtained from the $k_\perp$-algorithm are shown, where d_i is the scale in an event where i jets are clustered into $i-1$ jets. These are parton-level distributions and are especially sensitive to the behaviour of the merging procedure close to the merging/matching scale. Note that in the plots showing the difference the wiggles stem from both the individual codes and from the ALPGEN reference.

Also shown in Fig. 4.6 is the separation in $\Delta R = \sqrt{\Delta\eta^2 + \Delta\phi^2}$ between successive jet pairs ordered in hardness. The ΔR_{12} is dominated by the transversal-plane back-to-back peak at $\Delta R_{12} = \pi$, while for larger ΔR in all cases the behaviour is more dictated by the correlations in pseudo-rapidity. For these larger values a weaker correlation in ARIADNE and SHERPA is found, which can be expected from their broader rapidity distributions in Fig. 4.3.

Finally, in Fig. 4.5 $H_\perp$ is displayed, the scalar sum of the transverse momenta of the charged lepton, the neutrino and the jets. This is a variable in which one often does experimental cuts in searches for new phenomena and is not expected to be very sensitive to the particulars in the merging schemes. The results show good agreement below 100 GeV, but at higher

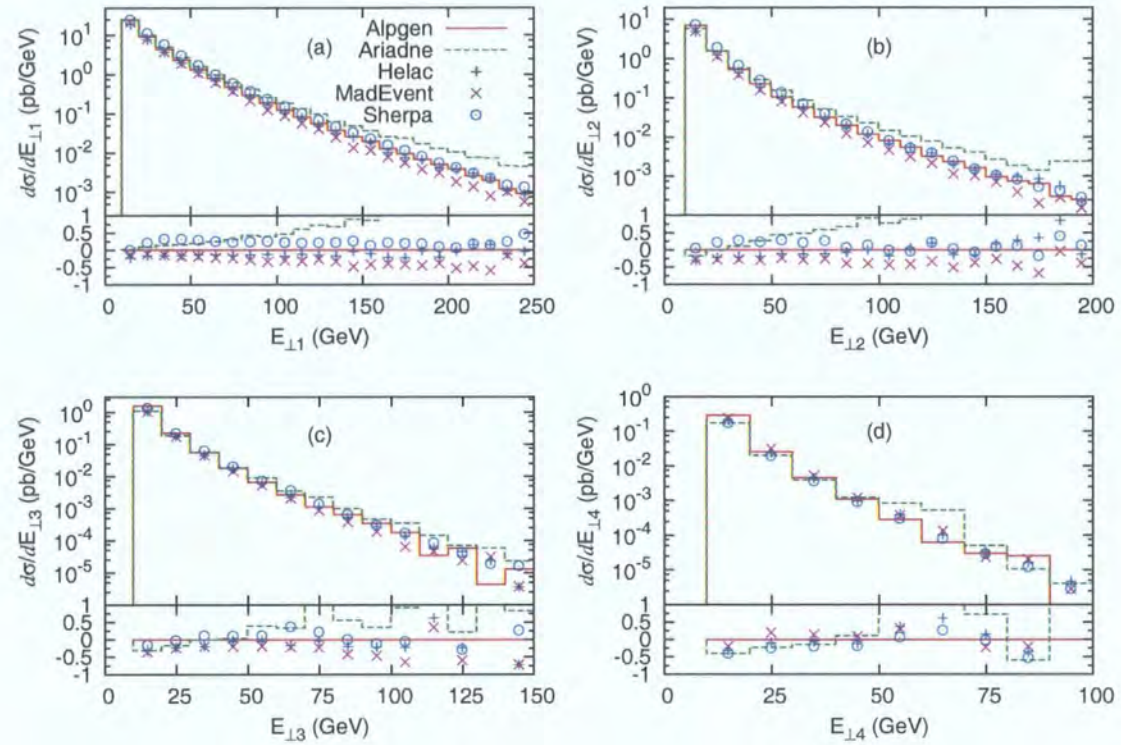

Fig. 4.2 Inclusive $E_\perp$ spectra of the leading 4 jets at the Tevatron (pb/GeV). In all cases the full line gives the ALPGEN results, the dashed line gives the ARIADNE results and the "+", "x" and "o" points give the HELAC, MADEVENT and SHERPA results, respectively.

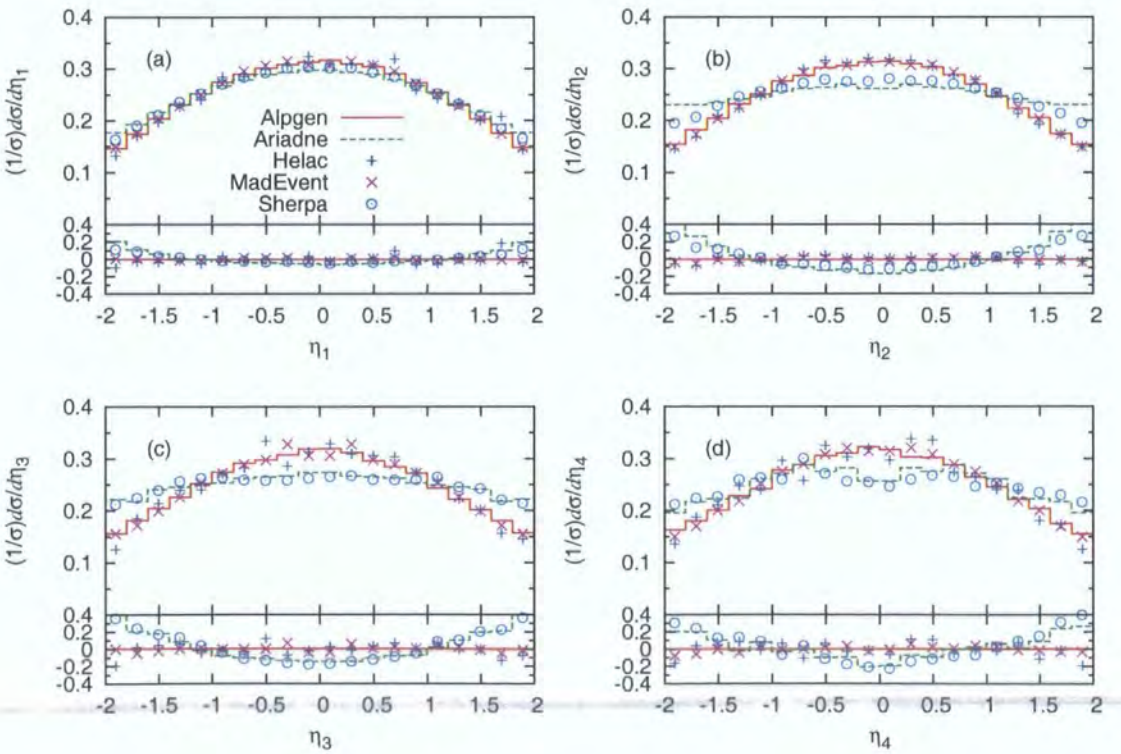

Fig. 4.3 Inclusive η spectra of the 4 leading jets at the Tevatron. All curves are normalised to unit area. Lines and points are as in Fig. 4.2.

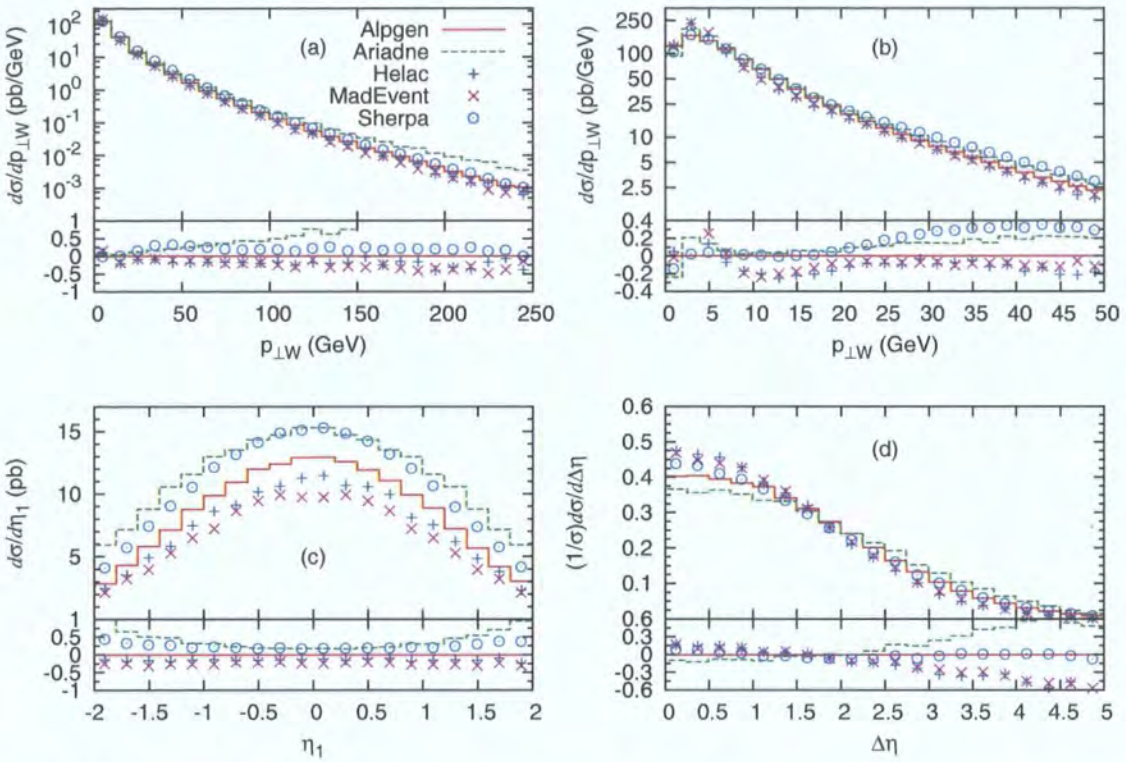

Fig. 4.4 (a) and (b) $p_\perp$ spectrum of $W^\pm$ bosons at the Tevatron (pb/GeV). (c) Inclusive η spectrum of the leading jet, for $p_\perp^{\text{jet1}} > 50$ GeV; absolute normalisation (pb). (d) Pseudo-rapidity separation between the W and the leading jet, $\Delta\eta = |\eta_W - \eta_{\text{jet1}}|$, for $p_\perp^{\text{jet1}} > 30$ GeV, normalised to unit area. Lines and points are as in Fig. 4.2.

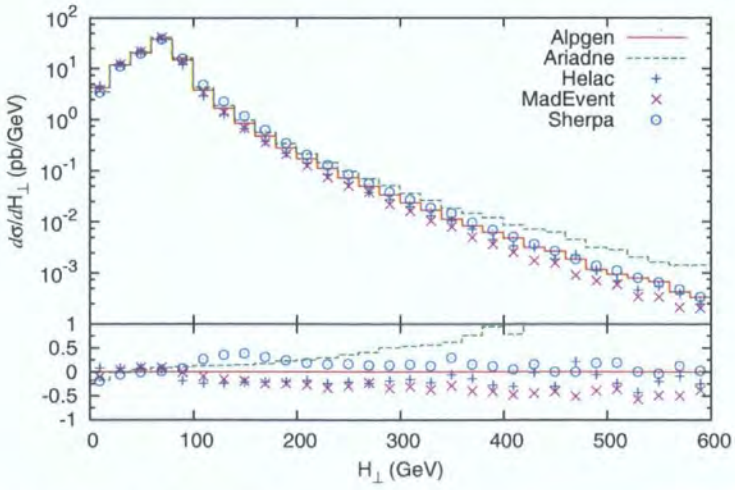

Fig. 4.5 The scalar sum of the transverse momentum of the charged lepton, the neutrino and the jets at the Tevatron. Lines and points are as in Fig. 4.2.

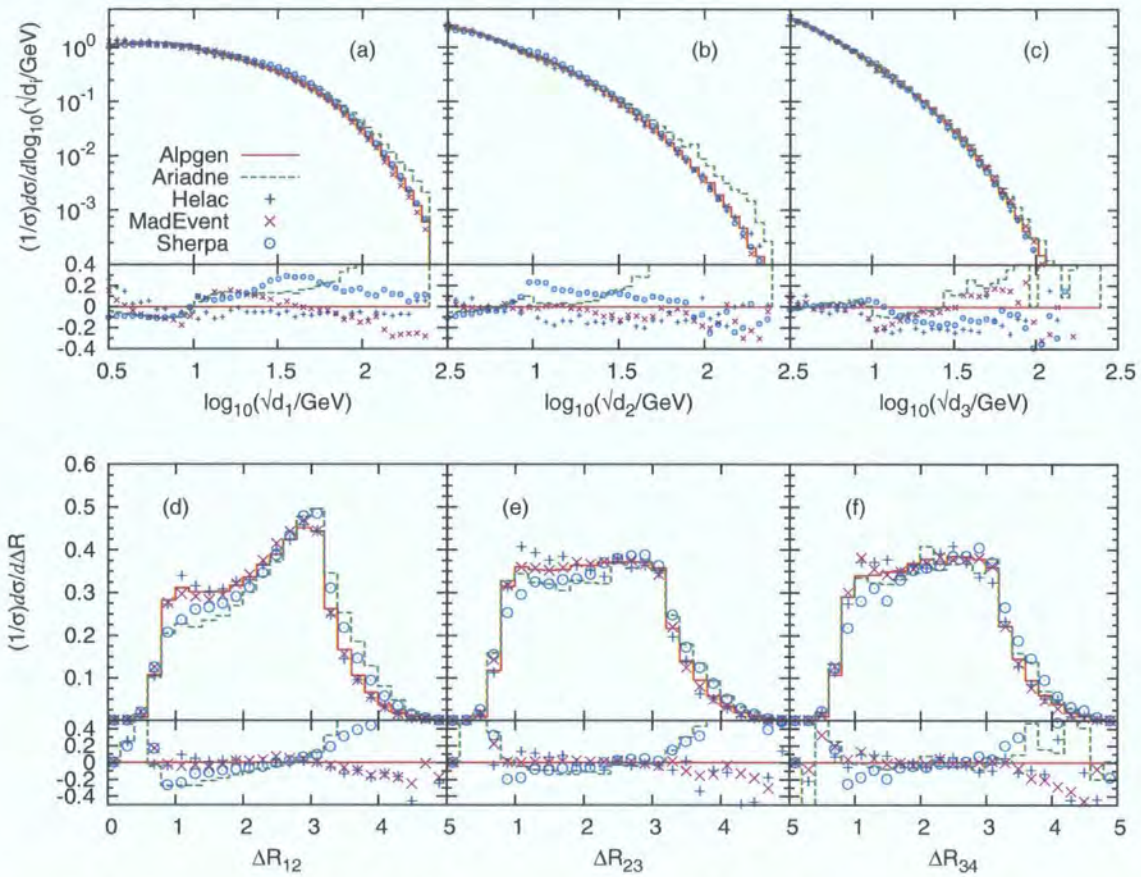

Fig. 4.6 (a)–(c) d_i ($i = 1, 2, 3$) spectra, where d_i is the scale in a parton-level event where i jets are clustered into $i-1$ jets using the $k_\perp$-algorithm. (d)–(f) ΔR separations at the Tevatron between jet 1 and 2, 2 and 3, and 3 and 4. All curves are normalised to unit area. Lines and points are as in Fig. 4.2.

values, as expected from the differences in the hardness of the jet and $p_{\perp W}$ spectra, ARIADNE has harder spectra than SHERPA and ALPGEN, while MADEVENT and HELAC has slightly softer spectra.

4.4 LHC Studies

Event rates

The tables (Tab. 4.3 and 4.4) and figure (Fig. 4.7) of this section correspond to those shown earlier for the Tevatron. The largest rate variation is, similarly to the Tevatron rates, determined by the scale changes. The main feature of the LHC results is the significantly larger rates predicted by ARIADNE, which are outside the systematics ranges of the other

Code	σ[tot]	$\sigma[\geq 1$ jet]	$\sigma[\geq 2$ jet]	$\sigma[\geq 3$ jet]	$\sigma[\geq 4$ jet]
ALPGEN, def	**10170**	**2100**	**590**	**171**	**50**
ALpt30	10290	2200	555	155	46
ALpt40	10280	2190	513	136	41
ALscL	10590	2520	790	252	79
ALscH	9870	1810	455	121	33
ARIADNE, def	**10890**	**3840**	**1330**	**384**	**101**
ARpt30	10340	3400	1124	327	88
ARpt40	10090	3180	958	292	83
ARscL	11250	4390	1635	507	154
ARscH	10620	3380	1071	275	69
ARs	11200	3440	1398	438	130
HELAC, def	**10050**	**1680**	**442**	**118**	**36**
HELpt40	10150	1760	412	116	37
HELscL	10340	1980	585	174	57
HELscH	9820	1470	347	84	24
MADEVENT, def	**10830**	**2120**	**519**	**137**	**42**
MEkt30	10080	1750	402	111	37
MEkt40	9840	1540	311	78.6	22
MEscL	10130	2220	618	186	62
MEscH	10300	1760	384	91.8	27
SHERPA, def	**8800**	**2130**	**574**	**151**	**41**
SHkt30	8970	2020	481	120	32
SHkt40	9200	1940	436	98.5	24
SHscL	7480	2150	675	205	58
SHscH	10110	2080	489	118	30

Tab. 4.3 Cross sections (in pb) for the inclusive jet rates at the LHC, according to the default and alternative settings of the various codes.

codes. Aside from this and the fact that SHERPA gives a smaller total cross section, the comparison among the other codes shows an excellent consistency, with a pattern of the details similar to what is seen for the Tevatron. Details on the internal systematics of the programs are presented in Ref. [100].

Kinematical distributions

Following the same sequence of the Tevatron study, firstly in Fig. 4.8 the inclusive $E_\perp$ spectra of the leading 4 jets are shown. The absolute rate predicted by each code is used, in units of pb/GeV.

Except for ARIADNE, good agreement is found among the codes, with ARIADNE having

Code	$\sigma^{[\geq 1]}/\sigma^{[tot]}$	$\sigma^{[\geq 2]}/\sigma^{[\geq 1]}$	$\sigma^{[\geq 3]}/\sigma^{[\geq 2]}$	$\sigma^{[\geq 4]}/\sigma^{[\geq 3]}$
ALPGEN, def	**0.21**	**0.28**	**0.29**	**0.29**
ALpt30	0.21	0.25	0.28	0.30
ALpt40	0.21	0.23	0.27	0.30
ALscL	0.24	0.31	0.32	0.31
ALscH	0.18	0.25	0.27	0.27
ARIADNE, def	**0.35**	**0.35**	**0.29**	**0.26**
ARpt30	0.33	0.33	0.29	0.27
ARpt40	0.32	0.30	0.30	0.28
ARscL	0.39	0.37	0.31	0.30
ARscH	0.32	0.32	0.26	0.24
ARs	0.31	0.41	0.31	0.30
HELAC, def	**0.17**	**0.26**	**0.27**	**0.31**
HELpt40	0.17	0.23	0.28	0.32
HELscL	0.19	0.30	0.30	0.33
HELscH	0.15	0.24	0.24	0.29
MADEVENT, def	**0.20**	**0.24**	**0.26**	**0.31**
MEkt30	0.17	0.23	0.28	0.33
MEkt40	0.16	0.20	0.25	0.28
MEscL	0.22	0.27	0.30	0.34
MEscH	0.17	0.22	0.24	0.29
SHERPA, def	**0.24**	**0.27**	**0.26**	**0.27**
SHkt30	0.23	0.24	0.25	0.27
SHkt40	0.21	0.22	0.23	0.24
SHscL	0.29	0.31	0.30	0.28
SHscH	0.21	0.24	0.24	0.25

Tab. 4.4 Cross-section ratios for $(n+1)/n$ inclusive jet rates at the LHC, according to the default and alternative settings of the various codes.

significantly harder leading jets, while for sub-leading jets the increased rates noted in Fig. 4.7 mainly come from lower $E_\perp$. Among the other codes, HELAC and SHERPA have consistently somewhat harder jets than ALPGEN, while MADEVENT is a bit softer, but these differences are not as pronounced.

For the pseudo-rapidity spectra of the jets in Fig. 4.9 it is clear that ARIADNE has a much broader distribution in all cases. Also SHERPA has broader distributions, although not as pronounced, while the other codes are very consistent.

The $p_\perp$ distribution of W^+ bosons in Fig. 4.10 follows the trend of the leading-jet $E_\perp$ spectra. The differences observed in the $p_{\perp W}$ region below 10 GeV are not due to the choice of merging approach, but are entirely driven by the choice of shower algorithm. Notice

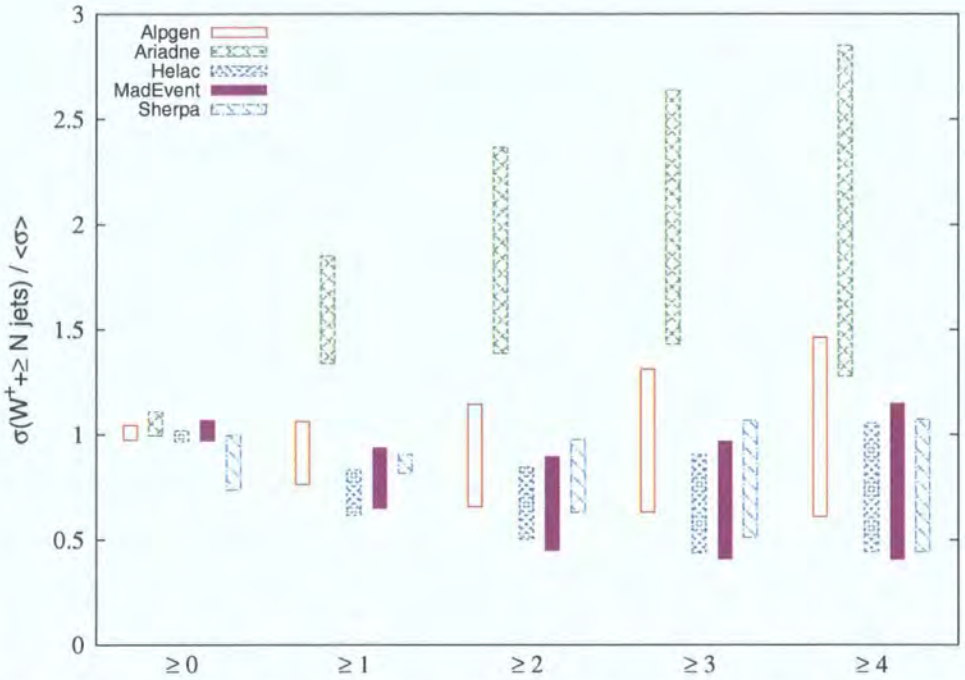

Fig. 4.7 Range of variation for the LHC cross-section rates of the five codes, normalised to the average value of the default settings for all codes in each multiplicity bin.

for example the similarity of the HELAC and MADEVENT spectra, and their peaking at lower p_T than the HERWIG spectrum built into the ALPGEN curve, a result well known from the comparison of the standard PYTHIA and HERWIG generators. Increasing the transverse momentum of the leading jet in Fig. 4.10a does not change the conclusions much for its pseudo-rapidity distribution. Also the rapidity correlation between the leading jet and the W^+ follows the trend found for the Tevatron, but the differences are larger, with a much weaker correlation for ARIADNE. Also SHERPA shows a somewhat weaker correlation, while HELAC is somewhat stronger than ALPGEN and MADEVENT.

For the distribution in clustering scale in Fig. 4.12, it is found again that ARIADNE is by far the hardest. The results given by the other codes are comparable, with the only exception that for the d_1 distribution, SHERPA gives a somewhat harder prediction compared to the ones made by the MLM-based approaches.

The ΔR distributions, in Fig. 4.12, show at large separation a behaviour consistent with the broad rapidity distributions found for SHERPA, and in particular for ARIADNE, in Fig. 4.9. This increase at large ΔR is then compensated by a depletion with respect to the other codes at small separation.

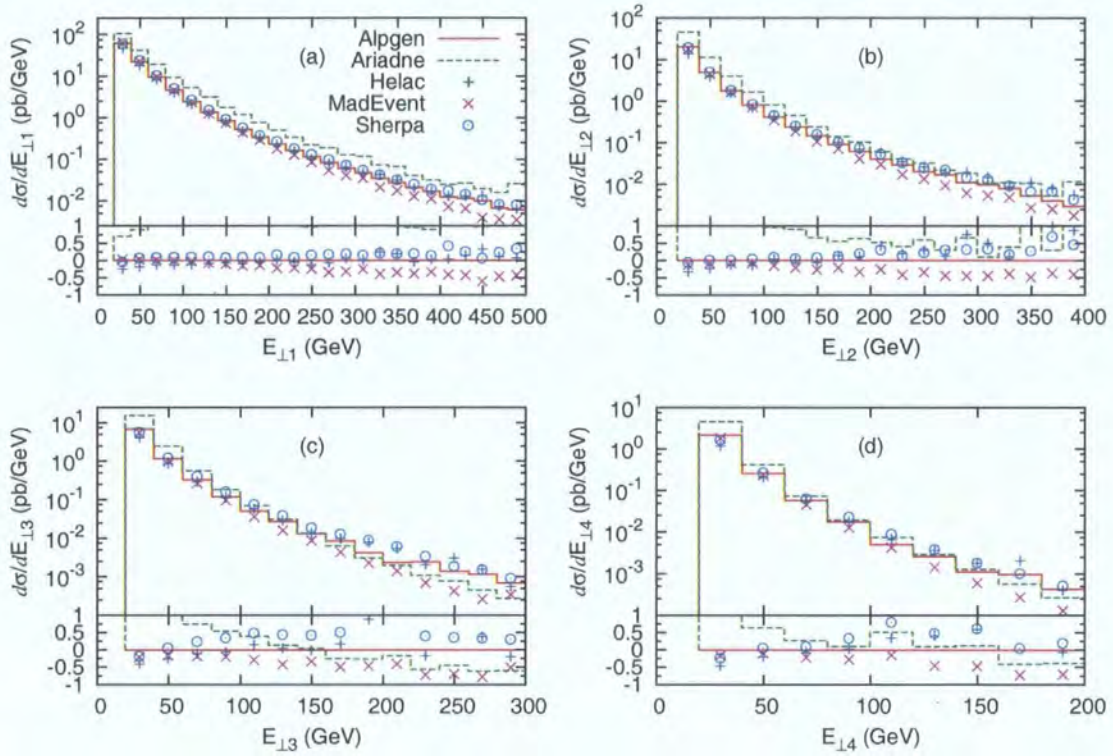

Fig. 4.8 Inclusive $E_\perp$ spectra of the leading 4 jets at the LHC (pb/GeV). In all cases the full line gives the ALPGEN results, the dashed line gives the ARIADNE results and the "+", "x" and "o" points give the HELAC, MADEVENT and SHERPA results respectively.

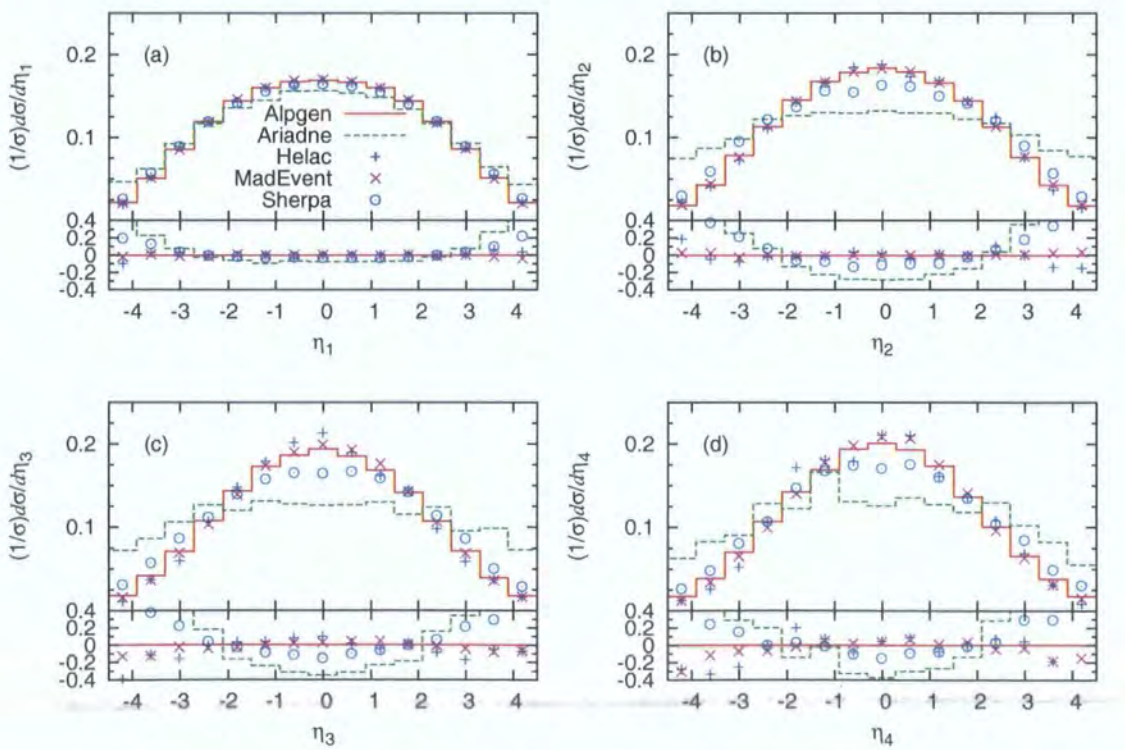

Fig. 4.9 Inclusive η spectra of the 4 leading jets at the LHC. All curves are normalised to unit area. Lines and points are as in Fig. 4.8.

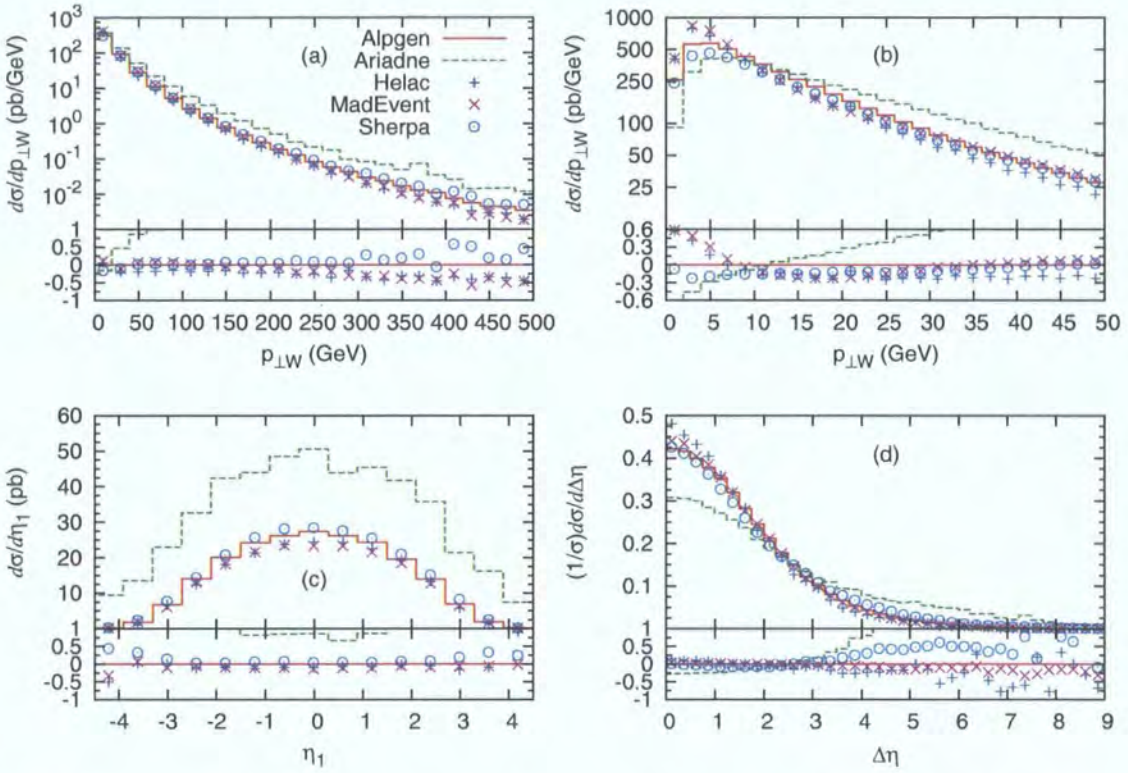

Fig. 4.10 (a) and (b) $p_\perp$ spectrum of W^+ bosons at the LHC (pb/GeV). (c) η spectrum of the leading jet, for $p_\perp^{\text{jet1}} > 100$ GeV; absolute normalisation (pb). (d) Pseudo-rapidity separation between the W^+ and the leading jet, $\Delta\eta = |\eta_{W^+} - \eta_{\text{jet1}}|$, for $p_\perp^{\text{jet1}} > 40$ GeV, normalised to unit area. Lines and points are as in Fig. 4.8.

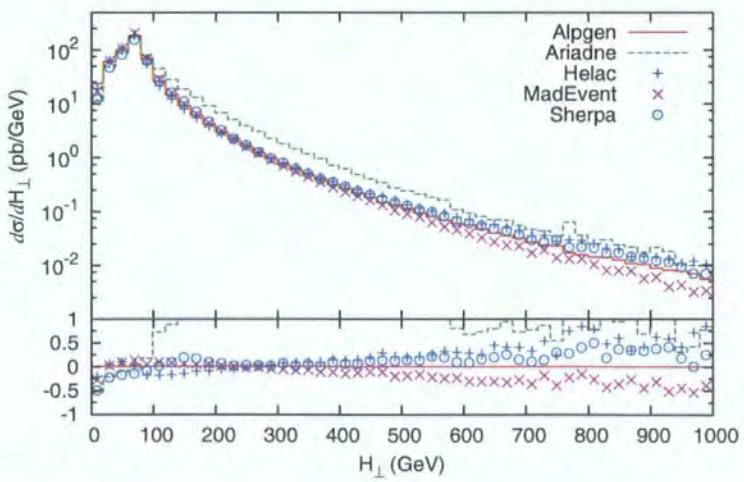

Fig. 4.11 The scalar sum of the transverse momentum of the charged lepton, the neutrino and the jets at the LHC. Lines and points are as in Fig. 4.8.

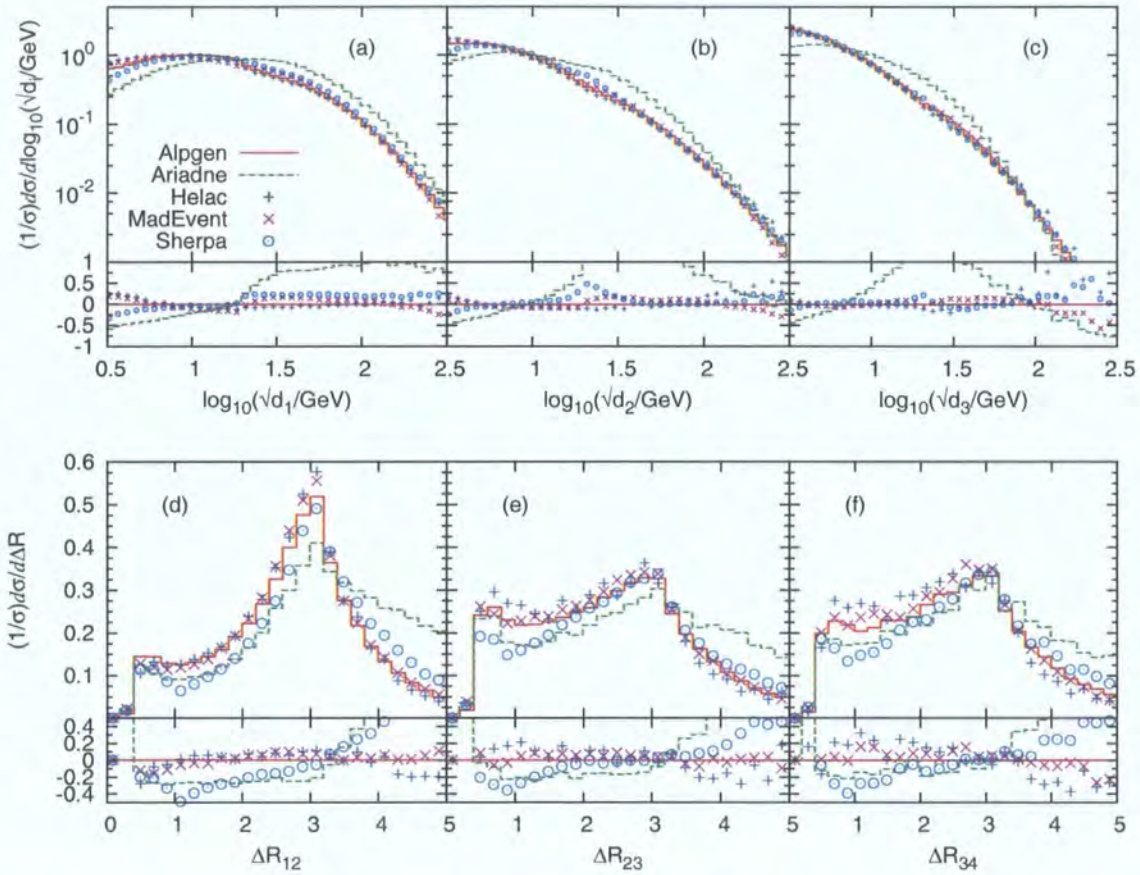

Fig. 4.12 (a)–(c) d_i ($i = 1, 2, 3$) spectra, where d_i is the scale in a parton-level event where i jets are clustered into $i-1$ jets using the $k_\perp$-algorithm. (d)–(f) ΔR separations at the LHC between jet 1 and 2, 2 and 3, and 3 and 4. All curves are normalised to unit area. Lines and points are as in Fig. 4.8.

The scalar transverse momentum sum in Fig. 4.11 shows significantly larger deviations as compared to the results for the Tevatron. ARIADNE has a much harder spectra than the other codes, while SHERPA and HELAC are slightly harder than ALPGEN and MADEVENT is significantly softer. As in the Tevatron case, it is a direct reflection of the differences in the hardness of the jet and $p_{\perp W}$ spectra, although the increased phase space for jet production at the LHC makes the $p_{\perp W}$ contribution less important at high $H_\perp$ values.

4.5 Summary of findings

This chapter summarises the comparisons of five independent approaches to the problem of merging matrix elements and parton showers. The codes under study, ALPGEN, ARIADNE,

HELAC, MADEVENT and SHERPA, differ in which matrix-element generator is used, which merging scheme (CKKW or MLM) is used and the details in the implementation of these schemes, as well as in which parton shower is used.

It is found that, while the three approaches (CKKW, L, and MLM) aim at a simulation based on the same idea, namely describing jet production and evolution by matrix elements and the parton shower, respectively, the corresponding algorithms are quite different. The main differences can be found in the way in which the combination of Sudakov reweighting of the matrix elements interacts with the vetoing of unwanted jet production inside the parton shower. This makes it very hard to compare those approaches analytically and to formalise the respective level of their logarithmic dependence. In addition, the different showering schemes used by the different methods blur the picture further. For instance virtuality ordering with explicit angular vetoes is used in SHERPA as well as in the HELAC and MADEVENT approach, both of which employ PYTHIA to do the showering, $p_\perp$ordering is the characteristic feature of ARIADNE, and, through its usage of HERWIG it is angular ordering that enters into the ALPGEN merging approach. However, although the formal level of agreement between the codes is not worked out, the results show a reasonably good agreement. This proves that the variety of methods for merging matrix elements and parton showers can be employed with some confidence in vector boson plus jet production.

The comparison also points to differences, in absolute rates as well as in the shape of individual distributions, which underline the existence of an underlying systematic uncertainty. Most of these differences are at a level that can be expected from merging tree-level matrix elements with leading-log parton showers, in the sense that they are smaller than, or of the order of, differences found by making a standard change of scale in α_s. In most cases the differences within each code are as large as the differences between the codes. And as the systematics at the Tevatron is similar to that at the LHC, it is conceivable that all the codes can be tuned to Tevatron data to give consistent predictions for the LHC.

5 Multi-jet events in the k_T factorisation scheme

Hard scattering at hadron colliders is usually described in the framework of collinear factorisation. As explained in Chapter 1, the full scattering amplitude is factorised into a hard perturbative parton scattering matrix element and process-independent universal parton distributions. In this factorisation scheme, all initial state partons are on-shell and have zero transverse momenta. An alternative approach is the framework of $k_\perp$- or high-energy factorisation. There, unintegrated PDFs (UPDFs) are convoluted with off-shell matrix elements. The PDFs are unintegrated in terms of the initial partons' $k_\perp$. Initially, $k_\perp$-factorisation has been formulated for heavy quark production [136]. The approach has been further investigated in other channels, see for instance Refs. [137]. The $k_\perp$-factorisation scheme has apparent advantages over conventional collinear factorisation: First, in the high-energy limit, i.e. for $t \ll s$ with s being large, the QCD cross section for jet production is dominated by gluon exchange diagrams, which diverge in this limit. The divergence is alleviated or even removed by realising that the $1/t$ terms in the matrix element can be identified with divergences of the form $1/k_\perp^2$ and thus using a suitable form of unintegrated PDFs, vanishing fast enough for $k_\perp \to 0$. Second, employing UPDFs means including the leading logarithmic contribution of higher order corrections to a given process, since the effect of additional QCD radiation is encoded in them [138, 139].

Taking the high-energy limit in a given process is equivalent to the Balitsky-Fadin-Kuraev-Lipatov (BFKL) limit [140], which builds on t-channel dominance of scattering cross sections and the reggeisation of t-channel gluons [141], cf. Sec. 5.1. In the past, there have been

various approaches, aiming at a solution of the BFKL dynamics with Monte Carlo methods and thus producing exclusive final states. An approximation, aiming at a correct description of essential features of the BFKL equation and a correct extrapolation to the DGLAP regime, has been proposed in the linked dipole chain model [142]. This model has been implemented in Ref. [143]. The scope of the approach is closely related to the Catani-Ciafaloni-Fiorani-Marchesini (CCFM) equation [144] Event generators based on this evolution equation have been presented in [145]. An iterative solution of the pure BFKL equation has been proposed in [146], iterative Monte Carlo solutions in [147, 148]. Later on, this prescription has been extended to next-to-leading logarithmic accuracy [149, 150].

In this chapter, a different implementation of $k_\perp$-factorisation for the case of multi-jet production is discussed. Emphasis is put on finding a gauge invariant form of the corresponding expressions and on identifying their matching to unintegrated PDFs derived from conventional collinear ones through the Kimber-Martin-Ryskin-Watt (KMRW) procedure presented in Refs. [151, 152]. It turns out that this in fact can be achieved by working in the high-energy limit, using as basic building blocks splitting functions in the limit $z \to 0$,[1] in conjunction with a proper reggeisation of all t-channel propagators as introduced in Sec. 5.1. Since four-momentum conservation can explicitly be imposed in a Monte Carlo solution, this approach clearly includes effects beyond the naive leading order BFKL limit, cf. Refs. [153, 154, 150], Furthermore, identifying the probabilistic interpretation of each emission in the high-energy limit, the Monte Carlo solution has for the first time been implemented as a Markovian approach, similar to conventional parton shower event generators. This enables generation of an a priori arbitrary number of emissions, which is important at high energies, where corrections due to large final state multiplicities are sizable.

This chapter is organised as follows. Section 5.1 briefly recalls the basics of high-energy parton evolution and the resulting BFKL equation. In Sec. 5.2 the KMRW procedure of Refs. [151, 152, 155] to generate doubly unintegrated PDFs (DUPDFs) and the corresponding angular ordering constraints are reviewed. In Sec. 5.3 it is then shown that the leading $\ln(1/x)$ terms are correctly taken into account when combining the two prescriptions. Section 5.4 contains the description of the Markovian Monte Carlo procedure to generate event

[1] In addition to the pure gluonic ladders of the high-energy limit, here also vertices for quark production are included.

topologies with an a priori undetermined number of final state partons. In Sec. 5.6 first results are presented.

5.1 The reggeised gluon

A particle of mass m and spin J is said to reggeise, if the amplitude $\mathcal{A}$ for the exchange of the quantum numbers of that particle in the t-channel behaves asymptotically in s, i.e. for $s \to \infty$, t fixed, like [156, 157]

$$\mathcal{A}(s,t) \propto s^{\alpha(t)} . \tag{5.1}$$

Here, $\alpha(t)$ is called the Regge trajectory of this particle. The basic idea for reggeisation [158] is inspired by non-relativistic quantum mechanics, where bound states of a spherically symmetric potential can be characterised in the partial wave expansion. Associated partial wave amplitudes are essentially proportional to the Legendre polynomials, which, in the high-energy limit, induce a behaviour of $\mathcal{A}$ as given by Eq. (5.1). The advantage of this formalism is evident. No assumptions have to be made about the underlying theory, instead the behaviour of the full scattering amplitude in any given process can be fitted to obtain the corresponding $\alpha(t)$. This has been done for example in Ref. [159], where the total proton-proton and other hadronic cross sections were parametrised using Regge theory.
The optical theorem implies that the total cross section for a process which is dominated by the leading Regge trajectory $\alpha(t)$ with intercept $\alpha(0)$ satisfies

$$\sigma_{tot} \propto s^{\alpha(0)-1} . \tag{5.2}$$

It was proved in Refs. [160] that in any scattering process with exchange of charges the total cross section must vanish asymptotically as s increases. This is called the Pomeranchuk theorem [161]. Conversely, it was shown in Ref. [162] that if the cross section does not fall as s increases, the scattering must be dominated by the exchange of vacuum quantum numbers. At present, there is no evidence that QCD cross sections decrease for large s. On the contrary, a slow rise has been observed experimentally. Thus, if single Reggeon exchange causes this rise, the corresponding Regge trajectory must have an intercept of

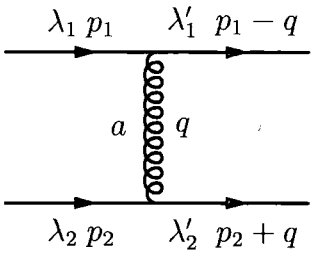

Fig. 5.1 Leading order amplitude for quark quark scattering into two quarks at $|t| \ll s$.

$\alpha(0) > 1$ and the corresponding Reggeon must carry the quantum numbers of the vacuum. This trajectory, $\alpha_P(t)$, is called the Pomeron. Particles which would provide the resonances at integer values of $\alpha_P(t)$ have not yet been identified. However they might exist as bound states of gluons and it is natural to try and establish a relation between QCD and Regge theory.

A number of authors showed that the QCD gluon reggeises to all orders in perturbation theory, which implies large logarithmic contributions of the form $\log(s/|t|)^\epsilon$ to the cross section. These terms can be resummed to all orders, leading to a recursive equation for t channel gluon emission, known as the BFKL equation. It is connected to the analytic properties of this equation, that it has been seen in the strict high–energy limit, $|t| \ll s$, for a long time. It has therefore not lead to many reliable predictions of observable QCD final states. As was discussed for example in [153, 154, 150], the implementation of four-momentum conservation and running α_s effects strongly modifies naive leading order BFKL predictions. In Refs. [147, 148] it was shown that the BFKL equation can be implemented in a Monte Carlo fashion, thus allowing to conserve energy and momentum in each step of the recursion. This procedure yields a significant improvement over the old approaches. In the following section, the arguments of Fadin, Kuraev and Lipatov [140] will briefly be recalled to introduce the basic formalism, before the method presented in Refs. [147,148] is outlined.

Eikonal couplings and the Lipatov effective vertex

Consider the scattering of two quarks of different flavour due to a colour-octet exchange in the t–channel and let $m_i^2, |t| \ll s$. According to the Feynman rules given in [87] the upper part of the leading order amplitude depicted in Fig. 5.1 is given by

$$-ig_s\bar{u}(\lambda_1{}', p_1 - q)\,\gamma^\mu\,u(\lambda_1, p_1)\,T^a_{ij}\,, \tag{5.3}$$

where the λ's denote helicities, p are momenta and T is a generator of the colour group in the fundamental representation. In the relevant high-energy limit, all components of the exchanged momentum q are small because $|q^2| = |t|$ and $(p_1 - q)^2 = (p_2 + q)^2 = 0$. The upper part of the amplitude can then be replaced with $-ig_s\bar{u}(\lambda_1{}', p_1)\,\gamma^\mu\,u(\lambda_1, p_1)\,T^a_{ij}$. This translates into an eikonal coupling to the fermion line,

$$-2ig_s\;p_1^\mu\,\delta_{\lambda_1{}'\lambda_1}\,T^a_{ij}\,. \tag{5.4}$$

The eikonal approximation is valid whenever the gauge particle exchange is "soft", more precisely, for all components of the exchanged momenta being small compared to those of the emitting particle. This eikonal structure of the coupling generalises also to theories with scalars and even the gauge particle itself. It is closely related to the soft gluon limit discussed for example in Sec. 1.3. If the quarks in Fig. 5.1 are replaced with gluons, one obtains

$$g_s\,f^{abc}\,[\,(2p_1 - q)^\rho g^{\mu\nu} + (p_1 - 2q)^\mu g^{\nu\rho} - (q + p_1)^\nu g^{\rho\mu}\,]\,. \tag{5.5}$$

Provided that the incoming and outgoing gauge particles are on–shell and therefore have transverse polarisations only, this translates into the eikonal coupling

$$2g_s\,p_1^\rho\,g^{\mu\nu}\,f^a_{bc}\,, \tag{5.6}$$

Finally the amplitude for quark-quark scattering into two quarks due to colour-octet exchange at lowest order becomes

$$\mathcal{A}_0^{(8)} \;=\; g_s^2\,2p_1^\mu\,\frac{g_{\mu\nu}}{q^2}\,2p_2^\nu\,\delta_{\lambda_1{}'\lambda_1}\delta_{\lambda_2{}'\lambda_2}G_0^{(8)} \;=\; 8\pi\alpha_s\,\frac{s}{t}\,\delta_{\lambda_1{}'\lambda_1}\delta_{\lambda_2{}'\lambda_2}G_0^{(8)}\,. \tag{5.7}$$

The term $G_0^{(8)}$ denotes the colour factor $T^a_{ij}T^a_{kl}$ related to colour-octet exchange. In covariant gauges there are no self–energy or vertex corrections which contribute to the amplitude in the Regge limit. The first corrections arise from box and crossed box diagrams, where both contributions can be related through crossing relations. It turns out to be convenient to

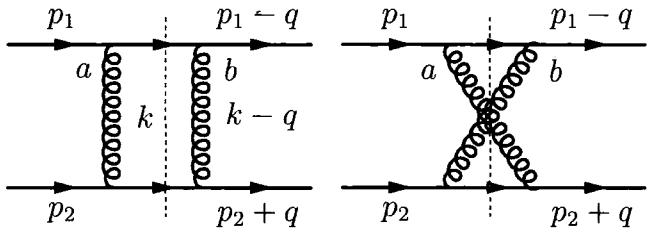

Fig. 5.2 Box and crossed box diagram for quark-quark scattering. The convention is such that momenta to the left of the cut are oriented downwards, while momenta to the right of the cut direct upwards.

decompose such amplitudes into two parts as depicted in Fig. 5.2 and to use the Cutkosky rules to obtain the full result. Furthermore, it proves useful to rewrite the corresponding phase space integration as an integration in t–channel momenta k. These momenta are then decomposed into Sudakov parameters α and β, defined through

$$k = \alpha p_1 + \beta p_2 + k_\perp \,, \tag{5.8}$$

such that the phase space integral over intermediate states becomes

$$\begin{aligned} \int \mathrm{d}\Phi^{(1)} &= \frac{1}{(2\pi)^2} \int \mathrm{d}^4k\, \delta((p_1 - k)^2)\, \delta((p_2 - k)^2) \\ &= \frac{s}{8\pi^2} \int \mathrm{d}\alpha\, \mathrm{d}\beta\, \mathrm{d}^2\mathrm{k}_\perp \delta(-\beta(1-\alpha)s - \mathrm{k}_\perp^2)\, \delta(\alpha(1+\beta)s - \mathrm{k}_\perp^2) \,. \end{aligned} \tag{5.9}$$

Since all components of the momentum q exchanged in the t–channel are small compared to s and all are of the same order, the virtuality of q is dominated by its transverse component, i.e. $t = q^2 \approx -\mathrm{q}_\perp^2$. The transverse momentum $\mathrm{k}_\perp$ will then, on average, also be of the order of $\sqrt{|t|}$. The delta functions in the phase space integral lead to $\beta = -\alpha$ and $|\beta| = \alpha \approx \mathrm{k}_\perp^2/s \ll 1$. Hence

$$k^2 \approx -\,\mathrm{k}_\perp^2 \,, \qquad \text{and} \qquad (k-q)^2 \approx -\,(\mathrm{k}-\mathrm{q})_\perp^2 \,. \tag{5.10}$$

Absorbing the delta functions into the integration over k_0 and k_3 yields

$$\mathfrak{Im}\,\mathcal{A}_1^{(8)} = 8\pi\alpha_s \frac{s}{t}\, \delta_{\lambda_1'\lambda_1} \delta_{\lambda_2'\lambda_2}\, G_{1,a}^{(8)}\, \frac{\alpha_s}{2\pi} \int \mathrm{d}^2\mathrm{k}_\perp \frac{t}{\mathrm{k}_\perp^2 (\mathrm{k}-\mathrm{q})_\perp^2} \,, \tag{5.11}$$

where $G^{(8)}_{1,a}$ is the associated colour factor of the uncrossed box. Using the analytic continuation of the logarithm, $\log(x) = \log(|x|) - i\pi\,,\ \forall\ x < 0$ this implies that the real part of the amplitude reads

$$\mathfrak{Re}\,\mathcal{A}_1^{(8)} = -\,8\pi\alpha_s\frac{s}{t}\,\delta_{\lambda_1'\lambda_1}\delta_{\lambda_2'\lambda_2}\,G^{(8)}_{1,a}\,\log\left(\frac{s}{\mathrm{k}_\perp^2}\right)\frac{\alpha_s}{2\pi^2}\int \mathrm{d}^2\mathrm{k}_\perp\,\frac{t}{\mathrm{k}_\perp^2(\mathrm{k}-\mathrm{q})_\perp^2}\,. \tag{5.12}$$

The complete one–loop amplitude for colour octet exchange is the sum of uncrossed and crossed boxes

$$\mathcal{A}_1^{(8)} = \mathcal{A}_0^{(8)}\,\epsilon(t)\,\log\left(\frac{s}{\mathrm{k}_\perp^2}\right)\,, \tag{5.13}$$

where

$$\epsilon(t) = \frac{N_C\alpha_s}{4\pi^2}\int \mathrm{d}^2\mathrm{k}_\perp\,\frac{t}{\mathrm{k}_\perp^2(\mathrm{k}-\mathrm{q})_\perp^2}\,. \tag{5.14}$$

Obviously $\epsilon(t)$ is infrared divergent. The corresponding singularity is naively lifted by the fact that external partons are never on–shell but typically have a virtuality of $\mathrm{k}_\perp^2 \approx \Lambda^2_{\mathrm{QCD}}$ arising from a primordial $\mathrm{k}_\perp$ distribution inside the parent hadron.[2]

To arrive at the order α_s^2–correction to the quark-quark scattering shown in Fig. 5.1, all possible combinations of the cut graphs shown in figure 5.3 must be taken into account. This time both, k_1 and k_2 are decomposed according to Eq. (5.8). The leading logarithmic contribution stems from the region where the Sudakov parameters obey a strong ordering

$$\begin{aligned} \alpha_2 &\ll \alpha_1 \ll 1 \\ |\beta_1| &\ll |\beta_2| \ll 1\,. \end{aligned} \tag{5.15}$$

The on–shell condition for the emitted gluon yields

$$\alpha_1\beta_2 s = -(\mathrm{k}_1 - \mathrm{k}_2)_\perp^2, \tag{5.16}$$

such that $k_1^2 \approx -\mathrm{k}_{1\perp}^2$ and $k_2^2 \approx -\mathrm{k}_{2\perp}^2$. The squared transverse momenta $\mathrm{k}_{1\perp}^2$ and $\mathrm{k}_{2\perp}^2$ are hence both of the same order. In this limit, the Lorentz structures of all diagrams in

[2]Fadin, Kuraev and Lipatov showed that it is also possible to obtain an infrared finite integral by spontaneously breaking the gauge group symmetry [140].

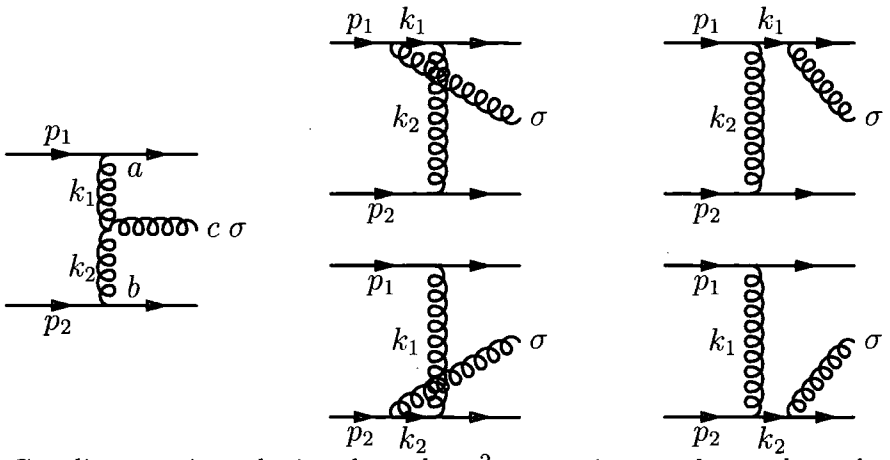

Fig. 5.3 Cut diagrams introducing the order α_s^2–corrections to the total quark quark scattering amplitude.

Fig. 5.3 may be combined to form an effective non–local vertex, called the Lipatov effective vertex [141]

$$\Gamma^{\sigma}_{\mu\nu}(k_1,k_2) = \frac{2p_{2\mu}p_{1\nu}}{s}\left[\left(\alpha_1+\frac{2\mathrm{k}_{1\perp}^2}{\beta_2 s}\right)p_1^{\sigma}+\left(\beta_2+\frac{2\mathrm{k}_{2\perp}^2}{\alpha_1 s}\right)p_2^{\sigma}-(k_1+k_2)^{\sigma}_{\perp}\right] . \tag{5.17}$$

In terms of this vertex the amplitude for the cut diagram becomes

$$\mathcal{A}_2^{(8)\sigma} = -\frac{2ig^3\,2p_1^{\mu}p_2^{\nu}}{\mathrm{k}_{1\perp}^2\mathrm{k}_{2\perp}^2}\,\delta_{\lambda_1'\lambda_1}\delta_{\lambda_2'\lambda_2}\,f_{abc}\,T^a\otimes T^b\,\Gamma^{\sigma}_{\mu\nu}(k_1,k_2) . \tag{5.18}$$

Although this result has been obtained working in Feynman gauge, the Lipatov vertex is gauge invariant. It can be employed for any t channel emission in bigger diagrams, such that the result for multiple t channel gluon exchange reads

$$\mathcal{A}_{n+2}^{(8)\sigma_1\ldots\sigma_n} = i2sg^{n+2}\,\delta_{\lambda_1'\lambda_1}\delta_{\lambda_2'\lambda_2}\,G_n^{(8)}\,\frac{i}{\mathrm{k}_{1\perp}^2}\prod_{i=1}^{n}\left\{\frac{2p_1^{\mu_i}p_2^{\nu_i}}{s}\,\frac{i}{\mathrm{k}_{i+1\perp}^2}\,\Gamma^{\sigma_i}_{\mu_i\nu_i}(k_i,k_{i+1})\right\} . \tag{5.19}$$

A remarkable observation was made in Ref. [163], where the equivalence of MHV amplitudes and BFKL amplitudes in the high–energy limit is proved. The corresponding analysis leads to a very compact form of the Lipatov vertex and corresponding amplitudes $\mathcal{A}_{n+2}^{(8)}$.

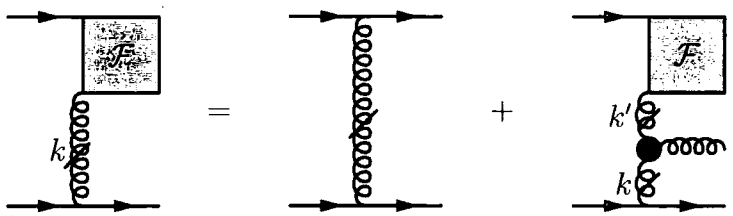

Fig. 5.4 Pictorial representation of the recursion relation for $\mathcal{F}^{(R)}$. Dashes on vertical gluon lines denote the reggeisation of the corresponding particle. In the second term on the right hand side an integration over the internal momentum k' is understood.

The BFKL equation

To determine the integrated n-gluon exchange amplitude, an iterative procedure can be applied. At each step of the iteration, the amplitude has the form of a t channel tree-amplitude with effective vertices and t channel propagators corresponding to reggeised gluons. Such a gluon propagator is given by

$$\tilde{D}_{\mu\nu}(s_i, k_i^2) = \frac{i g_{\mu\nu}}{\mathrm{k}_{i\perp}^2} \left(\frac{s_i}{\mathrm{k}_{i\perp}^2}\right)^{\epsilon(k_i^2)} . \tag{5.20}$$

where $\epsilon(k_i^2)$ is determined from Eq. (5.14). For further analyses, it is convenient to define the Mellin transform $f^{(R)}$ through

$$f^{(R)}(w,t) = \int_1^\infty \mathrm{d}\left(\frac{s}{|t|}\right) \left(\frac{s}{|t|}\right)^{-w-1} \frac{\mathfrak{Im}\mathcal{A}^{(R)}(s,t)}{s} . \tag{5.21}$$

The leading order process can be extracted using the definition

$$f^{(R)}(w,t) = (4\pi\alpha_s)^2 \, G^{(R)} \int \frac{\mathrm{d}^2\mathrm{k}_\perp}{(2\pi)^2} \frac{\mathcal{F}^{(R)}(w, \mathrm{k}_\perp, \mathrm{q}_\perp)}{\mathrm{k}_\perp^2 (\mathrm{k}-\mathrm{q})_\perp^2} , \tag{5.22}$$

and investigating $\mathcal{F}^{(R)}$ instead of $f^{(R)}$. Indices (R) stand for either colour octet or colour singlet exchange. Correspondingly

$$G^{(8)} = -\frac{N_C}{8} \qquad \text{and} \qquad G^{(1)} = \frac{N_C^2 - 1}{4N_C} . \tag{5.23}$$

The function $\mathcal{F}^{(R)}$ fulfils the recursion schematically depicted in Fig. 5.4. The first term on the right hand side describes the exchange of a single gluon on either side of the cut. The

second term gives the contribution from the addition of one more gluon, exchanged in the t channel, which couples to the ladder rungs through effective vertices.

$$\begin{aligned}\left[w-\epsilon(k^2)-\epsilon((k-q)^2)\right]\,\mathcal{F}^{(R)}(w,\mathrm{k}_\perp,\mathrm{q}_\perp)\\ =\;1-\frac{\alpha_s\,\eta^{(R)}}{8\pi^2}\int\frac{\mathrm{d}^2\mathrm{k}'_\perp}{\mathrm{k}'^2_\perp(\mathrm{k}'-\mathrm{q})^2_\perp}\,K(\mathrm{q}_\perp,\mathrm{k}_\perp,\mathrm{k}'_\perp)\,\mathcal{F}^{(R)}(w,\mathrm{k}'_\perp,\mathrm{q}_\perp)\;.\end{aligned}\tag{5.24}$$

Here $\eta^{(8)}=4N_C$, while $\eta^{(1)}=2N_C$. The BFKL evolution kernel $K(\mathrm{q}_\perp,\mathrm{k}_\perp,\mathrm{k}'_\perp)$ is given by

$$K(\mathrm{q}_\perp,\mathrm{k}_\perp,\mathrm{k}'_\perp)\;=\;\mathrm{q}^2_\perp-\frac{\mathrm{k}^2_\perp(\mathrm{k}'-\mathrm{q})^2_\perp+\mathrm{k}'^2_\perp(\mathrm{k}-\mathrm{q})^2_\perp}{(\mathrm{k}-\mathrm{k}')^2_\perp}\;.\tag{5.25}$$

It corresponds to the contraction of the two Lipatov vertices connecting k and k' on either side of the cut. For colour octet exchange, the solution to Eq. (5.24) reads

$$\mathcal{F}^{(8)}(w,\mathrm{q}_\perp)\;=\;\frac{1}{w-\epsilon(-\mathrm{q}^2_\perp)}\;,\tag{5.26}$$

which gives

$$\mathfrak{Im}\mathcal{A}^{(8)}(s,t)\;=\;2\pi^2\alpha_s\,\epsilon(t)\left(\frac{s}{|t|}\right)^{1+\epsilon(t)}\;.\tag{5.27}$$

The analytic continuation yields an intercept of the reggeised gluon trajectory of $\alpha_G(t)=1+\epsilon(t)$. Its numerical value does however not agree with that of the Pomeron as deduced from total hadronic cross sections, which indicates the need for higher order corrections.

Colour singlet exchange and cut ladders

Equation (5.24) can be employed for a different type of analysis. Consider colour singlet exchange for $q=0$. This corresponds to the situation where the outgoing partons on the right hand side carry exactly the same quantum numbers as the incoming ones and have exactly the same momenta. The imaginary part of the amplitude with n intermediate rungs then corresponds to the full matrix element squared for the scattering of the incoming

partons into $2+n$ real final states. In this case, Eq. (5.24) can be rewritten as

$$w\,F(w,\mathrm{k}_\perp,\mathrm{k}'_\perp) = \delta(\mathrm{k}_\perp-\mathrm{k}'_\perp)+\frac{\alpha_s\,N_C}{\pi^2}\int\frac{\mathrm{d}^2\mathrm{k}_\perp}{(\mathrm{k}-\mathrm{k}')^2_\perp} \times\left[\,F(w,\mathrm{k}_\perp,\mathrm{k}'_\perp)-\frac{\mathrm{k}^2_\perp}{\mathrm{k}'^2_\perp+(\mathrm{k}-\mathrm{k}')^2_\perp}\,F(w,\mathrm{k}_\perp,\mathrm{k}'_\perp)\,\right]. \tag{5.28}$$

where F is related to $\mathcal{F}^{(1)}$ by

$$\mathcal{F}^{(1)}(w,\mathrm{k}_\perp,\mathrm{q}_\perp) = \int\frac{\mathrm{d}^2\mathrm{k}'_\perp}{\mathrm{k}'^2_\perp}\,\mathrm{k}^2_\perp\,F(w,\mathrm{k}_\perp,\mathrm{k}'_\perp,\mathrm{q}_\perp)\,. \tag{5.29}$$

The inverse Mellin transform of Eq. (5.28) can be cast into an integro-differential equation in rapidity and transverse momentum using the on-shell condition of ladder rungs in multi Regge kinematics, $\delta\,(\alpha_i s-\mathrm{k}^2_\perp)$.

$$\frac{\mathrm{d}F(\Delta y,\mathrm{k}_\perp,\mathrm{k}'_\perp)}{\mathrm{d}\Delta y} = \frac{\alpha_s\,N_C}{\pi^2}\int\frac{\mathrm{d}^2\mathrm{k}_\perp}{(\mathrm{k}-\mathrm{k}')^2_\perp} \times\left[\,F(w,\mathrm{k}_\perp,\mathrm{k}'_\perp)-\frac{\mathrm{k}^2_\perp}{\mathrm{k}'^2_\perp+(\mathrm{k}-\mathrm{k}')^2_\perp}\,F(w,\mathrm{k}_\perp,\mathrm{k}'_\perp)\,\right]. \tag{5.30}$$

The rapidity difference Δy corresponds to the interval spanned by the s-channel partons initiating the t-channels k and k'. It was proved in Refs. [146, 147], that Eq. (5.30) can be cast into the more suitable form

$$F(\Delta y,\mathrm{k}_\perp,\mathrm{k}'_\perp) = \sum_{n=1}^{\infty}F_n(\Delta y,\mathrm{k}_\perp,\mathrm{k}'_\perp)\,. \tag{5.31}$$

The n-emission part of the kernel is hereby defined through

$$F_n\,(\Delta y,\,\mathrm{k}_\perp,\,\mathrm{k}'_\perp) = \exp\left\{-\frac{\alpha_s\,N_C}{\pi}\,\ln\frac{\mathrm{q}^2_{0\perp}}{\mu^2_0}\Delta y_0\right\}\frac{1}{2}\delta\,(\mathrm{k}'_\perp+\mathrm{q}_{n\perp}) \times\int\prod_{i=1}^{n}\left[\frac{\alpha_s\,N_C}{\pi}\,\mathrm{d}y_i\frac{\mathrm{d}\mathrm{k}^2_{i\perp}}{\mathrm{k}^2_{i\perp}}\frac{\mathrm{d}\phi_i}{2\pi}\exp\left\{-\frac{\alpha_s\,N_C}{\pi}\,\ln\frac{\mathrm{q}^2_{i\perp}}{\mu^2_0}\Delta y_i\right\}\right], \tag{5.32}$$

where

$$\mathrm{q}_{i\perp} = \mathrm{k}_\perp+\sum_{j=1}^{i}\mathrm{k}_{i\perp}\,. \tag{5.33}$$

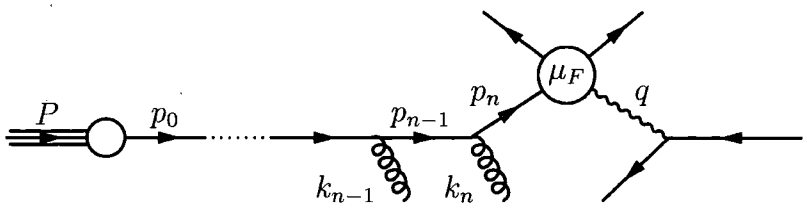

Fig. 5.5 Multiple gluon emission in deep inelastic lepton-nucleon scattering. The hard scattering process is characterised by the scale μ. Usually this scale is also employed as the factorisation scale.

The advantage of Eq. (5.31) over Eq. (5.30) becomes evident if one realises the similarity of the exponential term in Eq. (5.31) and the Sudakov form factor in Eq. (1.15). The basic idea is to generate an unconstrained cascade of independent parton branchings in the spirit of a parton shower to solve the leading order BFKL equation. Thus an arbitrary n-gluon final state can be generated without the need for explicit computation of a hard, perturbative cross section. The corresponding procedure has been presented in Ref. [164] and will be introduced in Sec. 5.4.

5.2 Unintegrated PDFs and the KMRW procedure

In this section, the KMRW procedure of constructing unintegrated PDFs from conventional DGLAP PDFs [151,152,155] is reviewed. Discussion and notation closely follow Refs. [152, 155].

In collinear factorisation, where the transverse momenta $\mathrm{k}_\perp$ of incoming partons are taken to be zero, the parton densities obey the DGLAP evolution equation [80,81], which determines the μ_F-dependence at fixed light-cone momenta. This evolution equation resums leading logarithmic parts of higher perturbative orders. In a Monte Carlo formulation, real emission corrections can be implemented as a Markov chain of $1 \to 2$ parton splittings [86,87,165]. However, a study of QCD beyond double leading logarithmic order reveals that quantum coherence effects suppress parton emissions in regions of phase space, where the emission angle of the emitted parton is larger than the opening angle of the emitting colour dipole [90]. To exemplify this, consider a parton evolution chain in the initial state of a DIS event, as depicted in Fig. 5.5. If angular ordering is fulfilled, the momenta k_i of the radiated partons will be distributed such that their angle θ_i with respect to the beam direction increases from

the incoming proton towards the hard scattering. To investigate the implications of this constraint, it is convenient to start with a Sudakov decomposition of the momenta [82],

$$p_i = x_i P + \tilde{\beta}_i q' - k_{i\perp} , \qquad k_i = \alpha_i P + \beta_i q' + k_{i\perp} , \tag{5.34}$$

where P is the proton momentum, q is the photon momentum and $q' = q + x_B P$, with x_B being the Bjørken x. In the high-energy limit, the proton mass can be neglected, $m_p^2 \ll Q^2 = -q^2$. Hence $q'^2 = 0$ and in the Breit frame the momenta read

$$\begin{aligned} P &= \frac{1}{2x_B}(Q, \mathbf{0}, Q) , \\ q' &= \frac{1}{2}(Q, \mathbf{0}, -Q) \quad \text{and} \\ k_{i\perp} &= (0, \mathbf{k}_{i\perp}, 0) . \end{aligned} \tag{5.35}$$

All emitted partons are on-shell, which allows to relate their Sudakov parameters through

$$\beta_i = (\tilde{\beta}_{i-1} - \tilde{\beta}_i) = \frac{z_i}{1 - z_i} \frac{\mathrm{k}_{i\perp}^2/Q^2}{x_i/x_B} , \tag{5.36}$$

where $z_i = x_i/x_{i-1}$. Imposing angular ordering for the emissions results in ordering of the corresponding rapidities y_i, since

$$y_i = \frac{1}{2} \ln \xi_i = -\ln \tan \frac{\theta_i}{2} , \tag{5.37}$$

where $\xi_i = k_i^+/k_i^- = \alpha_i/x_B\,\beta_i$ and θ_i is the angle of k_i with respect to the beam axis. According to Eq. (5.34)

$$\xi_i = \frac{x_i^2}{x_B^2} \left(\frac{1 - z_i}{z_i} \frac{Q}{\mathrm{k}_{i\perp}} \right)^2 = \frac{x_i^2}{x_B^2} \left(\frac{Q}{z_i \bar{\mathrm{k}}_i} \right)^2 , \tag{5.38}$$

where the rescaled transverse momentum $\bar{\mathrm{k}}_i = \mathrm{k}_{i\perp}/(1 - z_i)$ has been introduced. Hence angular ordering requirements yield the constraints

$$z_i \bar{\mathrm{k}}_i < \bar{\mathrm{k}}_{i+1} \quad \text{and} \quad z_n \bar{\mathrm{k}}_n < \bar{p} . \tag{5.39}$$

Here $\bar{p} = x_{n+1} Q \sqrt{\Xi}/x_B$ is the maximal rescaled transverse momentum which is fixed by

the hard process through $\Xi = (1+\tilde{\beta}_{n+1})/(x_{n+1}/x_B - 1)$. Typically, in an angular ordered evolution of the parton distributions, $\bar{p}$ plays the role of the factorisation scale μ_F [144]. The above ordering procedure can be generalised to hadron-hadron collisions. In this case, both incoming particles have a partonic substructure. In general, this leads to two separate factorisation scales, $\mu_F^{(1)}$ and $\mu_F^{(2)}$, for the two parton densities, respectively.

In [151, 152, 155] it has been shown that doubly unintegrated PDFs (DUPDFs) may be inferred from conventional DGLAP PDFs. In the following, DUPDFs will be denoted by $f_a(x, z, \mathrm{k}_\perp^2, \mu_F^2)$, while their conventional DGLAP counterpart will be denoted by $f_a(x, \mu_F^2)$. The DUPDFs must satisfy the normalisation condition

$$\int_x^1 \mathrm{d}z \int \frac{\mathrm{dk}_\perp^2}{\mathrm{k}_\perp^2} f_a(x, z, \mathrm{k}_\perp^2, \mu_F^2) \;=\; x\, f_a(x, \mu_F^2)\,. \tag{5.40}$$

Employing the Sudakov form factor[3]

$$\tilde{\Delta}_a(\mathrm{k}_\perp^2, \mu_F^2) \;=\; \exp\left\{ -\int_{\mathrm{k}_\perp^2}^{\mu_F^2} \frac{\mathrm{dk}'^2_\perp}{\mathrm{k}'^2_\perp} \frac{\alpha_s(\mathrm{k}'^2_\perp)}{2\pi} \frac{1}{2} \sum_b \int_0^1 \mathrm{d}\zeta\, \tilde{P}_{ab}(\zeta) \right\}\,, \tag{5.41}$$

with $\tilde{P}_{ab}(\zeta)$ denoting regularised DGLAP splitting functions for the splitting $a \to b$, a singly unintegrated parton distribution $\tilde{f}_a(x, \mathrm{k}_\perp^2, \mu_F^2)$ is obtained through

$$\tilde{f}_a(x, \mathrm{k}_\perp^2, \mu_F^2) = \frac{\partial}{\partial \ln \mathrm{k}_\perp^2} \left[x\, f_a(x, \mathrm{k}_\perp^2)\, \tilde{\Delta}_a(\mathrm{k}_\perp^2, \mu_F^2) \right]\,. \tag{5.42}$$

In the region $\mathrm{k}_\perp^2 > \mu_F^2$ this UPDF is set to zero. This procedure leaves some minimum $\mathrm{k}_\perp^2$-scale to be defined, below which DGLAP parton evolution is not valid. In the following, this scale will be denoted by μ_0^2. Relation (5.42) then holds only above μ_0^2, which yields the constraint

$$\int_0^{\mu_0^2} \frac{\mathrm{dk}_\perp^2}{\mathrm{k}_\perp^2} \tilde{f}_a(x, \mathrm{k}_\perp^2, \mu_F^2) \;=\; x\, f_a(x, \mu_0^2)\, \tilde{\Delta}_a(\mu_0^2, \mu_F^2) \tag{5.43}$$

on the singly unintegrated PDF. Whenever UPDFs, satisfying this normalisation condition, are applied in $\mathrm{k}_\perp$-factorisation, physical observables must be insensitive to details of the infrared behaviour of $\tilde{f}_a(x, \mathrm{k}_\perp^2, \mu_F^2)$, i.e. below μ_0^2.[4] Therefore, a choice can be made, for

[3] The factor of 1/2 in the sum over the parton species avoids double-counting s- and t-channel partons.

[4] It turns out that there is no need for an explicit form of the DUPDFs below μ_0^2, since the t-channel

example [155]

$$\tilde{f}_a(x,z,\mathrm{k}_\perp^2,\mu_F^2)\Big|_{\mu_F^2<\mu_0^2} = \frac{\mathrm{k}_\perp^2}{\mu_0^2}\left[A_a\left(x,z,\mu_F^2\right)+\frac{\mathrm{k}_\perp^2}{\mu_0^2}B_a\left(x,z,\mu_F^2\right)\right] \tag{5.44}$$

where

$$\begin{aligned} A_a\left(x,z,\mu_F^2\right) &= -\tilde{f}_a\left(x,z,\mu_0^2,\mu_F^2\right)+\frac{2x}{1-x}f_a(x,\mu_0^2)\,\tilde{\Delta}_a(\mu_0^2,\mu_F^2)\,, \\ B_a\left(x,z,\mu_F^2\right) &= 2\tilde{f}_a\left(x,z,\mu_0^2,\mu_F^2\right)-\frac{2x}{1-x}f_a(x,\mu_0^2)\,\tilde{\Delta}_a(\mu_0^2,\mu_F^2)\,. \end{aligned} \tag{5.45}$$

This choice implies that the UPDF vanishes with $\mathrm{k}_\perp^2$ for $\mathrm{k}_\perp \to 0$, as required by gauge invariance [166].

Instead of the regularised splitting functions $\tilde{P}_{ab}(z)$, unregularised splitting functions $P_{ab}(z)$ may safely be used here. This is because the splitting kernels are implicitly regularised by imposing the rapidity ordering constraint Eq. (5.39). Inserting corresponding Θ-functions in z results in the singly unintegrated quark and gluon distributions $f_q(x,\mathrm{k}_\perp^2,\mu_F^2)$ and $f_g(x,\mathrm{k}_\perp^2,\mu_F^2)$, respectively [152, 155]. The term singly unintegrated indicates that these PDFs depend on one additional variable w.r.t. the collinear ones. It is straightforward, however, to introduce an additional z-dependence by simply dropping the z-integration in Eq. (5.40). Such defining the DUPDF

$$\begin{aligned} f_a(x,z,\mathrm{k}_\perp^2,\mu_F^2) = \Delta_a(\mathrm{k}_\perp^2,\mu_F^2)\,\frac{\alpha_s(\mathrm{k}_\perp^2)}{2\pi}\sum_b P_{ba}(z)\,\frac{x}{z}\,f_b\left(\frac{x}{z},\mathrm{k}_\perp^2\right) \\ \times\left[(1-\delta_{ab})+\delta_{ab}\,\Theta\left(\frac{\mu_F}{\mu_F+\mathrm{k}_\perp}-z\right)\right] \end{aligned} \tag{5.46}$$

the desired relation, Eq. (5.40), is satisfied for both parton species. To guarantee the consistency of the approach, the conventional DGLAP PDF employed to obtain the DUPDFs should be determined using the leading order unregularised splitting kernels employed in Eq. (5.46). Furthermore, a consistent treatment of the running coupling α_s should be imposed.

parton chains contain a natural cutoff in $\mathrm{k}_\perp^2$, cf. [147], by imposing phase space cuts given by physical observables like mini-jets.

5.3 DUPDFs as impact factors for LL BFKL evolution

In this section it is proved that the DUPDFs defined above may be employed as impact factors in the calculation of multi-gluon cross sections in the high-energy limit. The argument works at leading logarithmic (LL) accuracy. The starting point is the integrated LL gluon branching probability $\Gamma_g^{(LL)} = -\log \Delta_g^{(LL)}$, which determines the behaviour of the DGLAP evolution of the gluon density.[5]

$$\Gamma_g^{(LL)}(\mu^2, \tilde{\mu}^2) = \Gamma_{gg}^{(LL)}(\mu^2, \tilde{\mu}^2) + \sum_q \Gamma_{gq}^{(LL)}(\mu^2, \tilde{\mu}^2) \,, \tag{5.47}$$

where

$$\Gamma_{ab}^{(LL)}(\mu^2, \tilde{\mu}^2) = \int_{\ln \mu^2}^{\ln \tilde{\mu}^2} \mathrm{d} \ln \mathrm{k}_\perp^2 \int_{\frac{\mathrm{k}_\perp}{\tilde{\mu}+\mathrm{k}_\perp}}^{\frac{\tilde{\mu}}{\tilde{\mu}+\mathrm{k}_\perp}} \mathrm{d}z \, \frac{\alpha_s}{2\pi} P_{ab}(z) \,, \tag{5.48}$$

with $P_{ab}(z)$ again denoting the unregularised DGLAP splitting kernels and the integration boundaries determined by angular ordering, cf. the Θ-function in Eq. (5.46). To simplify the discussion one firstly focuses on $\Gamma_{gg}^{(LL)}$ only. The corresponding part of the Sudakov form factor reads

$$\Delta_{gg}^{(LL)}(\mu^2, \tilde{\mu}^2) = \exp\left\{-\Gamma_{gg}^{(LL)}(\mu^2, \tilde{\mu}^2)\right\} \,. \tag{5.49}$$

Replacing the splitting variable z of the emitter parton by the rapidity y of the emission, which, according to Eq. (5.38) is given by

$$y = \frac{1}{2} \ln \xi = \ln\left(\frac{x}{x_B} \frac{Q}{\mathrm{k}_\perp}\right) - \ln \frac{z}{1-z} \tag{5.50}$$

results in

$$\begin{aligned} \Gamma_{gg}^{(LL)}(\mu^2, \tilde{\mu}^2) &= -\int_{\ln \mu^2}^{\ln \tilde{\mu}^2} \mathrm{d} \ln \mathrm{k}_\perp^2 \int_{y(z_{\max})}^{y(z_{\min})} \mathrm{d}y \, \frac{2C_A \left(1 - z(1-z)\right)^2}{P_{gg}(z)} \, \frac{\alpha_s}{2\pi} P_{gg}(z) \\ &= \int_{\ln \mu^2}^{\ln \tilde{\mu}^2} \mathrm{d} \ln \mathrm{k}_\perp^2 \int_{y(z_{\max})}^{y(z_{\min})} \mathrm{d}y \, \tilde{\alpha}_s \left(1 - z(1-z)\right)^2 , \end{aligned} \tag{5.51}$$

[5]The factor 1/2 contained in Eq. (5.41) must be cancelled here in order to restore the t/u-symmetry of the splitting process.

where $\tilde{\alpha}_s = \alpha_s C_A/\pi$. The term $z(1-z)$ in the numerator corresponds to helicity non-conserving configurations in the $1 \to 2$ parton splittings and thus in the impact factor [54]. These configurations are absent in the high-energy limit, which simplifies the integrand of Eq. (5.51), such that the part of the integrated LL gluon branching probability induced by $g \to gg$ splittings reads

$$\Gamma_{gg}^{(LL)}(\mu^2, \tilde{\mu}^2) = \int_{\ln \mu^2}^{\ln \tilde{\mu}^2} \mathrm{d} \ln \mathrm{k}_\perp^2 \int_{y(z_{\max})}^{y(z_{\min})} \mathrm{d}y \; \tilde{\alpha}_s \; . \tag{5.52}$$

Keeping in mind that $\tilde{\alpha}_s$ depends on transverse degrees of freedom only, performing the y-integration results in

$$\begin{aligned} \Gamma_{gg}^{(LL)}(\mu^2, \tilde{\mu}^2) &= \int_{\ln \mu^2}^{\ln \tilde{\mu}^2} \mathrm{d} \ln \mathrm{k}_\perp^2 \; \tilde{\alpha}_s \left\{ \ln\left(\frac{\tilde{\mu}}{\mathrm{k}_\perp} \frac{xQ}{x_B \mathrm{k}_\perp} \right) - \ln\left(\frac{\mathrm{k}_\perp}{\tilde{\mu}} \frac{xQ}{x_B \mathrm{k}_\perp} \right) \right\} \\ &= \frac{1}{2} \int_0^{\ln^2 \tilde{\mu}^2/\mu^2} \mathrm{d} \ln^2 \frac{\tilde{\mu}^2}{\mathrm{k}_\perp^2} \; \tilde{\alpha}_s \; . \end{aligned} \tag{5.53}$$

The order of integration in Eq. (5.52) may be changed,

$$\Gamma_{gg}^{(LL)}(\mu^2, \tilde{\mu}^2) = \int_y^{\tilde{y}} \mathrm{d}y' \int_0^{\ln \tilde{\mu}^2/\mu^2} \mathrm{d} \ln \frac{\tilde{\mu}^2}{\mathrm{k}_\perp^2} \; \tilde{\alpha}_s \, \Theta\left(\ln \tilde{\mu}^2/\mathrm{k}_\perp^2 + y - y' \right) \; , \tag{5.54}$$

where $\tilde{y} = \ln x/x_B + \ln Q/\tilde{\mu}$ and $\tilde{y} - y = \ln \tilde{\mu}^2/\mu^2$.

If the running coupling is treated identically, this result agrees with the reggeisation factor of the t-channel gluon propagator found in Eq. (5.32),

$$\begin{aligned} F_n\left(y_{ab}, \mathrm{p}_{a\perp}, \mathrm{p}_{b\perp}\right) = \int \prod_{i=1}^{n} \left[\bar{\alpha}_s \mathrm{d}y_i \frac{\mathrm{dk}_{i\perp}^2}{\mathrm{k}_{i\perp}^2} \frac{\mathrm{d}\phi_i}{2\pi} \exp\left\{ -\bar{\alpha}_s \ln \frac{\mathrm{q}_{i\perp}^2}{\mu_0^2} \Delta y_i \right\} \right] \\ \times \exp\left\{ -\bar{\alpha}_s \ln \frac{\mathrm{q}_{0\perp}^2}{\mu_0^2} \Delta y_0 \right\} \frac{1}{2} \delta\left(\mathrm{p}_{b\perp} + \mathrm{q}_{n\perp} \right) \; , \end{aligned} \tag{5.55}$$

where $\bar{\alpha}_s = \alpha_s C_A/\pi$ and $q_i = p_a - \sum_{j=1}^{i} k_j$. The exponential term in the square brackets is readily identified as

$$\bar{\Delta}(y, \tilde{y}) = \exp\left\{ -\bar{\Gamma}_g^{(LL)}(y, \tilde{y}) \right\} \; , \tag{5.56}$$

where

$$\bar{\Gamma}_g^{(LL)}(y,\tilde{y}) = \int_y^{\tilde{y}} \mathrm{d}y' \int_0^{\ln \mathrm{q}_\perp^2/\mu_0^2} \mathrm{d}\ln \frac{\mathrm{q}_\perp^2}{\mathrm{k}_\perp^2}\, \bar{\alpha}_s \;, \tag{5.57}$$

which is the desired result. It has been pointed out e.g. in [139] that the comparison with NLO BFKL calculations suggests the choice $\alpha_s = \alpha_s(\mathrm{k}_\perp^2)$, similar to the DGLAP case. Employing

$$\alpha_s(\mathrm{k}_\perp^2) = \frac{1}{\beta_0 \log \mathrm{k}_\perp^2/\Lambda^2} \;, \quad \text{where} \quad \beta_0 = \frac{11 - 2/3N_f}{4\pi} \;, \tag{5.58}$$

one then ends up with the result presented in Ref. [148],

$$\bar{\Gamma}_g^{(LL)}(y,\tilde{y}) = (\tilde{y} - y)\, \frac{C_A}{\pi\beta_0} \log\left(\frac{\alpha_s(\mu_0^2)}{\alpha_s(q_\perp^2)}\right) \;. \tag{5.59}$$

In numerical analyses, Λ is chosen consistent with the input PDF. Equation (5.55) can be used to construct the full LL BFKL kernel f through

$$f\,(y_{ab},\, \mathrm{p}_{a\perp},\, \mathrm{p}_{b\perp}) \;=\; \sum_{n=0}^{\infty} f^n\,(y_{ab},\, \mathrm{p}_{a\perp},\, \mathrm{p}_{b\perp}) \;. \tag{5.60}$$

Since rapidity ordering is trivially satisfied in the BFKL evolution, the explicit ordering requirement incorporated in the Θ-function of Eq. (5.54) may be dropped whenever $\bar{\Delta}(y,\tilde{y})$ is employed.

Following the same reasoning, $\Gamma_{gq}^{(LL)}$ is given by

$$\Gamma_{gq}^{(LL)}(\mu^2,\tilde{\mu}^2) \;=\; \int_{\ln\mu^2}^{\ln\tilde{\mu}^2} \mathrm{d}\ln \mathrm{k}_\perp^2 \int_{y(z_{\max})}^{y(z_{\min})} \mathrm{d}y\; \tilde{\alpha}_s \frac{T_R}{C_A} \frac{1}{2} z(1-z)\left(z^2 + (1-z)^2\right) \;. \tag{5.61}$$

In principle, this term vanishes in the high-energy limit due to the prefactor $z(1-z)$, thus allowing to identify $\bar{\Delta}(y,\tilde{y})$ with $\Delta_g^{(LL)}(\mu^2,\tilde{\mu}^2)$. However, it may be used to model quark production along the BFKL ladder, as will be discussed in Sec. 5.5.

Similar considerations may be applied to the integrated quark branching probability. Starting from the expression

$$\Gamma_q^{(LL)}(\mu^2,\tilde{\mu}^2) \;=\; \Gamma_{qg}^{(LL)}(\mu^2,\tilde{\mu}^2) + \Gamma_{qq}^{(LL)}(\mu^2,\tilde{\mu}^2)$$

and again replacing the splitting variable z by the rapidity y results in

$$\Gamma_{qg}^{(LL)}(\mu^2,\tilde{\mu}^2) = \int_{\ln\mu^2}^{\ln\tilde{\mu}^2} \mathrm{d}\ln \mathrm{k}_\perp^2 \int_{y(z_{\max})}^{y(z_{\min})} \mathrm{d}y\, \tilde{\alpha}_s \frac{C_F}{2C_A}\,(1-z)\left(1+(1-z)^2\right)\,. \tag{5.62}$$

By identifying $z=-t/s$, all factors $1-z$ become unity in the high-energy limit. Thus,

$$\Gamma_{qg}^{(LL)}(\mu^2,\tilde{\mu}^2) = \frac{C_F}{C_A}\,\Gamma_{gg}^{(LL)}(\mu^2,\tilde{\mu}^2)\,. \tag{5.63}$$

Simultaneously, due to the denominator part $(1-z)$ in $P_{qq}(z)$ quark production in the t-channel is suppressed, hence allowing to identify

$$\Gamma_{q}^{(LL)}(\mu^2,\tilde{\mu}^2) = \frac{C_F}{C_A}\,\Gamma_{g}^{(LL)}(\mu^2,\tilde{\mu}^2)\,. \tag{5.64}$$

However, $\Gamma_{qq}^{(LL)}(\mu^2,\tilde{\mu}^2)$ may be employed to model gluon emission from t-channel quark lines, as will be described in Sec. 5.5.

The above considerations show that to leading logarithmic accuracy the DUPDFs, Eq. (5.46), resemble all features of the BFKL evolution. Therefore, they can safely be employed as impact factors for the calculation of cross sections in the high-energy limit.

5.4 Markovian Monte Carlo solution of the ln(1/x)-evolution

The Markovian approach to the calculation of cross sections and differential distributions in the high-energy limit will be presented in this section. The advantage of the algorithm is that the number of emissions stays a priori undetermined, similar to the case of conventional parton showers employed to solve $\log(Q^2/\mu^2)$-evolution [86,87,165]. The factorisation of the radiation pattern into individual emissions, which depend on each other merely through the correct ordering, allows to model further physics effects involving the produced outgoing partons, like for instance adding final state radiation.

The basis of the formalism is encoded in Eq. (7) in Ref. [147] and Eq. (5.56). These equations translate into the probability for having an additional emission from the BFKL kernel being

approximately distributed according to the function

$$\gamma\left(1, \Gamma_g^{(LL)}(y_i, y_n)\right) = \Gamma_g^{(LL)}(y_i, y_n) \exp\left\{-\Gamma_g^{(LL)}(y_i, y_n)\right\} . \tag{5.65}$$

Here, y_i is the rapidity of the previous and y_n is the rapidity of the final emission. Such distributions may be generated employing the veto algorithm, described for example in Ref. [165]. It allows to simultaneously select the rapidity and transverse momentum of the new emission.[6] In the following, the superscripts $^{(LL)}$ will be dropped.

To determine the corresponding z-k$_\perp$-factorisation formula, the simplest case, a gluon ladder with no emission, is investigated. This corresponds to a "2 $\to$ 0 process" in the z-k$_\perp$-factorisation approach. When working in collinear factorisation rather than with the DUPDF prescription of Ref. [155], it is a 2 $\to$ 2 process. The corresponding phase space element can thus be determined by factorising the collinear matrix element and its phase space integral. The starting point is

$$\begin{aligned}\sigma = \sum_{a^{(1)},a^{(2)}} \int \mathrm{d}\xi^{(1)} \int \mathrm{d}\xi^{(2)} \int \frac{\mathrm{d}^4 k_1}{(2\pi)^3} \int \frac{\mathrm{d}^4 k_2}{(2\pi)^3} \delta\left(k_1^2\right) \delta\left(k_2^2\right) (2\pi)^4 \delta^{(4)}(P - k_1 - k_2) \\ \times f_{a^{(1)}}(x^{(1)}, Q^2)\, f_{a^{(2)}}(x^{(2)}, Q^2)\, \frac{|M_{a^{(1)}\, a^{(2)}}|^2}{2\,\xi^{(1)}\xi^{(2)} S} \frac{1}{2} ,\end{aligned} \tag{5.66}$$

where the factor 1/2 is due to the identity of the final state particles, Q^2 denotes the factorisation scale, $P^2 = s$, $s = \xi^{(1)}\xi^{(2)} S$, $\xi = x/z$, and the superscripts $^{(1)}$ and $^{(2)}$ refer to the left and right beam, respectively. The matrix element reads

$$|M_{gg}|^2 = (4\pi\alpha_s)^2 \frac{C_A^2}{2} \left(3 - \frac{tu}{s^2} - \frac{us}{t^2} - \frac{st}{u^2}\right) . \tag{5.67}$$

Employing $z_1 = z_2 = z$, $t = -zs$ and $u = -(1-z)s$ transforms this into

$$|M_{gg}|^2 = (4\pi\alpha_s)^2 \frac{1}{8} \left[P_{gg}(z)\right]^2 \left\{1 + \mathcal{O}\left(z(1-z)\right)\right\} \tag{5.68}$$

where terms proportional to $z(1-z)$ in the numerator vanish in the high-energy limit and are not explicitly displayed.

The phase space element of the general case of a gluon ladder with an arbitrary number of

[6] In fact applying a veto is not necessary here, as long as quark production is neglected in the approach.

gluons emitted between the two outermost jets can be derived by combining their momenta into one final state momentum K. Ignoring the substructure of K, the differential two-particle initial and final state phase space element for the remaining degrees of freedom reads

$$\mathrm{d}\Phi_2 = \mathrm{d}\xi^{(1)}\mathrm{d}\xi^{(2)}\,\frac{\mathrm{d}^4k_1}{(2\pi)^3}\,\frac{\mathrm{d}^4k_2}{(2\pi)^3}\,\delta\left(k_1^2\right)\,\delta\left(k_2^2\right)\,(2\pi)^4\,\delta^{(4)}\left(P-K-k_1-k_2\right)\,, \tag{5.69}$$

with P again the total four momentum of the process. Employing the four-dimensional δ-function and the relations $\mathrm{d}\xi^{(1)}\mathrm{d}\xi^{(2)} = \mathrm{d}y\mathrm{d}s/S$ and $\mathrm{d}p_z = \mathrm{d}\left(\sqrt{s_\perp}\sinh y\right) = \sqrt{s_\perp}\cosh y\,\mathrm{d}y = E\,\mathrm{d}y$ results in

$$\mathrm{d}\Phi_2 = \frac{2\pi}{S}\,\mathrm{d}s\,\mathrm{d}y\,\frac{\mathrm{d}y_1\,\mathrm{dk}_{1\perp}^2\mathrm{d}\phi_1}{4(2\pi)^3}\,\delta\left((P-K-k_1)^2\right)\,. \tag{5.70}$$

Furthermore, the definition $\bar{P} = P - k_2$ allows to rewrite

$$\frac{\mathrm{d}y}{\mathrm{d}y_2} = \frac{\mathrm{d}}{\mathrm{d}y_2}\,\frac{1}{2}\ln\frac{\bar{P}^+ + m_{2\perp}e^{+y_2}}{\bar{P}^- + m_{2\perp}e^{-y_2}} = \frac{1}{2}\left(\frac{m_{2\perp}e^{+y_2}}{P^+} + \frac{m_{2\perp}e^{-y_2}}{P^-}\right) = \frac{Pk_2}{s}\,. \tag{5.71}$$

Using $P = \sqrt{s}\,(\cosh y, \vec{0}, \sinh y)$ gives

$$\mathrm{d}s\,\delta\left(s + K^2 - 2P(K+k_1) + 2Kk_1\right) = \frac{s}{s - P(K+k_1)} = \frac{s}{Pk_2}\,, \tag{5.72}$$

such that

$$\mathrm{d}\Phi_2 = \frac{1}{4S\,(2\pi)^2}\,\mathrm{d}y_2\,\mathrm{d}y_1\,\mathrm{dk}_{1\perp}^2\mathrm{d}\phi_1\,. \tag{5.73}$$

Finally, when fixing the factorisation scale in Eq. (5.66) and the renormalisation scale in Eq. (5.67) to be the transverse momentum in the process and adding a Regge suppression factor for the t-channel gluon, the z-$\mathrm{k}_\perp$-factorisation formula reads

$$\begin{aligned}\sigma = {} & \frac{\pi^2}{2S}\int\mathrm{d}y_1\int\mathrm{dk}_{1\perp}^2\int\mathrm{d}\phi_1\int\mathrm{d}y_2 \\ & \times\,\bar{f}_g(x^{(1)},z,\mathrm{k}_\perp^2,\bar{\mathrm{k}}_\perp^2)\,\bar{f}_g(x^{(2)},z,\mathrm{k}_\perp^2,\bar{\mathrm{k}}_\perp^2)\,\frac{1}{2\,\xi^{(1)\,2}\xi^{(2)\,2}S}\,\frac{1}{\bar{\Delta}_g(y_1,y_2)}\,.\end{aligned} \tag{5.74}$$

Here, $\bar{f}_g$ is defined such that only gluon splittings are contained in the sum over parton

species of Eq. (5.46) and angular ordering is implemented by the DUPDFs, while $\bar{\Delta}_g(y_1, y_2)$ is given by Eq. (5.56). The superscripts $^{(1)}$ and $^{(2)}$ refer to the left and right beam, respectively. Since the emitted gluons are distinguishable due to rapidity ordering, the symmetry factor 1/2 appearing in Eq. (5.67) must be dropped. The factorisation scale μ_F of each DUPDF introduced in Eq. (5.46) is unambiguously determined by the rescaled transverse momentum $\bar{\mathrm{k}}_\perp$ of the emissions.

Equation (5.74) describes a gluon ladder with no rung, but it can be easily extended to final states with an arbitrary number of gluons. In contrast to the previous case, the momentum fractions $z^{(1)}$ and $z^{(2)}$ are then generally different from each other. Hence the rescaled transverse momenta $\bar{\mathrm{k}}^{(1)}_{2\perp} = \mathrm{k}_{2\perp}/(1-z^{(1)})$ and $\bar{\mathrm{k}}^{(2)}_{n-1\perp} = \mathrm{k}_{n-1\perp}/(1-z^{(2)})$ are defined. Employing Eq. (7) of [147], the cross section for the $2 \to n$ gluon scattering reads

$$\begin{aligned}\sigma = {} & \frac{\pi^2}{2S} \int \mathrm{d}y_1 \int \mathrm{d}\mathrm{k}^2_{1\perp} \int \mathrm{d}\phi_1 \int \mathrm{d}y_n \\ & \times \bar{f}_g(x^{(1)}, z^{(1)}, \mathrm{k}^2_{1\perp}, \bar{\mathrm{k}}^{(1)2}_{2\perp})\, \bar{f}_g(x^{(2)}, z^{(2)}, \mathrm{k}^2_{n\perp}, \bar{\mathrm{k}}^{(2)2}_{n-1\perp}) \, \frac{1}{2\,\xi^{(1)\,2}\xi^{(2)\,2} S} \\ & \times \frac{1}{\bar{\Delta}_g(y_1, y_2)} \left[\prod_{i=2}^{n-1} \int \frac{\mathrm{d}\phi_i}{2\pi} \int \mathrm{d}y_i \int \frac{\mathrm{d}\mathrm{k}^2_{i\perp}}{\mathrm{k}^2_{i\perp}} \frac{\alpha_s(\mathrm{k}^2_{i\perp})}{\pi} C_{gg}\, \bar{\Delta}_g(y_i, y_{i-1}) \right] ,\end{aligned} \tag{5.75}$$

where

$$C_{gg} = C_A \, . \tag{5.76}$$

The corresponding Monte Carlo event generation algorithm can be described as follows:

1. Determine the kinematics of the first emission and the rapidity of the last emission according to the modified z-$k_\perp$-factorisation formula, Eq. (5.75).

2. As long as phase space allows, choose a new rapidity y_i according to Eq. (5.65) and a new transverse momentum $\mathrm{k}_{i\perp}$. The corresponding cuts on the individual emissions have already been discussed in Ref. [147]. In the notation employed ibidem, they are given by

$$\mathrm{k}^2_{i\perp} > \mu_0^2 \quad \text{and} \quad \mathrm{q}^2_{i\perp} > \mu_0^2 \, .$$

3. Fix the transverse momentum of the last emission
   through overall momentum conservation.

It should be stressed that the results presented in Sec. 5.6 have been cross-checked with an alternative phase space integration algorithm. An iterative approach to generate the event topology for the process $p_a p_b \to p_1 \dots p_n$ is then employed, considering the equivalent $2 \to 2$-scattering in each emission step. Previous steps are taken into account by combining the particle momenta $p_a, p_1 \dots p_i$ into p_{a_i} and thereby considering the $2 \to 2$-process $p_{a_i} p_b \to p_i p_n$. When denoting by $s_i = m_i^2$ and $s_{i\perp}$ the squared mass and squared transverse mass of the particle i, in the centre of mass frame of $p_{a_i b}$ one obtains the integration boundaries

$$E_i^{\max} = \frac{1}{2\, m_{a_i b}} \left(s_{a_i b} + s_i - s_n\right) ,$$
$$\mathrm{k}_{i\perp}^{2\,\max} = \frac{1}{4\, s_{a_i b}} \lambda^2 \left(s_{a_i b}, s_i, s_n\right) ,$$

where $\lambda^2 (s, s_1, s_2) = (s - s_1 - s_2)^2 - 4 s_1 s_2$. The corresponding rapidity interval is fixed by

$$y_i^{max} = \frac{1}{2} \ln \frac{1 + \sqrt{1 - s_{i\perp}/E_i^{\max\,2}}}{1 - \sqrt{1 - s_{i\perp}/E_i^{\max\,2}}} ,$$

and may be computed once $\mathrm{k}_{i\perp}^2$ is selected. The $\mathrm{k}_{i\perp}^2$ selection itself is performed employing a divergence-free distribution, such as $(\mathrm{k}_{i\perp}^2)^\alpha$, where $\alpha > -1$. Since the above boundaries are unambiguously determined, the n-particle phase space may be completely filled.

5.5 A model for quark production

So far, it has been shown that Eq. (5.75) yields the correct LL gluon evolution in the high-energy limit. In this limit quark production is strongly suppressed due to the spin structure entering the corresponding vertices. However, energies and rapidity intervals at real colliders are finite and quarks do appear as final state partons. Since, for instance, heavy quark production is of large phenomenological interest, it needs to be described. The aim is, however, not to spoil the high-energy gluon evolution. Therefore one can choose to model quark production within the BFKL ladder structure by simply adding a $g^* q^* \to q$ effective vertex, which vanishes in the high-energy limit, but keeping the finite, non-leading terms.

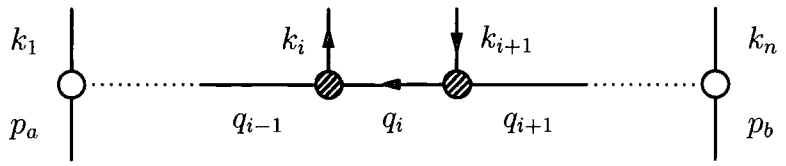

Fig. 5.6 Multi-Regge amplitude including the emission of a quark pair with the particle indices i and $i+1$. The shaded blobs represent the vertices proposed in Eq. (5.77).

Additionally, quarks can be produced by employing $qg^* \to q$ and $qq^* \to g$ impact factors contained within the DUPDFs. These quarks may further radiate gluons, which is modelled by a $q^*q^* \to g$ vertex. Figure 5.6 shows a possible configuration of quark production.

Following Sec. 5.3, the remaining vertices are then readily determined. At leading logarithmic accuracy they are given by the corresponding DGLAP splitting functions in the high-energy limit,

$$\begin{aligned} C_{qg} &= C_F \,, \\ C_{qq}(z_i) &= \frac{1}{2} C_F \, z_i \,, \\ C_{gq}(z_i) &= \frac{1}{2} T_R \, z_i \,. \end{aligned} \tag{5.77}$$

Then, the general case of a parton cascade in the high-energy limit reads

$$\begin{aligned} \sigma = {} & \frac{\pi^2}{2S} \sum_{a^{(1)}} \int \mathrm{d}y_1 \int \mathrm{d}\mathrm{k}_{1\perp}^2 \int \mathrm{d}\phi_1 \int \mathrm{d}y_n \\ & \times f^{(1)}(x^{(1)}, z^{(1)}, \mathrm{k}_{1\perp}^2, \bar{\mathrm{k}}_{2\perp}^{(1)2}) \, f^{(2)}(x^{(2)}, z^{(2)}, \mathrm{k}_{n\perp}^2, \bar{\mathrm{k}}_{n-1\perp}^{(2)2}) \, \frac{1}{2\xi^{(1)\,2}\xi^{(2)\,2} S} \, \frac{1}{\Delta_{a_1}(y_1, y_2)} \\ & \times \left[\prod_{i=2}^{n} \int \frac{\mathrm{d}\phi_i}{2\pi} \int \mathrm{d}y_i \int \frac{\mathrm{d}\mathrm{k}_{i\perp}^2}{\mathrm{k}_{i\perp}^2} \, \frac{\alpha_s(\mathrm{k}_{i\perp}^2)}{\pi} \sum_{a_i} C_{a_{i-1}a_i}(\mathrm{q}_{i-1}, \mathrm{k}_i) \, \Delta_{a_i}(y_i, y_{i-1}) \right] , \end{aligned} \tag{5.78}$$

where now both quarks and gluons are contained in the sums over parton species.

If heavy quarks are included in the simulation, their masses are taken care of in the Reggeisation factor and the phase space integration. Following the discussion in Ref. [115], the branching probability $\Gamma_Q^{(LL)}(\tilde{y}, \tilde{y})$ for heavy quarks of mass m is modified by

$$C_{qg} \quad \longrightarrow \quad \frac{\mathrm{k}_\perp^2}{\mathrm{k}_\perp^2 + m^2} \, C_{qg} \,. \tag{5.79}$$

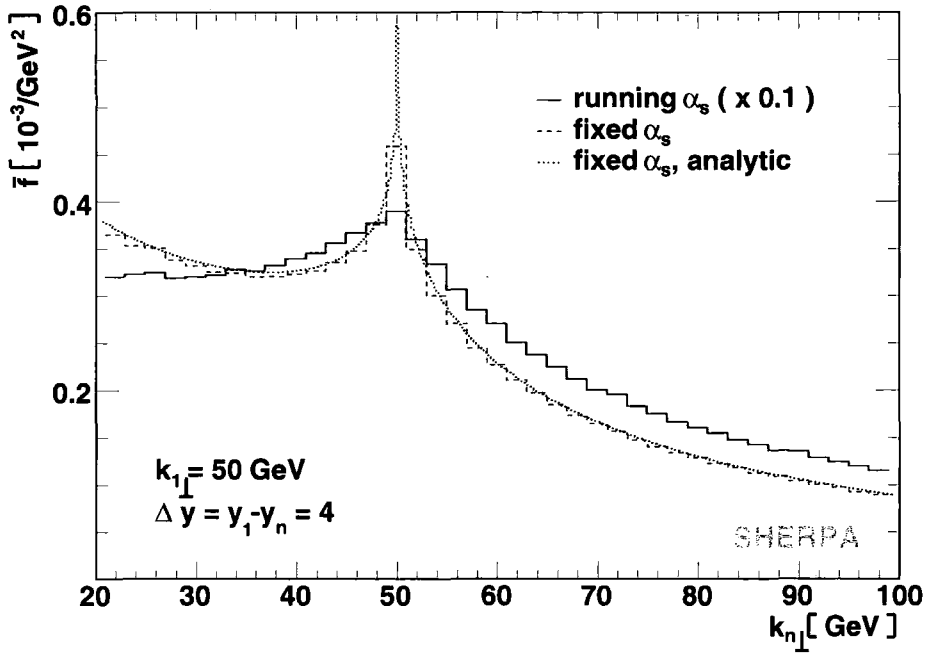

Fig. 5.7 Transverse momentum spectra $\bar{f}(k_{n\perp})$ for fixed and running coupling solution of Eq. (5.75) at fixed $k_{1\perp}$ and Δy. Note that the result for running coupling has been rescaled by a factor of 0.1.

Accordingly all external momenta are constructed employing the correct on-shell masses of the corresponding particles.

5.6 Results

In this section, results obtained with the Monte Carlo algorithm described above will be presented. All of them have been obtained with an implementation into the MC event generator SHERPA [19]. To eliminate possible dependencies on the phase space integration, calculations were cross-checked with the second integration method outlined in Sec. 5.4. No deviations from the results generated in the Markovian approach have been found.

Firstly, the focus is on purely gluonic processes, reflecting the behaviour of the LO BFKL equation. This essentially translates into invoking Eq. (5.75) for event generation. In Fig. 5.7 the azimuthally averaged $k_{n\perp}$ spectrum $\bar{f}(k_{n\perp}) = \langle f(k_{n\perp})\rangle_\phi$ is shown, where $k_{1\perp} = 50$ GeV and $\Delta y = 4$, and where the DUPDFs have been set to 1. Therefore, this plot investigates the behaviour of the BFKL kernel, Eq. (5.60), only. As collider setup, the LHC with a c.m. energy of 14 TeV has been chosen. In the fixed coupling solution α_s has been evaluated

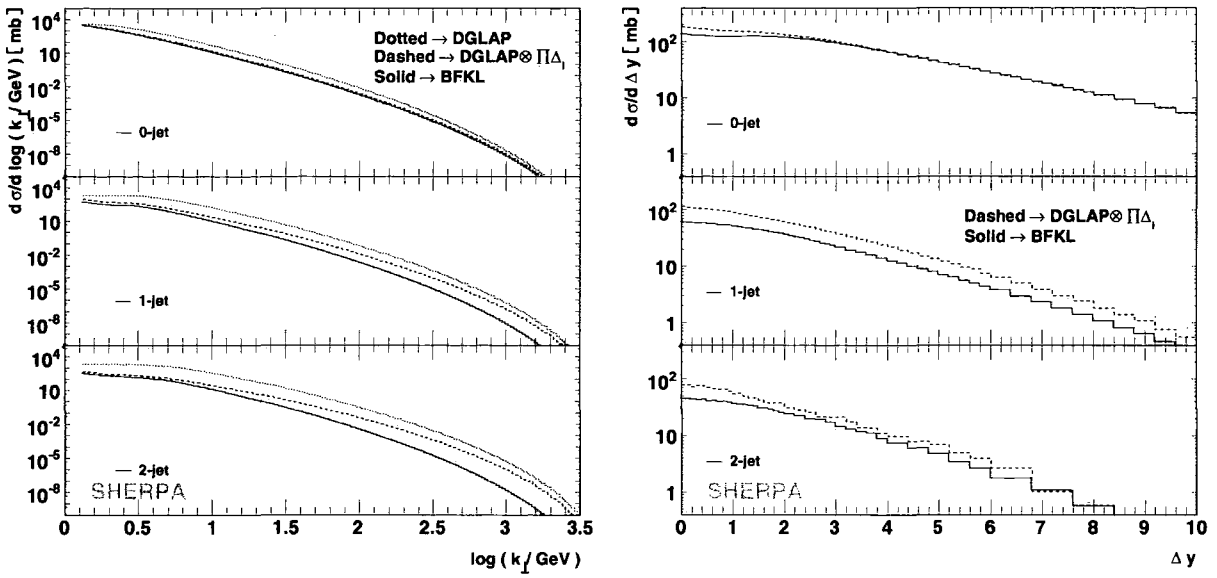

Fig. 5.8 Left panel: Comparison of $\log(\mathrm{k}_\perp)$-distributions between BFKL and reweighted DGLAP matrix elements. Right panel: Comparison between BFKL and reweighted DGLAP matrix elements for the Δy-distributions.

at scale $\mathrm{k}_{1\perp}^2$. The figure shows the effect of going from a fixed coupling and unconstrained kinematics to a running coupling with kinematical constraints, which considerably widens the distribution. Also, since α_s is typically evaluated at smaller scales, $\bar{f}$ is significantly enhanced. The large influence of kinematical constraints and running coupling on the BFKL dynamics has already been noted, e.g. in Refs. [154, 150].

As a next step, jet-production is investigated, comparing the results of the new algorithm to those obtained in collinear factorisation with on-shell matrix elements, which in the following will be denoted by DGLAP. The DGLAP results have been subject to the following corrections and constraints:

- ordering of final state momenta in rapidity,
- setting $\mu_F^{(1)\,2} = \mathrm{k}_{1\perp}^2$ and $\mu_F^{(2)\,2} = \mathrm{k}_{n\perp}^2$,
- evaluating the coupling weight as $\prod_i \alpha_s(\mathrm{k}_{i\perp}^2)$.

However, without any t-channel reggeisation factor in the DGLAP matrix elements there are still large differences. Applying a t-channel reggeisation weight to the DGLAP calculation results in much smaller discrepancies. The corresponding comparison for the $\log(\mathrm{k}_\perp)$- and Δy-spectra is shown in Fig. 5.8. Due to the formal equivalence of Eqs. (5.66) and (5.74) at

leading logarithmic accuracy, agreement is to be expected and can be interpreted as another indication for the validity of the approach. Sizable deviations occur for $k_\perp > 5$ GeV, which is due to the fact that the BFKL approach is bound to describe large energy partons only incompletely. In order to verify this, the BFKL matrix elements were reweighted with the exact matrix element obtained in collinear factorisation. The corresponding correction weight for a $2 \to n$ gluonic process reads

$$\omega = \frac{8\, n!\, M_{gg\to ng}(1,\ldots,n)}{(4\pi\alpha_s)^2\, P_{gg}(z^{(1)}) P_{gg}(z^{(2)}) \prod_{i=2}^{n-1} 16\pi^2 \bar{\alpha}_s / k_{i\perp}^2} ,$$

where the factor $n!$ occurs due to the rapidity ordering in the BFKL approach and cancels the symmetrisation of the full DGLAP matrix element $M_{gg\to ng}$. Performing this reweighting yields exact agreement between the two approaches.

Finally results are compared to recent experimental data. Firstly a comparison to data obtained by the CDF collaboration [167] is shown. The corresponding prediction of jet-$k_\perp$-spectra from the MC implementation is depicted in Fig. 5.9. It fits the data considerably well, both in their shape and their normalisation. Note that no K-factor has been employed in the calculations. Although a tilt of the distribution is observed, which potentially arises from missing s-channel contributions to quark production, this is a quite remarkable result considering the fact that a modified LO BFKL kernel is employed for event generation. As can be seen in Fig. 5.9, deviations are up to $\approx$50%, which is well within the expected leading logarithmic accuracy.

Secondly the decorrelation observable investigated in Ref. [168] is addressed. As can be seen in Fig. 5.10 the presented approach does not completely describe the data. However, deviations are of similar size as in Ref. [148]. Note that the data have not been corrected to the parton level and therefore correlated and systematic errors might have an impact.

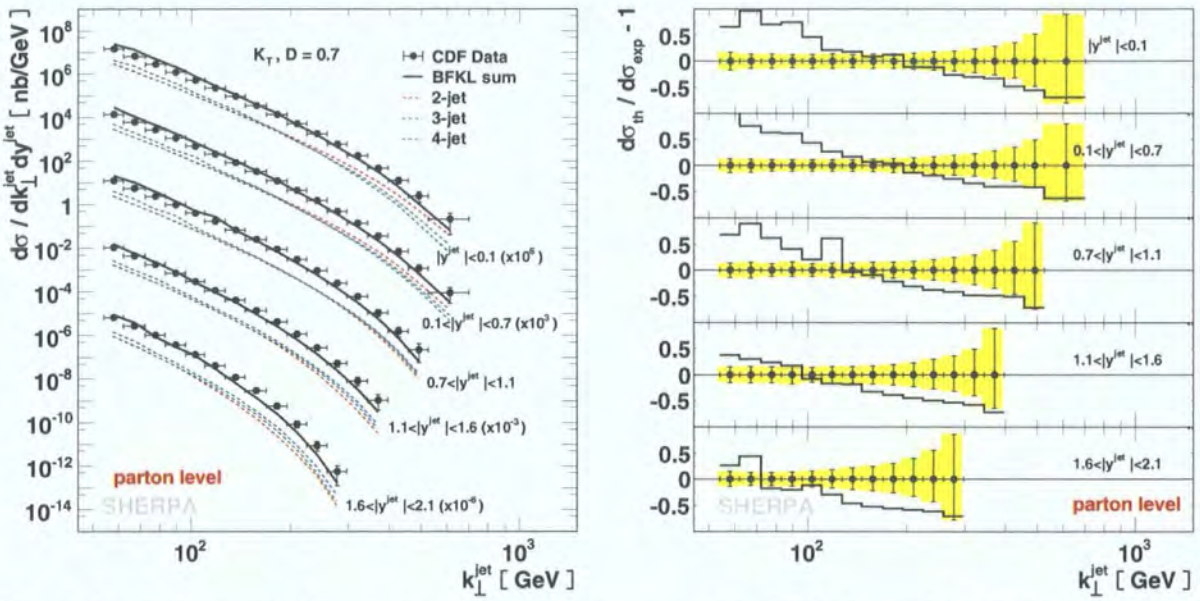

Fig. 5.9 Left panel: Comparison of jet-$k_\perp$-spectra with CDF data. Details of the analysis can be found in [167]. Dashed lines show contributions from subsamples of 2- to 4-particle final states. Right panel: Relative differences in jet-$k_\perp$-spectra compared between Monte Carlo results and CDF data.

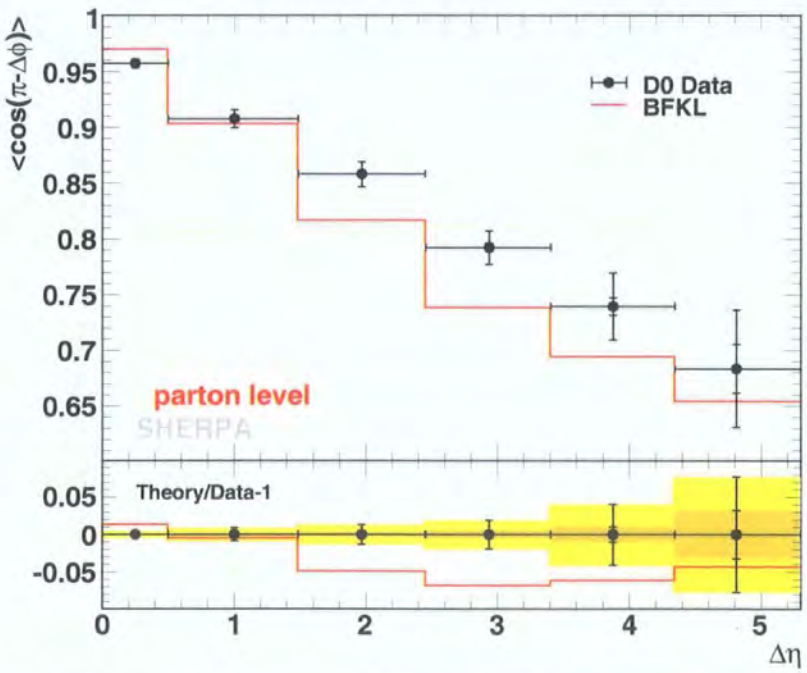

Fig. 5.10 Comparison of the jet decorrelation observable presented in [168] with DØ data. The full error bars include both statistical and systematic errors, whereas statistical errors are independently highlighted by the smaller error bars.

6 Conclusions

In this part of the thesis improved algorithms for matrix element parton shower merging were presented and a natural way to incorporate colour into the CKKW algorithm was outlined. A new type of jet measure has been introduced, which is based on the identification of potential collinear and soft enhancements of the matrix elements and corresponding singularities in the evolution kernels of shower algorithms. A brief comparison has been performed for the improved CKKW method, including colour information and using algorithms described in the first part of the thesis. Corresponding systematics have been studied. The findings are promising especially with respect to the consistency of the new methods upon changing the matrix element generator. It should be noted that the corresponding implementation will soon be publicly available and allows a straightforward application of the improved CKKW merging to any QCD associated process in the Standard Model, which, at leading order, contains no disconnected QCD subprocesses.

A detailed comparison of matrix element parton shower merging approaches was presented. Five different implementations of merging prescriptions have been compared, which are implemented into the programs ALPGEN, ARIADNE, HELAC, MADEVENT and SHERPA. As testing ground, the production of W^+-bosons at the Tevatron and LHC colliders has been chosen. The results show a reasonably good agreement between the codes, which means that the variety of methods for merging matrix elements and parton showers can be employed with some confidence. Differences arise, due to the different ways in which Sudakov suppression of the matrix elements and veto procedures in the parton shower are realised in the corresponding code and how they interact with each other. Also the usage of potentially different shower algorithms (virtuality or angular ordered showers) plays a role.

Apart from the aforementioned analyses and improvements of multi-jet merging, a new Monte Carlo algorithm for the description of particle production through the BFKL evolution equation was presented. The algorithm has been written in a Markovian approach, iterating independent emissions in order to obtain the full BFKL radiation picture. It has been discussed how doubly unintegrated PDFs, obtained from conventional PDFs through the KMRW procedure can be employed as impact factors, retaining essential features of small-x physics encoded in the BFKL equation.

The numerical implementation of this algorithm was presented. Corresponding results show that the proposed algorithm correctly reproduces the BFKL features visible in analytical calculations. They also show the important effect of a running of the coupling and of kinematical constraints, which go beyond the LO BFKL approach. The realisation of the Markovian algorithm is straightforward. Using DUPDFs obtained from collinear PDFs allows to compare results for jet production to those obtained in the collinear factorisation approach. Comparably good agreement between both approaches is obtained, when effects that are not present in both approaches, such as t-channel reggeisation and rapidity ordering, are taken into account.

This work is a first step towards a unified description of particle production in the regime of high and low transverse momenta, i.e. of jet and mini-jet production. The formalism presented here can be extended to the simulation of multiple parton interactions, which constitute an important part of the underlying event. Also diffractive processes and quarkonia production may be included in the description.

Appendix

Appendix A Lorentz functions in COMIX

In this appendix explicit expressions are listed for all possible Lorentz vertex structures occuring in the Berends-Giele recursion defined by the Standard Model. They are sorted ascending in the spin of connecting particles and the following notation is employed.

- S Scalar,
- F Fermion,
- V Vector Boson,
- T Antisymmetric tensor of rank two.

Note that all interaction terms occuring in the Standard Model Lagrangian yield no more than three-particle vertices of the above defined particle types with the possible couplings listed in Appendix B. The quantities listed in Tab. A.1 in explicit form are given by

$$\bar{u} j^\mu \gamma_\mu \frac{1-\gamma^5}{2} = \left(0, 0, \bar{u}_0 j^- - \bar{u}_1 j_\perp, -\bar{u}_0 j_\perp^* + \bar{u}_1 j^+\right) , \tag{A.1}$$

$$j^\mu \gamma_\mu \frac{1-\gamma^5}{2} v = \begin{pmatrix} 0 \\ 0 \\ j^+ v_0 + j_\perp^* v_1 \\ j_\perp v_0 + j^- v_1 \end{pmatrix} , \qquad \bar{u} \gamma^\mu \frac{1-\gamma^5}{2} v = \begin{pmatrix} \bar{u}_0 v_2 + \bar{u}_1 v_3 \\ \bar{u}_0 v_3 + \bar{u}_1 v_2 \\ i\left(\bar{u}_1 v_2 - \bar{u}_0 v_3\right) \\ \bar{u}_0 v_2 - \bar{u}_1 v_3 \end{pmatrix} , \tag{A.2}$$

Vertex ID	**Lorentz structures**		
FFS	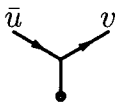	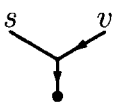	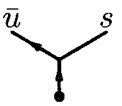
	$\bar{u}\,v$	$s\,v$	$\bar{u}\,s$
FFV$^-$	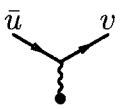	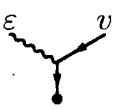	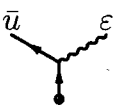
	$\bar{u}\gamma^\mu\dfrac{1-\gamma^5}{2}v$	$\varepsilon^\mu\gamma_\mu\dfrac{1-\gamma^5}{2}v$	$\bar{u}\varepsilon^\mu\gamma_\mu\dfrac{1-\gamma^5}{2}$
FFV$^+$	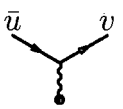	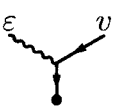	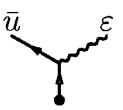
	$\bar{u}\gamma^\mu\dfrac{1+\gamma^5}{2}v$	$\varepsilon^\mu\gamma_\mu\dfrac{1+\gamma^5}{2}v$	$\bar{u}\varepsilon^\mu\gamma_\mu\dfrac{1+\gamma^5}{2}$
VVS	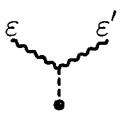	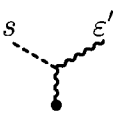	
	$\varepsilon^\mu\varepsilon'_\mu$	$s\,\varepsilon'^\mu$	
VVV(p,q)	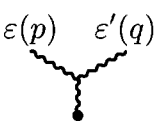		
	$\Gamma^{\nu\sigma\rho}(p,q)\,\varepsilon_\sigma\varepsilon'_\rho$		
VVT	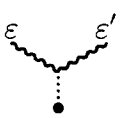	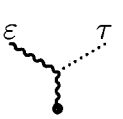	
	$T^{\mu\nu}(\varepsilon,\varepsilon')$	$\varepsilon_\nu T^{\mu\nu}$	

Tab. A.1 Lorentz structures of Standard Model interactions.

$$\bar{u}j^{\mu}\gamma_{\mu}\frac{1+\gamma^5}{2} = \left(\bar{u}_2 j^{+} + \bar{u}_3 j_{\perp}, \bar{u}_2 j_{\perp}^{*} + \bar{u}_3 j^{-}, 0, 0\right) \ , \tag{A.3}$$

$$j^{\mu}\gamma_{\mu}\frac{1+\gamma^5}{2}v = \begin{pmatrix} j^{-}v_2 - j_{\perp}^{*}v_3 \\ -j_{\perp}v_2 + j^{+}v_3 \\ 0 \\ 0 \end{pmatrix} \ , \qquad \bar{u}\gamma^{\mu}\frac{1+\gamma^5}{2}v = \begin{pmatrix} \bar{u}_2 v_0 + \bar{u}_3 v_1 \\ -\bar{u}_2 v_1 - \bar{u}_3 v_0 \\ i\left(\bar{u}_2 v_1 - \bar{u}_3 v_0\right) \\ -\bar{u}_2 v_0 + \bar{u}_3 v_1 \end{pmatrix} \ , \tag{A.4}$$

$$\Gamma^{\nu\sigma\rho}\left(p,q\right)\varepsilon_{\sigma}\varepsilon'_{\rho} = \varepsilon\varepsilon'\left(p-q\right)^{\nu} + \varepsilon'\left(2q+p\right)\varepsilon^{\nu} - \varepsilon\left(2p+q\right)\varepsilon'^{\nu} \ , \tag{A.5}$$

$$\tau^{\mu\nu}\left(\varepsilon,\varepsilon'\right) = \frac{1}{2}\left(g^{\mu\sigma}g^{\nu\rho} - g^{\mu\rho}g^{\nu\sigma}\right)\varepsilon_{\sigma}\varepsilon'_{\rho} \ . \tag{A.6}$$

Due to the antisymmetry of $\tau^{\mu\nu}$, the following identity holds

$$\frac{1}{2}\left(g^{\mu}_{\alpha}g^{\nu}_{\beta} - g^{\mu}_{\beta}g^{\nu}_{\alpha}\right)\tau^{\alpha\beta} = \tau^{\mu\nu} \tag{A.7}$$

Corresponding replacements in the recursive relations lead to an asymmetric form of the VVT vertex, and a slight decrease in evaluation time.

Appendix B Vertices and propagators in COMIX

In this appendix all vertices occuring in the recursive relations for the Standard Model as formulated in Sec. 3.1 are listed explicitly. Their Lorentz structures are defined in Appendix A.

QCD interactions

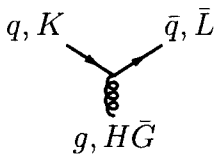

$$= -i\,\frac{g_s}{\sqrt{2}}\left[\,\delta^K_H\delta^{\bar{L}}_{\bar{G}} - \frac{1}{N_C}\delta_{H\bar{G}}\delta^{K\bar{L}}\right]\,\left(\,\mathrm{FFV}^- + \mathrm{FFV}^+\,\right)$$

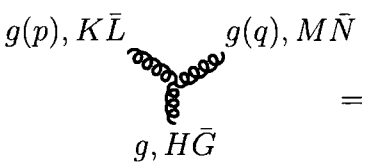

$$= i\,\frac{g_s}{\sqrt{2}}\left[\,\delta^M_H\delta^{K\bar{N}}\delta^{\bar{L}}_{\bar{G}}\,\mathrm{VVV}\,(p,q) - \delta^K_H\delta^{\bar{L}M}\delta^{\bar{N}}_{\bar{G}}\,\mathrm{VVV}\,(q,p)\,\right]$$

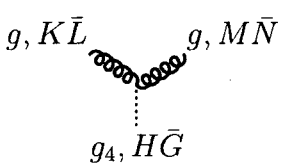

$$= i\,\frac{g_s}{\sqrt{2}}\left[\,\delta^M_H\delta^{K\bar{N}}\delta^{\bar{L}}_{\bar{G}} + \delta^K_H\delta^{\bar{L}M}\delta^{\bar{N}}_{\bar{G}}\,\right]\,\mathrm{VVT}$$

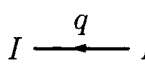

$$= i\,\delta^H_I\,\frac{\hat{p}+m}{p^2-m^2}$$

$$= i\,\delta^H_I\delta^{\bar{G}}_{\bar{J}}\,\frac{-g_{\mu\nu}}{p^2}$$

$\rho\sigma, I\bar{J}$ $\overset{g_4}{\cdots\cdots}$ $\mu\nu, H\bar{G} =$ $\quad -i\,\delta_I^H \delta_{\bar{J}}^{\bar{G}}\, D_{\mu\nu}^{\rho\sigma}$

QED interactions

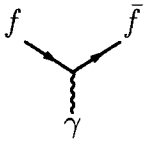

$= \quad -i\, g_e Q_f \,\left(\mathrm{FFV}^- + \mathrm{FFV}^+ \right)$

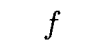

$= \quad i\,\dfrac{\hat{p} + m_f}{p^2 - m_f^2}$

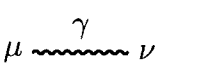

$= \quad i\,\dfrac{-g_{\mu\nu} + p^\mu p^\nu / p^2}{p^2}$

Electroweak interactions

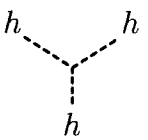

$= \quad i\,\dfrac{3\,m_h^2}{v}$

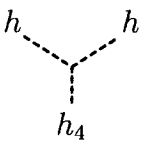

$= \quad i\,\dfrac{m_h^2}{v^2}$

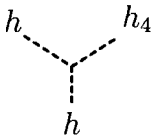

$= \quad i$

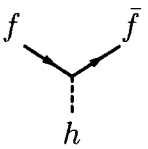

$= \quad -i\,\dfrac{m_f}{v}\,\mathrm{FFS}$

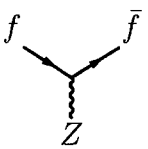

$= \quad -i\,\dfrac{g_w}{2\cos\theta_W}\,\left\{ (V_f + A_f)\,\mathrm{FFV}^- + (V_f - A_f)\,\mathrm{FFV}^+ \right\}$

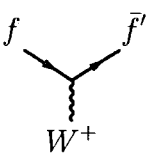

$= \quad -i\,\dfrac{g_w}{\sqrt{2}}\,T^+_{ff'}\,\mathrm{FFV}^-$

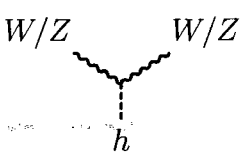

$= \quad -i\,\dfrac{g_w\, m_{W/Z}}{\lambda_{W/Z}}\,VVS \qquad \text{where} \qquad \begin{array}{l} \lambda_W = 1 \\ \lambda_Z = \cos\theta_W \end{array}$

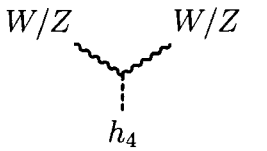

$$= -i\,\frac{g_w^2}{2\,\lambda_{W/Z}^2}\,VVS \qquad \text{where} \qquad \begin{aligned} \lambda_W &= 1 \\ \lambda_Z &= \cos\theta_W \end{aligned}$$

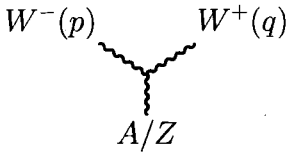

$$= i\,g_w\,\kappa_{A/Z}\,VVV\,(p,q) \qquad \text{where} \qquad \begin{aligned} \kappa_A &= \sin\theta_W \\ \kappa_Z &= \cos\theta_W \end{aligned}$$

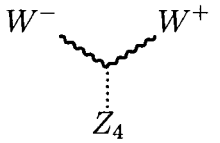

$$= i\,g_w\,VVT$$

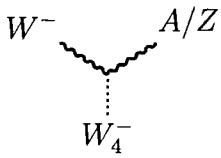

$$= i\,g_w\,\kappa_{A/Z}\,VVT \qquad \text{where} \qquad \begin{aligned} \kappa_A &= \sin\theta_W \\ \kappa_Z &= \cos\theta_W \end{aligned}$$

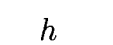

$$= \frac{i}{p^2 - m_h^2}$$

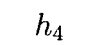

$$= i$$

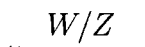

$$= i\,\frac{-g_{\mu\nu} + p^\mu p^\nu / m_{W/Z}^2}{p^2 - m_{W/Z}^2}$$

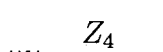

$$= -i\,D_{\mu\nu}^{\rho\sigma}$$

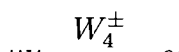

$$= i\,D_{\mu\nu}^{\rho\sigma}$$

The following definitions are employed

$$V_f = T_f^3 - 2Q_f \sin^2\theta_W, \qquad A_f = T_f^3\,.$$

Appendix C The HAAG integrator

The HAAG phase space generator [33] is designed to produce momenta distributed approximately according to a QCD antenna function for an n-particle process

$$A_n(p_0, p_1, ..., p_{n-1}) = \frac{1}{(p_0p_1)(p_1p_2)...(p_{n-2}p_{n-1})(p_{n-1}p_0)}. \tag{C.1}$$

Different antennas can be obtained from permutations of the momenta p_i. Cyclic permutation and reversion of the order will however lead to the same structure. Generally HAAG relies on the phase space factorisation formula, Eq. (3.20). In Ref. [33] two algorithms are proposed which are referred to as closed and open antenna and which differ in the decomposition of the 2-particle phase space $d\Phi_2$. Only the closed antenna contains all factors in Eq. (C.1), while in the open antenna one factor (p_ip_{i+1}) is missing. Although the closed antenna seems to be more symmetric, in practice it turns out that the open antenna is more efficient. This is mainly due to its simpler structure and less additional weight factors that appear within the algorithm.[1] In the following the focus will therefore be on open antennas. The algorithm is reviewed for the case of massless external particles, however it can easily be generalised to the massive case.

Antenna Generation

In the following, a classification of antenna types by the position of the incoming momenta, p_0 and p_1, within the antenna will be used, see Fig. C.1. The type is then given by Min$(m-1, n-m-1)$.

[1] These weights are nonsingular in any of the products (p_ip_j).

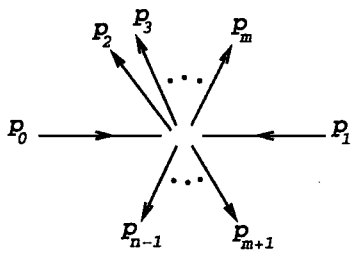

$$\sim \frac{1}{(p_0\cdot p_2)(p_2\cdot p_3)\ldots(p_m\cdot p_1)(p_1\cdot p_{m+1})\ldots(p_{n-2}\cdot p_{n-1})(p_{n-1}\cdot p_0)}$$

Fig. C.1 Antenna configuration.

The basic building block for antenna generation is the split of a massive momentum according to the phase space element $\mathrm{d}s\,\mathrm{d}\Phi_2(Q;p,P;q)$, where $P^2 = s$ and the last argument, q, defines an axis for the momentum generation. The 2-particle phase space is decomposed according as

$$\mathrm{d}\Phi_2(Q;p,P;q) = \mathrm{d}a\,\mathrm{d}\phi\,, \quad \text{where} \quad a = \frac{q\cdot p}{q\cdot P} \tag{C.2}$$

and where ϕ is an azimuthal angle around q.

The phase space for a single split, now defined through the variables s, a, ϕ, is constructed as follows[2]:

1. Dice s according to $1/s$ in $[s_{\min}, s_{\max}]$.

2. Dice a according to $1/a$ in $[a_{\min}, a_{\max}]$.

3. Dice ϕ according to a flat distribution in $[0, 2\pi]$.

4. The momenta are given by

$$\begin{aligned} p &= \left(\frac{Q^2-s}{2\sqrt{Q^2}}, \vec{p}\right)\,, \\ P &= \left(\frac{Q^2+s}{2\sqrt{Q^2}}, -\vec{p}\right)\,, \\ \vec{p} &= \left(h\cos\phi, h\sin\phi, \frac{Q^2(1-2a)-s}{2\sqrt{Q^2}}\right), \quad \text{where} \quad h = \sqrt{Q^2a(1-a)-as}. \end{aligned} \tag{C.3}$$

[2]Frame dependent quantities are defined in the centre-of-mass frame of Q with the z-axis along q

5. The weight is given by

$$\frac{g(s_{\min}, s_{\max})}{s} \frac{g(a_{\min}, a_{\max})}{a} \frac{1}{2\pi}, \quad \text{where} \quad g(x_{\min}, x_{\max}) = \log \frac{x_{\max}}{x_{\min}}. \tag{C.4}$$

Type 0 antennae

The phase space for type 0 antenna configurations can be obtained by a direct multiple application of the basic building block:

$$\begin{aligned} \mathrm{d}\Phi_n(p_0, p_1; p_2, ..., p_{n-1}) = \quad & \mathrm{d}s_2 \, \mathrm{d}\Phi_2(p_0 + p_1; p_2, Q_2; p_1) \\ & \times \mathrm{d}s_3 \, \mathrm{d}\Phi_2(Q_2; p_3, Q_3; p_2) \\ & \vdots \\ & \times \mathrm{d}s_{n-3} \, \mathrm{d}\Phi_2(Q_{n-4}; p_{n-3}, Q_{n-3}; p_{n-4}) \\ & \times \mathrm{d}\Phi_2(Q_{n-3}; p_{n-1}, p_{n-2}; p_{n-3}) \, . \end{aligned} \tag{C.5}$$

The corresponding total weight is given by

$$w \sim \frac{\prod_{j=1}^{n-3} p_j \left(\sum_{i=j+1}^{n-1} p_i\right)}{\prod_{j=3}^{n-3} \left(\sum_{i=j}^{n-1} p_i\right)^2} \frac{1}{(p_1 \cdot p_2)(p_2 \cdot p_3) \cdots (p_{n-2} \cdot p_{n-1})}, \tag{C.6}$$

where the contributions from boundary dependent functions g have been omitted.

Type 1 antennae

For this configuration the following phase space decomposition is considered:

$$\begin{aligned} \mathrm{d}\Phi_n(p_0, p_1; p_2, ..., p_{n-1}) = \quad & \mathrm{d}s_2 \, \mathrm{d}\Phi_2(p_0 + p_1; p_2, Q_2; p_0) \\ & \times \mathrm{d}s_3 \, \mathrm{d}\Phi_2(Q_2; p_3, Q_3; p_1) \\ & \times \mathrm{d}s_4 \, \mathrm{d}\Phi_2(Q_3; p_4, Q_4; p_3) \\ & \vdots \\ & \times \mathrm{d}s_{n-3} \, \mathrm{d}\Phi_2(Q_{n-4}; p_{n-3}, Q_{n-3}; p_{n-4}) \\ & \times \mathrm{d}\Phi_2(Q_{n-3}; p_{n-1}, p_{n-2}; p_{n-3}) \, . \end{aligned} \tag{C.7}$$

In the first momentum split, $\mathrm{d}\Phi_2(p_0+p_1;p_2,Q_2;p_0)$, the variable a is now diced according to $\frac{1}{a(1-a)}$. All following splits are generated according to the basic building block. The corresponding total weight is given by

$$w \sim p_0{\cdot}(p_0+p_1-p_2)\,p_1{\cdot}(p_0+p_1-p_2)\frac{\prod_{j=3}^{n-3} p_j\left(\sum_{i=j+1}^{n-1} p_i\right)}{\prod_{j=3}^{n-3}\left(\sum_{i=j}^{n-1} p_i\right)^2}\,\frac{1}{(p_0{\cdot}p_2)(p_1{\cdot}p_3)\cdots(p_{n-2}{\cdot}p_{n-1})}\,. \tag{C.8}$$

Type k (≥ 2) antennae

In this case the following decomposition is employed:

$$\begin{aligned}
\mathrm{d}\Phi_n(p_0,p_1;p_2,\ldots,p_{n-1}) = \quad & \mathrm{d}s_2\mathrm{d}s_k\;\mathrm{d}\Phi_2(p_0+p_1;p_2,Q_k;p_0)\\
& \times \mathrm{d}s_3\;\mathrm{d}\Phi_2(Q_2;p_3,Q_3;p_0)\\
& \quad\vdots\\
& \times \mathrm{d}s_{k-2}\;\mathrm{d}\Phi_2(Q_{k-3};p_{k-2},Q_{k-2};p_{k-3})\\
& \times \mathrm{d}\Phi_2(Q_{k-2};p_{k-1},p_k;p_{k-2})\\
& \times \mathrm{d}s_{k+1}\;\mathrm{d}\Phi_2(Q_k;p_{k+1},Q_{k+1};p_1)\\
& \quad\vdots\\
& \times \mathrm{d}s_{n-3}\;\mathrm{d}\Phi_2(Q_{n-4};p_{n-3},Q_{n-3};p_{n-4})\\
& \times \mathrm{d}\Phi_2(Q_{n-3};p_{n-1},p_{n-2};p_{n-3})\,.
\end{aligned} \tag{C.9}$$

All splittings are generated according to the basic building block. The corresponding total weight is given by

$$\begin{aligned}
w \sim \quad & p_1{\cdot}(p_{k+1}+\ldots+p_{n-1})\frac{\prod_{j=2}^{k-2} p_j\left(\sum_{i=j+1}^{k} p_i\right)}{\prod_{j=2}^{k-2}\left(\sum_{i=j}^{k} p_i\right)^2}\,\frac{\prod_{j=k+1}^{n-3} p_j\left(\sum_{i=j+1}^{n-1} p_i\right)}{\prod_{j=k+1}^{n-3}\left(\sum_{i=j}^{n-1} p_i\right)^2}\\
& \times \frac{1}{(p_0{\cdot}p_2)(p_2{\cdot}p_3)\cdots(p_{k-1}{\cdot}p_k)(p_1{\cdot}p_{k+1})\cdots(p_{n-2}{\cdot}p_{n-1})}\,.
\end{aligned}$$

Symmetrisation of antennae

As well as the antenna function in Eq. (C.1), each HAAG channel can be labeled by a specific permutation of the momenta. Since the described algorithm always starts from incoming momenta, the channels are invariant with respect to cyclic permutations of the momenta. However, unlike the antenna function itself, different channels are obtained if the order of the momenta is reversed. This is due to the fact that the open antenna algorithm is used.

In order to recover symmetry, the two channels given by a permutation and its reverse are combined into into one, i.e. one of the two configurations is chosen with equal probability and the weight is given by the average of the two.

Note that all channels of the same type are in principle equivalent, i.e. they can be obtained from each other by simply relabeling the final state momenta.

HAAG and variance reducing techniques

To generate an adequate phase space integrator for realistic n-particle QCD processes, different HAAG channels can be combined using the multi-channel method [30]. Symbolically one can write a single channel as a map X from uniformly distributed random numbers $\vec{a} \in [0,1]^{3n-4}$ to the four-momenta $\vec{p} = (p_1, \ldots, p_n)$ of external particles, The corresponding phase space weight g is given by

$$\frac{1}{g} = \frac{\mathrm{d}\Phi_n(X(\vec{a}))}{\mathrm{d}\vec{a}} . \tag{C.10}$$

The multi-channel method now combines several maps X_i to a new map as follows:

$$\mathbf{X}(\vec{a}, \tilde{\alpha}) = X_k(\vec{a}) , \quad \text{for} \quad \sum_{l=1}^{k-1} \alpha_l < \tilde{\alpha} < \sum_{l=1}^{k} \alpha_l , \tag{C.11}$$

requiring an additional random number $\tilde{\alpha}$ and arbitrary coefficients α_k with $\alpha_k > 0$ and $\sum_k \alpha_k = 1$. The corresponding phase space weight is given by

$$G = \sum_k \alpha_k \, g_k . \tag{C.12}$$

The coefficients α_k can be adapted such that the variance of the phase space integral is minimised.

The efficiency of the integrator is improved if additionally the VEGAS algorithm [31] is applied to the single channels. VEGAS is very efficient in the numerical adaptation to functions, whose peaking behaviour is not too extreme and which are factorisable to a product of one-dimensional functions. Although this is usually not the case for full differential cross sections, it can be used to better adapt the antenna-like structures in a single HAAG-channel to the corresponding structures in the matrix elements, including phase space cuts.

For each channel k, VEGAS is used to generate a mapping ξ_k from uniformly distributed random numbers to a non-uniform distribution, still inside the interval $[0,1]$, and a corresponding weight v_k. To combine this with the multi-channel method the mapping $X(\vec{a})$ for single channels must be invertible, which is true for HAAG channels. The full map reads

$$\mathbf{X}(\vec{a},\tilde{\alpha}) \;=\; X_k(\xi_k(\vec{a}))\;,\quad \text{for}\quad \sum_{l=1}^{k-1}\alpha_l < \tilde{\alpha} < \sum_{l=1}^{k}\alpha_l\;. \tag{C.13}$$

For a momentum configuration $\vec{p}$ the weight is therefore given by

$$G(\vec{p}) = \sum_k \alpha_k\; g_k(\vec{p})\; v_k(X_k^{-1}(\vec{p}))\;. \tag{C.14}$$

One can make use of the equivalence of HAAG-channels of the same type, such that all of them employ the same VEGAS map. This alleviates the adaptation significantly, since one is left with only very few maps and a linear growth with the number of particles.

Appendix D NLL Sudakov form factors

In this section, the connection between the notation of Sudakov form factors, Eq. (2.4), Part II, Chapter 2 and the commonly used form in terms of the jet measure, cf. Ref. [96] is established. The focus will be on massless partons, such that, to next-to-leading logarithmic accuracy, the Sudakov form factors are given by

$$\begin{aligned}\Delta_q(q,Q) &= \exp\left\{-\int_q^Q \mathrm{d}\bar{q}\,\Gamma_q(\bar{q},Q)\right\}\\ \Delta_g(q,Q) &= \exp\left\{-\int_q^Q \mathrm{d}\bar{q}\,\left[\Gamma_g(\bar{q},Q)+\Gamma_f(\bar{q},Q)\right]\right\}\,,\end{aligned} \tag{D.1}$$

Note that they depend on the jet measure only. This is in contrast to what is employed in Eq. (2.18) and allows to compute jet rates to next-to-leading logarithmic accuracy, while only the respective jet measure scales of parton production are needed as an input. The functions $\Gamma(q,Q)$ are given by

$$\begin{aligned}\Gamma_q^{(F)}(q,Q) &= \frac{2C_F}{\pi}\frac{\alpha_s(q)}{q}\left[\ln\left(\frac{Q}{q}\right)-\frac{3}{4}\right]\,,\\ \Gamma_g^{(F)}(q,Q) &= \frac{2C_A}{\pi}\frac{\alpha_s(q)}{q}\left[\ln\left(\frac{Q}{q}\right)-\frac{11}{12}\right]\,, \qquad \Gamma_f^{(F)}(q) = \frac{2T_R}{\pi}\frac{\alpha_s(q)}{q}\frac{N_f}{3}\,.\end{aligned} \tag{D.2}$$

The above formulae are derived using the coherent branching formalism, based on the standard evolution equation, Eq. (2.1). Collinear factorisation as in the shower generator

APACIC++, cf. Sec. 3.1, is employed while the evolution parameter is the angular variable

$$t \to \tilde{q}^2 = \frac{k_\perp^2}{z^2(1-z)^2} = \frac{p^2}{z(1-z)} , \tag{D.3}$$

with z the light-cone momentum fraction in the splitting and p^2 the virtuality of the (massless) mother parton.

Comparing this to the standard shower algorithm in APACIC++ (cf. Sec. 3.1), the main difference arises because angular ordering is implemented directly. However, since $\mathrm{d}\log(\tilde{q}^2/\mu^2) = \mathrm{d}\log(p^2/\mu^2)$ and since APACIC++ effectively implements angular ordering, both schemes are formally equivalent. The evolution within APACIC++ can then be cast into the form employed in Ref. [96] and the respective Sudakov form factors agree because in the soft-collinear regime and for massless partons, the jet measure, Eqs. (3.7) and (3.8) effectively encodes the Durham scheme

$$Q^2_{a\to bc} = \min\left\{E_b^2, E_c^2\right\}\,(1-\cos\theta_{bc}) \ . \tag{D.4}$$

The lower scale q of the above Sudakov factors then corresponds to the jet veto scale Q_{cut}, while the upper scale is set by the nodal Q-value of the branching where the respective parton was produced.

Bibliography

[1] F. Abe et al., CDF collaboration, *Measurement of Double Parton Scattering in $\bar{p}p$ collisions at $\sqrt{s} = 1.8\,\mathrm{TeV}$*, Phys. Rev. Lett. **79** (1997), 584–589. F. Abe et al., CDF collaboration, *Double parton scattering in $\bar{p}p$ collisions at $\sqrt{s} = 1.8\,\mathrm{TeV}$*, Phys. Rev. **D56** (1997), 3811–3832. T. Affolder et al., CDF collaboration, *Charged jet evolution and the underlying event in proton-antiproton collisions at 1.8 TeV*, Phys. Rev. **D65** (2002), 092002. D. E. Acosta et al., CDF collaboration, *Underlying event in hard interactions at the Fermilab Tevatron $\bar{p}p$ collider*, Phys. Rev. **D70** (2004), 072002, [hep-ex/0404004].

[2] T. Sjöstrand and M. van Zijl, *A multiple-interaction model for the event structure in hadron collisions*, Phys. Rev. **D36** (1987), 2019.

[3] T. Sjöstrand and P. Z. Skands, *Transverse-momentum-ordered showers and interleaved multiple interactions*, Eur. Phys. J. **C39** (2005), 129–154, [hep-ph/0408302].

[4] J. M. Butterworth, J. R. Forshaw and M. H. Seymour, *Multiparton Interactions in Photoproduction at HERA*, Z. Phys. **C72** (1996), 637–646, [hep-ph/9601371]. I. Borozan and M. H. Seymour, *An eikonal model for multiparticle production in hadron-hadron interactions*, JHEP **09** (2002), 015, [hep-ph/0207283]. M. Bähr, S. Gieseke and M. H. Seymour, *Simulation of multiple partonic interactions in HERWIG++*, JHEP **07** (2008), 076, [arXiv:0803.3633 [hep-ph]].

[5] J. Bartels, M. Salvadore and G. P. Vacca, *AGK cutting rules and multiple scattering in hadronic collisions*, Eur. Phys. J. **C42** (2005), 53–71, [hep-ph/0503049].

[6] T. Sjöstrand, S. Mrenna and P. Skands, *PYTHIA 6.4 physics and manual*, JHEP **05** (2006), 026, [hep-ph/0603175].

[7] G. Corcella et al., *HERWIG 6.5 Release Note*, hep-ph/0210213.

[8] T. Sjöstrand, S. Mrenna and P. Skands, *A brief introduction to PYTHIA 8.1*, Comput. Phys. Commun. **178** (2008), 852–867, [arXiv:0710.3820 [hep-ph]].

[9] M. Bähr et al., *Herwig++ Physics and Manual*, arXiv:0803.0883 [hep-ph].

[10] J. Campbell and R. K. Ellis, *Next-to-leading order corrections to W+2 jet and Z+2 jet production at hadron colliders*, Phys. Rev. **D65** (2002), 113007, [hep-ph/0202176].

[11] S. Frixione and B. R. Webber, *Matching NLO QCD computations and parton shower simulations*, JHEP **06** (2002), 029, [hep-ph/0204244]. S. Frixione, P. Nason and B. R. Webber, *Matching NLO QCD and parton showers in heavy flavour production*, JHEP **08** (2003), 007, [hep-ph/0305252]. S. Frixione, E. Laenen, P. Motylinski and B. R. Webber, *Single-top production in MC@NLO*, JHEP **03** (2006), 092, [hep-ph/0512250].

[12] S. Frixione, P. Nason and C. Oleari, *Matching NLO QCD computations with parton shower simulations: the POWHEG method*, JHEP **11** (2007), 070, [arXiv:0709.2092 [hep-ph]].

[13] S. Frixione and B. R. Webber, *The MC@NLO 3.3 Event Generator*, hep-ph/0612272.

[14] O. Latunde-Dada, S. Gieseke and B. Webber, *A positive-weight next-to-leading-order Monte Carlo for e^+e^- annihilation to hadrons*, JHEP **02** (2007), 051, [hep-ph/0612281]. K. Hamilton, P. Richardson and J. Tully, *A Positive-Weight Next-to-Leading Order Monte Carlo Simulation of Drell-Yan Vector Boson Production*, arXiv:0806.0290 [hep-ph]. O. Latunde-Dada, *Applying the POWHEG method to top pair production and decays at the ILC*, arXiv:0806.4560 [hep-ph].

[15] M. L. Mangano, M. Moretti, F. Piccinini, R. Pittau and A. D. Polosa, *ALPGEN, a generator for hard multiparton processes in hadronic collisions*, JHEP **07** (2003), 001, [hep-ph/0206293].

[16] A. Kanaki and C. G. Papadopoulos, *HELAC: A package to compute electroweak helicity amplitudes*, Comput. Phys. Commun. **132** (2000), 306–315, [hep-ph/0002082]. C. G. Papadopoulos, *PHEGAS: A phase-space generator for automatic cross-section computation*, Comput. Phys. Commun. **137** (2001), 247–254, [hep-ph/0007335].

[17] F. Maltoni and T. Stelzer, *MadEvent: automatic event generation with MadGraph*, JHEP **02** (2003), 027, [hep-ph/0208156].

[18] F. Krauss, R. Kuhn and G. Soff, *AMEGIC++ 1.0: A Matrix Element Generator In C++*, JHEP **02** (2002), 044, [hep-ph/0109036].

[19] T. Gleisberg, S. Höche, F. Krauss, A. Schälicke, S. Schumann and J. Winter, *SHERPA 1.α, a proof-of-concept version*, JHEP **02** (2004), 056, [hep-ph/0311263].

[20] R. Kuhn, F. Krauss, B. Ivanyi and G. Soff, *APACIC++ 1.0: A PArton Cascade In C++*, Comput. Phys. Commun. **134** (2001), 223–266, [hep-ph/0004270]. F. Krauss, A. Schälicke and G. Soff, *APACIC++ 2.0: A PArton Cascade In C++*, Comput. Phys. Commun. **174** (2006), 876–902, [hep-ph/0503087].

[21] J.-C. Winter, F. Krauss and G. Soff, *A modified cluster-hadronisation model*, Eur. Phys. J. **C36** (2004), 381–395, [hep-ph/0311085].

[22] F. Krauss, T. Laubrich and F. Siegert, *Simulation of hadron decays in SHERPA*, in preparation.

[23] F. Krauss and M. Schönherr, *Soft photon radiation in particle decays in SHERPA*, in preparation.

[24] S. Schumann and F. Krauss, *A parton shower algorithm based on Catani-Seymour dipole factorisation*, JHEP **03** (2008), 038, [arXiv:0709.1027 [hep-ph]].

[25] J.-C. Winter and F. Krauss, *Initial-state showering based on colour dipoles connected to incoming parton lines*, JHEP **07** (2008), 040, [arXiv:0712.3913 [hep-ph]].

[26] K. Hagiwara et al., *Supersymmetry simulations with off-shell effects for the CERN LHC and an ILC*, Phys. Rev. **D73** (2006), 055005, [hep-ph/0512260].

[27] T. Gleisberg, F. Krauss, K. T. Matchev, A. Schälicke, S. Schumann and G. Soff, *Helicity formalism for spin-2 particles*, JHEP **09** (2003), 001, [hep-ph/0306182].

[28] R. Kleiss and W. J. Stirling, *Spinor techniques for calculating $p\bar{p} \to W^{\pm}/Z^0$+jets*, Nucl. Phys. **B262** (1985), 235–262. A. Ballestrero and E. Maina, *A New method for helicity calculations*, Phys. Lett. **B350** (1995), 225–233, [hep-ph/9403244].

[29] E. Byckling and K. Kajantie, *N-particle phase space in terms of invariant momentum transfers*, Nucl. Phys. **B9** (1969), 568–576.

[30] R. Kleiss and R. Pittau, *Weight optimization in multichannel Monte Carlo*, Comput. Phys. Commun. **83** (1994), 141–146, [hep-ph/9405257].

[31] G. P. Lepage, *VEGAS - An Adaptive Multi-dimensional Integration Program*, CLNS-80/447.

[32] R. Kleiss, W. J. Stirling and S. D. Ellis, *A new Monte Carlo treatment of multiparticle phase space at high energies*, Comput. Phys. Commun. **40** (1986), 359. P. D. Draggiotis, A. van Hameren and R. Kleiss, *SARGE: An algorithm for generating QCD-antennas*, Phys. Lett. **B483** (2000), 124–130, [hep-ph/0004047].

[33] A. van Hameren and C. G. Papadopoulos, *A hierarchical phase space generator for QCD antenna structures*, Eur. Phys. J. **C25** (2002), 563–574, [hep-ph/0204055].

[34] T. Gleisberg and F. Krauss, *Automating dipole subtraction for QCD NLO calculations*, Eur. Phys. J. **C53** (2008), 501–523, [arXiv:0709.2881 [hep-ph]].

[35] S. Catani, F. Krauss, R. Kuhn and B. R. Webber, *QCD matrix elements + parton showers*, JHEP **111** (2001), 063, [hep-ph/0109231].

[36] F. Krauss, *Matrix elements and parton showers in hadronic interactions*, JHEP **0208** (2002), 015, [hep-ph/0205283].

[37] S. Alekhin et al., *HERA and the LHC - A workshop on the implications of HERA for LHC physics: Proceedings Part A*, hep-ph/0601012.

[38] T. Sjöstrand and P. Z. Skands, *Multiple interactions and the structure of beam remnants*, JHEP **03** (2004), 053, [hep-ph/0402078].

[39] X. Artru and G. Mennessier, *String model and multiproduction*, Nucl. Phys. **B70** (1974), 93–115. M. G. Bowler, e^+e^- *production of heavy quarks in the string model*, Z. Phys. **C11** (1981), 169. B. Andersson, G. Gustafson and B. Söderberg, *A general model for jet fragmentation*, Z. Phys. **C20** (1983), 317.

[40] T. Sjöstrand, *The Lund Monte Carlo for Jet Fragmentation*, Comput. Phys. Commun. **27** (1982), 243.

[41] R. D. Field and S. Wolfram, *A QCD model for* e^+e^- *annihilation*, Nucl. Phys. **B213** (1983), 65. B. R. Webber, *A QCD model for jet fragmentation including soft gluon interference*, Nucl. Phys. **B238** (1984), 492.

[42] H. Hoeth, *Messung der Vierjet–Winkelverteilungen und Bestimmung der QCD–Farbfaktoren mit Hilfe des Apacic++–Generators*, Diploma Thesis, Fachbereich Physik, Bergische Universität Wuppertal [WUD 03-11], in German. DØ collaboration, *Z+jet production in the DØ experiment: A comparison between data and the PYTHIA and SHERPA Monte Carlos*, DØ note 5066.

[43] I. Bird et al., *LHC computing Grid. Technical design report*, CERN-LHCC-2005-024. P. J. W. Faulkner et al., GridPP collaboration, *GridPP: Development of the UK computing Grid for particle physics*, J. Phys. **G32** (2006) J. Andreeva, S. Campana, F. Fanzago and J. Herrala, *High-energy physics on the Grid: The ATLAS and CMS experience*, J. Grid Comput. **6** (2008), 3–13.

[44] T. Gleisberg and S. Höche, *Comix, a new matrix element generator*, arXiv:0808.3674 [hep-ph].

[45] D. A. Kosower, *Antenna factorization of gauge-theory amplitudes*, Phys. Rev. **D57** (1998), 5410–5416, [hep-ph/9710213]. A. Daleo, T. Gehrmann and D. Maitre, *Antenna subtraction with hadronic initial states*, JHEP **04** (2007), 016, [hep-ph/0612257]. A. Gehrmann-De Ridder, T. Gehrmann and E. W. N. Glover, *Antenna subtraction at NNLO*, JHEP **09** (2005), 056, [hep-ph/0505111].

[46] T. G. Birthwright, E. W. N. Glover, V. V. Khoze and P. Marquard, *Multi-gluon collinear limits from MHV diagrams*, JHEP **05** (2005), 013, [hep-ph/0503063]. T. G. Birthwright, E. W. N. Glover, V. V. Khoze and P. Marquard, *Collinear limits in QCD from MHV rules*, JHEP **07** (2005), 068, [hep-ph/0505219].

[47] C. Duhr and F. Maltoni, *Antenna functions from MHV rules*, arXiv:0808.3319 [hep-ph].

[48] C. Duhr, S. Höche and F. Maltoni, *Color-dressed recursive relations for multi-parton amplitudes*, JHEP **08** (2006), 062, [hep-ph/0607057].

[49] M. Dinsdale, M. Ternick and S. Weinzierl, *A comparison of efficient methods for the computation of Born gluon amplitudes*, JHEP **03** (2006), 056, [hep-ph/0602204].

[50] T. Gleisberg, S. Höche, F. Krauss and R. Matyskiewicz, *How to calculate colourful cross sections efficiently*, arXiv:0808.3672 [hep-ph].

[51] M. L. Mangano, S. J. Parke and Z. Xu, *Duality and multi-gluon scattering*, Nucl. Phys. **B298** (1988), 653.

[52] R. Kleiss and H. Kuijf, *Multi-gluon cross-sections and five jet production at hadron colliders*, Nucl. Phys. **B312** (1989), 616.

[53] F. Maltoni, K. Paul, T. Stelzer and S. Willenbrock, *Color-flow decomposition of QCD amplitudes*, Phys. Rev. **D67** (2003), 014026, [hep-ph/0209271].

[54] V. del Duca, A. Frizzo and F. Maltoni, *Factorization of tree QCD amplitudes in the high-energy limit and in the collinear limit*, Nucl. Phys. **B568** (2000), 211–262, [hep-ph/9909464]. V. Del Duca, L. J. Dixon and F. Maltoni, *New color decompositions for gauge amplitudes at tree and loop level*, Nucl. Phys. **B571** (2000), 51–70, [hep-ph/9910563].

[55] L. J. Dixon, *Calculating scattering amplitudes efficiently*, hep-ph/9601359.

[56] S. Dittmaier, *Weyl-van der Waerden formalism for helicity amplitudes of massive particles*, Phys. Rev. **D59** (1999), 016007, [hep-ph/9805445].

[57] K. Hagiwara and D. Zeppenfeld, *Helicity amplitudes for heavy lepton production in e^+e^- annihilation*, Nucl. Phys. **B274** (1986), 1.

[58] H. Weyl, *The Theory of Groups and Quantum Mechanics*, Dover, New York, USA, 1931. B. L. van der Waerden, *Group Theory and Quantum Mechanics*, Springer, Berlin, Germany, 1974, Die Grundlehren der math. Wissenschaften.

[59] F. A. Berends and W. T. Giele, *Recursive calculations for processes with n gluons*, Nucl. Phys. **B306** (1988), 759.

[60] D. A. Kosower, *Light-cone recurrence relations for QCD amplitudes*, Nucl. Phys. **B335** (1990), 23.

[61] S. J. Parke and T. R. Taylor, *Amplitude for n-Gluon scattering*, Phys. Rev. Lett. **56** (1986), 2459.

[62] E. Witten, *Perturbative Gauge Theory as a String Theory in Twistor Space*, Commun. Math. Phys. **252** (2004), 189–258, [hep-th/0312171].

[63] F. Cachazo and P. Svrček, *Lectures on Twistor Strings and Perturbative Yang-Mills Theory*, PoS **RTN2005** (2005), 004, [hep-th/0504194].

[64] F. Cachazo, P. Svrček and E. Witten, *MHV vertices and tree amplitudes in gauge theory*, JHEP **09** (2004), 006, [hep-th/0403047].

[65] I. Bena, Z. Bern and D. A. Kosower, *Twistor-space recursive formulation of gauge-theory amplitudes*, Phys. Rev. **D71** (2005), 045008, [hep-th/0406133].

[66] R. Britto, F. Cachazo and B. Feng, *New recursion relations for tree amplitudes of gluons*, Nucl. Phys. **B715** (2005), 499–522, [hep-th/0412308]. R. Britto, F. Cachazo, B. Feng and E. Witten, *Direct Proof of the Tree-Level Scattering Amplitude Recursion Relation in Yang-Mills Theory*, Phys. Rev. Lett. **94** (2005), 181602, [hep-th/0501052].

[67] M.-X. Luo and C.-K. Wen, *Compact formulas for all tree amplitudes of six partons*, Phys. Rev. **D71** (2005), 091501, [hep-th/0502009]. D. de Florian and J. Zurita, *Seven parton amplitudes from recursion relations*, JHEP **05** (2006), 073, [hep-ph/0605291].

[68] L. J. Dixon, E. W. N. Glover and V. V. Khoze, *MHV rules for Higgs plus multi-gluon amplitudes*, JHEP **12** (2004), 015, [hep-th/0411092].

[69] M.-X. Luo and C.-K. Wen, *Recursion relations for tree amplitudes in super gauge theories*, JHEP **03** (2005), 004, [hep-th/0501121]. S. D. Badger, E. W. N. Glover, V. V. Khoze and P. Svrček, *Recursion relations for gauge theory amplitudes with massive particles*, JHEP **07** (2005), 025, [hep-th/0504159].

[70] K. J. Ozeren and W. J. Stirling, *MHV techniques for QED processes*, JHEP **11** (2005), 016, [hep-th/0509063].

[71] P. D. Draggiotis, R. H. P. Kleiss and C. G. Papadopoulos, *Multi-jet production in hadron collisions*, Eur. Phys. J. **C24** (2002), 447–458, [hep-ph/0202201].

[72] C. G. Papadopoulos and M. Worek, *Multi-parton cross sections at hadron colliders*, Eur. Phys. J. **C50** (2007), 843–856, [hep-ph/0512150]. A. Cafarella, C. G. Papadopoulos and M. Worek, *HELAC-PHEGAS: a generator for all parton level processes*, arXiv:0710.2427 [hep-ph].

[73] J. Alwall et al., *MadGraph/MadEvent v4: The new web generation*, JHEP **09** (2007), 028, [arXiv:0706.2334 [hep-ph]].

[74] F. A. Berends and W. Giele, *The six-gluon process as an example of Weyl-van der Waerden spinor calculus*, Nucl. Phys. **B294** (1987), 700. F. A. Berends, W. T. Giele and H. Kuijf, *Exact expressions for processes involving a vector boson and up to five partons*, Nucl. Phys. **B321** (1989), 39. F. A. Berends, W. T. Giele and H. Kuijf, *On six-jet production at hadron colliders*, Phys. Lett. **B232** (1989), 266.

[75] F. James, *Monte-Carlo phase space*, CERN-68-15.

[76] F. Caravaglios, M. L. Mangano, M. Moretti and R. Pittau, *A new approach to multi-jet calculations in hadron collisions*, Nucl. Phys. **B539** (1999), 215–232, [hep-ph/9807570].

[77] G. C. Blazey et al., *Run II jet physics*, hep-ex/0005012.

[78] `http://mlm.home.cern.ch/mlm/mcwshop03/mcwshop.html`.

[79] S. Jadach, *Foam: Multi-dimensional general purpose Monte Carlo generator with self-adapting simplical grid*, Comput. Phys. Commun. **130** (2000), 244–259, [`physics/9910004`].

[80] V. N. Gribov and L. N. Lipatov, *Deep inelastic e-p scattering in perturbation theory*, Sov. J. Nucl. Phys. **15** (1972), 438–450. L. N. Lipatov, *The parton model and perturbation theory*, Sov. J. Nucl. Phys. **20** (1975), 94–102. Y. L. Dokshitzer, *Calculation of the structure functions for deep inelastic scattering and e^+e^- annihilation by perturbation theory in quantum chromodynamics*, Sov. Phys. JETP **46** (1977), 641–653.

[81] G. Altarelli and G. Parisi, *Asymptotic freedom in parton language*, Nucl. Phys. **B126** (1977), 298–318.

[82] V. V. Sudakov, *Vertex parts at very high-energies in quantum electrodynamics*, Sov. Phys. JETP **3** (1956), 65–71.

[83] J. M. Cornwall and G. Tiktopoulos, *Infrared behavior of nonabelian gauge theories*, Phys. Rev. **D13** (1976), 3370. J. Frenkel and J. C. Taylor, *Exponentiation of leading infrared divergences in massless Yang-Mills theories*, Nucl. Phys. **B116** (1976), 185. E. C. Poggio and G. Pollak, *Nonleading contributions to the asymptotic behavior of the quark form-factor*, Phys. Lett. **B71** (1977), 135. A. V. Smilga, *Next-to-leading logarithms in the high-energy asymptotics of the quark form-factor and the jet cross-section*, Nucl. Phys. **B161** (1979), 449–468. V. V. Belokurov and N. I. Usyukina, *On exponentiation of the singlet quark form-factor in the leading logarithm approximation*, Phys. Lett. **B94** (1980), 251–253. G. P. Korchemsky, *Sudakov form-factor in QCD*, Phys. Lett. **B220** (1989), 629.

[84] J. C. Collins and G. Sterman, *Soft partons in QCD*, Nucl. Phys. **B185** (1981), 172. J. C. Collins and D. E. Soper, *Back-to-back jets in QCD*, Nucl. Phys. **B193** (1981), 381. J. C. Collins and D. E. Soper, *Parton distribution and decay functions*, Nucl. Phys. **B194** (1982), 445. J. C. Collins and D. E. Soper, *The theorems of perturbative QCD*, Ann. Rev. Nucl. Part. Sci. **37** (1987), 383–409. J. C. Collins, D. E. Soper and G. Sterman, *Soft gluons and factorization*, Nucl. Phys. **B308** (1988), 833–856. J. C. Collins, D. E. Soper and G. Sterman, *Factorization of hard processes in QCD*, Adv. Ser. Direct. High Energy Phys. **5** (1988), 1–91, [`hep-ph/0409313`].

[85] K. Konishi, A. Ukawa and G. Veneziano, *A simple algorithm for QCD jets*, Phys. Lett. **B78** (1978), 243. K. Konishi, A. Ukawa and G. Veneziano, *Jet calculus: A simple algorithm for resolving QCD jets*, Nucl. Phys. **B157** (1979), 45–107. J. Kalinowski,

K. Konishi and T. R. Taylor, *Jet calculus beyond leading logarithms*, Nucl. Phys. **B181** (1981), 221.

[86] R. D. Field, *Applications of perturbative QCD*, Addison-Wesley, Redwood City, USA, 1989, Frontiers in physics, 77.

[87] R. K. Ellis, W. J. Stirling and B. R. Webber, *QCD and collider physics*, ed. 1, vol. 8, Cambridge Monogr. Part. Phys. Nucl. Phys. Cosmol., 1996.

[88] R. P. Feynman, *Photon-hadron interactions*, Reading, MA, USA: Benjamin, 1972.

[89] T. Sjöstrand, *A model for initial state parton showers*, Phys. Lett. **B157** (1985), 321.

[90] S. Catani and L. Trentadue, *Resummation of the QCD perturbative series for hard processes*, Nucl. Phys. **B327** (1989), 323. A. H. Mueller, *On the multiplicity of hadrons in QCD jets*, Phys. Lett. **B104** (1981), 161–164. B. I. Ermolaev and V. S. Fadin, *Log-Log Asymptotic Form of Exclusive Cross-Sections in Quantum Chromodynamics*, JETP Lett. **33** (1981), 269–272. A. Bassetto, M. Ciafaloni, G. Marchesini and A. H. Mueller, *Jet multiplicity and soft gluon factorization*, Nucl. Phys. **B207** (1982), 189. Y. L. Dokshitzer, V. S. Fadin and V. A. Khoze, *Double Logs of Perturbative QCD for Parton Jets and Soft Hadron Spectra*, Z. Phys. **C15** (1982), 325.

[91] A. E. Chudakov, Ser. Fiz., Izv. Akad. Nauk SSSR **19** (1955), 650.

[92] S. Catani and M. H. Seymour, *A general algorithm for calculating jet cross sections in NLO QCD*, Nucl. Phys. **B485** (1997), 291–419, [hep-ph/9605323].

[93] M. H. Seymour, *Matrix-element corrections to parton shower algorithms*, Comp. Phys. Commun. **90** (1995), 95–101, [hep-ph/9410414]. E. Norrbin and T. Sjöstrand, *QCD radiation off heavy particles*, Nucl. Phys. **B603** (2001), 297–342, [hep-ph/0010012].

[94] G. Corcella and M. H. Seymour, *Matrix element corrections to parton shower simulations of heavy quark decay*, Phys. Lett. **B442** (1998), 417–426, [hep-ph/9809451].

[95] F. Krauss, A. Schälicke, S. Schumann and G. Soff, *Simulating W/Z + jets production at the Fermilab Tevatron*, hep-ph/0409106. F. Krauss, A. Schälicke, S. Schumann and G. Soff, *Simulating W/Z + jets production at the CERN LHC*, Phys. Rev. **D72** (2005), 054017, [hep-ph/0503280]. T. Gleisberg, F. Krauss, A. Schälicke, S. Schumann and J.-C. Winter, *Studying W^+W^- production at the Fermilab Tevatron with SHERPA*, Phys. Rev. **D72** (2005), 034028, [hep-ph/0504032].

[96] S. Catani, Y. L. Dokshitzer, M. Olsson, G. Turnock and B. R. Webber, *New clustering algorithm for multijet cross sections in e^+e^- annihilation*, Phys. Lett. **B269** (1991), 432–438. S. Catani, Y. L. Dokshitzer and B. R. Webber, *The $k_\perp$ clustering algorithm for jets in deep inelastic scattering and hadron collisions*, Phys. Lett. **B285** (1992), 291–299. S. Catani, Y. L. Dokshitzer, M. H. Seymour and B. R. Webber,

Longitudinally-invariant $k_\perp$-clustering algorithms for hadron–hadron collisions, Nucl. Phys. **B406** (1993), 187–224.

[97] L. Lönnblad, *Correcting the colour-dipole cascade model with fixed order matrix elements*, JHEP **05** (2002), 046, [hep-ph/0112284].

[98] M. L. Mangano, M. Moretti and R. Pittau, *Multijet matrix elements and shower evolution in hadronic collisions: $Wb\bar{b}$ + n-jets as a case study*, Nucl. Phys. **B632** (2002), 343–362, [hep-ph/0108069].

[99] S. Höche et al., *Matching Parton Showers and Matrix Elements*, hep-ph/0602031.

[100] J. Alwall et al., *Comparative study of various algorithms for the merging of parton showers and matrix elements in hadronic collisions*, Eur. Phys. J. **C53** (2008), 473–500, [arXiv:0706.2569 [hep-ph]].

[101] D. Amati, R. Petronzio and G. Veneziano, *Relating hard QCD processes through universality of mass singularities*, Nucl. Phys. **B140** (1978), 54. D. Amati, R. Petronzio and G. Veneziano, *Relating hard QCD processes through universality of mass singularities. 2*, Nucl. Phys. **B146** (1978), 29–49.

[102] G. Gustafson, *Dual description of a confined colour field*, Phys. Lett. **B175** (1986), 453. G. Gustafson and U. Pettersson, *Dipole formulation of QCD cascades*, Nucl. Phys. **B306** (1988), 746.

[103] L. Lönnblad, *Ariadne version 4: A program for simulation of QCD cascades implementing the colour dipole model*, Comput. Phys. Commun. **71** (1992), 15–31.

[104] Z. Nagy and D. E. Soper, *Matching parton showers to NLO computations*, JHEP **10** (2005), 024, [hep-ph/0503053]. Z. Nagy and D. E. Soper, *A new parton shower algorithm: Shower evolution, matching at leading and next-to-leading order level*, hep-ph/0601021.

[105] M. Dinsdale, M. Ternick and S. Weinzierl, *Parton showers from the dipole formalism*, Phys. Rev. **D76** (2007), 094003, [arXiv:0709.1026 [hep-ph]].

[106] A. Banfi, G. P. Salam and G. Zanderighi, *Infrared-safe definition of jet flavour*, Eur. Phys. J. **C47** (2006), 113–124, [hep-ph/0601139].

[107] S. Catani, S. Dittmaier, M. H. Seymour and Z. Trocsanyi, *The dipole formalism for next-to-leading order QCD calculations with massive partons*, Nucl. Phys. **B627** (2002), 189–265, [hep-ph/0201036].

[108] G. Ossola, C. G. Papadopoulos and R. Pittau, *Reducing full one-loop amplitudes to scalar integrals at the integrand level*, Nucl. Phys. **B763** (2007), 147–169, [hep-ph/0609007].

[109] S. Catani, S. Dittmaier and Z. Trocsanyi, *One-loop singular behaviour of QCD and SUSY QCD amplitudes with massive partons*, Phys. Lett. **B500** (2001), 149–160, [hep-ph/0011222].

[110] T. Sjöstrand, *PYTHIA 5.7 and JETSET 7.4 Physics and Manual*, hep-ph/9508391.

[111] S. Höche, F. Krauss, S. Schumann and F. Siegert, *A comprehensive approach to CKKW merging*, in preparation.

[112] M. Bengtsson and T. Sjöstrand, *A comparative study of coherent and non-coherent parton shower evolution*, Nucl. Phys. **B289** (1987), 810.

[113] Y. L. Dokshitzer, V. A. Khoze, A. H. Mueller and S. I. Troyan, *Basics of perturbative QCD*, Gif-sur-Yvette, France: Ed. Frontieres, 1991. A. Bassetto, M. Ciafaloni and G. Marchesini, *Jet structure and infrared sensitive quantities in perturbative QCD*, Phys. Rept. **100** (1983), 201–272.

[114] K. Hamilton and P. Richardson, *A simulation of QCD radiation in top quark decays*, JHEP **02** (2007), 069, [hep-ph/0612236].

[115] G. Rodrigo and F. Krauss, *Resummed jet rates for heavy quark production in e^+e^- annihilation*, Eur. Phys. J. **C33** (2004), 457–459, [hep-ph/0309325].

[116] S. Mrenna and P. Richardson, *Matching matrix elements and parton showers with HERWIG and PYTHIA*, JHEP **05** (2004), 040, [hep-ph/0312274].

[117] A. Schälicke and F. Krauss, *Implementing the ME+PS merging algorithm*, JHEP **07** (2005), 018, [hep-ph/0503281].

[118] T. Matsuura, S. C. van der Marck and W. L. van Neerven, *The calculation of the second order soft and virtual contributions to the Drell-Yan cross section*, Nucl. Phys. **B319** (1989), 570.

[119] S. Catani and L. Trentadue, *Fermion pair exponentiation in QED*, JETP Lett. **51** (1990), 83.

[120] B. Andersson, G. Gustafson and L. Lönnblad, *Gluon splitting in the color dipole cascades*, Nucl. Phys. **B339** (1990), 393–406.

[121] B. Andersson, G. Gustafson, L. Lönnblad and U. Pettersson, *Coherence effects in deep inelastic scattering*, Z. Phys. **C43** (1989), 625. L. Lönnblad, *Small x effects in W + jets production at the Tevatron*, Nucl. Phys. **B458** (1996), 215–230, [hep-ph/9508261].

[122] A. Aktas et al., H1 collaboration, *Forward jet production in deep inelastic scattering at HERA*, Eur. Phys. J. **C46** (2006), 27–42, [hep-ex/0508055].

[123] L. Lönnblad, *Rapidity gaps and other final state properties in the color dipole model for deep inelastic scattering*, Z. Phys. **C65** (1995), 285–292.

[124] N. Lavesson and L. Lönnblad, *W+jets matrix elements and the dipole cascade*, JHEP **07** (2005), 054, [hep-ph/0503293].

[125] T. Stelzer and W. F. Long, *Automatic generation of tree level helicity amplitudes*, Comput. Phys. Commun. **81** (1994), 357–371, [hep-ph/9401258].

[126] F. Gianotti et al., *Physics potential and experimental challenges of the LHC luminosity upgrade*, Eur. Phys. J. **C39** (2005), 293–333, [hep-ph/0204087].

[127] T. Gleisberg, F. Krauss, C. G. Papadopoulos, A. Schälicke and S. Schumann, *Cross sections for multi-particle final states at a linear collider*, Eur. Phys. J. **C34** (2004), 173–180, [hep-ph/0311273].

[128] J. Alwall et al., *A standard format for Les Houches Event Files*, Comput. Phys. Commun. **176** (2007), 300–304, [hep-ph/0609017].

[129] F. Abe et al., CDF collaboration, *Measurement of Jet Multiplicity in W Events Produced in $p\bar{p}$ Collisions at $\sqrt{s} = 1.8$ Tev*, Phys. Rev. Lett. **70** (1993), 4042–4046. F. Abe et al., CDF collaboration, *Properties of Jets in W Boson Events from 1.8 TeV $\bar{p}p$ collisions*, Phys. Rev. Lett. **79** (1997), 4760–4765, [hep-ex/9709016]. A. A. Affolder et al., CDF collaboration, *Test of enhanced leading order QCD in W boson plus jets events from 1.8 TeV $\bar{p}p$ collisions*, Phys. Rev. **D63** (2001), 072003. S. Abachi et al., DØ collaboration, *Study of the Strong Coupling Constant Using W + Jet Processes*, Phys. Rev. Lett. **75** (1995), 3226–3231.

[130] A. Messina, CDF collaboration, *Measurement of the W + Jet Cross Section at CDF*, Braz. J. Phys. **37** (2007), 840–842, [arXiv:0708.1380 [hep-ex]].

[131] V. M. Abazov et al., DØ collaboration, *Measurement of the ratios of the $Z/\gamma^* + \geq n$ jet production cross sections to the total inclusive Z/γ^* cross section in $p\bar{p}$ collisions at $\sqrt{s}$=1.96 TeV*, Phys. Lett. **B658** (2008), 112–119, [hep-ex/0608052].

[132] CDF collaboration, `http://www-cdf.fnal.gov/physics/new/qcd/zjets_07/public.pdf`.

[133] M. L. Mangano, M. Moretti, F. Piccinini and M. Treccani, *Matching matrix elements and shower evolution for top-pair production in hadronic collisions*, JHEP **01** (2007), 013, [hep-ph/0611129].

[134] M. H. Seymour, `http://hepwww.rl.ac.uk/theory/seymour/ktclus/`.

[135] N. Brook, R. G. Waugh, T. Carli, R. Mohr and M. Sutton, *Tuning Monte Carlo event generators to HERA data*, Prepared for Workshop on Future Physics at HERA (Preceded by meetings 25-26 Sep 1995 and 7-9 Feb 1996 at DESY), Hamburg, Germany, 30-31 May 1996.

[136] S. Catani, M. Ciafaloni and F. Hautmann, *High energy factorization and small-x heavy flavour production*, Nucl. Phys. **B366** (1991), 135–188. J. C. Collins and R. K. Ellis, *Heavy quark production in very high energy hadron collisions*, Nucl. Phys. **B360**

(1991), 3–30. E. M. Levin, M. G. Ryskin, Y. M. Shabelski and A. G. Shuvaev, *Heavy Quark Production in Parton Model and in QCD*, Sov. J. Nucl. Phys. **54** (1991), 867–871.

[137] P. Hägler, R. Kirschner, A. Schäfer, L. Szymanowski and O. V. Teryaev, *Direct J/ψ hadroproduction in k_T-factorization and the color octet mechanism*, Phys. Rev. **D63** (2001), 077501, [hep-ph/0008316]. A. V. Lipatov and N. P. Zotov, *Higgs boson production at hadron colliders in the k_T-factorization approach*, Eur. Phys. J. **C44** (2005), 559–566, [hep-ph/0501172]. A. V. Lipatov and N. P. Zotov, *Prompt photon photoproduction at DESY HERA in the k_T-factorization approach*, Phys. Rev. **D72** (2005), 054002, [hep-ph/0506044].

[138] M. G. Ryskin, A. G. Shuvaev and Y. M. Shabelski, *Charm Hadroproduction within k_T-Factorization Approach*, Phys. Atom. Nucl. **64** (2001), 120–131, [hep-ph/9907507].

[139] B. Andersson et al., Small x collaboration, *Small x phenomenology: summary and status*, Eur. Phys. J. **C25** (2002), 77–101, [hep-ph/0204115].

[140] E. A. Kuraev, L. N. Lipatov and V. S. Fadin, *The Pomeranchuk Singularity in Nonabelian Gauge Theories*, Sov. Phys. JETP **45** (1977), 199–204. I. I. Balitsky and L. N. Lipatov, *The Pomeranchuk Singularity in Quantum Chromodynamics*, Sov. J. Nucl. Phys. **28** (1978), 822–829.

[141] L. N. Lipatov, *Reggeization of the Vector Meson and the Vacuum Singularity in Nonabelian Gauge Theories*, Sov. J. Nucl. Phys. **23** (1976), 338–345.

[142] B. Andersson, G. Gustafson and J. Samuelsson, *The linked dipole chain model for DIS*, Nucl. Phys. **B467** (1996), 443–478. B. Andersson, G. Gustafson, H. Kharraziha and J. Samuelsson, *Structure functions and general final state properties in the linked dipole chain model*, Z. Phys. **C71** (1996), 613–624.

[143] H. Kharraziha and L. Lönnblad, *The linked dipole chain Monte Carlo*, JHEP **03** (1998), 006, [hep-ph/9709424].

[144] M. Ciafaloni, *Coherence effects in initial jets at small Q^2/s*, Nucl. Phys. **B296** (1988), 49–74. S. Catani, F. Fiorani and G. Marchesini, *QCD coherence in initial state radiation*, Phys. Lett. **B234** (1990), 339–345. S. Catani, F. Fiorani and G. Marchesini, *Small-x behavior of initial state radiation in perturbative QCD*, Nucl. Phys. **B336** (1990), 18–85. G. Marchesini, *QCD coherence in the structure function and associated distributions at small x*, Nucl. Phys. **B445** (1995), 49–80, [hep-ph/9412327].

[145] G. Marchesini and B. R. Webber, *Simulation of QCD initial state radiation at small x*, Nucl. Phys. **B349** (1991), 617–634. H. Jung and G. P. Salam, *Hadronic final state predictions from CCFM: the hadron-level Monte Carlo generator CASCADE*, Eur. Phys.

J. **C19** (2001), 351–360, [hep-ph/0012143]. H. Jung, *The CCFM Monte Carlo generator CASCADE*, Comput. Phys. Commun. **143** (2002), 100–111, [hep-ph/0109102]. K. Golec-Biernat, S. Jadach, W. Płaczek, P. Stephens and M. Skrzypek, *Markovian Monte Carlo solutions of the one-loop CCFM equations*, hep-ph/0703317.

[146] J. Kwiecinski, C. A. M. Lewis and A. D. Martin, *Observable jets from the BFKL chain*, Phys. Rev. **D54** (1996), 6664–6673, [hep-ph/9606375].

[147] C. R. Schmidt, *Monte Carlo Solution to the Balitsky-Fadin-Kuraev-Lipatov Equation for Resummation in Perturbative QCD*, Phys. Rev. Lett. **78** (1997), 4531–4535, [hep-ph/9612454].

[148] L. H. Orr and W. J. Stirling, *Dijet production at hadron-hadron colliders in the Balitskii-Fadin-Kuraev-Lipatov approach*, Phys. Rev. **D56** (1997), 5875–5884, [hep-ph/9706529].

[149] J. R. Andersen and A. Sabio-Vera, *Solving the BFKL equation in the next-to-leading approximation*, Phys. Lett. **B567** (2003), 116–124, [hep-ph/0305236]. J. R. Andersen and A. Sabio-Vera, *The gluon Green's function in the BFKL approach at next-to-leading logarithmic accuracy*, Nucl. Phys. **B679** (2004), 345–362, [hep-ph/0309331]. J. R. Andersen, *Quark-antiquark contribution to the fully exclusive BFKL Evolution at next-to-leading logarithmic accuracy*, Phys. Rev. **D74** (2006), 114008, [hep-ph/0611011].

[150] J. R. Andersen, *On the role of NLL corrections and energy conservation in the high energy evolution of QCD*, Phys. Lett. **B639** (2006), 290–293, [hep-ph/0602182].

[151] M. A. Kimber, A. D. Martin and M. G. Ryskin, *Unintegrated parton distributions and prompt photon hadroproduction*, Eur. Phys. J. **C12** (2000), 655–661, [hep-ph/9911379]. M. A. Kimber, A. D. Martin and M. G. Ryskin, *Unintegrated parton distributions*, Phys. Rev. **D63** (2001), 114027, [hep-ph/0101348].

[152] G. Watt, A. D. Martin and M. G. Ryskin, *Unintegrated parton distributions and inclusive jet production at HERA*, Eur. Phys. J. **C31** (2003), 73–89, [hep-ph/0306169].

[153] V. Del Duca and C. R. Schmidt, *Balitsky-Fadin-Kuraev-Lipatov approximation versus $\mathcal{O}(\alpha_s^3)$ corrections to large-rapidity dijet production*, Phys. Rev. **D51** (1995), 2150–2158, [hep-ph/9407359]. J. Kwieciński, A. D. Martin and P. J. Sutton, *Constraints on gluon evolution at small x*, Z. Phys. **C71** (1996), 585–594, [hep-ph/9602320].

[154] R. S. Thorne, *NLO BFKL equation, running coupling, and renormalization scales*, Phys. Rev. **D60** (1999), 054031, [hep-ph/9901331].

[155] G. Watt, A. D. Martin and M. G. Ryskin, *Unintegrated parton distributions and electroweak boson production at hadron colliders*, Phys. Rev. **D70** (2004), 014012, [hep-ph/0309096].

[156] J. R. Forshaw and D. A. Ross, *Quantum chromodynamics and the pomeron*, Cambridge, UK: Univ. Pr., 1997, Cambridge lecture notes in physics. 9.

[157] V. Barone and E. Predazzi, *High-energy particle diffraction*, Berlin, Germany: Springer, 2002.

[158] T. Regge, *Introduction to complex orbital momenta*, Nuovo Cim. **14** (1959), 951. T. Regge, *Bound states, shadow states and Mandelstam representation*, Nuovo Cim. **18** (1960), 947–956.

[159] A. Donnachie and P. V. Landshoff, *Total cross sections*, Phys. Lett. **B296** (1992), 227–232, [hep-ph/9209205].

[160] L. B. Okun and I. I. Pomeranchuk, *Isotopic invariance and cross section of interaction of high energy pi-mesons and nucleons with nucleons*, Sov. Phys. JETP **3** (1956), 307. I. I. Pomeranchuk, *Equality of the nucleon and antinucleon total interaction cross section at high energies*, Sov. Phys. JETP **7** (1958), 499.

[161] V. N. Gribov, I. Y. Pomeranchuk and K. A. Ter-Martirosian, *Moving Branch Points in j Plane and Regge-Pole Unitarity Conditions*, Phys. Rev. **139** (1965), B184–B202.

[162] L. F. Foldy and R. F. Peierls, *Isotopic Spin of Exchanged Systems*, Phys. Rev. **130** (1963), 1585–1589.

[163] V. del Duca, *Equivalence of the Parke-Taylor and the Fadin-Kuraev-Lipatov amplitudes in the high-energy limit*, Phys. Rev. **D52** (1995), 1527–1534, [hep-ph/9503340].

[164] S. Höche, F. Krauss and T. Teubner, *Multijet events in the k_T-factorisation scheme*, arXiv:0705.4577 [hep-ph].

[165] T. Sjöstrand, L. Lönnblad, S. Mrenna and P. Skands, *PYTHIA 6.3 Physics and Manual*, hep-ph/0308153.

[166] L. V. Gribov, E. M. Levin and M. G. Ryskin, *Semihard processes in QCD*, Phys. Rept. **100** (1983), 1–150.

[167] A. Abulencia et al., CDF collaboration, *Measurement of the inclusive jet cross section using the k_T algorithm in $p\bar{p}$ collisions at $\sqrt{s}$ = 1.96 TeV with the CDF II detector*, hep-ex/0701051.

[168] S. Abachi et al., DØ collaboration, *Azimuthal Decorrelation of Jets Widely Separated in Rapidity*, Phys. Rev. Lett. **77** (1996), 595–600, [hep-ex/9603010].

Publication list

Publications

- S. Höche, F. Krauss and T. Teubner,
  Multijet events in the k_T-factorisation scheme,
  to be published in Eur. Phys. J. **C**, [arXiv:0705.4577 [hep-ph]].

- J. Alwall et al.,
  Comparative study of various algorithms for the merging of parton showers and matrix elements in hadronic collisions,
  Eur. Phys. J. **C53** (2008), 473–500, [arXiv:0706.2569 [hep-ph]].

- C. Duhr, S. Höche and F. Maltoni,
  Color-dressed recursive relations for multi-parton amplitudes,
  JHEP **08** (2006), 062, [hep-ph/0607057].

- T. Gleisberg, S. Höche, F. Krauss, A. Schälicke, S. Schumann and J. Winter,
  Sherpa 1.α, a proof-of-concept version,
  JHEP **02** (2004), 056, [hep-ph/0311263].

Preprints

- T. Gleisberg and S. Höche,
  Comix, a new matrix element generator,
  arXiv:0808.3674 [hep-ph].

- T. Gleisberg, S. Höche, F. Krauss and R. Matyskiewicz,
  How to calculate colourful cross-sections efficiently,
  arXiv:0808.3672 [hep-ph].

- A. Dedes, T. Figy, S. Höche, F. Krauss and T. E. J. Underwood,
  Searching for Nambu-Goldstone Bosons at the LHC,
  arXiv:0807.4666 [hep-ph].

Conference proceedings

- J. Archibald et al.,
  Simulation of $\gamma\gamma$ interactions in hadron collisions with Sherpa,
  to be published in Nucl. Phys. **B** Proc. Suppl.

- T. Gleisberg et al.,
  New trends in modern event generators,
  arXiv:0705.4648 [hep-ph].

- S. Höche et al.,
  Matching Parton Showers and Matrix Elements,
  hep-ph/0602031.

- S. Alekhin et al.,
  HERA and the LHC - A workshop on the implications of HERA for LHC physics: Proceedings Part A and B,
  hep-ph/0601012 and hep-ph/0601013.

- T. Gleisberg et al.,
  Event generator for the LHC,
  Nucl. Instrum. Meth. **A559** (2006), 242–245, [hep-ph/0508315].

- T. Gleisberg, S. Höche, F. Krauss, A. Schälicke, S. Schumann, G. Soff and J. Winter,
  Predictions for multi-particle final states with SHERPA,
  Czech. J. Phys. **55** (2005), B529–B536, [hep-ph/0409122].

- T. Gleisberg, S. Höche, F. Krauss, A. Schälicke, S. Schumann, J. Winter and G. Soff,
  Towards a fragmentation model for SHERPA,
  hep-ph/0408245.

- T. Gleisberg, S. Höche, F. Krauss, A. Schälicke, S. Schumann, J. Winter and G. Soff,
  New tools for automatic cross section calculation,
  hep-ph/0407366.

- T. Gleisberg, S. Höche, F. Krauss, A. Schälicke, S. Schumann, J. Winter and G. Soff, *Monte Carlo models at the LHC*, hep-ph/0407365.

- A. Schälicke, T. Gleisberg, S. Höche, S. Schumann, J. Winter, F. Krauss and G. Soff, *Event generator for particle production in high-energy collisions*, Prog. Part. Nucl. Phys. **53** (2004), 329–338, [hep-ph/0311270].